

AD _____

Award Number: DAMD17-01-1-0809

TITLE: Influences of Nutrition and Physical Forces on Bone Structure/Function
Properties

PRINCIPAL INVESTIGATOR: Steven A. Goldstein, Ph.D.
Barbara McCreadie, Ph.D.
Michael Morris, Ph.D.

CONTRACTING ORGANIZATION: University of Michigan
Ann Arbor, MI 48109-1274

REPORT DATE: October 2005

TYPE OF REPORT: Final

PREPARED FOR: U.S. Army Medical Research and Materiel Command
Fort Detrick, Maryland 21702-5012

DISTRIBUTION STATEMENT: Approved for Public Release;
Distribution Unlimited

The views, opinions and/or findings contained in this report are those of the author(s) and should not be construed as an official Department of the Army position, policy or decision unless so designated by other documentation.

REPORT DOCUMENTATION PAGE

Form Approved
OMB No. 0704-0188

Public reporting burden for this collection of information is estimated to average 1 hour per response, including the time for reviewing instructions, searching existing data sources, gathering and maintaining the data needed, and completing and reviewing this collection of information. Send comments regarding this burden estimate or any other aspect of this collection of information, including suggestions for reducing this burden to Department of Defense, Washington Headquarters Services, Directorate for Information Operations and Reports (0704-0188), 1215 Jefferson Davis Highway, Suite 1204, Arlington, VA 22202-4302. Respondents should be aware that notwithstanding any other provision of law, no person shall be subject to any penalty for failing to comply with a collection of information if it does not display a currently valid OMB control number. PLEASE DO NOT RETURN YOUR FORM TO THE ABOVE ADDRESS.

1. REPORT DATE (DD-MM-YYYY) 01-10-2005		2. REPORT TYPE Final		3. DATES COVERED (From - To) 17 Sep 01 – 16 Sep 05	
4. TITLE AND SUBTITLE Influences of Nutrition and Physical Forces on Bone Structure/Function Properties				5a. CONTRACT NUMBER	
				5b. GRANT NUMBER DAMD17-01-1-0809	
				5c. PROGRAM ELEMENT NUMBER	
6. AUTHOR(S) Steven A. Goldstein, Ph.D., Barbara McCreddie, Ph.D., Michael Morris, Ph.D. E-Mail: steveglld@umich.edu				5d. PROJECT NUMBER	
				5e. TASK NUMBER	
				5f. WORK UNIT NUMBER	
7. PERFORMING ORGANIZATION NAME(S) AND ADDRESS(ES) University of Michigan Ann Arbor, MI 48109-1274				8. PERFORMING ORGANIZATION REPORT NUMBER	
9. SPONSORING / MONITORING AGENCY NAME(S) AND ADDRESS(ES) U.S. Army Medical Research and Materiel Command Fort Detrick, Maryland 21702-5012				10. SPONSOR/MONITOR'S ACRONYM(S)	
				11. SPONSOR/MONITOR'S REPORT NUMBER(S)	
12. DISTRIBUTION / AVAILABILITY STATEMENT Approved for Public Release; Distribution Unlimited					
13. SUPPLEMENTARY NOTES					
14. ABSTRACT The specific goals of this research program were to contribute to two major objectives in support of reducing the incidence of fracture: a. The development and application of micro-imaging and testing techniques in animal models to study bone structure function properties. b. Exploring the influence of calcium and vitamin D metabolism and physical forces on bone integrity. Using mouse models, this study demonstrated that the use of micro-imaging techniques (MicroCT, Raman Spectroscopy) and micro-mechanical testing methods (femoral 4 pt. bending, vertebral compression, tibial torsion) can effectively characterize the morphologic and mechanical properties of bone and how they may be altered by nutrition, exercise and gender. While the results illustrated little or no effect of exercise, the properties of the bone are significantly influenced by mouse strain, gender, and calcium intake.					
15. SUBJECT TERMS Bone Biomechanics, Mechanotransduction, Nutrition, Fragility, Osteoporosis					
16. SECURITY CLASSIFICATION OF:			17. LIMITATION OF ABSTRACT	18. NUMBER OF PAGES	19a. NAME OF RESPONSIBLE PERSON
a. REPORT U	b. ABSTRACT U	c. THIS PAGE U			USAMRMC
			UU	103	19b. TELEPHONE NUMBER (include area code)

Table of Contents

Cover.....	1
SF 298.....	2
Table of Contents.....	3
Introduction.....	4
Body.....	4
Key Research Accomplishments.....	12
Reportable Outcomes.....	13
Conclusions.....	14
References.....	None
Personnel List.....	16
Appendices.....	17

A. Introduction

It is well known that the maintenance and adaptation of bone integrity is dependent on a complex interaction of metabolic and environmental factors (mechanical stresses, nutritional status). Unfortunately, the specific relationship between these factors and the biomechanical competence of bone tissue remains incompletely quantified. As a result, strategies for preventing or effectively treating bone fragility or enhancing general bone health are far from being optimized. The specific goals of this research program were to contribute to two major objectives in support of reducing the incidence of fracture:

- a. The development and application of micro-imaging and testing techniques in animal models to study bone structure function properties.
- b. Exploring the influence of calcium and vitamin D metabolism and physical forces on bone integrity.

B. Body

The final progress report of this research program is described below. As will be gleaned from the report, essentially all of the work and tasks that were approved by the USAMRMC were accomplished, although some of the specific methodologic details varied from the original proposal. These few variations (as noted within the text) were implemented as a result of the ongoing findings of the study. It is also important to note that we undertook and have nearly completed some additional studies (funded from our own discretionary sources) that were inspired by the data from our study and others in the field. These will also be noted in the report.

A summary of the important research program results is provided below. The majority of the results and accomplishments are presented in the form of figures and tables. Methodologic details are freely available to any interested parties by contacting us directly. While the body of the report has a summary of selected research results, all of the data is presented in the Appendix.

1. Calcium Intake Studies

These studies were designed to test three primary hypotheses and 2 subhypotheses and used two specific mouse strains (C57BL/6J and C3H/HeJ):

H1: Reductions in dietary calcium results in changes in mechanical properties.

H1A: The effects are dependent on genetic background

H1B: The effects are dependent on dose of calcium

H2: The effects of altering calcium is gender dependent.

H3: The effects of altered calcium intake is influenced by intense exercise.

There were 24 experimental groups with variations in calcium dose (low intake (0.1%), normal (0.4% to 0.6%) and high (1.0%)), gender, and exercise (cage exercise and intense treadmill running).

The exercise involved running on a treadmill system developed as part of the research program. Since a primary aim of the program was to explore the use of microimaging and micromechanical testing methods for evaluating skeletal alteration in mouse models, the studies utilized numerous outcome measures including; MicroCT, whole bone mechanical tests, microspecimen preparation and mechanical tests, Raman spectroscopy and histologic analysis. By way of summary, the following numbers of animals were completed in the program:

Femoral Analyses

Studies	MicroCT scan	MicroCT analysis	Mechanical testing	Raman spectroscopy
Completed	392	392	368	130
Remaining to complete	0	0	0	0

Vertebral Body analyses

Studies	MicroCT scan	MicroCT analysis	Mechanical testing
Completed	382	381	394
Remaining to complete	0	0	0

Microspecimen production

Approximately **100 microspecimens** were produced for the program from these animals and the testing procedures were calibrated and validated. While the aim of exploring techniques for measuring ECM/tissue properties was completed, no changes in fundamental tissue properties were found. As a result, no further testing was performed.

Raman spectroscopy

More than **130 specimens** were prepared and analyzed using Raman spectroscopy. The results of these tests will be presented graphically below. This very time consuming procedure demonstrated very valuable methodology that we have already employed in other studies of mouse skeleton phenotyping.

Histologic analysis

The histologic studies were performed as a method of examining the character of the tissue morphology to determine if any specific pathologic conditions were induced by the exercise or diet alterations. More than **125 bones** were examined histologically; representative animals from every experimental group. As will be shown below, no pathologic features were noted.

Additional studies

As will be seen in the data graphs provided below, the effect of exercise was unexpectedly low in the femurs of the animals. This surprising finding lead us to explore other work designed to evaluate the effect of loading on bone by others in the scientific community. As a result of this search, we found at least one study that found exercise induced morphologic alterations in the tibia of mice. Based on a hypothesis that there might be a site-specific (anatomic site) effect, we extracted the tibias from 60 mice and did MicroCT analysis on them. As will be described, we found only a small effect of exercise on the bone morphology of the tibia as well.

Selected Results

A series of graphical results are presented below that summarize the results of the studies on nutrition, gender, and exercise on bone properties. A brief statement is provided with each to summarize the important attribute of the findings.

Figure 1: Example of mechanical femoral data. The results demonstrate no effect of exercise, although there were significant differences in properties as a function of strain and calcium intake. Similar effects were found for ultimate and yield properties, as well as all post-yield data.

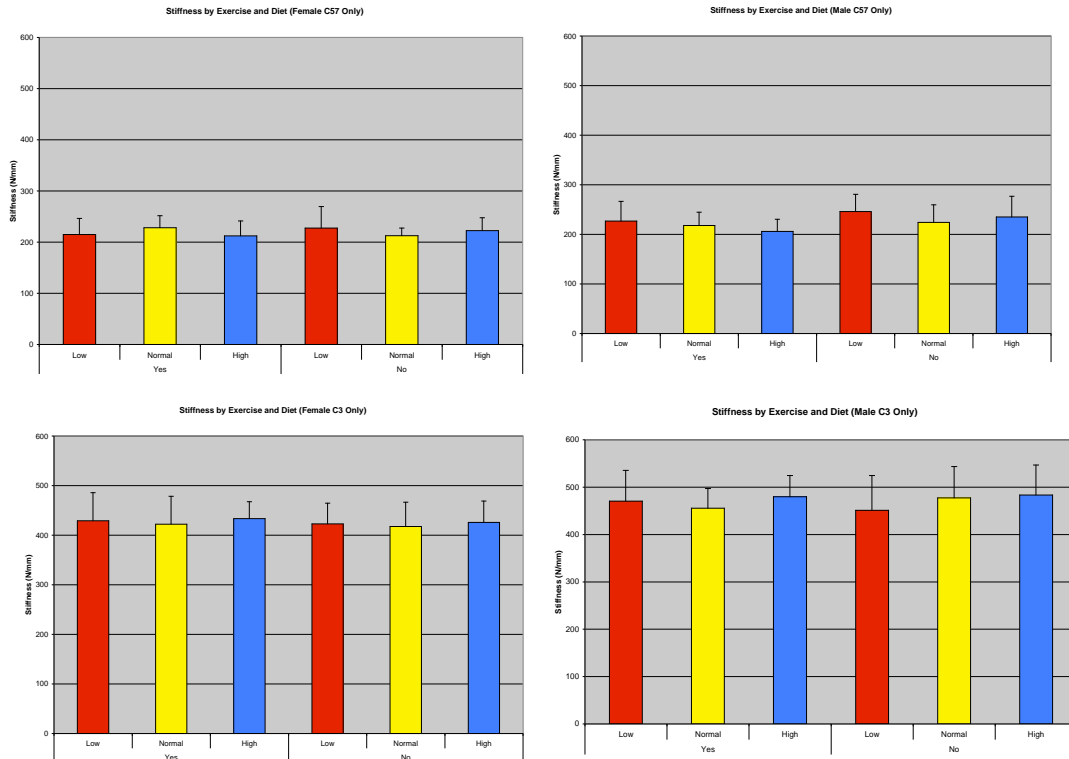


Figure 2: Example of bone mineral density data (from MicroCT). Once again, there was no effect of exercise, but there were significant differences across the mouse strains.

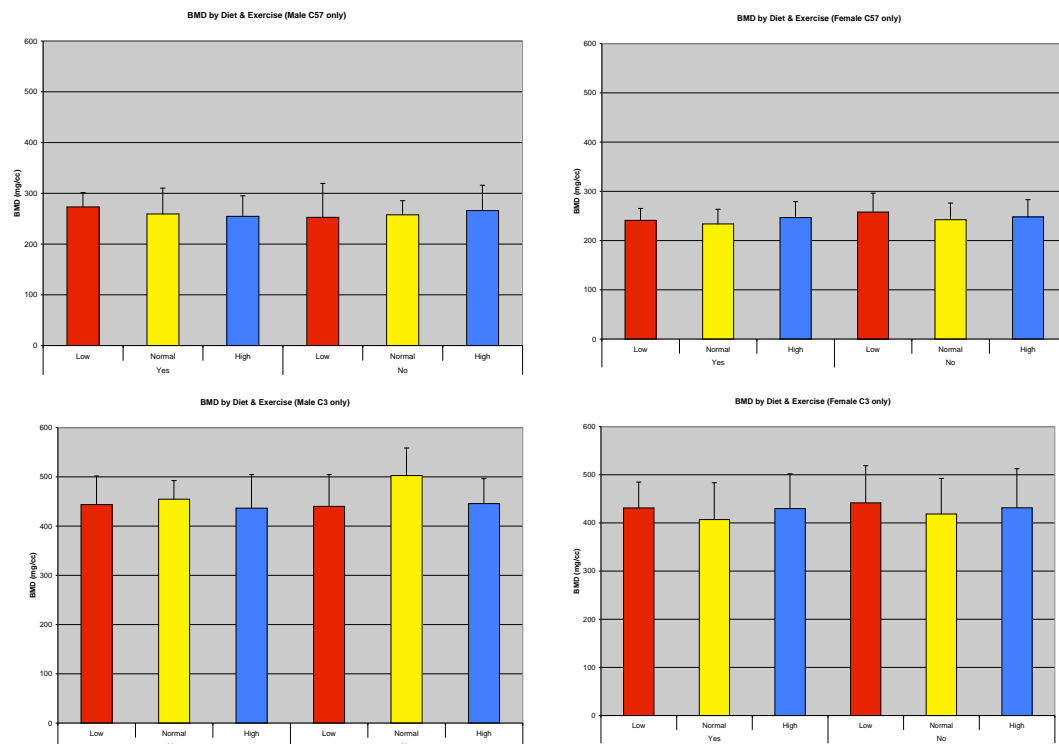


Figure 3: Raman spectroscopy data is illustrated. There is both a dose (calcium nutrition) and strain effect demonstrated. Interesting, the direction of the dose response is opposite in the C57 versus the C3He animals. This might suggest a fundamental genetic variation in response as a function of mouse genotype. It also demonstrates the power of the Raman technology to evaluate bone response.

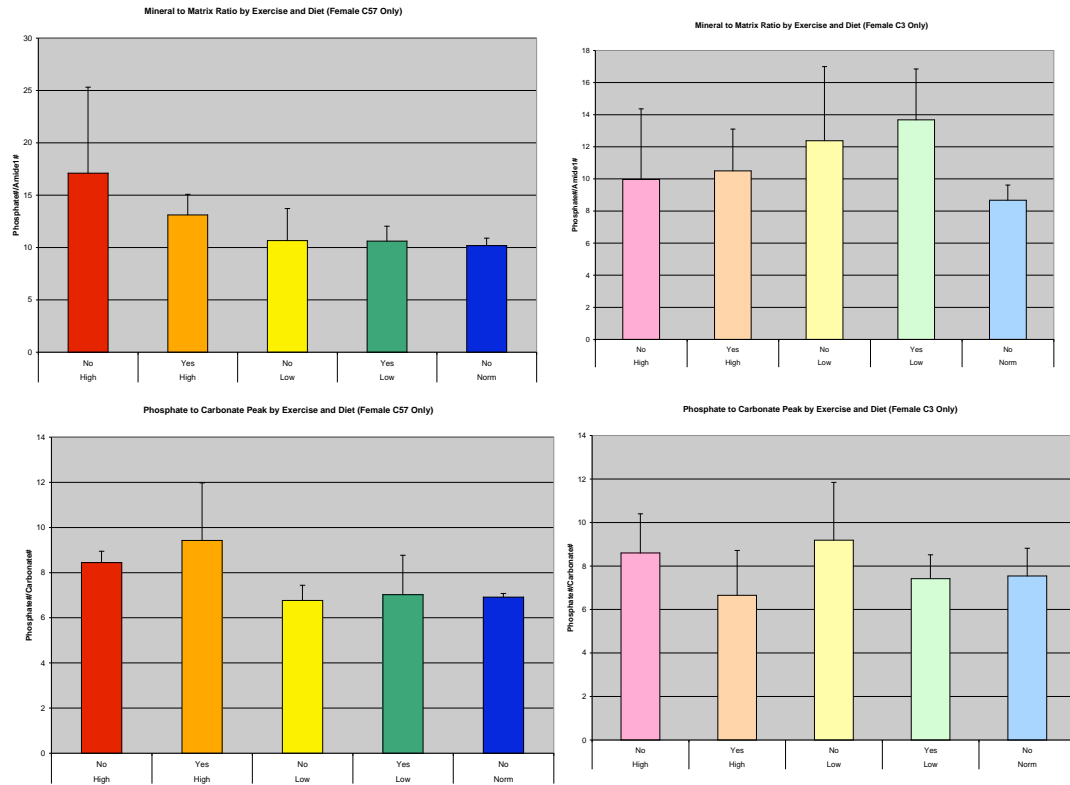


Figure 4: The effect of diet and exercise on mid-diaphyseal bending moment of inertia. There was a significant effect by level of calcium and mouse strain. There was no significant effect of exercise.

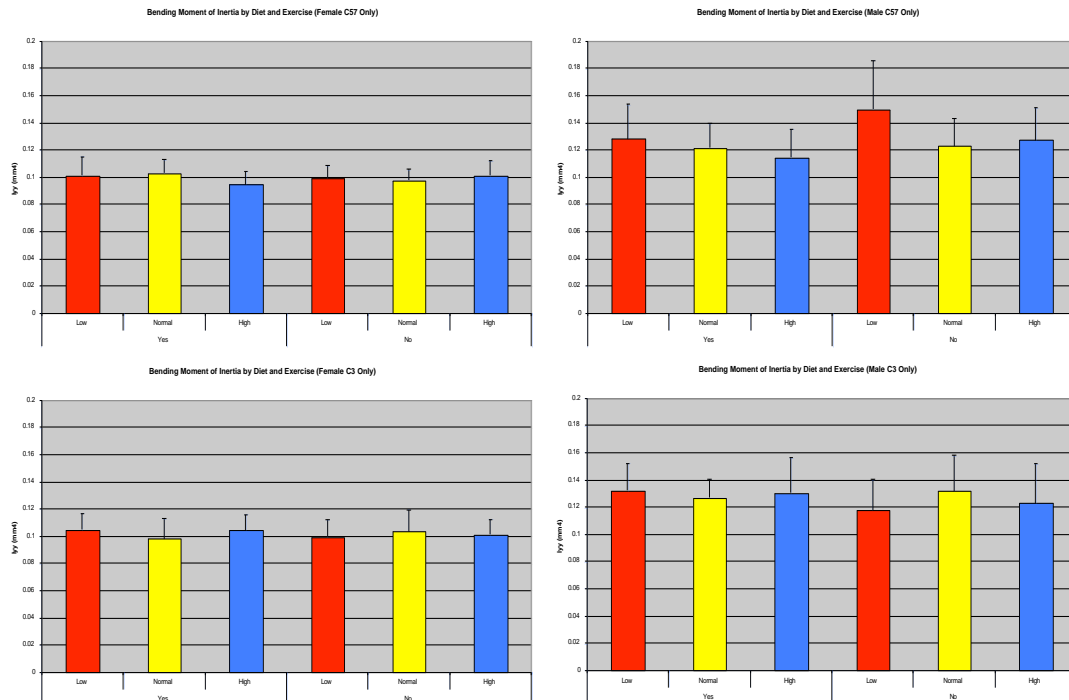


Figure 5: The results for the vertebral bodies paralleled those of the femur. As demonstrated here, there was a significant effect of mouse strain and diet, but no effect of exercise. As noted earlier, there are also baseline differences between males and females, but their responses are similar. These effects were observed for all morphologic and mechanical data from the vertebra.

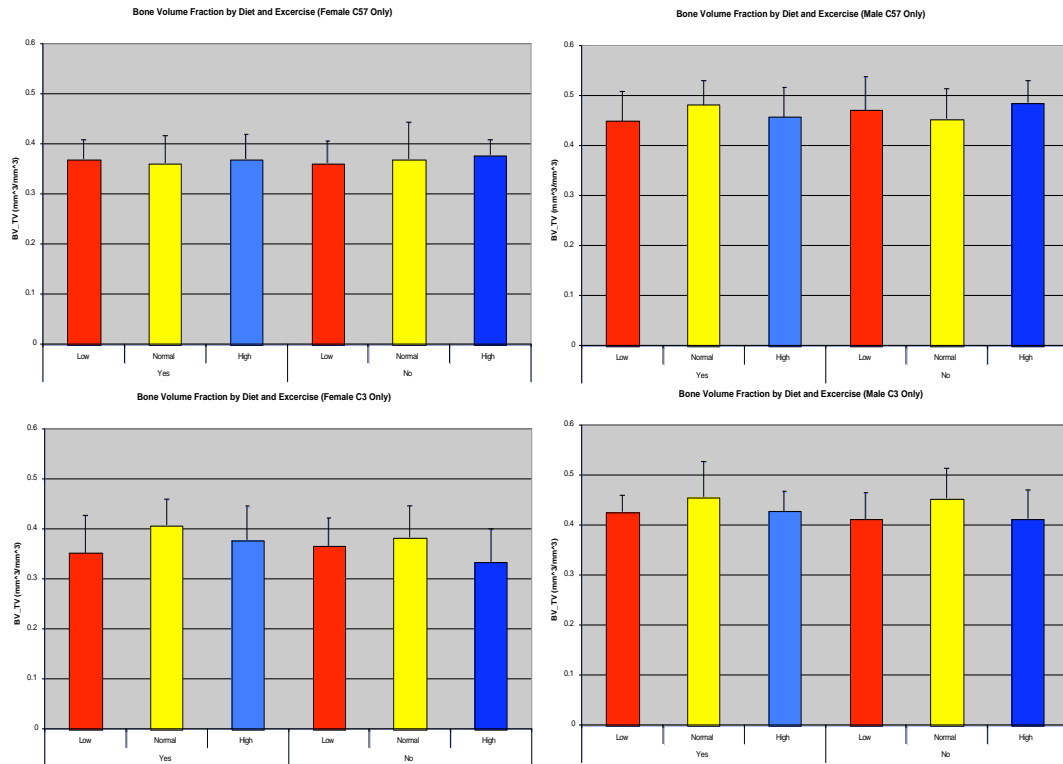


Figure 6: As noted earlier, the lack of exercise induced response in the femurs, stimulated us to perform additional studies in the tibias. We sampled 60 animals and examined their diaphyseal and metaphyseal bone. As noted in these figures, the mouse strain and diet effects were replicated in the tibias. In contrast, there was a potential effect of exercise seen in the tibias, but the results were not consistent. In the graph below, it appears that the males demonstrated an increase in bone volume fraction with exercise, in contrast to the females. These results, however, were not seen in many other variables and as a result, it is difficult to support a powerful effect of exercise.

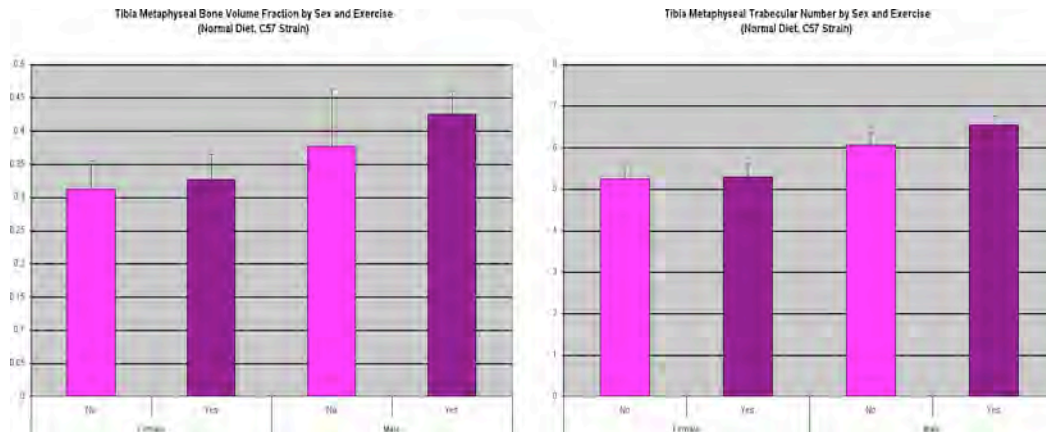
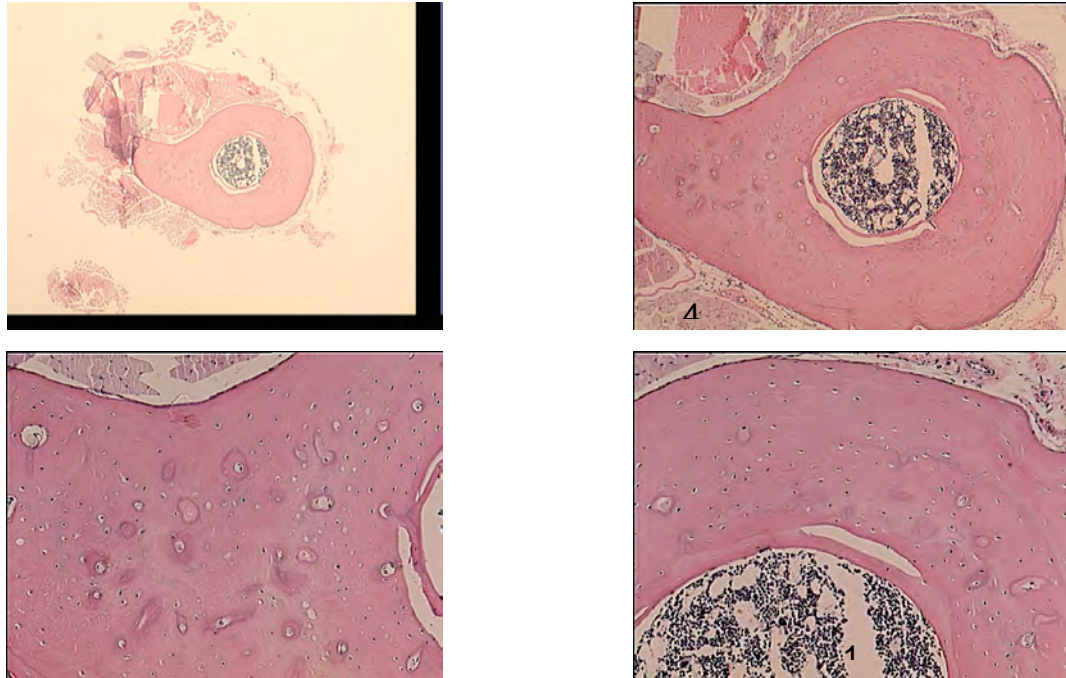


Figure 7: The histologic analysis demonstrated that the morphology, cellularity, and ECM organization appeared normal in all groups. An example of the histologic findings is illustrated below.



2. Vitamin D studies

The purpose of these studies was to explore the effect of reduced vitamin D on the mechanical and morphologic properties of the bone. The specific hypotheses to be tested were:

H1: Reduction in vitamin D metabolism results in reduction in mechanical properties.

H2: The effects of altered vitamin D metabolism and gender.

H3: The effects of altered vitamin D metabolism is independent of intense exercise.

The study was designed to utilize three specific groups of animals:

1. C57B1/6J Mouse (background control)
2. DBP^{-/-} Mouse with normal diet
3. DBP^{-/-} Mouse with vitamin D deficient diet (Purina diet No. 5826C-5)

The DBP (vitamin D binding protein knockout) mouse was described by our consulting investigator, Dr. Nancy Cooke and has already been shown to demonstrate significant

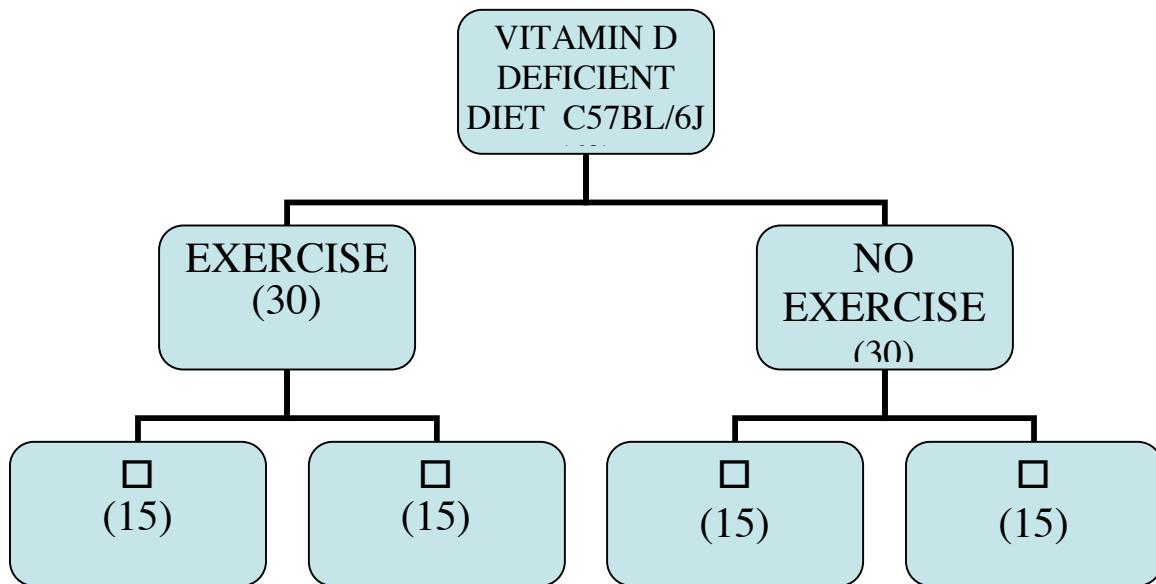
bone alterations when the vitamin D binding protein deficiency is combined with a vitamin D deficient diet.

Progress/Results

As noted in several of our yearly progress reports, the breeding of these mice was difficult and we had a viral infection outbreak during the study. This was managed, first by delaying the vitamin D studies until later in the program as well as we acquired several founders from different sources to try and raise the colony. Despite our enormous efforts on breeding and creating the colony (approximately an 18 month period of time with numerous colony starts and numerous alterations in breeding conditions) we were unable to establish a colony of these animals sufficient to conduct the proposed studies. As a result of this result, which occurred during the last year of funding (year 3.5 through year 4), we decided to take a new strategy in an effort to collect data in the face of vitamin deficiency. These studies (as will be described below) were conducted with the PI's own discretionary funds, in order to have a more complete set of data from this program. These studies are on-going and will likely be completed within the next 6 months. A brief summary is provided below.

Vitamin D deficiency study design

Using the C57BL/6J mice on the 'Normal' Ca^{2+} from part one of the study as a historical control group (60 mice), this study was designed to take 60 C57BL/6J mice and subject them to a modified diet. The diet was similar to the control (Normal) calcium diet from the groups described above, but was then altered to have reduced vitamin D. The mice were then exercised or not exercised according to the group assigned at time of delivery. The animals were randomly assigned to one of the groups illustrated below. The exercise protocol was the same as in our previous studies. A total of 60 animals were entered into the study.



The experimental phase of the study is completed, and 29 mice successfully completed the exercise regime along with the 30 non-exercised animals. All animals have been euthanized and their skeletal structures extracted.

Currently the left tibia from each animal has been fixed in EtOH and being stored until histological analysis can be performed.. 45 of the left femurs have been scanned using the GE MicroCT system to date and 14 have already been analyzed.

Within the next 6 months all the MicroCT studies and analyses will be complete as well as the mechanical testing of the femurs (4 pt. bending) and tibias (torsion). We will expect to add these data to our program database as well as publish the results.

C. Key Research Findings

- 394 mice that were entered into the study to evaluate effects of gender, strain, nutrition (vitamin C) and exercise on morphology and mechanical properties of bone (femurs, vertebra, tibia) have been studied.
- An additional 60 animals have been entered into a new vitamin D deficiency study and have been subjected to exercise while being supported by a vitamin D deficient diet. The complete results will be available in the next few months. This additional study was conducted after the failure of breeding the DBP mice.

- Mouse strain had a significant effect on geometric, morphologic and mechanical properties in the femurs, vertebra and tibias. C57BL/6J mice had a significantly smaller cross-sectional area and cortical thickness as compared to the C3H/HeJ mice
- Gender had a significant effect on all parameters (mechanical and morphologic) tested. In general the females were smaller and had lower mechanical properties. There were no consistent differences in the response to diet or exercise across genders.
- Exercise did not have a significant effect on any of the femoral or vertebral mechanical parameters.
- There were a few significant effects of exercise on tibial morphologic properties. This observation was not consistent, suggesting the effect was not robust.
- In vertebra, the normal dietary calcium group had a significantly higher bone volume fraction as compared to the low ($p=0.003$) and high ($p=0.003$) groups. The bone surface to volume ratio of the normal group was shown to be significantly lower than the low dietary calcium group ($p=0.030$), however no significant differences were seen between any of the other groupings.
- In vertebra, the normal dietary calcium group had a significantly higher trabecular thickness as compared to the low group ($p<0.000$) and marginally significant as compared to the high ($p=0.051$) group.
- Raman spectroscopy demonstrated significant variations in organic and inorganic constituents of the bone ECM across mouse strain and in response to calcium intake alterations.
- There were no histologic differences across any of the groups or treatments.
- The application of microimaging and micromechanical testing protocols was found to be outstanding with respect to characterizing the phenotypical properties of mouse bone.

D. Reportable Outcomes (Publications)

There were a number of publications (abstracts and full length papers) that have already been completed as a result of this research program. As can be gleaned from the numerous graphs of data in the appendix, we are continuing to work on the data and will have more publications directly from the data within the next 8 months. Three categories of outcomes are summarized below:

- a. Abstracts and papers that are a direct result of the data collected in this study
- b. Papers that were supported by the program that present the methodologies that are new to the field, but used specimens from a variety of studies.
- c. Papers that utilized the technologies developed in this program, but were not supported by the program. **Note:** since the major aim of this study was to develop techniques for evaluating the micro-properties of bone beyond traditional density measures, the

success of this program has already lead to other studies using the developed techniques.

Abstracts and papers directly supported and using data generated from the program

1. Influence of nutrition and physical forces on bone structure/function properties. *Kriegl, JM, *Oyserman, S, *Roller, SA, *Blumenfeld J, *Volkman SK, *Nashi S, *Hall JM, *McCreadie, BR and *Goldstein, SA. 50th Annual Orthopaedic Research Society, march 2004, San Francisco (abstract)
2. Mechanical loading effects structural morphology of male C57BL/6J tibia. Submitted for the 52 Orthopaedic Research Society Meeting, to be held in Chicago Ill., March 2006. (abstract)
3. Morris, MD, Crane, NJ, Gomez, LE. Ignelzi, MA. Compatibility of staining protocols for bone tissue with Raman spectroscopy. *Calcified Tissue Int.* 74:86-94, 2004
4. Additional papers in preparation to describe combined effects of exercise, gender and strain as described in the abstracts.

Papers supported by the program utilizing methods development

1. Carden, A., Morris, MD. Rajachar, RM, Kohn, DH. Ultrastructural changes accompanying the mechanical deformations: a Raman imaging study of bone tissue. *Calcified Tissue Int.* 72:166-175, 2003.

Papers using the successfully developed techniques, but not supported by the study funds.

1. Chen T, Kozloff KM, Goldstein SA, Morris MD: Bone tissue ultrastructural defects in a mouse model for osteogenesis imperfecta: A Raman spectroscopy study, *Proc. SPIE*, 5321, 85-92, 2004
2. Volkman SK, Galecki AJ, Burke DT, Miller RA, Goldstein SA: Quantitative trait loci that modulate femoral mechanical properties in a genetically heterogeneous mouse population. *J Bone Miner Res*, 19(9):1497-1505, 2004
3. Kozloff K, Carden A, Bergwitz C, Forlino A, Uveges T, Morris M, Marini JC, Goldstein SA: Brittle IV mouse model for osteogenesis imperfecta IV demonstrates postpubertal adaptations to improve whole bone strength. *J Bone Miner Res*, 19(4):614-622, 2004.

E. Conclusions

The research program has been very successful. The primary aim was to investigate the potential of microimaging, micromechanical and Raman spectroscopic techniques in characterizing the characteristics of bone in animal models. These studies demonstrated that the use of

1. MicroCT
2. micromechanical whole bone tests (femoral 4 pt. bending, vertebral

- compression, and tibial torsion)
- 3. microspecimen (100 micron beams) and nanoindentation studies of ECM tissues moduli
- 4. Raman spectroscopy
- 5. histologic morphology

can provide outstanding measures of bone phenotypic properties in mouse models. The studies also demonstrated several other key findings with respect to the influence of gender, nutrition and exercise.

1. Mouse strain is a significant factor influencing mechanical and morphologic properties of bone. The response to nutritional challenges is also dependent on mouse strain.
2. While gender effects are substantial in absolute morphologic and mechanical properties, the response to nutritional or other influences does not seem to be gender dependent. The one possible variation in these findings may be the response to exercise. At the protocol implemented, there was some suggestion of a male response to exercise that was not seen in females (only in tibia).
3. In general, the exercise protocol utilized in this program (treadmill, 8 weeks) was not sufficient to induce significant bone morphologic or mechanical property alterations. There was some evidence that the tibia of males responded. This may suggest that the loading threshold was too low to elicit a consistent response, and that the tibia are more sensitive to the treadmill stimulation. This is likely a local stress state phenomena that might be overcome by a variation in the boundary loading conditions (magnitude, rate, loading trajectory).

F. Personnel receiving pay from this research effort.

Steven Goldstein, PhD – Principal Investigator, 9/17/01 – 9/16/05
Barbara McCreadie, PhD – Co-Principal Investigator, 9/17/01 - 9/16/05
Maria Moalli, DVM – Co-Principal Investigator, 9/17/01 – 6/30/02
Michael Morris, PhD – Investigator, 9/17/01 – 9/16/05
Angela Carden, MS – Temporary Research Assistant, 5/1/02 - 6/18/02
John Baker, BS – Histologist, 9/17/01 - 9/16/05
Janet Blumenfeld, BS – Research Assistant, 10/1/01 – 12/31/02
William Finney, PhD – Post-Doctoral Research Fellow, 7/15/02 – 12/31/02; 7/15/03 – 7/31/05
Changning Guo, PhD - Post-Doctoral Research Fellow, 8/11/04 – 9/24/04
Pooja Gupta – Temporary Research Assistant, 7/1/03 – 7/31/03
Dennis Kayner, BS – Research Engineer, 9/17/01 - 9/16/05
Jaclynn Kreider, MS – Research Assistant, 5/1/03 - 9/16/05
Bonnie Nolan – Animal Technician, 4/1/03 – 9/16/05
Shrishail Nashi – Temporary Research Assistant, 10/1/02 – 4/30/03
Sivan Oyserman – Temporary Research Assistant, 5/15/02 – 12/31/04
Prysock, Adrainne, BS – Research Assistant, 9/1/04 – 12/31/04
Stephen Roller, BS – Research Assistant, 5/15/03 – 4/30/04
Kathleen Sweet, LVT – Animal Technician, 9/17/01 - 9/16/05
Suzanne Volkman, MS – Research Assistant, 10/1/02 – 5/31/03

Appendices

1. Influence of nutrition and physical forces on bone structure/function properties. *Kriegel, JM, *Oyserman, S, *Roller, SA, *Blumenfeld J, *Volkman SK, *Nashi S, *Hall JM, *McCreadie, BR and *Goldstein, SA. 50th Annual Orthopaedic Research Society, March 2004, San Francisco (abstract)
2. Mechanical loading effects structural morphology of male C57BL/6J tibia. Submitted for the 52 Orthopaedic Research Society Meeting, to be held in Chicago Ill., March 2006. (abstract)
3. Morris, MD, Crane, NJ, Gomez, LE. Ignelzi, MA. Compatibility of staining protocols for bone tissue with Raman spectroscopy. *Calcified Tissue Int.* 74:86-94, 2004
4. Carden, A., Morris, MD. Rajachar, RM, Kohn, DH. Ultrastructural changes accompanying the mechanical deformations: a Raman imaging study of bone tissue. *Calcified Tissue Int.* 72:166-175, 2003.
5. Chen T, Kozloff KM, Goldstein SA, Morris MD: Bone tissue ultrastructural defects in a mouse model for osteogenesis imperfecta: A Raman spectroscopy study, *Proc. SPIE*, 5321, 85-92, 2004
6. Volkman SK, Galecki AJ, Burke DT, Miller RA, Goldstein SA: Quantitative trait loci that modulate femoral mechanical properties in a genetically heterogeneous mouse population. *J Bone Miner Res*, 19(9):1497-1505, 2004
7. Kozloff K, Carden A, Bergwitz C, Forlino A, Uveges T, Morris M, Marini JC, Goldstein SA: Brittle IV mouse model for osteogenesis imperfecta IV demonstrates postpubertal adaptations to improve whole bone strength. *J Bone Miner Res*, 19(4):614-622, 2004.

All data generated in study represented in graphical form

Histologic images from all experimental groups

INFLUENCES OF NUTRITION AND PHYSICAL FORCES ON BONE STRUCTURE/FUNCTION PROPERTIES

*Kriegel, J M; *Oyserman, S ; *Roller, S A; *Blumenfeld J ; *Volkman S K; *Nashi S ; *Hall J M; *McCreadie, B R; +*Goldstein, S A
+*Orthopaedic Research Laboratories, University of Michigan, Ann Arbor, MI

INTRODUCTION

Maintenance of bone integrity is dependent on a complex interaction of metabolic (hormones, cytokines, growth factors) and environmental factors (mechanical forces, nutrition availability)¹. Unfortunately, the specific relationships between these factors and the biomechanical properties of bone tissue remain incompletely quantified. Understanding the influence of nutritional status and mechanical usage on the properties of bone may enhance our ability to prevent stress fractures associated with intense training or fragility fractures accompanying aging bone loss.

The purpose of this study was to investigate the interaction between calcium metabolism and exercise mediated mechanical load on the biomechanical properties of bone.

METHODS

C57BL/6J (n=84 male, n=90 female) and C3H/HeJ (n=69 male, n=67 female) mice were purchased from Jackson Laboratories (Bar Harbor, ME) and separated into groups based on strain, gender, diet, and exercise regime. A synthetic diet consisting of low (0.02% Ca), normal (0.95% Ca), and high (2.0% Ca) basal feed with 10% lactose and 0.67% phosphorus was purchased from Purina Test Diet (Richmond, IN)². An exercise protocol was established and implemented, which consisted of running the mice on a custom built treadmill with a 0° incline. The eight week regime consisted of ramping the speed from 10 to 17 m/min and increasing the duration from 15 to 30 min over the first 4 wks and holding the speed constant for an additional 4 wks³. The exercise regime and the controlled calcium diets (low, normal, high) were begun when the animals were 12 weeks old. The mice were humanely euthanized at 20 wks of age, the left femur and eighth caudal vertebrae were dissected free of soft tissue and frozen in LRS. This work was approved by The Animal Care and Use Committee.

Left femora and Cd8 vertebrae were scanned in distilled water on a GE.EVS Micro-CT system. Each scan was reconstructed at a mesh size of 18µm x 18µm x 18µm and a 3D digitized image was generated for each specimen. The femora and vertebrae images were rotated into a standard orientation and thresholded⁴. Geometric analyses were performed on a 3mm mid-diaphysis segment in order to obtain the cross-sectional area, cortical thickness, and moment of inertia (I_{yy}) for each femur. Two standardized volumes of trabecular bone were segmented from the proximal and distal ends of the vertebral bodies for analysis. The bone volume fraction, bone surface to volume ratio, trabecular thickness, trabecular number, trabecular spacing, and the degree of anisotropy were acquired from the vertebral morphologic analyses.

The data was analyzed using SPSS statistical software (Chicago, IL). Multivariate general linear models were used to test for main effects of four factors (gender, strain, diet and exercise) and for interaction effects among the four factors. *Post hoc* tests were used to compare the three levels of dietary calcium. Correlations were considered significant with a p-value less than 0.05.

RESULTS

Femora: Geometric data was collected from 323 femora. Mouse strain had a significant effect on geometric parameters. C57BL/6J mice had a significantly smaller cross-sectional area and cortical thickness as compared to the C3H/HeJ mice. Exercise did not have a significant effect on any of the geometric parameters, as shown in Table 1. Table 2 shows that differences in micro-CT measures by dietary calcium level are not significant.

Table 1: Exercise Effects on Cortical Parameters

Exercise	N	Cross Sectional Area (mm ²)	Cortical Thickness (mm)	Bending I_{yy} (mm ⁴)
No	168	0.892 (0.20)	0.256 (0.08)	0.116 (0.03)
Yes	155	0.877 (0.20)	0.250 (0.08)	0.114 (0.02)

Data are given as mean (STD)

Table 2: Dietary Effects on Cortical Parameters

Dietary Calcium	N	Cross Sectional Area (mm ²)	Cortical Thickness (mm)	Bending I_{yy} (mm ⁴)
Low	105	0.891 (0.19)	0.252 (0.08)	0.119 (0.03)
Normal	112	0.884 (0.20)	0.254 (0.08)	0.114 (0.02)
High	106	0.878 (0.21)	0.254 (0.08)	0.112 (0.02)

Data are given as mean (STD)

Vertebrae: Morphologic data was collected from 310 vertebrae. There was no significant effect for exercise on the trabecular parameters, as shown in Table 3. The differences in proximal trabecular parameters for the three dietary calcium groups are shown in Table 4. The normal dietary calcium group had a significantly higher bone volume fraction as compared to the low (p=0.003) and high (p=0.003) groups. The bone surface to volume ratio of the normal group was shown to be significantly lower than the low dietary calcium group (p=0.030), however no significant differences were seen between any of the other groupings. The normal dietary calcium group had a significantly higher trabecular thickness as compared to the low group (p<0.000) and marginally significant as compared to the high (p=0.051) group. Similar results were observed in the distal trabecular parameters.

Table 3: Exercise Effects on Proximal Trabecular Parameters

Exercise	N	Bone Volume Fraction (%)	Bone Surface to Volume Ratio (mm ² /mm ³)	Trabecular Thickness (mm)
No	161	40.9 (0.07)	30.08 (4.57)	0.074 (0.01)
Yes	149	41.9 (0.06)	29.30 (4.44)	0.077 (0.01)

Data are given as mean (STD)

Table 4: Dietary Effects on Proximal Trabecular Parameters

Dietary Calcium	N	Bone Volume Fraction (%)	Bone Surface to Volume Ratio (mm ² /mm ³)	Trabecular Thickness (mm)
Low	101	40.6 (0.07)*	30.29 (4.01)*	0.073 (0.01)*
Normal	109	42.8 (0.07)*	29.18 (5.26)*	0.078 (0.02)*
High	100	40.6 (0.06)*	29.69 (4.07)*	0.075 (0.01)*

Data are given as mean (STD) * Significant, p ≤ 0.05

DISCUSSION

As expected, the results indicate that geometric properties are dependent on genetic background. C57BL/6J mice had a significantly smaller cross-sectional area and cortical thickness as compared to the C3H/HeJ mice, as noted in previous studies⁵.

Differences due to nutritional status were seen only in trabecular bone of the vertebrae, where modeling phenomena are expected to occur more rapidly than in femoral cortical bone due to the greater biodynamic activity of trabecular bone. The loading regimen in this study appears to not have an effect on the femoral geometric or vertebral morphologic properties. The level of exercise did not compensate for the decrease in the trabecular parameters during dietary calcium alterations. This may be caused by an inadequate load stimulus. Preliminary biomechanical testing data suggests a difference in post-yield behavior in exercise groups. This may possibly suggest an interaction at the tissue level, which we will continue to explore.

REFERENCES

1. Silbermann et al. *Calcif Tissue Int*, 46: 80-93, 1990.
2. Cromphaut et al. *PNAS*, 98: 13324-13329, 2001.
3. Kohut et al. *Mech Ageing Dev*, 122: 1135-1150, 2001.
4. Kuhn et al. *J Orthop Res*, 8: 833-842, 1990.
5. Chen et al. *Bone*, 25: 413-420, 1990.

ACKNOWLEDGEMENTS

This work was supported by the Department of the Army DAMD 17-01-1-0809 and NIH AR46024. The authors would like to thank Kurt Hankenson, Dennis Kayner, Rajiv John, Bonnie Nolan, Charles Roehm, and Kathy Sweet for their contributions to this study.

MECHANICAL LOADING EFFECTS STRUCTURAL MORPHOLOGY OF MALE C57BL/6J TIBIAE

INTRODUCTION

Although it is known that bone integrity is dependent on a complex interaction of both metabolic and environmental factors, the specific relationship between these factors and the biomechanical properties of bone tissue remains incompletely quantified. Previous work¹ has illustrated a nutritional dependent response of vertebral trabecular and femoral cortical bone biomechanical properties of C57BL/6J and C3H/HeJ mice. The purpose of this study was to investigate the influence of forced exercise on the morphologic properties of cortical and trabecular bone in the tibiae of both male and female C57BL/6J mice.

METHODS

C57BL/6J (n=31 male, n=29 female) mice were purchased from Jackson Laboratories (Bar Harbor, ME). All protocols were approved by the Animal Care and Use Committee. Starting at 12 weeks of age, C57BL/6J mice were fed a standard synthetic diet composed of 0.95% Ca basal feed with 10% lactose and 0.67% phosphorus purchased from Purina Test Diet (Richmond, IN). Mice were allocated randomly to either exercise or control groups. Exercise involved running eight weeks on a custom built treadmill with a 0° incline. Over the 8-wk period, speed was ramped up from 10 to 17 m/min and duration was increased from 15 to 30 min in the first 4 wks and held constant for the second 4 wks. Exercise treatment began at 12wks of age. At the termination of the exercise regime, mice were humanely euthanized and the right tibiae were removed and dissected free of soft tissue and frozen in LRS.

The right tibiae were scanned in distilled water on a 3D Micro-Computed Tomography (micro-CT) system (GE Healthcare BioSciences). Scans were reconstructed at a mesh size of 25µm x 25µm x 25µm. The tibiae were rotated into a standard orientation and thresholded based on calibrated histograms to separate bone and no-bone voxels. In each tibia a 1.5mm long diaphyseal region of interest was defined just proximal to the distal tibiofibular joint and the bone was evaluated for cross-sectional area, cortical thickness, and volumetric bone mineral density (vBMD). Bone volume fraction, bone surface to volume ratio, trabecular thickness, trabecular separation, and trabecular number were calculated from morphometric analysis of a 2mm thick trabecular region just distal to the proximal growth plate. A 3D spline function was utilized to define the largest possible volume of trabecular bone in this region.

The data was analyzed using SPSS statistical software (Chicago, IL). Multivariate general linear models were used to test for main effects of two factors (gender and exercise) and for their interactions. Comparisons were considered significant with p-values of less than 0.05.

RESULTS

Cortical: Exercise induced a significant increase in cross-sectional area and cortical thickness (Table 1). The results demonstrated a significant gender effect on cross-sectional area and cortical thickness (Table 2).

Table 1: Exercise Effects on Cortical Parameters

Exercise	N	Cross-Sectional Area (mm ²)	Cortical Thickness (mm)	Volumetric Bone Mineral Density (mg/cc)
No	30	0.554(0.08)*	0.200(0.02)*	1441.328(64.8)
Yes	30	0.574(0.07)*	0.205(0.01)*	1417.172(38.4)

Data are given as mean (SD) * Significant, p ≤ 0.05

Table 2: Gender Effects on Cortical Parameters

Gender	N	Cross-Sectional Area (mm ²)	Cortical Thickness (mm)	Volumetric Bone Mineral Density (mg/cc)
Male	31	0.622(0.05)*	0.212(0.01)*	1431.834(57.2)
Female	29	0.502(0.03)*	0.193(0.01)*	1426.488(51.7)

Data are given as mean (SD) * Significant, p ≤ 0.05

Trabecular Morphology: Exercise was found to have a significant effect on bone volume fraction and trabecular number (Table 3). A gender effect was also demonstrated in the trabecular bone including bone volume fraction, trabecular number and vBMD (Table 4). Most importantly, evaluation of the interactions showed that only the male

C57BL/6J mice showed a significant increase in bone volume fraction, and trabecular number with exercise (Table 5). No significant effect was seen on trabecular parameters in female C57BL/6J mice (data not shown).

Table 3: Exercise Effects on Trabecular Parameters

Exercise	N	Bone Volume Fraction (%)	Trabecular Thickness (mm)	Trabecular Number (1/mm)	Volumetric Bone Mineral Density (mg/cc)
No	30	0.346(0.07)*	0.608(0.01)	5.66(0.53)*	544.496(20.8)
Yes	30	0.375(0.06)*	0.063(0.01)	5.90(0.69)*	547.698(24.1)

Data are given as mean (SD) * Significant, p ≤ 0.05

Table 4: Gender Effects on Trabecular Parameters

Gender	N	Bone Volume Fraction (%)	Trabecular Thickness (mm)	Trabecular Number (1/mm)	Volumetric Bone Mineral Density (mg/cc)
Male	31	0.400(0.07)*	0.063(0.01)	6.276(0.37)*	533.519(19.3)*
Female	29	0.319(0.04)	0.060(0.01)	5.258(0.34)	559.541(17.0)*

Data are given as mean (SD) * Significant, p ≤ 0.05

Table 5: Exercise Effects of Trabecular Parameters- Males

Exercise	N	Bone Volume Fraction (%)	Trabecular Thickness (mm)	Trabecular Number (1/mm)	Volumetric Bone Mineral Density (mg/cc)
No	30	0.376(0.08)*	0.062(0.01)	6.044(0.32)*	535.750(21.1)
Yes	30	0.452(0.03)*	0.065(0.01)	6.523(0.23)*	531.139(17.6)

Data are given as mean (SD) * Significant, p ≤ 0.05

DISCUSSION

Following earlier work^{1,2,3}, we anticipated that exercise would have a positive influence on the morphometric properties of the tibiae. In trabecular bone, the increases in both volume fraction and trabecular number suggest that the effect of exercise is dominantly expressed as an increase in the number of trabecular struts and not an increase in the thickness of individual struts. Importantly, gender related differences were documented. The sensitivity of males to exercise induced increases in bone mass and morphology (in contrast to females) may represent important differences in hormonal influences on mechanoregulation. These issues are important areas for future investigation as we continue to search for methods to enhance bone properties in the of face age or disease.

Compatibility of Staining Protocols for Bone Tissue with Raman Imaging

M. D. Morris,¹ N. J. Crane,¹ L. E. Gomez,² M. A. Ignelzi Jr²

¹Department of Chemistry, University of Michigan, 930 N. University Avenue, Ann Arbor, MI 48109-1055, USA

²Department of Orthodontics and Pediatric Dentistry, University of Michigan School of Dentistry, Ann Arbor, MI, USA

Received: 17 February 2003 / Accepted: 6 May 2003 / Online publication: 20 November 2003

Abstract. We report the use of Raman microscopy to image mouse calvaria stained with hematoxylin, eosin and toluidine blue. Raman imaging of stained specimens allows for direct correlation of histological and spectral information. A line-focus 785 nm laser imaging system with specialized near-infrared (NIR) microscope objectives and CCD detector were used to collect approximately $100 \times 450 \mu\text{m}$ Raman images. Principal components analysis, a multivariate analysis technique, was used to determine whether the histological stains cause spectral interference (band shifts or intensity changes) or result in thermal damage to the examined tissue. Image analysis revealed factors for tissue components and the embedding medium, glycol methacrylate, only. Thus, Raman imaging proved to be compatible with histological stains such as hematoxylin, eosin and toluidine blue.

Key words: Raman spectroscopy — Histological staining — Mineralized tissue — Bone — H&E — Toluidine blue

Raman microspectroscopy and Raman imaging are increasingly used to provide chemical structure information on tissue specimens. While spectroscopy provides valuable information, biomedical scientists usually wish to link the information to histological analysis [1–4]. Depending upon the staining protocols employed, histology may provide morphological information, identification of broad classes of molecules such as proteins and nucleic acids, or may provide highly specific identification by means of labeled antibodies or other molecules that bind uniquely to one protein. Histological analysis can also identify regions of a specimen that merit further investigation by spectroscopy. Correlative histological/Raman imaging may provide information that is beyond what is available by either methodology. For such reasons it is important to

understand the compatibility of histological and spectroscopic protocols and to identify any sources of incompatibility.

In this study we investigated the compatibility of hematoxylin and eosin (H&E) staining and toluidine blue staining with near-infrared (NIR) Raman imaging of fetal day 18.5 and postnatal day 21 mice calvaria, or flat bones that comprise the skull. Raman microspectroscopy and imaging provide molecular structure information with light microscopy spatial resolution [5]. Raman spectra are obtained by focusing a laser on the specimen. While low laser power is usually used, the possibility of thermal damage is always present. For Raman microscopy it is advantageous to use line-focused lasers that result in low power at any point along the line. This configuration simultaneously reduces the likelihood of laser damage and provides a quick survey of the tissue along the line.

We evaluated H&E staining because it is among the most widely used staining techniques. Hematoxylin is an acidophilic stain derived from the dye hematein. Staining with hematoxylin results in nuclei and basophilic cytoplasm colored blue. Eosin, a basophilic dye, is the common counterstain for hematoxylin. Acidophilic cytoplasm and connective tissue turn varying shades of pink to red with eosin. Together, H&E clearly contrast the different tissue components. We have also investigated the effects of toluidine blue, which is often used alone, but can be substituted for hematoxylin. Toluidine blue also stains nuclei and basophilic cytoplasm blue [6].

Raman spectroscopy of tissue specimens is generally excited with NIR lasers. NIR lasers are preferred to the more common visible wavelength lasers because NIR light does not excite native fluorescence from most fluorophores in tissues, although fluorescence is excited over most of the range of visible wavelengths (400–700 nm). Red stains, such as eosin, absorb at blue-green to ultraviolet wavelengths (250–500 nm) but not at red or near-infrared wavelengths. However, blue stains, such as hematoxylin, absorb at red wavelengths (650–700 nm) and their absorbance spectra may extend into the

near-infrared (> 700 nm). Thus, blue stains cannot be considered innocuous for Raman spectroscopy until their absorption spectra have been examined for absorbance at the laser excitation wavelength being used.

We have previously shown that Raman image contrast of bone tissue shows both morphology and chemistry [7–10]. Using multivariate data analysis (principal component analysis, PCA) even minor components of the specimen can be identified [1] and in some cases can be imaged. Serial sections can be used to compare spectroscopic results with histological results. One section is examined by spectroscopy and an adjacent section is subjected to histological analysis. It is accepted that there are small histological variations between serial sections, which makes it somewhat inaccurate to compare sections. A more objective approach of correlative studies between spectroscopy and histopathology would be to examine spectroscopically the same sections that are examined histologically. In many previous studies, spectroscopic sample preparation consists of snap freezing tissue and sectioning with a cryostat [11–14]. The examined tissue is unfixed and unstained [14–16]. The sections subjected to histological analysis are fixed, typically in formalin which retains tissue rigidity and prevents bacterial growth, then embedded and stained with H&E.

Correlative studies depend on the staining being compatible with the spectroscopic technique. There are two main concerns with staining and Raman microscopy. The first is whether or not the stain will interfere spectroscopically. If there is Raman signal from the stain, it must be distinguishable from other tissue components by PCA. The second concern is whether the stain will absorb at the laser wavelength and generate heat which in turn will destroy the specimen. Previous studies show that basic fuchsin does not interfere spectroscopically nor does it cause thermal damage [9]. Here we determine the compatibility of Raman microscopy and tissues stained with H&E and toluidine blue.

Materials and Methods

Experimental Subjects

B6CBA F₁/J wild-type mice (The Jackson Laboratory, Bar Harbor, ME) were harvested at fetal day 18.5 and postnatal day 21. We used two ages of mice to determine compatibility of staining and Raman imaging with delicate tissue (fetal day 18.5) and more mature tissue with more mineral (postnatal day 21). The calvaria, flat bones from the topmost portion of the skull, were excised and rinsed with a phosphate-buffered saline solution at pH 7.2. Specimens were then fixed in either formalin or ethanol and stored at 4°C. Prior to embedding with glycol methacrylate (Technovit 1800 GMA; Energy Beam Sciences, Agawam, MA), calvaria were dissected and placed in a 50/50 mixture of infiltrating solution and absolute ethanol for 2 hours and then in infiltrating solution overnight. Infil-

trated specimens were oriented in the polyethylene mold tray, submerged with embedding solution and topped with a plastic holder for sectioning. Specimens were left to cure overnight at 4°C.

Embedded specimens were sectioned at 20 μm with glass knives in a JB-4 microtome (Energy Beam Sciences) and then mounted onto a glass microscope slide (Probe-On Plus, Fisher Scientific, Pittsburgh, PA) and allowed to air dry. H&E staining procedures for GMA-embedded tissue were followed for a portion of the sections [17]. Other sections were used to study modified staining protocols in which submersion time in hematoxylin solution was varied (30 sec, 1 min, 2 min, 5 min and 7 min). Other sections were stained with toluidine blue and eosin, again following the GMA-embedded tissue protocol.

Raman Analysis

The Raman imaging system has been described previously [7]. Briefly, about 160 mW of line-focused laser light from a 785 run diode laser (Invictus, Kaiser Optical Systems, Inc., Ann Arbor, MI) is delivered to the sample via epi-illumination with a microscope (BH-2; Olympus, Inc., Melville, NY) equipped with a NIR-optimized 20 \times 0.75 NA objective (Fluar Series, Carl Zeiss, Inc., Thornwood, NY). Raman scatter collected through the objective is focused into an axial-transmissive spectrograph (HoloSpec f/1.8i, Kaiser Optical Systems, Inc., Ann Arbor, MI) operated at 3–4 cm^{-1} resolution (25 μm entrance slit). The dispersed signal is collected by a 1024 \times 128 pixel charge coupled device camera (DU401-BR-DD; Andor Technology, South Windsor, CT) operated at -75°C . To obtain an image, a stepper-motor controlled x-y translation microscope stage (NEAT, Salem, NH) moves the sample in 1.5 μm steps for the desired number of frames, providing 3 μm spatial resolution, with 3 min acquisitions per frame. In most cases 150 frames were collected, to yield a 126 \times 150 pixel image containing information from all 18,900 Raman spectra. Brightfield images were collected by a color video camera (TMC-7; Pulnix, Sunnyvale, CA) mounted on the microscope frame. All absorbance spectra were collected with a Shimadzu 2101 Scanning UV-Visible Spectrophotometer. All scans were performed from 550–800 nm, with 0.1 nm slit width, 0.5 nm sampling intervals and a fast scan speed.

Factor Analysis

Factor analysis [19], which has been discussed previously [10, 18], was performed with Matlab 5.3 (MathWorks, Inc., Natick, MA), using both manufacturer-supplied routines as well as in-house developed routines. The entire set of 18,900 Raman spectra that comprise an image is treated as a matrix of 18,900 rows (spectra) and 1024 columns (Raman shifts). The principal components, which are the eigenvectors of this matrix, are calculated and then sorted by their magnitudes, called eigenvalues. The standard procedure for calculating eigenvectors is called “singular value decomposition” and is included in Matlab. The eigenvectors are a mathematically orthogonal coordinate system (i.e., extensions of the familiar 3-dimensional Cartesian coordinate system) from which the original data set can be calculated. The number of eigenvectors found is equal to the number of Raman spectra. However, almost all of the non-random variation in the image data set can be described by the eigenvectors with the largest magnitudes. Usually between four to eight eigenvectors are sufficient. The remaining eigenvectors describe the random noise in the data set and are not used in the data analysis. The criterion for eigenvector retention is that addition of the next eigenvector describes no more than 0.1% of the variation in the data set. The intensities of these eigenvectors are called scores.

Principal components are mathematically orthogonal and so may contain both positive and negative bands. They are sums and differences of the underlying Raman spectra. To convert

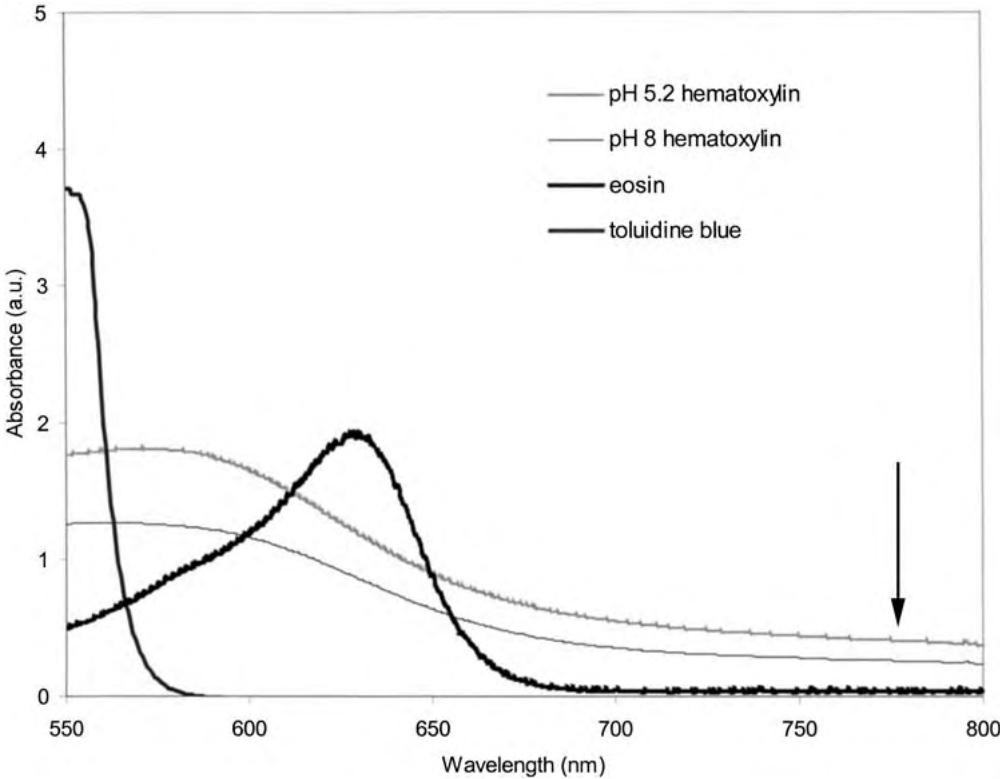


Fig. 1. Absorbance spectra of 0.01% hematoxylin solution at pH 5.2 and 8, 0.01% eosin solution and 0.01% toluidine blue solution. The arrow points to absorbances at the wavelength of excitation, approximately 785 nm.

the retained principal components to Raman spectra, weighted sums and differences are calculated, with the weighting subject to two constraints. The first constraint is that at each Raman shift the calculated weighted sums and differences be non-negative, as are the Raman spectra. A second constraint is that at each point the reconstructed Raman spectra must add up to the original intensity. These constraints are sufficient to guarantee that the reconstructed spectra, called factors, will be directly proportional to the real Raman spectra. The relative intensity (score) images will be positive and will be maps of the spatial distribution and relative amounts of indicating where and how much of the components are present in the specimen.

Results

Absorption of Histological Stains

In order to determine if eosin, hematoxylin and toluidine blue would cause sufficient heating upon laser exposure to cause tissue damage, the absorption at the laser wavelength was determined. Figure 1 shows the absorption spectra of eosin, hematoxylin and toluidine blue from 550 nm to 800 nm. Although the spectra were obtained in solutions of the stains for experimental convenience, the spectra of the solid phase stains are similar. Eosin shows no detectable absorbance at 785 nm, as would be expected for a red stain. Toluidine blue absorbs weakly at 785 nm (0.04 from a 0.01% solution). Hematoxylin absorbs more strongly at 785 nm (0.4 at pH 5.2 and 0.3 at pH 8, from a 0.01% solution).

Light Microscopy of Stained Specimens

Brightfield images of mouse calvaria embedded in GMA and stained according to the protocols are shown (Fig. 2). Raman images of regions of these specimens are presented and discussed below. The image of a control section of GMA (no tissue), part of which is stained with eosin, is shown in Figure 2a. The image of a second control, a section of GMA-embedded and unstained calvarial tissue from a 21-day-old wild-type mouse is shown in Figure 2b. Figure 2c shows the same section after staining with eosin. Note, the holes in 2b and 2c are a result of the embedding process, not tissue damage by the laser. Consistent with the data presented in Figure 1, no thermal damage was detectable after Raman imaging was performed on these sections. Figure 2d shows a section of fetal day 18.5 calvarial tissue stained with eosin and toluidine blue. The presence of toluidine blue did not result in any detectable thermal damage, even though it is weakly absorbing at 785 nm.

Several H&E protocols resulted in enough bound hematoxylin to cause thermal damage under 785 nm laser illumination. Figure 2e shows a section of calvarial tissue from a 21-day-old wild-type mouse stained by an H&E protocol that consisted of requiring 15 min immersion in hematoxylin. Note the laser damage to the upper right hand corner of the specimen. Visible damage, burning of the tissue, often accompanied by noticeable

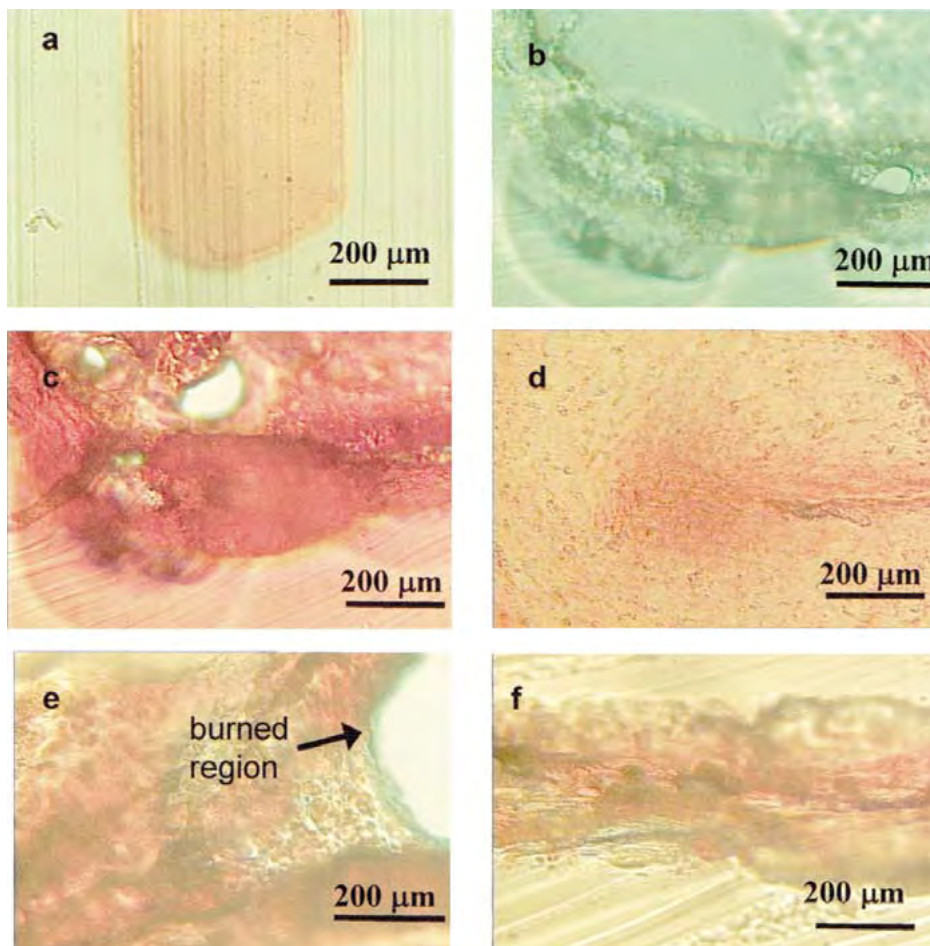


Fig. 2. Brightfield images of sections studied with Raman imaging. Sections were of the following: (a) GMA partially stained with eosin, (b) postnatal day 21 mouse calvaria embedded in GMA and unstained, (c) postnatal day 21 mouse calvaria embedded in GMA and stained with eosin, (d) fetal

day 18.5 mouse calvaria embedded in GMA and stained with toluidine blue and eosin, (e) fetal day 18.5 mouse calvaria embedded in GMA and stained by standard H&E protocol, (f) fetal day 18.5 mouse calvaria embedded in GMA and stained by modified H&E protocol.

odor, occurred as soon as the laser was incident on the specimen. A video image was obtained less than 1 second later. Not surprisingly then, protocols requiring longer immersion in hematoxylin also resulted in damage.

Hematoxylin immersion was reduced in a series of steps to find conditions that resulted in good contrast in reflectance imaging with no visible or spectroscopically detectable thermal damage. Fetal tissue was used for testing these protocols because it is more easily damaged than mature tissue. Immersion times of 7, 5, 2, 1 and 0.5 min were examined. Sections immersed in hematoxylin for 2, 5, and 7 min burned immediately. Specimens immersed in hematoxylin for 1 min sustained 1.5 min of laser exposure before visible damage was observed. Immersion in hematoxylin solution for 0.5 min resulted in no thermal damage, even after more than 5 min of exposure to the laser. There was little difference in contrast obtained after the 0.5-minute immersion and the longer H&E staining protocols, as shown by comparison (Fig. 2e,f).

Raman Imaging of GMA Stained with Alcoholic Eosin

Figure 2a shows a reflectance brightfield image of a GMA section (no tissue) that was used to test for spectroscopic interference from eosin (only part of the section was stained with eosin). Figure 3a shows the only Raman factor recovered from the Raman imaging experiment and 3b shows the corresponding score image.

In Figure 3a only the spectral bands between 420 cm^{-1} and 1045 cm^{-1} are shown in order to bring out detail that emphasizes the similarities between corresponding factors obtained here and in the staining protocol experiments described below. Spectra were obtained over the $420\text{--}1800\text{ cm}^{-1}$ range and contain additional Raman bands that are not shown. For consistency, the Raman images throughout the paper have similar dimensions to the image of Figure 3b, approximately $100\text{ }\mu\text{m} \times 450\text{ }\mu\text{m}$.

If the eosin stain produces a Raman spectrum that is detectable, there will be eosin bands in the Raman

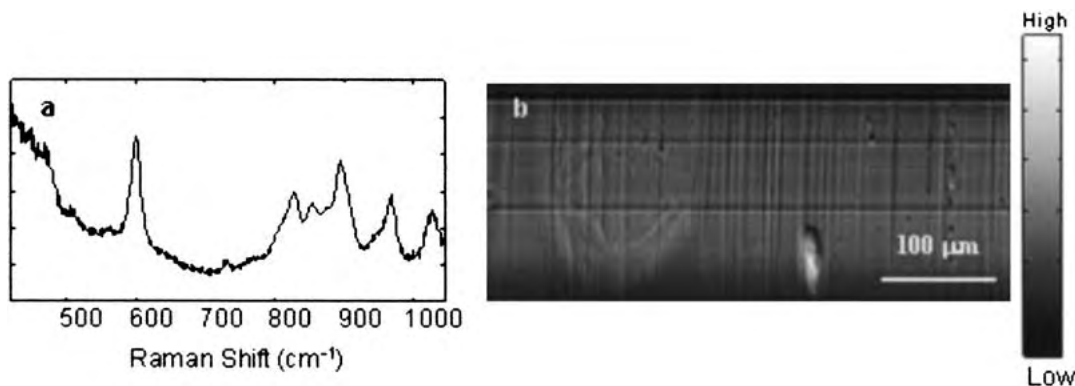


Fig. 3. Raman factor for a section of GMA partially stained with eosin (**a**) and the corresponding score image (**b**). Note only GMA is detectable. The section examined was 20 μm thick, mounted on a glass microscope slide. Laser power incident to the sample was 185 mW.

spectra from this part of the section but not from the unstained part. The extra bands should be resolvable by factor analysis even if they are not readily visible upon inspection. However, as indicated in Figure 3, the eosin is not visible spectroscopically. Only one factor containing Raman bands is obtained. This factor is representative of the typical GMA spectrum, with signature bands at 600 cm^{-1} and 968 cm^{-1} . The score (intensity) is uniform across the section, with no difference between the stained and unstained regions. Only striations from the microtome glass knife and one surface irregularity mar the otherwise flat surface. We conclude that if eosin spectra are present, they must contribute much less than 1% to the total observed Raman intensity.

Raman Imaging of Calvaria Embedded in GMA and Unstained

To determine whether spectral interference would result from the application of histological stains, we first resolved the factors of the GMA embedded tissue without staining. Figure 2b is the reflectance brightfield image of the region of a section of calvaria from a 21-day postnatal mouse. The specimen here, calvaria from a 21-day postnatal mouse, is embedded in GMA and unstained. It serves as a control for comparison with images from stained specimens. Three non-background Raman spectrum factors are observed. The factors and the corresponding score images are shown in Figure 4.

The GMA factor (Fig. 4a) is identical to the GMA factor shown in Figure 3a. Bone matrix (Fig. 4c) and bone mineral (Fig. 4e) factors are also obtained. These are identical to factors that we have previously reported for similar mouse calvaria specimens [7]. The corresponding score images are Figures 4b (GMA), 4d (bone matrix) and 4f (bone mineral). There is some overlap between the GMA image and the bone mineral and matrix images, but it is not great. Though there may be some infiltration into the tissue, the GMA shows greatest intensity where bone is not present in the sec-

tion. It is clear that factor analysis adequately separates the components of the specimen, which is composed of GMA (Fig. 4a), bone matrix (Fig. 4c) and bone mineral (Fig. 4e).

Raman Imaging of Calvaria Embedded in GMA and Stained

In Figure 5 Raman score images from a selected region of eosin-stained tissue specimen of Figure 2c are shown. Three non-background factors that contain Raman spectral information for the specimen were found. The remaining factors contained only background luminescence and were not included. The three Raman factors correspond to GMA (Fig. 5a), bone mineral (Fig. 5c) and bone matrix (Fig. 5e). As found for the unstained GMA-embedded calvaria, the GMA is found (Fig. 5b) mostly where the bone mineral (Fig. 5d) is absent, although it does fill small depressions in the tissue. In comparing the bone mineral and matrix (Fig. 5f) score images there is a relatively uniform distribution of mineral on the matrix, as would be expected of a small region of mature tissue such as this 21-day-old mouse. There was no factor found for the eosin. The stain is probably present in a sufficiently thin layer that it cannot be detected spectroscopically.

A fetal day 18.5 mouse calvarial section stained with toluidine blue and eosin is shown in Figure 6. As discussed above, the tissue was chosen because it is more easily damaged than mature tissue. There are two non-background factors, GMA (Fig. 6a) and bone (Fig. 6c). The corresponding score images are shown as Fig. 6b and 6d. Although mineralization is expected and present in this tissue, it is not as extensive as in the postnatal day 21 tissue. The bone factor appears at lower signal/noise ratio than in the more mature tissue specimens used in the Figs. 4 and 5. No Raman factors are found for toluidine blue because the stain is present in a thin layer.

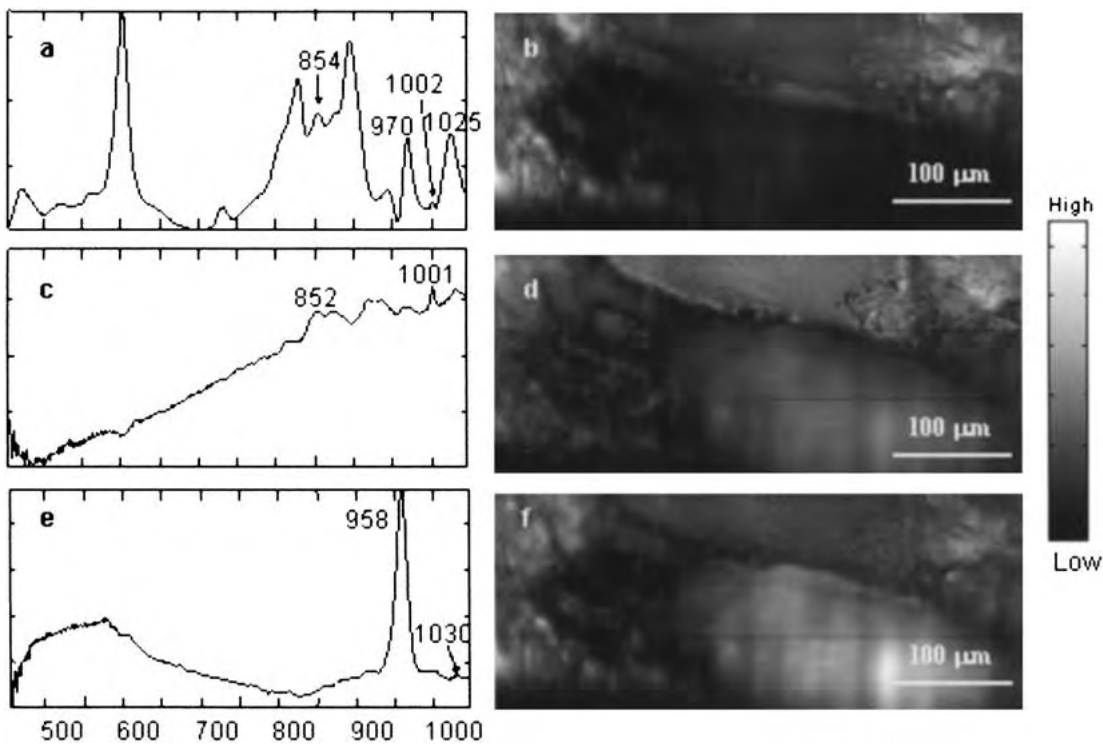


Fig. 4. Raman factors and score images for postnatal day 21 mouse calvaria embedded in GMA and unstained. Shown is the Raman factor for GMA (a), the Raman factor for bone matrix (c) and the Raman factor for bone mineral (e). The corresponding score images are shown in b, d and f. Note, in

the score image, the GMA is least intense where the bone mineral is the most intense. The section examined was 20 μm thick and mounted on a glass microscope slide. Laser power incident to the sample was 153 mW.

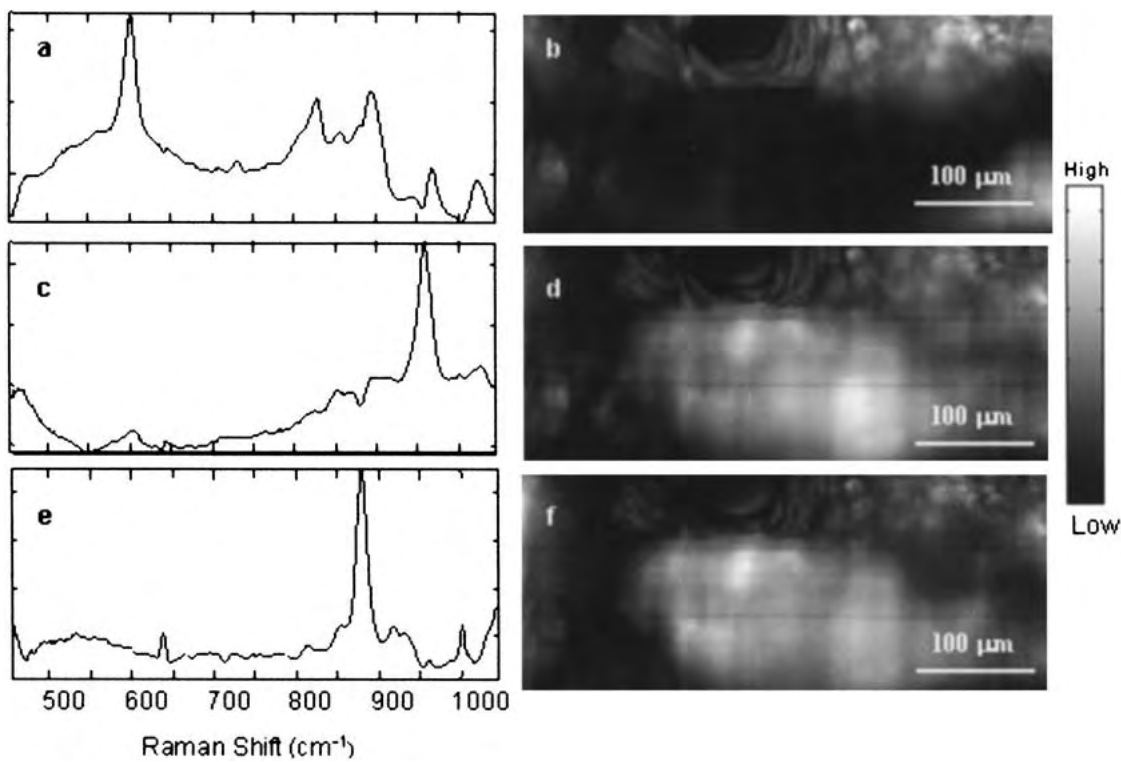


Fig. 5. Raman factors and score images for postnatal day 21 mouse calvaria embedded in GMA and stained with eosin. Shown is the Raman factor for GMA (a), the Raman factor for bone mineral (c) and the Raman factor for bone matrix (e).

The corresponding score images are shown in b, d and f. The section examined was 20 μm thick and mounted on a glass microscope slide. Laser power incident to the sample was 157 mW.

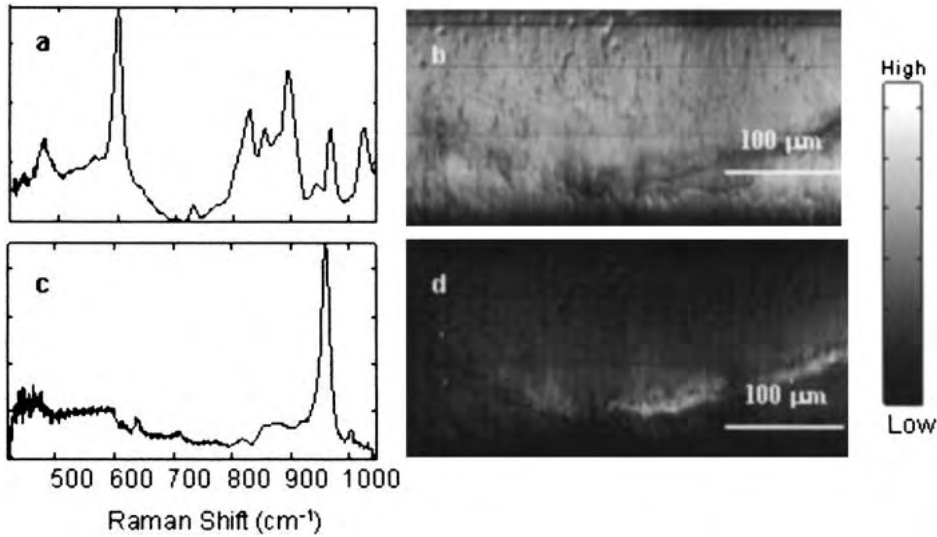


Fig. 6. Raman factors and score images for fetal day 18.5 mouse calvaria embedded in GMA and stained with toluidine blue and eosin. Shown is the Raman factor for GMA (a) and the Raman factor for bone mineral (c). The-corresponding

score images are shown in (b) and (d). The section examined was 20 μm thick and mounted on a glass microscope slide. Laser power incident to the sample was 185 mW.

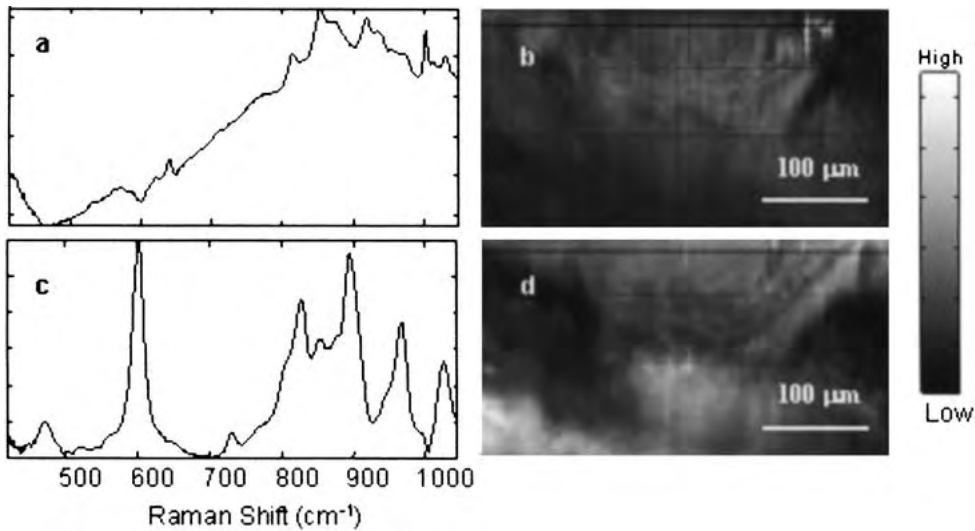


Fig. 7. Raman factors and score images for fetal day 18.5 mouse calvaria embedded in GMA and stained with H&E. The Raman factor for bone matrix (a) and the Raman factor for GMA (c). The corresponding score images are shown in (b) and (d). The section examined was 20 μm thick and mounted on a glass microscope slide. Laser power incident to the sample was 185 mW.

Figure 7 shows data from the suture of fetal day 18.5 tissue stained with H&E. This is the most delicate and spectroscopically challenging tissue used in this study because collagen is a significantly weaker Raman scatterer than the mineral in bone. The factor shown in Figure 7a is the spectrum of bone matrix. The score image is shown in 7b. The other non-background factor is GMA (Fig. 7c); its score image is seen in Fig. 7d. Calvarial sections stained according to the 1, 2, 5, 7 and 15 min H&E protocols suffered immediate thermal damage. No Raman spectra were obtainable from

damaged areas. However, spectral images were easily obtainable from tissue stained by immersion for 30 seconds in hematoxylin. No hematoxylin factor was found and no hematoxylin bands are present in the factors.

Discussion

Because light absorption can result in sufficient local heating to damage tissues, staining protocols were tested

for thermal compatibility with Raman imaging. From the absorption spectra, one would expect that eosin staining would not result in thermal damage, even to delicate tissue, but that damage could result from absorption by either of the blue stains, hematoxylin or toluidine blue. Stained sections should always be inspected for thermal damage after exposure to the laser light. Additionally, even if there is no visual evidence of thermal damage, Raman spectra from control unstained sections and adjacent stained sections should be compared for subtle differences. In particular, Raman shift frequencies and band intensities change when a protein is denatured thermally or chemically. Any changes must be presumed to be evidence of thermal damage to the tissue, unless further study demonstrates otherwise. Similarly, chemical alterations as a result of staining could result in Raman factors different from the Raman factors of unaffected tissue. However, the stain is usually a superficial layer that affects a small fraction of the specimen. All band frequency and intensity changes in this study are attributed to sample-to-sample variations.

General conclusions can be drawn about the compatibility of Raman microspectroscopy or imaging and histological staining. There are no compatibility problems if a stain does not absorb laser radiation. If near-infrared lasers are used, one would not expect thermal damage resulting from red stains such as eosin or basic fuchsin. Blue stains cannot be assumed to be innocuous. With the 785 nm laser used in these experiments, toluidine blue does not cause any thermal damage because it is only weakly absorbing at this wavelength. Hematoxylin absorbs 785 nm more strongly but by reducing the hematoxylin immersion time to 0.5 min, thermal damage was eliminated with only slight loss in contrast. It may be necessary to modify standard staining protocols when using a laser line that lies within the absorption spectrum of a given stain.

A second concern when using Raman imaging is whether or not the stain(s) will spectroscopically interfere with the Raman signal of tissue components. It is clear that stains, i.e., eosin, hematoxylin and toluidine blue, do not interfere with Raman imaging as evidenced by lack of Raman factors in Figures 3, 4, 5, 6, 7. Immersion in these stains does not interfere with resolution of tissue components by factor analysis. Comparisons with unstained specimens revealed that the factors representing bone mineral and bone matrix are unchanged. Close examination and comparison of Figures 4 (unstained mouse calvaria embedded in GMA) and 5 (mouse calvaria embedded in GMA and stained with eosin) reveal no spectral differences.

NIR Raman spectroscopy is favored for tissue specimens because tissue fluorescence is only weakly excited. Line focusing reduces local power density more than 100× compared to point focusing of the same laser beam [20, 21]. This advantage is obtained even if the goal of an

experiment is not acquisition of a complete two-dimensional spectroscopic image of a specimen. While line focusing reduces the likelihood of damage to delicate specimens, it cannot eliminate the problem completely. Therefore, it is prudent to test for thermal damage before attempting Raman microspectroscopy or imaging of tissue that has been subjected to blue staining.

Acknowledgments. Research was supported by NIH DE11530 (to M.A.I), NIH AR47969 (to M.D.M.), U.S. Army Research Office DAMD17-01-1-0809 (to M.D.M.), and University of Michigan Rackham School of Graduate Studies Summer Research Opportunity Program Fellowship (L.E.G.). The authors would like to thank John Baker (University of Michigan) for his assistance with sample preparation.

References

1. Manoharan R, Shafer K, Perelman L, Wu J, Chen K, Deinum G, Fitzmaurice M, Myles J, Crowe J, Dasari RR, Feld MS (1998) Raman spectroscopy and fluorescence photon migration for breast cancer diagnosis and imaging. *Photochem Photobiol* 67:15–22
2. Romer TJ, Brennan III JF, Fitzmaurice M, Feldstein ML, Deinum G, Myles J, Kramer JR, Lees RS, Feld MS (1998) Histopathology of human coronary atherosclerosis by quantifying its chemical composition with Raman spectroscopy. *Circulation* 97:878–885
3. Fitzmaurice M (2000) Principles and pitfalls of diagnostic test development: implications for spectroscopic tissue diagnosis. *J Biomed Optics* 5:119–130
4. Zonios G, Cothren R, Crawford JM, Fitzmaurice M, Manoharan R, van Dam J, Feld MS Spectral pathology. *Ann NY Acad Sci*, pp 108–115
5. Carden A, Morris MD (2000) Application of vibrational spectroscopy to the study of mineralized tissues (review). *J Biomed Optics* 5:259–268
6. Opperman LA, Passarelli RW, Morgan EP, Reintjes M, Ogle RC (1995) Cranial sutures require tissue interactions with dura mater to resist osseous obliteration *in vitro*. *J Bone Miner Res* 10:1978–1987
7. Tarnowski CP, Ignelzi MA, Morris MD (2002) Mineralization of developing mouse calvaria as revealed by Raman microspectroscopy. *J Bone Miner Res* 17:1118–1126
8. Lin D-L, Tarnowski CP, Zhang J, Dai J, Rohn E, Patel AH, Morris MD, Keller ED (2001) Bone metastatic LNCaP-derivative C4-2B prostate cancer cell line mineralizes *in vitro*. *Prostate* 47:212–221
9. Timlin J, Carden A, Morris MD, Rajachar RM, Kohn DH (2000) Raman spectroscopic imaging markers for fatigue-related microdamage in bovine bone. *Anal Chem* 72:2229–2236
10. Timlin JA, Carden A, Morris MD (1999) Chemical microstructure of cortical bone probed by Raman transsects. *Appl Spectroscopy* 53:1429–1435
11. Bakker Schut TC, Puppels GJ, Kraan YM, Greve J, van der Maas LLJ, Figdor CG (1997) Intracellular carotenoid levels measured by Raman microspectroscopy: comparison of lymphocytes from lung cancer patients and healthy individuals. *Int J Cancer* 74:20–25
12. Bakker Schut TC, Witjes MJH, Sterenborg HJCM, Speelman OC, Roodenburg JLN, Marple ET, Bruining HA, Puppels GJ (2000) *In vivo* detection of dysplastic tissue by Raman spectroscopy. *Anal Chem* 72:6010–6018
13. Manoharan R, Wang Y, Feld MS (1996) Histochemical analysis of biological tissues using Raman spectroscopy. *Spectrochim Acta* 52:215–249
14. Buschman HP, Deinum G, Motz JT, Fitzmaurice M, Kramer JR, van der Laarse A, Bruschke AV, Feld MS

- (2001) Raman microspectroscopy of human coronary atherosclerosis: biochemical assessment of cellular and extracellular morphologic structures *in situ*. *Cardiovasc Pathol* 10:69–82
15. Deinum G, Rodriguez D, Römer TJ, Fitzmaurice M, Kramer JR, Feld MS (1999) Histological classification of Raman spectra of human coronary artery atherosclerosis using principal component analysis. *Appl Spectroscopy* 53:938–942
16. Lasch P, Haensch W, Lewis EN, Kidder LH, Naumann D (2002) Characterization of colorectal adenocarcinoma sections by spatially resolved FT-IR microspectroscopy. *Appl Spectroscopy* 56:1–9
17. Gerrits PO, van Leeuwen MBM (1987) Glycol methacrylate embedding in histotechnology: the hematoxylin-eosin stain as a method for assessing the stability of glycol methacrylate sections. *Stain Technol* 62:181–190
18. Shaver JM, Christensen KA, Pezzuti JA, Morris MD (1998) Structure of dihydrogen phosphate ion aggregates by Raman-monitored serial dilution. *Appl Spectroscopy* 52:259–264
19. Malinowski ER (2002) Factor analysis in chemistry. John Wiley and Sons, New York
20. Treado PJ, Morris MD (1989) A 1000 points of light - the Hadamard-transform in chemical analysis and instrumentation. *Anal Chem* 61:723A
21. Zhang D, Hanna JD, Jiang Y, Ben-Amotz D (2001) Influence of laser illumination geometry on the power distribution advantage. *Appl Spectroscopy* 55:61–65

Ultrastructural Changes Accompanying the Mechanical Deformation of Bone Tissue: A Raman Imaging Study

A. Carden,¹ R. M. Rajachar,^{2,3} M. D. Morris,¹ D. H. Kohn^{2,3}

¹Department of Chemistry, University of Michigan, Ann Arbor, Michigan 48109-1078, USA

²Department of Biologic and Materials Sciences, University of Michigan, Ann Arbor, Michigan 48109-1055, USA

³Department of Biomedical Engineering, University of Michigan, Ann Arbor, Michigan 48109-2125, USA

Received: 12 April 2002 / Accepted: 1 July 2002 / Online publication: 10 December 2002

Abstract. Raman spectroscopy and imaging are known to be valuable tools for the analysis of bone, the determination of protein secondary structure, and the study of the composition of crystalline materials. We have utilized all of these attributes to examine how mechanical loading and the resulting deformation affects bone ultrastructure, addressing the hypothesis that bone spectra are altered, in both the organic and inorganic regions, in response to mechanical loading/deformation. Using a cylindrical indenter, we have permanently deformed bovine cortical bone specimens and investigated the ultrastructure in and around the deformed areas using hyperspectral Raman imaging coupled with multivariate analysis techniques. Indent morphology was further examined using scanning electron microscopy. Raman images taken at the edge of the indents show increases in the low-frequency component of the amide III band and high-frequency component of the amide I band. These changes are indicative of the rupture of collagen crosslinks due to shear forces exerted by the indenter passing through the bone. However, within the indent itself no evidence was seen of crosslink rupture, indicating that only compression of the organic matrix takes place in this region. We also present evidence of what is possibly a pressure-induced structural transformation occurring in the bone mineral within the indents, as indicated by the appearance of additional mineral factors in Raman image data from indented areas. These results give new insight into the mechanisms and causes of bone failure at the ultrastructural level.

Key words: Raman — Bone — Biomechanics — Spectroscopic imaging — Fracture

Like most tissues, bone is hierarchical in structure [1]. Any study of bone properties must investigate the tissue at several levels of organization in order to gain a complete understanding of the influence of structure and composition on these properties. This is especially true when studying mechanical properties. Many studies have looked at the effect of applied load on bone, but on

a macroscopic level [1]. A few have looked at a lower, microstructural level; for example, studies of microcracking [2–4], tensile properties of single osteons [5], and nanoindentation studies of individual lamellae [6, 7]. However, studies at an ultrastructural or chemical level have been impossible using the most common techniques. As a result of these limitations, it is not known definitively how individual collagen fibrils or mineral crystallites react to mechanical load in either the elastic or plastic deformation regimes. There are many hypotheses—rupture of crosslinks in the collagen fibrils, mineral phase transformations or rearrangements, separation of fibrils, and/or relative motion (“gliding”) of fibrils [8, 9]. However, new technical approaches are needed to address these hypotheses and to study the ultrastructural mechanisms guiding the response of bone to mechanical loading.

In recent years, vibrational spectroscopy has enjoyed increasing success as a technique for studying bone properties [10]. Infrared and Raman spectroscopies have been used to study normal and osteoporotic tissue, as well as to investigate compositional changes associated with various bone diseases [10–13]. Raman spectroscopy has proven particularly useful because of its ability to be used on intact specimens as well as its lack of strong interferences from water. Raman spectra can be collected with micron-scale spatial resolution and give simultaneous information about the mineral and organic matrix components of bone. Raman spectra can also be collected over a two-dimensional area to give spatially relevant image information. With the use of multivariate statistics, small local variations in bone composition can be resolved [14–16]. Information from the mineral component and the organic matrix is obtained simultaneously, creating a complete picture of bone composition in the area surveyed. The phosphate ν_1 band at approximately 960 cm^{-1} and the bands associated with collagen (amide III at $\sim 1250\text{ cm}^{-1}$, CH_2 wag at $\sim 1450\text{ cm}^{-1}$, and amide I at $\sim 1665\text{ cm}^{-1}$) are of particular interest for bone compositional studies [10].

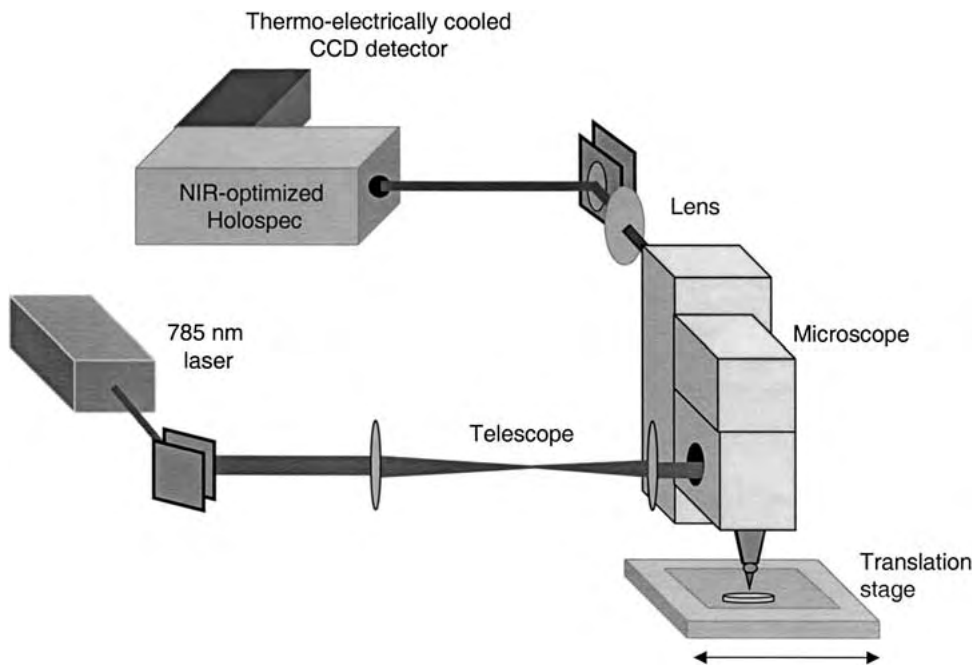


Fig. 1. Raman imaging apparatus.

Raman spectroscopy is a well-established technique for looking at changes brought on by mechanical loading in such materials as polymers [17, 18] and protein films [19], as well as changes in protein structure in solution [20]. Generally, structural changes induced by an applied load cause shifts in bands in the Raman spectrum [17–19]. The amide I band, at about 1665 cm^{-1} , and the amide III band, at about 1250 cm^{-1} , are known to be especially good indicators of protein conformation because of the amide moiety's role in crosslinking and bonding [21]. Spectra of crystalline materials such as silicon or calcium hydroxyapatite also show shifts in spectral bands with applied load, presumably as a result of pressure-induced rearrangement of the crystalline lattice [22–25].

Recent experiments in this lab using Raman spectroscopy have started to provide insight into damage mechanisms at the ultrastructural level. Increases in the number of mineral factors (phosphate ν_1 spectral components) have been observed at the leading edge of fatigue-induced microcracks in cortical bone [14]. It was not clear from these studies whether the spectroscopic changes were a cause or an effect of the damage. Subsequent studies, which analyzed spectral changes in real-time during compressive and tensile loading of bone, provided support for the hypothesis that spectral shifts result from mechanical damage, and demonstrated that changes in the organic matrix also result from mechanical loading [26]. In the present study, we address the hypothesis that bone spectra are altered, in both the organic and inorganic regions, in response to mechanical loading/deformation.

We report here the results of experiments on bovine tissue that was mechanically loaded and locally deformed

via cylindrical indentation. Our results show that most of the damage to the organic matrix occurs at the edges of indents rather than in the center. This damage is in the form of ruptured cross-links, as indicated by spectroscopic shifts in amide I and amide III bands. Additionally, there is evidence that mineral structural transitions are occurring within the indented areas, as evidenced by the increased numbers of mineral factors obtained from the analysis of Raman image data from these regions relative to control areas. These results support the hypothesis that additional mineral factors observed in areas of damage are an effect rather than a cause of the damage.

Materials and Methods

Specimens

Bovine bone from skeletally mature animals was obtained from a local abattoir. A section from the lateral anterior portion of the central annulus of a femur was milled into a flat rectangular beam approximately $3\text{ cm} \times 1\text{ cm} \times 15\text{ cm}$ and stored frozen at -64°C . For these experiments, the beam was cut into 4 pieces, 1 of which was reserved for a separate experiment and was not used further in these studies. The remaining specimens were polished on one side using a graded series of grits, followed by a $0.3\text{ }\mu\text{m}$ alumina slurry. The specimens were sonicated briefly to remove any particles and were then placed in a calcium-buffered antibacterial saline solution. Storage in such solutions at concentrations previously determined to maintain equilibrium has been found to maintain bone mechanical properties by minimizing the diffusion of calcium from the tissue [27]. The specimens were stored at 4°C until needed.

Indentations

Cylindrical indentations were made with a custom-built cylindrical indenter tip attached to an Instron servo-hydraulic

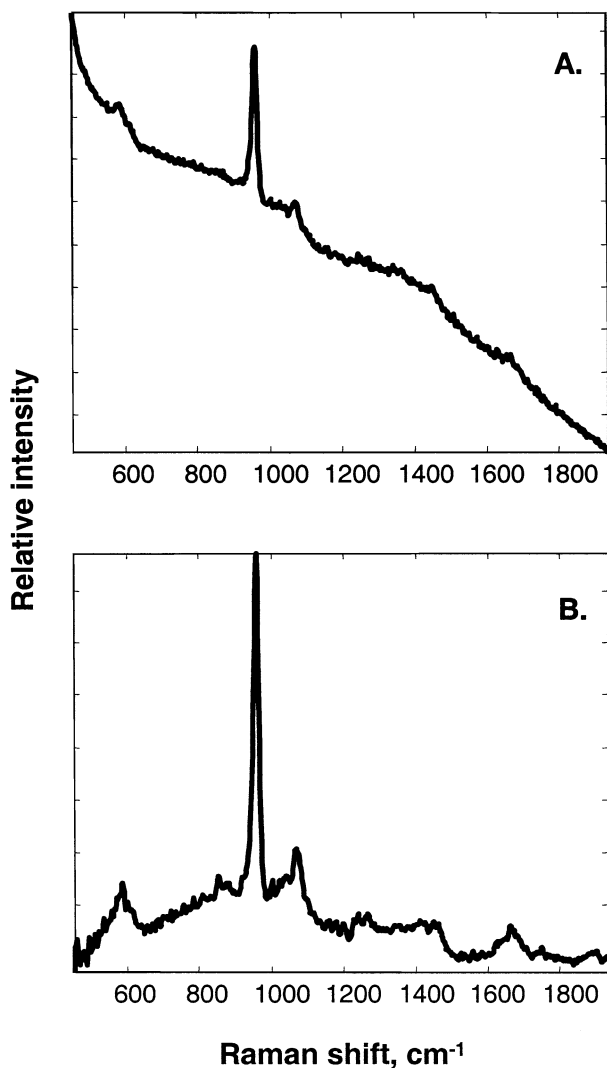


Fig. 2. Advantages of factor analysis: signal-to-noise improvement and background removal. (A) Raw Raman spectrum of bone from one of the image data sets discussed in this work. (B) Factor, representing the Raman spectrum of bone, derived from factor analysis of the entire image data set (approximately 3100 spectra total). For clarity, additional background factors resulting from luminescence are not shown.

mechanical testing machine (model 8521). Using a cylindrical indenter is useful for spectroscopic imaging purposes because the floor of the indent is flat, allowing spectroscopic investigation within the indent as well as at its edges. Indentations resulting from two different loads were made upon each specimen. The shallower (low load) indents (approximate depth 10 μm) were made with loads ranging from 70 to 110 N, and the loads for the deeper (high load) indents (approximate depth 100–150 μm) were in the range of 230–240 N.

Raman Imaging

Our Raman imaging system (Fig. 1) has been previously described [14, 16, 28, 29]. Briefly, it consists of a 785 nm external cavity diode laser (Kaiser Optical Systems, Inc.) with a high-aspect-ratio rectangular beam profile. The beam size is reduced using a telescope and the beam is coupled into a modified epifluorescence microscope (Olympus, Inc.). A 10x/0.5 NA objective (Zeiss) focuses the line-shaped laser beam (length ~ 200

μm) onto the specimen. A complete Raman spectrum is collected simultaneously from every point along the line by the objective, focused by a collection lens, and directed into an axial-transmissive spectrograph (Kaiser Optical Systems, Inc.) which disperses the Raman scatter. The signal is then detected by a thermo-electrically cooled CCD camera (Andor Technologies, Inc.) and stored on a personal computer. A two-dimensional image is built up by moving the specimen in approximately 1 μm steps under the laser beam using a translation stage (New England Affiliated Technologies, Inc.) and acquiring a new line of spectra at each new stage position. An image data set thus consists of a matrix with every point containing a complete Raman spectrum.

For these studies, Raman images were taken in three locations for each indent: within the indent on the indent floor, at the very edge of the indent on the bone surface, and at least 500 μm outside the indent area. A total of 18 images (3 images/indent \times 2 indents/specimen \times 3 specimens) were obtained. Each image contained 25 lines of spectra; the approximate size of each area imaged was 200 \times 35 μm . The total laser power at the specimen was approximately 230 mW, spread into a rectangle approximately 200 μm long and 6 μm wide. It should be noted that because of the shape of the laser beam, power density is relatively low, and heat dissipation is highly efficient [30]. Heat damage to mineralized tissue specimens of the size used in this study has not been observed with this technique [31].

Data Analysis

Both univariate and multivariate analysis techniques were used to examine the data. A spectroscopic parameter proportional to the mineral-to-organic-matrix ratio was used. Similar parameters have been frequently employed by infrared spectroscopists [13, 32]. This spectroscopic mineral-to-organic-matrix ratio was calculated for all of the areas imaged by dividing the spectra from each image into 10 random groups, calculating the mean spectrum from each group, fitting this mean spectrum to a third-order polynomial to remove the effects of luminescent background, then dividing the maximum height of the phosphate ν_1 band at $\sim 959\text{ cm}^{-1}$ by the maximum height of the CH_2 wag band at $\sim 1450\text{ cm}^{-1}$. The CH_2 wag band was chosen since it is less likely than the amide bands to change shape or shift due to changes in protein structure caused by applied load [33]. Ten mineral-to-organic-matrix ratio values were generated for each image, and a standard deviation was calculated from these 10 values.

Factor analysis was also performed on each image data set. Factor analysis is a well-established multivariate image analysis technique [34] used in such fields as magnetic resonance imaging [35–37] and fluorescence imaging [38]. We have frequently used this data analysis approach for the analysis of Raman spectroscopy and image data [39–41]. In this technique, the data are considered as matrices with one spatial and one spectral dimension. The covariance matrix of this matrix is calculated, and a singular value decomposition is performed to obtain the eigenvalues and eigenvectors of the covariance matrix. The eigenvectors can then be combined in linear combinations (or “rotated”) using non-negativity and band-shape constraints to produce Raman spectra. This is not a random process. Spectra cannot be created by rotation; however, they can be separated from backgrounds very effectively. In addition, because factor analysis is an averaging technique, the signal-to-noise ratio in factors is generally significantly better than in raw spectra (Fig. 2). Factor analysis is useful for separating species that may have overlapping spectra, but differ in their spatial distributions. Thus, if two species have different spectra but identical spatial distributions, their spectra will not be separated.

Once the eigenvectors (now called factors) have been effectively rotated, each individual factor’s distribution in the area surveyed can be calculated by regressing the factors back onto the data. The resulting image is called a score image and

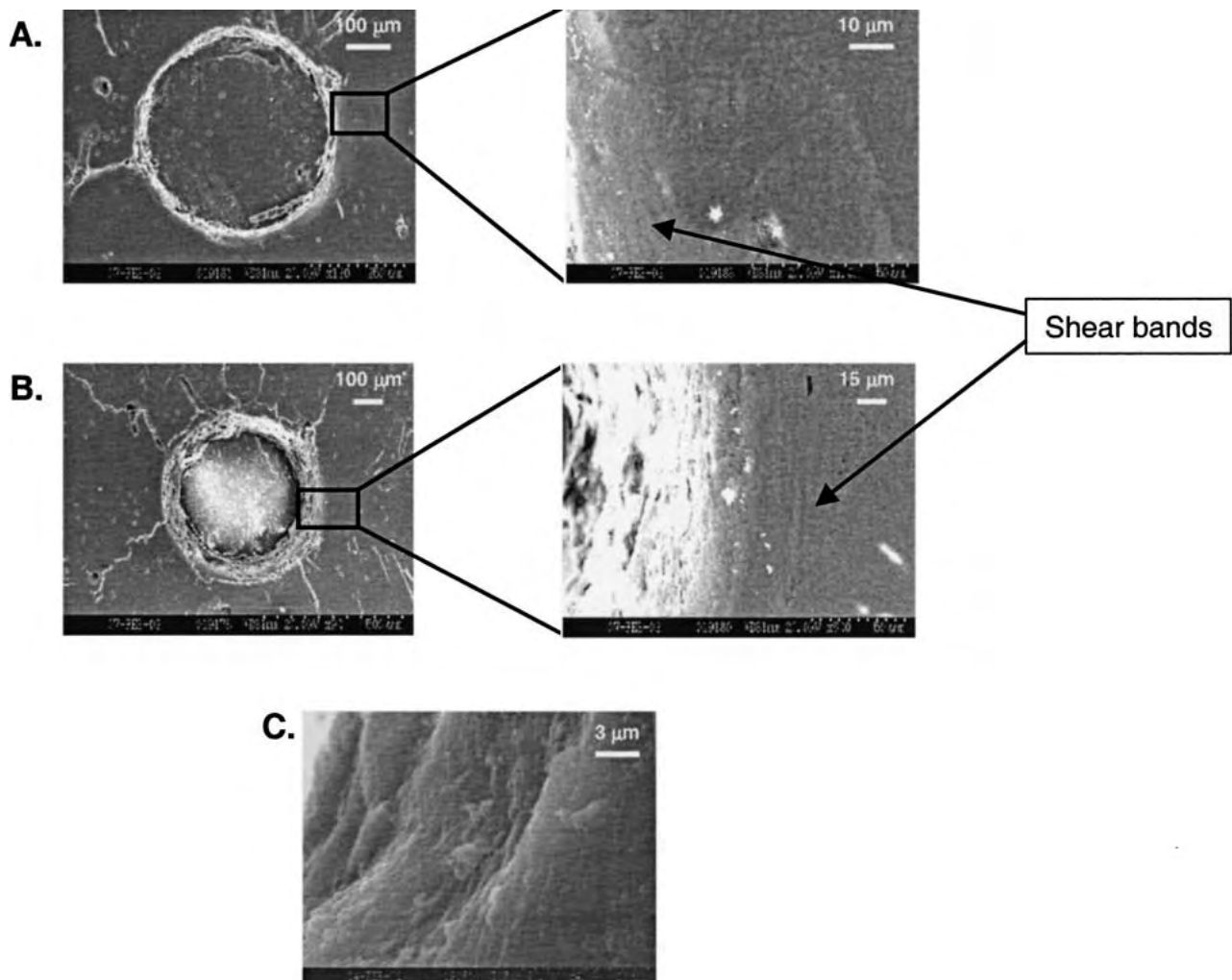


Fig. 3. SEM images of cylindrical indents. **(A)** Low-load indent on specimen #3. Note the shear bands visible in the high-magnification image on the right. **(B)** High-load indent on the same specimen. Again, shear bands are visible in the higher-

magnification image. Shear-induced radial cracking is also visible in both lower-magnification images. **(C)** High-magnification view of shear bands along the indent wall.

is a plot of the spatial distribution of factor intensity within the area imaged.

For these experiments the image data were divided into two spectral subregions: a “mineral subregion” (approximately $500\text{--}1200\text{ cm}^{-1}$) containing the most intense and characteristic bands of the mineral components, and an “organic matrix subregion” (approximately $1200\text{--}1800\text{ cm}^{-1}$) containing the most intense bands attributable to the collagenous matrix. Each spectral subregion was analyzed separately. Factor analysis was performed in MATLAB software (Mathworks, Inc.); both vendor-supplied and locally written scripts were used.

SEM Imaging

Indentation specimens were prepared for SEM analysis with a thin coating of colloidal carbon for electron conductivity. A Hitachi S3200N Scanning Electron Microscope was used for all imaging under conventional high-vacuum mode and secondary electron scintillator detection mode. The electron beam energy was kept at 20 kV and the operating distance was adjusted to 15 mm. Digital images were captured and stored with Quartz PCI acquisition software.

Results

SEM Images

Images of both low- and high-load indents clearly showed shear bands around the circumference of the indent, indicating the presence of shear forces caused by the indenting process (Fig. 3).

Mineral-to-Organic-Matrix Ratio

The spectroscopic mineral-to-organic-matrix ratio for image areas was calculated in order to confirm that the areas imaged were comparable in terms of composition, and that any changes we observed were a result of mechanical loading and deformation, not compositional variations. Because Raman band intensity varies linearly with the number of scattering centers, the phosphate ν_1/CH_2 wag band height ratio is proportional to the

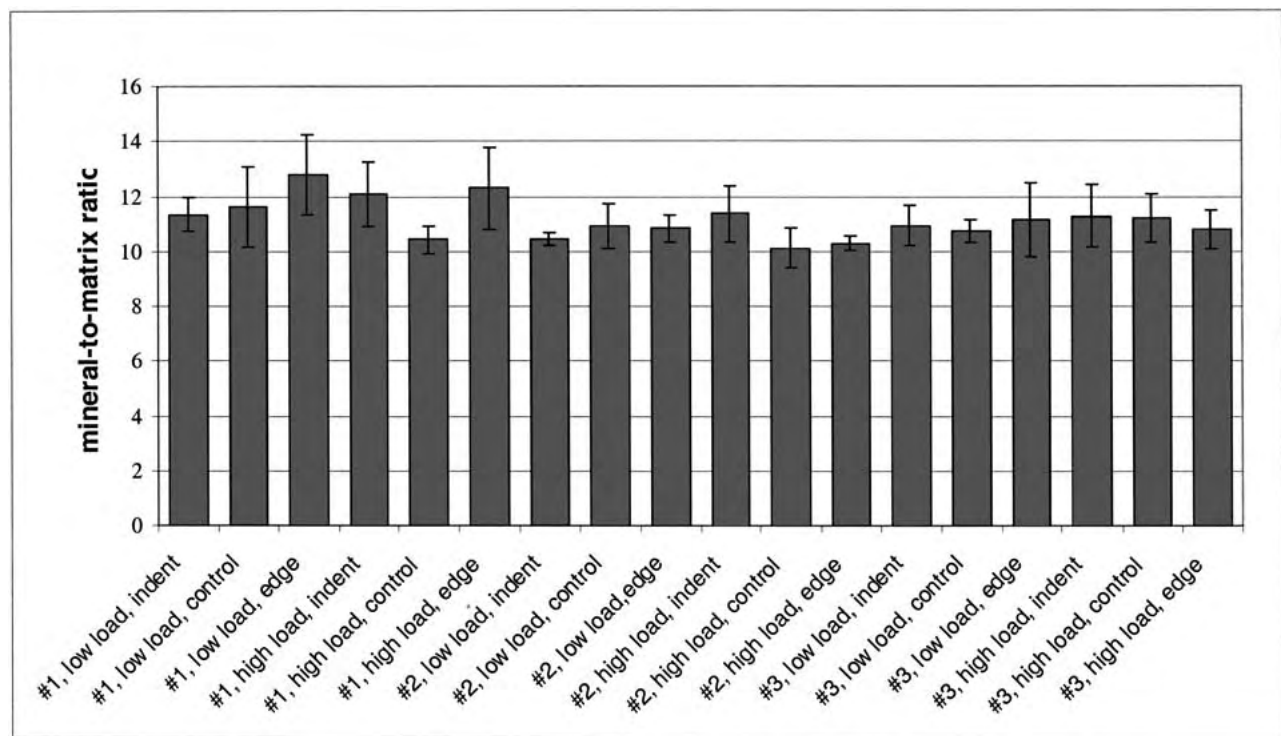


Fig. 4. Bar graph of spectroscopic mineral-to-organic-matrix ratio (phosphate ν_1 maximum intensity divided by CH_2 wag band maximum intensity) calculated for all areas imaged. Error bars are ± 1 SD.

chemical mineral-to-organic-matrix ratio. Figure 4 shows a bar graph of the calculated mineral-to-organic-matrix values for all the areas imaged. The values are relatively consistent. Two-way ANOVA revealed that while there were no statistically significant differences between any of the areas on specimens 2 and 3 ($P < 0.05$), specimen 1 was significantly different from the other two specimens in the edge and indent areas. It should be noted that there were no statistically significant differences in the spectroscopic mineral-to-organic-matrix ratio among the widely spaced control areas on any of the specimens ($P < 0.207$). Statistical variations in the indent and edge regions therefore could be the result of damage resulting from the indent process. Based on these results, we concluded that the differences in spectroscopic mineral-to-organic-matrix ratio among the three specimens were not significant, and that comparisons among the different specimens were valid.

Factor Analysis: Organic Matrix Subregion

In all images of control areas and areas within indentations, only one organic matrix factor was observed (Fig. 5). This factor contained the bands commonly observed in Raman spectra of bone organic matrix [10]: the amide III band at $\sim 1250 \text{ cm}^{-1}$, the CH_2 wag at $\sim 1447 \text{ cm}^{-1}$, and the amide I band at $\sim 1667 \text{ cm}^{-1}$. Score images associated with this single factor showed a

relatively uniform distribution throughout the imaged area.

Different results were obtained from the images taken at the edge of the indents. Here, two organic matrix factors were observed (Fig. 6). One represented the commonly observed Raman spectrum of bone organic matrix described above. The second factor displayed similar bands, but the amide III band showed a distinct increase in its lower-frequency component, whereas the amide I band was shifted to higher wavenumbers ($\sim 1678 \text{ cm}^{-1}$). The score images of these two factors were complementary, with the first factor having higher intensity closer to the indent and the second having higher intensity further away from the indent.

Factor Analysis: Mineral Subregion

Multiple mineral factors containing the phosphate ν_1 peak in different positions were observed in most of the areas imaged (Fig. 7). It is not uncommon to observe more than one mineral factor in Raman data from a given bone specimen owing to tissue heterogeneity resulting from the aging and remodeling processes [42]. Slight local variations in the chemical composition of the mineral result in Raman spectra with varied phosphate ν_1 band positions, which are easily separated by factor analysis. However, an interesting trend was observed in the entire set of images. In almost every image group, more mineral factors were observed within the indented

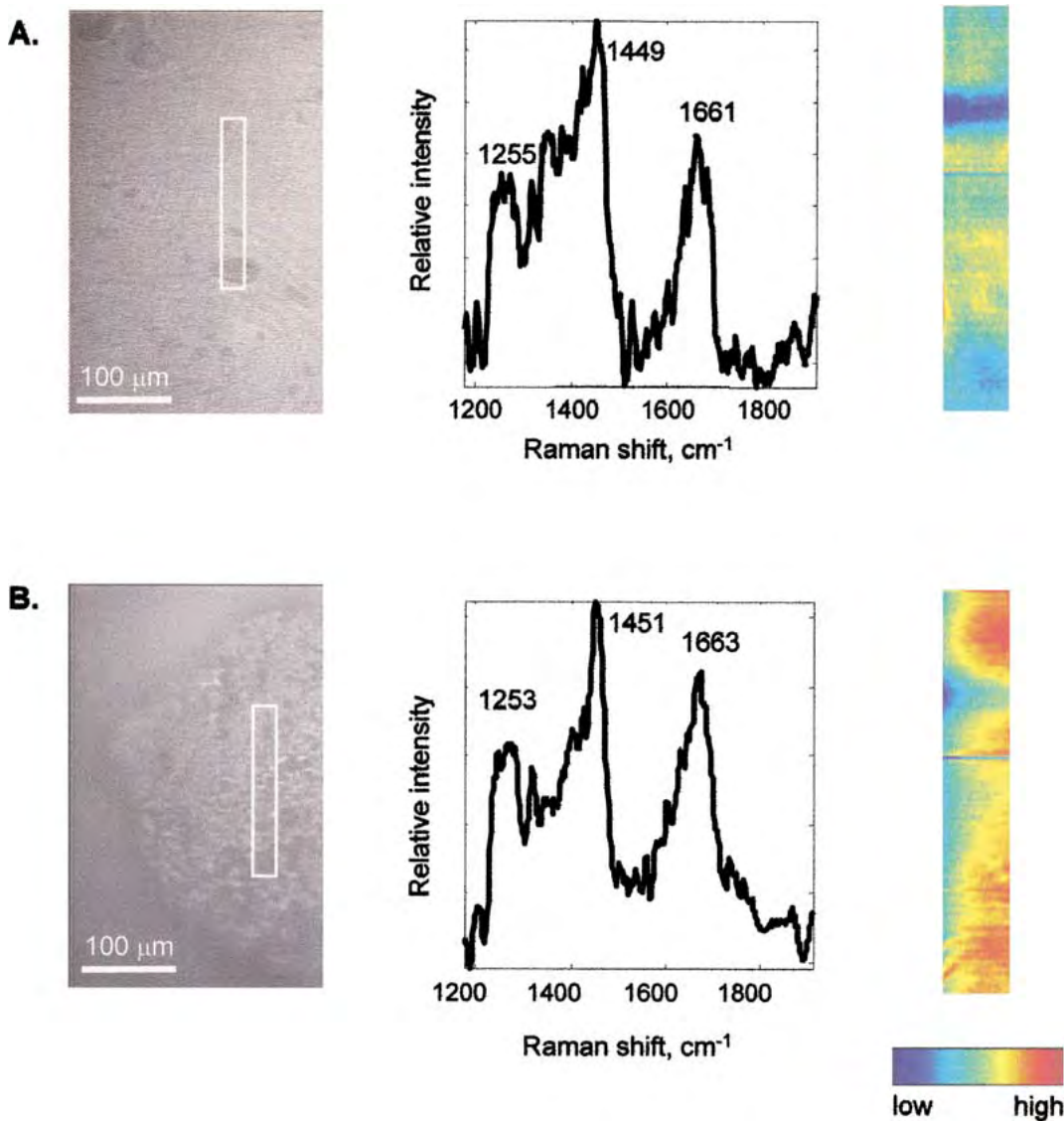


Fig. 5. Images of control regions and regions with indentations for the high-load indent on specimen #3. **(A)** Brightfield image showing the control area imaged for the 230 N indent on specimen #3 (the indent, which is approximately 500 μm away, is out of the field of view). The white box indicates the area imaged. To the right is the single organic matrix factor ob-

tained for this image together with its score image. **(B)** A single organic matrix factor is also obtained for the area imaged within the indent. Image size in both cases is approximately $200 \times 35 \mu\text{m}$. For clarity, the additional background factors resulting from luminescence are not shown.

area than at the edge of the indent or in the control areas. Table 1 shows these results, with the bands corresponding to new factors that appeared after indentation underlined. In most cases a lower-frequency calcium phosphate component appeared; in one case, a higher-frequency calcium phosphate component appeared. This trend is consistent with other studies from this laboratory showing an increase in the number of mineral factors present in Raman data collected from areas of damage [14, 43].

Discussion

We attribute the appearance of the additional collagen factor to damage. This factor containing shifted amide

bands is indicative of the presence of collagen that has undergone a transformation from its normal triple-helical state to a disordered state, presumably as a result of the loading and deformation induced by the indentation process. The appearance of this factor is consistent with observations made by other researchers on protein films and protein solutions [19]. The higher-frequency amide I band and the lower-frequency amide III band observed in this second collagen factor are known spectral signatures of collagen in which crosslinks have been reduced or broken [44]; similar bands have also been observed in studies of collagen denaturation [45–47]. The breaking of crosslinks in mature tissue is thought to be the last process that happens before fracture [8].

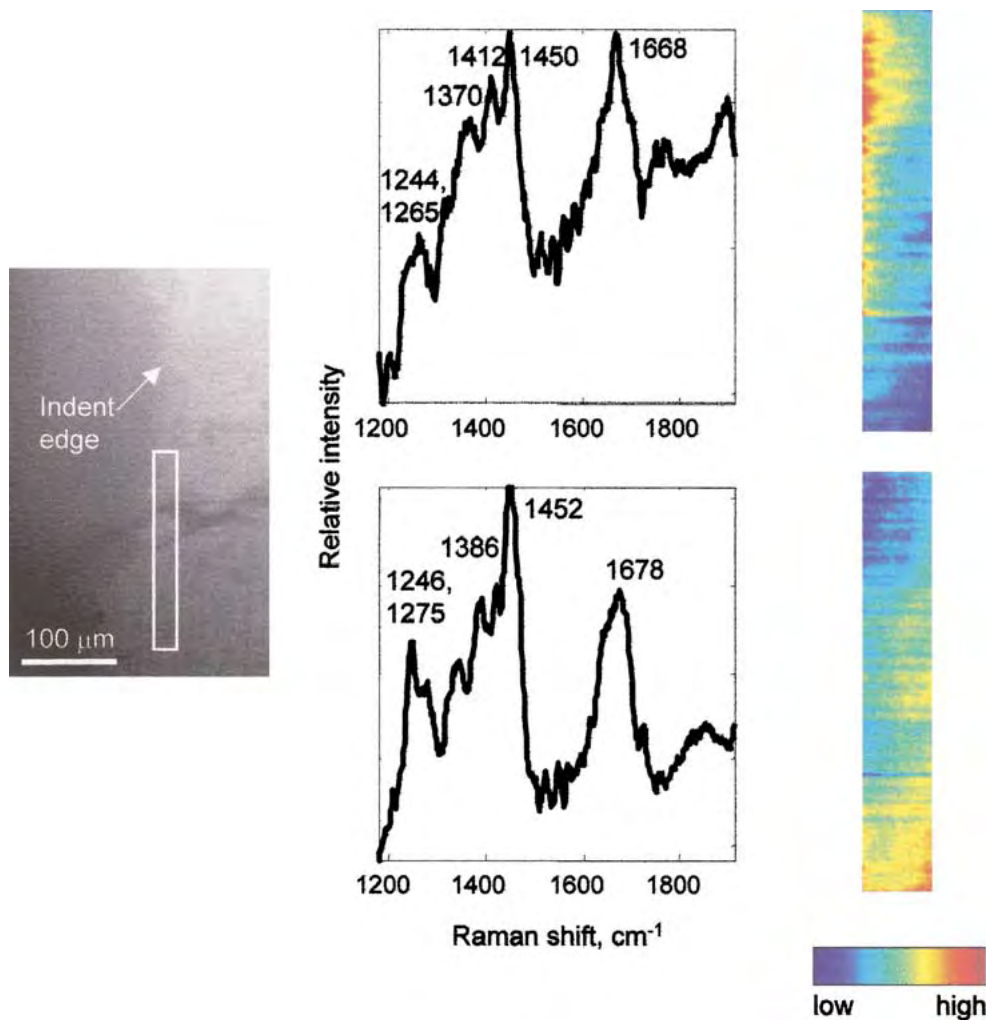


Fig. 6. Brightfield image showing the edge of the high-load indent on specimen #3. The white box indicates the area imaged. To the right are the two organic matrix factors obtained for this image together with their score images. The factor on the top is the Raman spectrum of normal collagen. The factor on the bottom represents a Raman spectrum of disorganized collagen, showing an increase in the low frequency component

of the amide III band and high frequency component of the amide I band, typical of collagen that has lost its structure through crosslink rupture. Note that the score images are complementary. Image size in both cases is approximately $200 \times 35 \mu\text{m}$. For clarity, the additional background factors resulting from luminescence are not shown.

It is interesting that this damaged collagen factor is only observed at the edge of the indents, not within the indent area itself. We hypothesize that at the edge of the indents, the collagen fibrils experience shear forces caused by the edge of the indenter pushing into the bone. These shear forces cause the rupture of crosslinks. Shear behavior in the area of indentations is well characterized. For the case of a cylindrical indenter, a simple analytical description of the elastic and plastic stress field below the punch was given by Sneddon [48]. Unlike sharp indenters, friction is important for indenters that are flat or rounded. With friction, the pressure needed to penetrate to any given depth increases, and shear failure along the indenter/material interface nucleates cracks which travel outward from the compressive zone directly under the indenter [49]. These cracks are clearly visible in the SEM image of the high-load indent in Figure 4. In

addition, closer observation of the SEM images shows the presence of a shear banding pattern at the indent edges. Similar shear banding patterns have been observed at the edges of spherical indentations [50], and shear banding and pile up at the edge of an indentation have also been generated by foreign object-induced damage in metal alloys [51]. In all these cases the material was exposed to an indenting process that allowed shearing to occur under the indent. In the case of the cylindrical punch, the complete region below the indent is subject to a compressive force limiting the appearance of local shear bands to just outside the pile-up zone at the edge of the indent. The fact that the damaged collagen factor does not appear in the data acquired from the middle of the indented area suggests that the collagen in this area is not damaged in a way that is spectroscopically visible; i.e., it is compressed but crosslinks

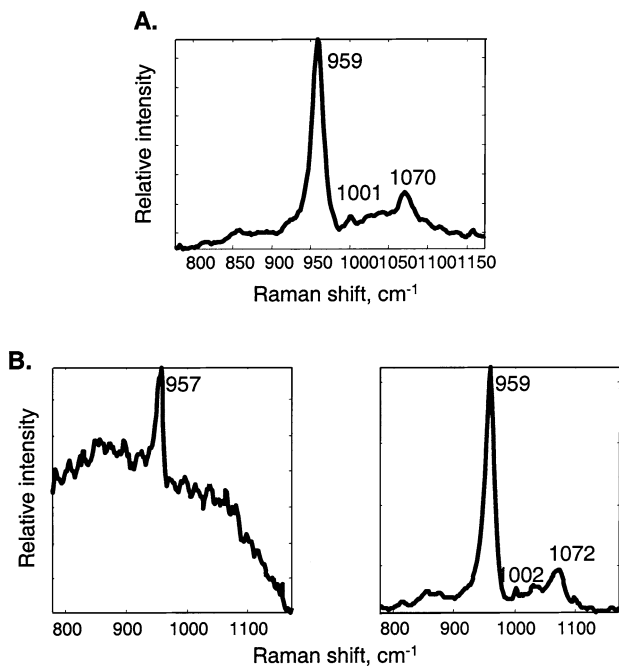


Fig. 7. Example of multiple mineral factors observed in indented specimens. (A) Single factor obtained from analysis of the control area on specimen #3. (B) Factors representing multiple mineral factors obtained from analysis of the high-load indent on specimen #3. For clarity, the additional background factors resulting from luminescence are not shown.

are not broken. This is consistent with the stress behavior described for cylindrical indentations.

The appearance of additional mineral factors within the indented area may indicate a pressure-induced structural transition of the mineral. The addition of either a higher- or lower-frequency component is consistent with high-pressure spectroscopy studies on calcium hydroxyapatite, which show an increase in frequency of the phosphate ν_1 band followed by a decrease with increasing pressure [23, 25]. The loads applied in this experiment result in stresses ranging from 0.4 GPa, yielding the shallow indents, to 1.2 GPa, yielding the deep indents; these values are comparable to those applied in the high-pressure spectroscopy studies in which a structural transition was observed. We therefore believe that the additional factors represent spatially distinct mineral species formed as a consequence of pressure-induced structural transitions within the bone mineral lattice [23, 25]. We have earlier observed the appearance of additional mineral factors accompanying permanent deformation in bone; for example, in the macroscopic fracture of mouse femora [43] as well as in microcracks within bovine bone [14]. However, in these studies we could not establish whether the additional mineral factors observed were a cause or an effect of the fracture process. The results from the current experiments indicate that the additional mineral factors are in fact an effect of mechanical loading. The fact that we can resolve multiple factors rather than seeing one mineral factor with a

shifted phosphate ν_1 band indicates that not all the mineral present undergoes the transition, possibly because the local pressure was not high enough to drive the transition to completion, or because not all the mineral species present were able to undergo the transition.

The nature of the structural transition occurring in the bone mineral is not known. Xu et al. [23] postulate that the structural transition occurring in pure hydroxyapatite is the result of a rearrangement of hydroxyl groups. However, bone mineral is thought not to contain hydroxyl groups in any appreciable concentration [52–54]. In addition, the additional substituents in bone mineral undoubtedly affect the response of the mineral to applied load. It is known that carbonation in bone mineral causes vacancies in the mineral lattice, creating an opportunity for pressure-induced movement and structural changes [53]. Further spectroscopic and X-ray diffraction studies are required to better elucidate the nature of this transformation.

Conclusions

Spectroscopic changes resulting from mechanical loading of bone were observed in these studies, indicating two different damage mechanisms for different bone tissue components. The organic matrix showed clear evidence of crosslink rupture, consistent with what is known of the mechanical behavior of other collagenous tissues, particularly more mature tissues which contain more crosslinks [8, 9]. This rupture occurred only in areas where shear forces were present (indent edges), rather than where only compression occurred (indent floor). The mineral phase of the tissue, on the other hand, was found to be altered where only compression had occurred. The possibility of a pressure-induced structural transition occurring in bone mineral is particularly intriguing. This could be a method by which energy is dissipated with minimal damage to the surrounding tissue. Similar behavior has been observed in ceramic materials subjected to stress, a phenomenon known as “transformation toughening” [55, 56]. These processes have also recently been postulated to occur in bone [57]. We propose that the bone mineral structural transitions that we have observed are the source of this transformation toughening. Aging, as well as bone diseases that alter bone mineral crystallite structure, such as osteoporosis, could hinder this transition and contribute to increased fragility. If this is the case, new and different treatment options may be realized from these results.

Acknowledgments. The authors gratefully acknowledge financial support from the following sources: Rackham Graduate School Predoctoral Fellowship (AC), the University of Michigan Bone Core Research Center (NIH grant P30 AR46024) (AC,MDM), NSF grant BES 9410303 (DHK), the Whitaker Foundation (DHK), and NIH Training Grant T32 DE 07057 (RMR).

Table 1. Number of mineral factors, and phosphate ν_1 band positions for those factors, observed for all specimens. Factors that appeared after indentation (relative to the control) are underlined.

	#1, low load	#1, high load	#2, low load	#2, high load	#3, low load	#3, high load
Control	2 species 955 959	3 species 954 959 962	2 species 959 965	1 species 959	1 species 959	1 species 959
Edge of Indent	Not observed due to fluorescence	1 species 960	2 species 956 960	1 species 960	1 species 960	1 species 960
Within Indent	3 species 954 957 <u>962</u>	2 species 955 959	3 species <u>954</u> <u>958</u> 962	2 species <u>953</u> <u>959</u>	2 species <u>957</u> <u>960</u>	2 species <u>957</u> <u>959</u>

References

- Kaplan FS, Hayes WC, Keaveny TM, Boskey A, Einhorn JP, Iannotti JP (1994) Form and function of bone. In: Simon SR (ed) Orthopaedic basic science. American Academy of Orthopaedic Surgeons, Rosemont, Illinois, pp 127–184
- Rajachar RM, Chow DL, Kohn DH (2002) Incipient fatigue mechanisms in bovine cortical bone as detected by acoustic emission. *J Biomech* (in press)
- Reilly GC (2000) Observations of microdamage around osteocyte lacunae in bone. *J Biomech* 33:1131–1134
- Ramtani S, Zidi M (1999) Remodeling of the bone material containing microcracks: a theoretical analysis. *Euro Phys J* 8:257–263
- Ascenzi A, Bonucci E (1967) The tensile properties of single osteons. *Anat Record* 158:375–386
- Zysset P, Guo XE, Hoffer CE, Moore KE, Goldstein SA (1999) Elastic modulus and hardness of cortical and trabecular bone lamellae measured by nanoindentation in the human femur. *J Biomech* 32:1005–1012
- Hoffer CE, Moore KE, Kozloff K, Zysset PK, Brown SA, Goldstein SA (2000) Heterogeneity of bone lamellar-level elastic moduli. *Bone* 26:603–609
- Silver FH, Kato YP, Ohno M, Wasserman AJ (1992) Analysis of mammalian connective tissue: relationship between hierarchical structures and mechanical properties. *J Long-Term Effects Med Implants* 2:165–198
- Fratzl P, Misof K, Zizak I, Rapp G, Amenitsch H, Bernstorff S (1997) Fibrillar structure and mechanical properties of collagen. *J Struct Biol* 122:119–122
- Carden A, Morris MD (2000) Application of vibrational spectroscopy to the study of mineralized tissues (review). *J Biomed Optics* 5:259–268
- Magne D, Weiss P, Boulter J-M, Laboux O, Daculsi G (2001) Study of the maturation of the organic (type I collagen) and mineral (nonstoichiometric apatite) constituents of a calcified tissue (dentin) as a function of location: a Fourier transform infrared microspectroscopic investigation. *J Bone and Miner Res* 16:750–757
- Ou-Yang H, Paschalis EP, Mayo WE, Boskey AL, Mendelsohn R (2001) Infrared microscopic imaging of bone: spatial distribution of CO_3^{2-} . *J Bone Miner Res* 16:893–900
- Gadaleta SJ, Boskey AL, Paschalis E, Carlson C, Menschik F, Baldini T, Peterson M, Rimnac CM (2000) A physical, chemical, and mechanical study of lumbar vertebrae from normal, ovariectomized, and nandrolone decanoate-treated cynomolgus monkeys (*Macaca fascicularis*). *Bone* 27:541–550
- Timlin JA, Carden A, Morris MD, Rajachar RM, Kohn DH (2000) Raman spectroscopic imaging markers for fatigue-related microdamage in bovine bone. *Analyt Chem* 72:2229–2236
- Timlin JA, Morris MD, Bonadio JF, Hoffer ICE, Kozloff SA, Goldstein SA (1999) Spatial distribution of phosphate species in mature and newly generated mammalian bone by hyperspectral Raman imaging. *J Biomed Optics* 4:28–34
- Pezzuti JA, Morris MD, Bonadio JF, Goldstein SA (1998) Hyperspectral Raman imaging of bone growth and re-growth chemistry. *Proc of the SPIE* 3261:270–276
- Yeh W-Y, Young RJ (1998) Deformation processes in poly(ethyleneterephthalate) fibers. *J Macromol Sci Phys* B37:83–118
- Yeh W-Y, Young RJ (1999) Molecular deformation processes in aromatic high modulus polymer fibers. *Polymer* 40:857–870
- Frushour BG, Koenig JL (1974) Raman spectroscopic study of mechanically deformed poly-L-alanine. *Biopolymers* 13:455–474
- Renugopalakrishnan V (1985) Low-frequency Raman spectra as a conformational probe for polypeptides and proteins. *Macromolecules* 18:1786–1788
- Bandekar J (1992) Amide modes and protein conformation. *Biochim Biophys Acta* 1120:123–143
- Kailer A, Nickel KG, Gogotsi YG (1999) Raman microspectroscopy of nanocrystalline and amorphous phases in hardness indentations. *J Raman Spectroscopy* 30:939–946
- Xu J, Gilson DFR, Butler IS, Stangel I (1996) Effect of high external pressures on the vibrational spectra of biomedical materials: calcium hydroxyapatite and calcium fluorapatite. *J Biomed Mater Res* 30:239–244
- Butler IS, Gilson DFR (1997) Recent studies of the high-pressure vibrational microspectra of solid inorganic materials. *J Mol Struct* 408/409:39–45
- Vaidya SN, Karunakaran C, Pande BM, Gupta NM, Iyer SB, Karweer SB (1997) Pressure-induced crystalline to amorphous transition in hydroxylapatite. *J Mater Sci* 32:3213–3217
- Morris MD, Carden A, Rajachar RM, Kohn DH (2001) Bone microstructure deformation observed by Raman spectroscopy. *Proc SPIE* 4254:81–89
- Gustafson MB, Martin RB, Gibson V, Storms DH, Stover J, Gibeling J, Griffin L (1996) Calcium buffering is required to maintain bone stiffness in solution. *J Biomech* 29:1191–1194
- Christensen K, Morris MD (1998) Hyperspectral Raman microscopic imaging using Powell lens line illumination. *Appl Spectroscopy* 52:1145–1147
- Jestel NL, Shaver JM, Morris MD (1998) Hyperspectral Raman line imaging of an aluminosilicate glass. *Appl Spectroscopy* 52:64–69
- Zhang D, Hanna JD, Jiang Y, Ben-Amotz D (2001) Influence of laser illumination geometry on the power distribution advantage. *Appl Spectroscopy* 55:61–65

31. Carden A (2002) Effects of applied load on bone ultrastructure explored using Raman microspectroscopy and imaging. Ph.D. dissertation, University of Michigan, Ann Arbor, Michigan
32. Boskey AL, Camacho NP, Mendelsohn R, Doty SB, Binderman I (1992) FT-IR microscopic mappings of early mineralization in chick limb bud mesenchymal cell cultures. *Calci Tissue Int* 51:443–448
33. Bussian BM, Sander C (1989) How to determine protein secondary structure in solution by Raman spectroscopy: practical guide and test case DNase I. *Biochemistry* 28:4271–4277
34. Adams MJ (1995) Chemometrics in analytical spectroscopy. The Royal Society of Chemistry, Cambridge
35. Grahn H, Szeverenyi NM, Roggenbuck MW, Delaglio F, Geladi P (1989) Data analysis of multivariate magnetic resonance images. I. A principal component analysis approach. *Chemometrics and Intelligent Laboratory Systems* 5:311–322
36. Geladi P, Grahn H (1996) Multivariate image analysis. John Wiley and Sons, Chichester
37. Geladi P, Isaksson H, Lindqvist L, Wold S, Esbensen K (1989) Principal components analysis of multivariate images. *Chemomet Intel lab systems* 5:209–220
38. Kawata, Satoshi, Sasaki, Keiji (1996) Multispectral image processing for data analysis. In: Wang X.F., Herman B. (eds) *Fluorescence imaging spectroscopy and microscopy*. John Wiley and Sons, NY, pp 55–85
39. Drumm CA, Morris MD (1995) Microscopic Raman line-imaging with principal components analysis. *Applied Spectroscopy* 49:1331–1337
40. Shaver JM, Christensen KA, Pezzuti JA, Morris MD (1998) Structure of dihydrogen phosphate ion aggregates by Raman-monitored serial dilution. *Appl Spectroscopy* 52:259–264
41. Morris MD, Timlin JA, Garden A, Tarnowski CP, Edwards CM (2000) Multivariate data reduction techniques for hyperspectral Raman imaging. *Proc SPIE* 3920:151–158
42. Tarnowski CP, Ignelzi Jr MA, Morris MD (2002) Mineralization of developing mouse calvaria as revealed by Raman microspectroscopy. *J Bone Miner Res* 17:1118–1126
43. Morris MD, Carden A, Rajachar RM, Kohn DH (2002) Effects of applied load on bone tissue as observed by Raman spectroscopy. *Proc SPIE* 4614:47–54
44. Paschalis EP, Verdelis K, Doty SB, Boskey AL, Mendelsohn R, Yamauchi M (2001) Spectroscopic characterization of collagen crosslinks in bone. *J Bone Miner Res* 16:1821–1828
45. Lazarev YA, Lazareva AV (1978) Infrared spectra and structure of synthetic polypeptides. *Biopolymers* 17:1197–1214
46. Lazarev YA, Grishovsky BA, Khromova TB (1985) Amide I band of IR spectrum and structure of collagen and related polypeptides. *Biopolymers* 24:1449–1478
47. Frushour BG, Koenig JL (1975) Raman scattering of collagen, gelatin, and elastin. *Biopolymers* 14:379–391
48. Sneddon IN (1965) The relation between load and penetration in axisymmetric Boussinesq problem for a punch of arbitrary profile. *Int J Eng Sci* 3:47–57
49. Baran G, Shin W, Abbas A, Wunder S (1994) Indentation cracking of composite matrix materials. *J Dent Res* 73:1450–1456
50. Guiberteau F (1993) Indentation fatigue. A simple cyclic Hertzian test for measuring damage accumulation in polycrystalline ceramics. *Philos Mag A* 68:1003–1016
51. Ritchie RO (1999) Thresholds for high-cycle fatigue in a turbine Engine Ti-6Al-4V alloy. *Int J Fatigue* 21:653–662
52. Rey C, Collins B, Goehl T, Dickson IR, Glimcher MJ (1989) The carbonate ion environment in bone mineral: a resolution-enhanced Fourier transform infrared spectroscopy study. *Calcif Tissue Int* 45:157–164
53. Rey C, Miquel JL, Facchini L, Legrand AP, Glimcher MJ (1995) Hydroxyl groups in bone mineral. *Bone* 16:583–586
54. Loong C-K, Rey C, Kuhn LT, Combes C, Wu Y, Chen S-H, Glimcher MJ (2000) Evidence of hydroxyl-ion deficiency in bone apatites: an inelastic neutron-scattering study. *Bone* 26:599–602
55. Belnap JD, Tsai J-F, Shetty DK (1994) Direct measurement of crack shielding in ceramics by the application of Raman microprobe spectroscopy. *J Mat Res* 9:3183–3193
56. Green DJ, Hannink RHJ, Swain MV (1989) Transformation toughening of ceramics. CRC Press, Inc., Boca Raton, FL
57. Vashishth D, Behiri JC, Bonfield W (1997) Crack growth resistance in cortical bone: concept of microcrack toughening. *J Biomech* 30:763–769

Bone tissue ultrastructural defects in a mouse model for osteogenesis imperfecta: a Raman spectroscopy study

Tsoching Chen¹, Kenneth M. Kozloff², Steven A. Goldstein², Michael D. Morris^{*1}

¹Department of Chemistry, University of Michigan, Ann Arbor, MI 48109-1055

²Orthopaedic Research Laboratories, University of Michigan Medical School, Ann Arbor, MI 48109-0486

ABSTRACT

Osteogenesis imperfecta (OI) is genetic defect in which the genes that code for the $\alpha 1(I)$ or $\alpha 2(I)$ chains of type I collagen are defective. The defects often result in substitution of a bulky amino acid for glycine, causing formation of collagen that can not form the normal triple helix. Depending on the details of the defects, the outcomes range from controllable to lethal. This study focuses on OI type IV, a more common and moderately severe form of the disease. People with the disease have a substantial increase in the risk and rate of fracture. We examine the spectroscopic consequences of these defects, using a mouse model (BRTL) that mimics OI type IV. We compare Raman images from tibial cortical tissue of wild-type mice and BRTL mice with single copy of mutation and show that both mineral to matrix ratios and collagen inter-fibril cross-links are different in wild-type and mutant mice.

Keywords: Raman spectroscopy, Raman Imaging, Osteogenesis Imperfecta, bone tissue, collagen, cross-links

1. INTRODUCTION

Bone is composed of two major components: inorganic mineral and an organic matrix: About 90% of the organic matrix is type I collagen. Collagen provides a supporting matrix on which mineralization occurs. The mineral is a highly carbonated form of apatite, where CO_3^{2-} may substitute either for PO_4^{3-} (B-type carbonation) or OH^- (A-type carbonation). A variety of other anions and cations may also substitute for sites of the crystal lattice^[1].

Osteogenesis imperfecta (OI), also known as brittle bone disease, is a genetic defect affecting bone matrix collagen^[2]. As a result of mutations in one of the two genes (COL1A1 and COL1A2) that encode the strands of type I collagen, risk of fracture significantly increases. Collagen is a heterotrimer, composed of two copies of the $\alpha 1$ chain and one copy of the $\alpha 2$ chain. Each chain is a string of triplets containing glycine followed by two other amino acids, frequently proline and hydroxyproline^[3]. The mutations causing OI most commonly result from a substitution of glycine by a larger amino acid, disrupting the triple helix. This alteration in the triple helix structure may alter normal collagen cross linking and matrix mineralization, depending on the location of the defect along the collagen chain(s).

Four types of OI have been attributed to collagen mutations, and range from mild (Type I) to perinatal lethal (Type II)^[4].^[5] In this study we investigate tissue from the BRTL mouse, a model for OI type IV, a moderately severe but survivable form of the disease. BRTL has an $\alpha 1(I)$ Gly³⁴⁹ – Cys substitution in type I collagen, mimicking the genetic mutation found in an OI type IV patient (Forlino et al, 1999)^{[6],[9]}. Just as humans with OI get fewer fractures as they age, biomechanical tests show that at two months of age, BRTL mice have lower bone strength and stiffness than wild-type mice, but at six months, these parameters improve to WT levels. This alteration is accomplished without corresponding improvements in the geometry of the bone, implying that the changes are due to improvements in the material properties of the bone matrix (Kozloff et al, 2004)^{[7],[8],[10]}.

* mdmorris@umich.edu; Tel: 1 734 763-0477; Fax: 1 734 615-3790; <http://www.umich.edu/~morgroup>

Raman microspectroscopy has matured into an important complement to traditional methods for detection, quantification and imaging of local variations in the molecular structures of bone matrix and mineral. While similar information is available from infrared spectroscopy, Raman spectroscopy is equally applicable to specimens as thin as a few microns or as thick as intact tissue and offers superior spatial resolution. As a microspectroscopy, Raman scattering provides micron-level spatial resolution and can be used to generate images that map chemical structure or physical property variations.

2. APPARATUS AND METHODS

2.1 Raman microspectroscopic imaging system

Our epi-illumination Raman microspectroscopic imaging system with a line-focused laser beam is shown in Figure 1. We focus an external cavity 785 nm diode laser onto the specimen through a 10X/ 0.5 NIR-coated objective. Raman scatter is collected through the same objective and focused onto the entrance slit of a NIR optimized spectrograph fitted with a cooled back-illuminated CCD. By using a line-focused beam, we can simultaneously collect a line of 254 spectra, and then by translating the specimen under the objective in small increments, an image is built up line-by-line.

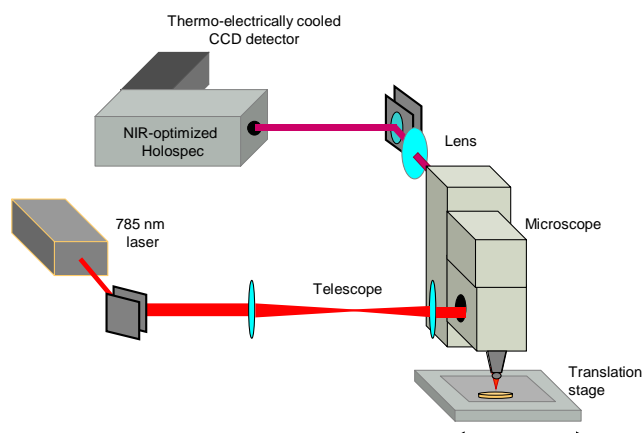


Figure 1. Raman microspectroscopic imaging system

2.2 Data analysis

The data obtained is analyzed using both univariate analysis and multivariate analysis (i.e., band target entropy minimization, or BTEM)^{[11], [12]}. In BTEM, singular value decomposition is used to calculate the eigenvectors of the spectroscopic image data set. Bands in non-noise eigenvectors that would normally be used for recovery of spectra are examined for localized spectral features. For a targeted (identified) band, information entropy minimization or a closely related algorithm is used to recover the spectrum containing this feature from the non-noise eigenvectors, plus the next 5-30 eigenvectors, in which noise predominates. By adding or subtracting the recovered spectra, known as “factors,” in linear combinations and regressing them back into the original data, the distribution, or “score,” of each factor in the imaged data can be obtained. The univariate data analysis is performed using GRAMS32, and the multivariate data analysis is performed using MATLAB (Version 6.1, Mathworks, Inc.).

3. EXPERIMENTS

Tissue from previously sacrificed 2 month male mice with single copies of the mutation (BRTL, n=5), and wild-type mice (WT, n=5) were employed in this study. Tibias were prepared by embedding in a weakly exothermic polymer,

sectioning at the midshaft using a low-speed diamond saw, and polishing to near the tibio-fibular junction. Five transects, each containing a line of 254 Raman spectra, were taken along each transverse cross section, extending from the endosteal to the periosteal surface of the posterior aspect of the tibia. Following baselining, areas under the phosphate ν_1 ($903\text{--}991\text{ cm}^{-1}$), carbonate ν_1 ($1046\text{--}1110\text{ cm}^{-1}$), and amide I ($1616\text{--}1720\text{ cm}^{-1}$) bands were measured. Phosphate to amide I band area ratio was calculated as a measure of mineral maturity and mineral to matrix ratio. Additionally, to study the chemical structure variations, a 254×150 pixel image of an approximately $330 \times 200\mu\text{m}^2$ was taken from the same region of each specimen. After recovery of the bone spectra from the image data, curve-fitting was used to resolve the underlying bands of amide I, and areas under the amide I sub-bands bands were obtained.

4. RESULTS AND DISCUSSION

4.1 Abnormal mineral to matrix ratio in BRTL mouse

Two month old BRTL mice show approximately 15% lower mineral/matrix ratios than those of the wild-type mice at the same age. As shown in Figure 2 the mineral/matrix ratio for the wild type mice is 5.44 ± 0.402 , while in the BRTL it is 4.64 ± 0.180 . The lower mineral to matrix ratio of the BRTL mice suggests impaired mineral deposition on the defective matrix, caused by a single glycine to cysteine point substitution.

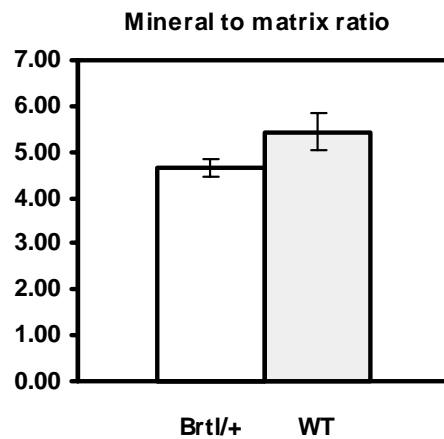


Figure 2. Mineral to matrix ratio of 2 month old WT and BRTL mice

4.2 Spectral differences and separated mineral factors found in the BRTL mouse

In the resulting data, we have found some spectral differences between BRTL and wild-type mice. The Amide I band of BRTL mouse slightly shifts to higher frequency, while the Amide III band shifts to lower frequency. The spectral difference on the matrix is what we would expect to see since the glycine to cysteine substitution disrupts the collagen triple helix structure and may cause collagen to unwind. The Raman spectrum of bone mineral has a prominent phosphate band at $958\text{--}960\text{ cm}^{-1}$. In addition to the spectral differences observed on the amide I band, band target entropy minimization extracted a mineral factor at 952 cm^{-1} , which likely reflects highly disordered crystallites^{[13],[14]}. While A-type carbonation is known to result in a highly deformed lattice^{[15],[16],[17]}, it would be a simplification to attribute this band to crystallites containing A-type carbonate. The mineral factor at 964 cm^{-1} is uncarbonated phosphate, implying a less mature tissue. Figure 3 shows the three mineral factors and their corresponding score images of a BRTL mouse. Background factors are omitted for clarity. The images give the spatial distribution of these factors in the imaged area. The multiple mineral factors found in the BRTL mouse indicates that the mineralization of the tissue is more heterogeneous than that of the wild-type mouse.

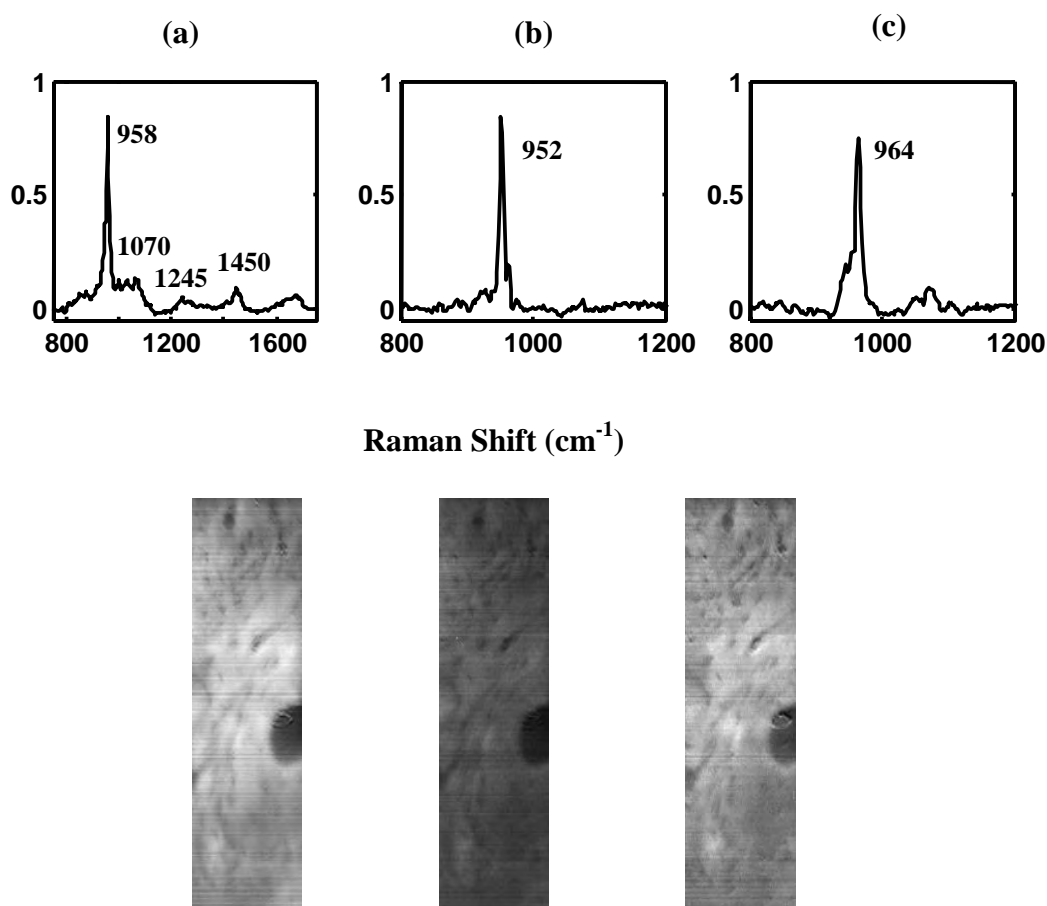


Figure 3. Factors and corresponding score images of a BRTL mouse. (a) the major bone factor with phosphate at 958 cm⁻¹, carbonate at 1070 cm⁻¹, amide III at 1245 cm⁻¹, CH₂ wag at 1450 cm⁻¹, and amide I at 1665 cm⁻¹. (b) the second mineral factor with phosphate at 952 cm⁻¹. (c) the third mineral factor with phosphate at 964 cm⁻¹.

4.3 Collagen cross-links

An important strength of both Raman and infrared spectroscopy is sensitivity to protein secondary structure. Amide I is usually an envelope that can be resolved into two or more bands and that can extend over much of the 1600-1700 cm⁻¹ region. Similar information is carried in amide II and amide III, although they are less frequently used to elucidate secondary structure.

Collagen is a special case because of its unusual triple helix structure. There are structural differences among the various types of collagen, of course, but the general patterns are the same throughout. While it is reasonable to assume that collagen amide I should resemble an α -helix spectrum, the actual spectrum is more complex. In uncrosslinked collagen (e.g. from rat or calf skin, a triple helix of α_1 chains) the amide I region can be resolved into several bands. The most prominent in the FTIR spectra are at 1630, 1660, and 1670 cm⁻¹, although these bands are shifted somewhat depending on the type of collagen. Based on studies of poly(gly-pro-pro), Lazarev and co-workers assign these bands to the carbonyl stretches of hydrogen-bonded glycine, proline-2 and proline-3 in a gly-pro-pro motif.^[20] However, these assignments must be considered approximate because they do not assume the presence of hydroxyproline, let alone other amino acids. Payne and Veis attribute a rat skin collagen band at 1660 cm⁻¹ to carbonyls of the X amino acid hydrogen bonded to glycine amide protons of an adjacent chain. Additionally, the simplified assignments do not take cognizance of the effects of interfibrillar cross-linking on the secondary structure of collagen and the consequent changes

in the amide I envelope. The high frequency component at 1685-1695 cm^{-1} is associated with disruption of hydrogen bonding, although the origin of the effect remains unclear.

Inter- and intra-fibril cross-links are a well-known feature of bone tissue collagen. Disruption or absence of these cross-links results in changes in the relative intensities of the major bands of amide I. The disruptions can include chemical perturbation of cross-links and their chemical cleavage as well as mechanical rupture. Similar effects are observed in immature tissue, where the crosslinks have not yet been formed.

It has been shown that denaturing collagen to gelatin causes a high frequency shoulder at 1685 cm^{-1} to become more prominent. Mendelsohn and co-workers recently showed that the 1690 cm^{-1} band intensity in bone matrix increases relative to the intensity of the 1663 cm^{-1} band when dehydrodihydroxylysinoxorleucine, dehydrohydroxylysinoxorleucine or dehydrohistindohydroxymerodesmosine cross-links are chemically reduced^[21]. Our own work with fetal murine calvarial tissue shows that the matrix amide I band in newly deposited tissue has a prominent shoulder at 1685 - 1690 cm^{-1} that becomes smaller as the tissue ages and cross-links are formed. Similarly an increase in the 1690 cm^{-1} /1660 cm^{-1} band intensity ratio accompanies mechanical rupture of cross-links by shearing. Although an exact assignment is not possible, the correlation of a matrix collagen band at 1685-1690 cm^{-1} and lack of mature intrafibril cross-links is clear.

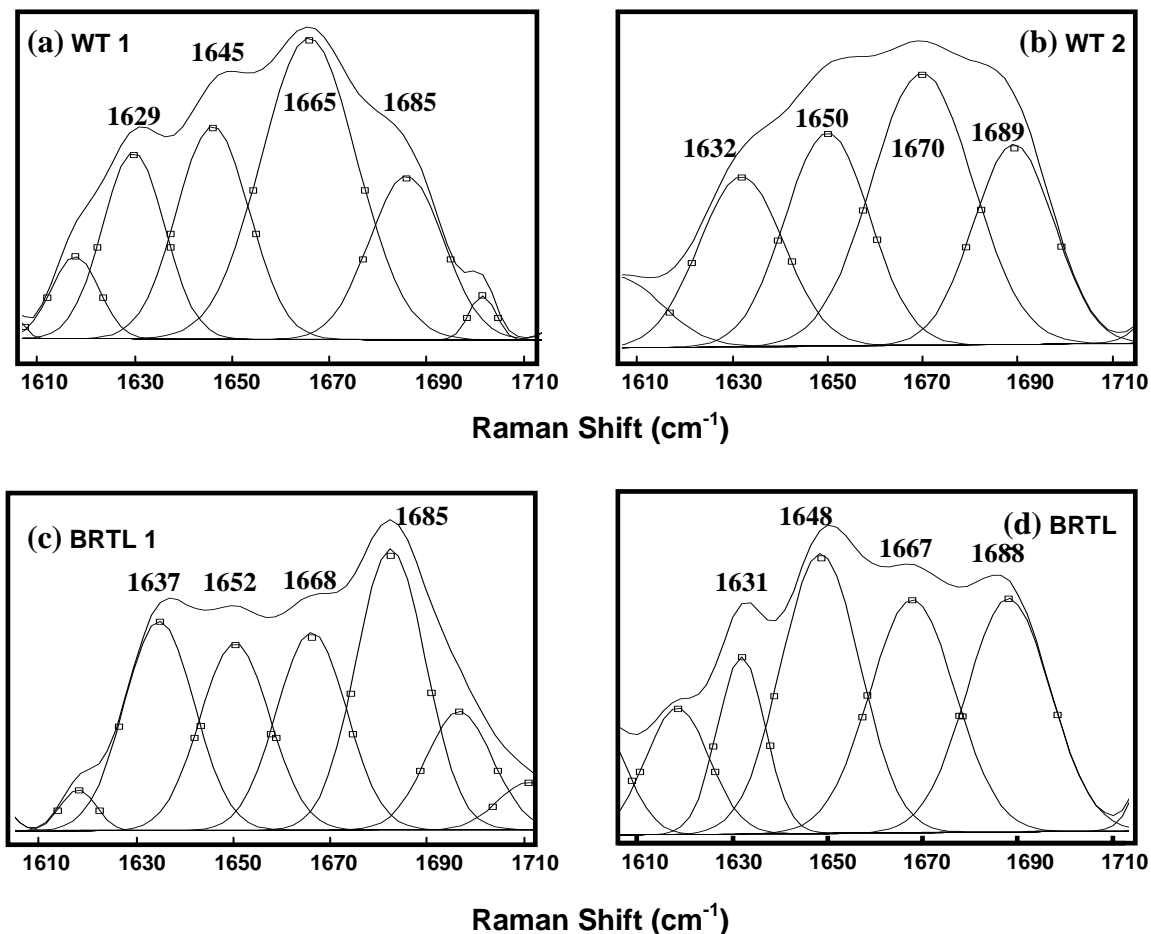


Figure 4. Curve-fitting of amide I band. (a), (b) 2 month old wild-type mouse (c), (d) 2 month old BRTL mouse

Here we have performed an empirical analysis of immature/mature cross-link ratios as the ratio of the areas of two amide I sub-bands centered at $\sim 1685\text{ cm}^{-1}$ and $\sim 1667\text{ cm}^{-1}$. The immature/mature cross-link ratio of BRTL mice is 32% higher than wild-type mice. As shown in Figure 5, the 1685/1667 band area ratio for BRTL mice is 0.985 ± 0.226 , while

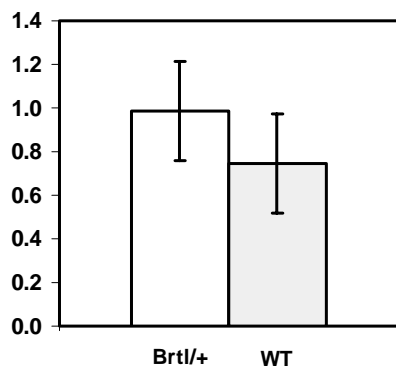


Figure 5. $1685\text{ cm}^{-1}/1667\text{ cm}^{-1}$ band area ratio.

in the wild-type mice is 0.745 ± 0.227 . In Figure 4, BRTL mice show more distinct 1685 cm^{-1} bands than those in wild-type mice. As we have discussed, an increase in the intensity of the 1685 cm^{-1} band is a marker for diminished interfibril cross-links. This data suggests that the glycine to cysteine mutation disrupts normal collagen interfibril cross linking. It is known that absence of collagen intrafibril cross-links weakens bone tissue^[22]. In recent studies of indentation of bone tissue, we have shown that the intrafibril cross-links are easily ruptured by shearing but are not measurably damaged by indentation to depths of $100\text{ }\mu\text{m}$ ^[23]. Using BRTL mice, in which substitution of cysteine for glycine-349 disrupts the triple helical structure we have shown that presence or absence of cross-links may be an important chemical composition contributor to the mechanical strength of bone tissue.

5. CONCLUSIONS

We have shown that the cortical bone tissue of two month old BRTL mice has a lower mineral to matrix ratio than that of wild-type mice of the same age. Equally important, we have shown that the mineral in BRTL differs from that in the wild type and that the differences are characteristic of less mature and less homogeneous mineralization. Similarly, the matrix collagen of BRTL differs from that of the wild type mouse. Our BRTL collagen amide I data is interpreted as disruption of cross-links. It is also possible, for example, that BRTL matrix collagen has a higher ratio of immature to mature cross-links than wild type tissue. A more quantitative description awaits the results of more extensive correlation of bone matrix amide I envelope data and independent cross-link analyses. Such measurements are underway in our laboratory. Information contained in the bone mineral and the bone matrix vibrational spectra may be useful predictors of stiffness and strength of the bone tissue. Raman or infrared spectroscopy of bone tissue may provide important information on the contribution of bone matrix to the mechanical properties of the tissue.

6. ACKNOWLEDGEMENTS

This work was supported in part by the University of Michigan Core Centers for Musculo-Skeletal Research by NIH grant P30 AR46204. The authors wish to thank Tomas Uveges and Joan Marini for supplying the BRTL mouse.

7. REFERENCES

1. Lowenstam, H. A. and Weiner, S. On Biomineralization. Oxford University Press. c1989. Chapter 9, pp.144-166
2. Byers, P. H. Connective tissue and its heritable disorders. New York: Wiley-Liss, c1993. Chapter 10.
3. Kielty, C. M.; Hopkinson, L.; Grant, M. E. The collagen family : structure, assembly, and organization in the extracellular matrix . Connective tissue and its heritable disorders , New York: Wiley-Liss, c1993. pp103-147
4. Cole, W. G. Advances in osteogenesis imperfecta. Clinical orthopaedics and related research 401, 6-16. 2002.
5. Marini, J. C. Osteogenesis Imperfecta: Comprehensive management. Advanced Pediatrics 35, 391-426. 1988.
6. Sarafova, A. P.; Hyeon C.; Forlino, A.; Gajko, A.; Cabral, W. A.; Tosi, L.; Reing, C. M.; Marini, J. C. Three novel type I collagen mutations in osteogenesis imperfecta type IV probands are associated with discrepancies between electrophoretic migration of osteoblast and fibroblast collagen. Human mutation 11, 395-403. 1998.
7. Kozloff, K. M.; Frankenburg, E. P.; Spurchise, M.; Carden, A.; Berwitz, C.; Forlino, A.; Morris, M. D.; Marini, J. C.; Goldstein, S. A. Alterations in bone matrix properties lead to postpubertal improvements in bone of knock-in mouse model (Brittle mouse) for osteogenesis imperfecta. Proceedings of the Orthopaedic Research Society . 2002.
8. Kozloff, K. M., Frankenburg, E. P., spurchise, M., Berwitz, C., Forlino, A., Marini, J. C., and Goldstein, S. A. Postpubertal improvement in bone of knock-in mouse model (Brittle mouse) for osteogenesis imperfecta is due to fundamental alterations in bone material properties. Proceedings of the American Society for Bone and Mineral Research . 2001.
9. Forlino, A., Porter, F. D., Lee, E. J., Westphal, H., and Marini, J. C. Use of the cre/lox recombination system to develop a non-lethal knock-in murine model for osteogenesis imperfecta with an $\alpha 1(I)$ G349C substitution. The journal of biological chemistry 274(53), 37923-37931. 99.
10. Kozloff, K. M. , Carden, A., Bergwitz, C., Forlino, A., Uveges, T. E., Morris, M. D., Marini, J. C., and Goldstein S. A. Brittle IV mouse model for osteogenesis imperfecta IV demonstrates postpubertal adaptations to improve whole bone strength. Journal of Bone and Mineral Research. 2004.
11. Widjaja, E., Li, C. Z., Chew, W., and Garland, M. Band Target Entropy Minimization. A General and Robust Algorithm for Pure Component Spectral Recovery. Anal. Chem. 75, 4499. 2003.
12. Ong, L. R.; Widjaja, E.; Stanforth, R.; Garland, M. Fourier Transform Raman Spectral Reconstruction of Inorganic Lead mixtures using novel Band-Target Entropy Minimization (BTEM) method. Journal of Raman Spectroscopy 34, 282. 2003.
13. Sauer, G. R.; Zunic, W. B.; Durig, J. R.; Wuthier, R. E. Fourier transform Raman spectroscopy of synthetic and biological calcium phosphates. Calcified tissue international 54, 414-420. 1994.
14. Boskey, A. L. Amorphous Calcium Phosphate : The Contention of Bone. J Dent. Res. 76(8), 1433-1436, 1997.
15. Ikoma, T; Kubo, Y.; Yamazaki, A.; Akao, M.; J. Tanaka. Effect of carbonate contents on crystal structure of A-Type carbonate apatites. Key Engineering Materials 192(1), 191-194, 2000.
16. Penel, G; Leroy, G.; Rey, C.; E. Bres. MicroRaman Spectral study of the PO₄ and CO₃ vibrational modes in synthetic and biological apatites. Calcified Tissue International 63, 475-481. 1998.
17. Suetsugu, Y. , Takahashi, Y., Okamura, F. P., and Tanaka, J. Structure analysis of A-type carbonate apatite by a single-crystal X-ray diffraction. Journal of Solid State Chemistry 155, 292-297. 2000.

18. Pelton, J. T. and McLean, L. R. Spectroscopic methods for analysis of protein secondary structure. *Analytical biochemistry* 277, 167-176. 2000.
19. Dong, A.; Huang, P.; Caughey, W. S. Protein secondary structure in water from second-derivative amide I infrared spectra. *Biochemistry* 29, 3303-3308. 1990.
20. Lazarev, Y. A.; Grishkovsky, B. A.; Khromova, T. B. Amide I band of IR spectrum and structure of collagen and related polypeptides. *Biopolymers* 24, 1449-1478. 1985.
21. Paschalis, E. P., Verdelis, K., Doty, S. B., Boskey, A. L., Mendelsohn, R., and Yamauchi, M. Spectroscopic characterization of collagen cross-links in bone. *Journal of bone and mineral research* 16(10), 1821. 2001.
22. Banse, X., SIMS, T. J., and Bailey, A. J. Mechanical properties of adult vertebral cancellous bone: correlation with collagen intermolecular cross-links. *Journal of bone and mineral research* 17(9), 1621. 2002.
23. Carden, A.; Rajachar, R. M.; Morris, M. D.; Kohn, D. H. Ultrastructure changes accompanying the mechanical deformation of bone tissue : A Raman imaging study. *Calcified Tissue International* 72(2), 166-175. 2003.

Quantitative Trait Loci That Modulate Femoral Mechanical Properties in a Genetically Heterogeneous Mouse Population

Suzanne K Volkman,¹ Andrzej T Galecki,² David T Burke,^{2,3} Richard A Miller,^{2,4} and Steven A Goldstein^{1,2}

ABSTRACT: The goal of this study was to investigate genetic effects on mechanical properties of the mouse femur. We found evidence for QTL on eight chromosomes that affect mechanical traits. Some of these QTL may have primary effects on body weight or femoral geometry, and others seem to affect bone quality directly.

Introduction: Previous studies have shown a dependence of fragility-related fracture risk on genetic background. Although many of these studies investigated the effect of genetics on BMD, basic measures of bone geometry and mechanical integrity may provide a more comprehensive characterization of the genetic effects on bone fragility. The purpose of this study was to identify quantitative trait loci (QTL) that affect mechanical and material properties of cortical bone in a genetically heterogeneous mouse population.

Materials and Methods: A total of 486 female UM-HET3 mice was used for this study. UM-HET3 mice are produced as the offspring of (BALB/cJ × C57BL/6J) F₁ females and (C3H/HeJ × DBA/2J) F₁ males. Femurs from 18-month-old mice were tested to failure in four-point bending to assess mechanical properties of cortical bone; these properties were compared with genotype data from 185 biallelic loci. A permutation-based test was used to detect significant associations between genetic markers and mechanical traits. This test generates *p* values that account for the effect of testing multiple hypotheses. Throughout the experiment, *p* ≤ 0.05 was considered statistically significant. Analysis of covariance was used to examine possible effects of body weight and femoral geometry.

Results: We found evidence for genes on maternal chromosomes 11 and 13 and paternal chromosomes 2, 4, 7, 10, 11, and 17 that affect mechanical and material properties of femoral bone. The total variance explained by genetic effects on each mechanical trait ranges from 2.9% to 15.4%. Most of the identified polymorphisms influence mechanical traits even after adjustment for body weight. Adjustment for femoral geometry reduces the effects of some of the QTL, but those on chromosomes 2 and 10 do not seem to be influenced by femoral geometry.

Conclusions: Many genes and chromosomes are involved in the genetic control over mechanical integrity of cortical bone. QTL on paternal chromosomes 4 and 11 may mediate mechanical properties, at least in part, by modulation of femoral geometry. Other QTL identified here may directly affect bone tissue quality.

J Bone Miner Res 2004;19:1497–1505. Published online on May 10, 2004; doi: 10.1359/JBMR.040506

Key words: mechanical properties, genetics, four-point bending, quantitative trait loci, mice

INTRODUCTION

THE NATIONAL OSTEOPOROSIS Foundation (NOF) estimates that 1.5 million fragility-related fractures occur annually in the United States. The direct costs of these fractures were an estimated \$17 billion in 2001, and this figure is rising. In addition to the staggering economic impact, osteoporosis often causes devastation to the lives of its victims and their families. Only 15% of hip fracture patients can walk across a room unaided 6 months after a fracture. An estimated 24% of hip fracture patients ≥50 years of age die within 1 year of their fracture.⁽¹⁾

The risk of fracture depends on factors such as the amount and structure of bone that is present and the mechanical integrity of the bone tissue. These factors may, in turn, be affected by the genetic background, hormonal milieu, age, disease status, and physical activity of the individual. At this time, the dependence of fracture risk on many of these factors is not well understood. A number of previous studies investigated the genetic control of fracture risk; however, most of these studies focused on BMD, because BMD is the primary factor used to predict fracture risk clinically. Twin and multigeneration family studies have estimated that 50–90% of the normal variability in BMD at various anatomical locations is genetically determined.^(2–6) Inbred mouse strains have also been used

The authors have no conflict of interest.

¹Orthopaedic Research Laboratories, Department of Orthopaedic Surgery, University of Michigan, Ann Arbor, Michigan, USA; ²Institute of Gerontology, University of Michigan, Ann Arbor, Michigan, USA; ³Department of Human Genetics, University of Michigan, Ann Arbor, Michigan, USA; ⁴Department of Pathology, Geriatrics Center, Ann Arbor VA Medical Center, University of Michigan, Ann Arbor, Michigan, USA.

to investigate the genetics of bone characteristics. Beamer et al.⁽⁷⁾ showed differences in BMD among 11 inbred strains of mice. Other studies have similarly reported differences in BMD between various inbred strains.^(8–11) A few studies have reported specific quantitative trait loci (QTL) that associate with BMD in mice.^(12–17) Although the findings of these studies are important, BMD may not be the best outcome measure to predict fracture risk. We believe that a more complete understanding of the genetic control of fracture risk can be attained by determining the effects of genetic background on specific measures of bone size, structure, elasticity, strength, and other indices of mechanical integrity. This type of analysis is obviously not feasible in humans, but inbred mouse strains can be used to develop suitable models, because detailed geometric and mechanical analysis can be performed on their bones. In addition, the genetic backgrounds of these animals are known, and differences in bone properties exist between strains.

In a previous study, we identified 14 QTL that regulate various measures of femoral geometry in a genetically heterogeneous mouse population.⁽¹⁸⁾ However, femoral geometry cannot completely predict fracture risk, because femoral strength depends on both the geometric and material properties of the bone. A few previous studies have begun to investigate the genetic determinants of cortical bone mechanical properties in mice. Differences in various mechanical properties have been shown between inbred strains.^(9,11,19,20) Other studies have identified specific QTL that associate with femoral strength⁽²¹⁾ and work to failure⁽²²⁾ in mice. The purpose of this study was to identify QTL that affect mechanical and material properties of cortical bone in a genetically heterogeneous mouse population to enhance our understanding of the genetic control of cortical bone. We hypothesized that we would discover some QTL whose effects on mechanical properties of cortical bone would be mediated by effects on femoral size and shape. We also predicted that other QTL would influence mechanical properties independently of femoral geometry, thus representing polymorphisms that directly affect the quality of cortical bone tissue in mice.

MATERIALS AND METHODS

Mice and husbandry

The animals used in this study are the same as those used in a previous report of genetic effects on geometric traits of cortical bone.⁽¹⁸⁾ Briefly, the mouse population is of the UM-HET3 stock and is derived from a four-way breeding among four inbred strains: BALB/cJ (C), C57BL/6J (B6), C3H/HeJ (C3), and DBA/2J (D2). The experimental animals are the female progeny of (C × B6) F₁ females and (C3 × D2) F₁ males.

The F₁ breeding animals were purchased from Jackson Laboratories (Bar Harbor, ME, USA) and were used to produce a total of 525 UM-HET3 mice. Animals were housed by sex in a single suite of specific-pathogen-free (SPF) rooms and were exposed to identical environmental conditions (12:12-h light/dark cycle, 23°C). Mice were given ad libitum access to water and laboratory mouse chow. The cages were covered with microisolator tops to

minimize the spread of infectious agents. Sentinel mice were tested every 3 months to verify the pathogen-free status of the population. All such tests were negative throughout the course of the study. UM-HET3 mice were entered into the study in a staggered fashion at a rate of 25–35 mice/month. Animals were killed at 18 months of age, at which time right femurs were removed, dissected free of soft tissue, and frozen in a PBS solution. This work was approved by the Animal Care and Use Committee at the University of Michigan.

Genotyping assays

Genomic DNA was prepared from 1-cm sections of tail from 4-week-old animals using a standard phenol-extraction method.⁽²³⁾ Final DNA preparations were tested for concentration, ability to sustain PCR amplification under standard conditions, and electrophoretic size distribution. DNA was genotyped using an ALFexpress automated sequence analyzer (Pharmacia, Piscataway, NJ, USA); the details of this genotyping method have been described previously.⁽²⁴⁾ Primer pairs were purchased from MWG Biotech (High Point, NC, USA). In total, 185 markers were examined from 99 genetic loci. Of the 99 loci, 86 markers were informative for both the maternal- and paternal-derived alleles, and 13 loci were only informative for either maternal or paternal alleles. The selection of genetic loci is described previously in detail.⁽¹⁸⁾ Chromosomal localization and order of markers were calculated using the MapMaker QTX program package (Whitehead Institute, MIT, Boston, MA, USA).

Mechanical testing

After the right femurs were scanned with μ CT for a previous geometric analysis, they were mechanically tested in four-point bending. A servohydraulic system (858 Mini Bionix II; MTS, Eden Prairie, MN, USA) with a custom testing apparatus (Fig. 1A) was used to test the femurs to failure at a constant displacement rate of 0.5 mm/s. The femurs were loaded in the anterior-posterior direction so that the posterior side of the bone was in tension and the anterior side was in compression (Fig. 1B). All four loading points were placed in contact with the bone by adjusting the heights of the upper two points independently. A 50-lb load cell (Model 41; Sensotec, Columbus, OH, USA) was used to measure the load applied to the bone, and the mid-diaphyseal displacement was measured with a linear variable differential transducer (010 MHR; Schaevitz Engineering, Pennsauken, NJ, USA). Load and displacement data were acquired using the TestStar IIs system (version 2.4; MTS) at a sampling frequency of 2000 Hz. MATLAB (version 6.5; The Mathworks, Natick, MA, USA) was used with a custom analysis program to determine stiffness, yield load and displacement, ultimate load and displacement, postyield displacement and energy to failure from the load, and displacement data. The analysis program contained an algorithm that determined the linear region of the load-displacement curve; stiffness was measured as the slope of this linear region. The yield point was defined as the point at which the secant stiffness differed by 10% from the initial tangential stiffness. Ultimate load was the maximum load attained before failure, and ultimate displacement was the

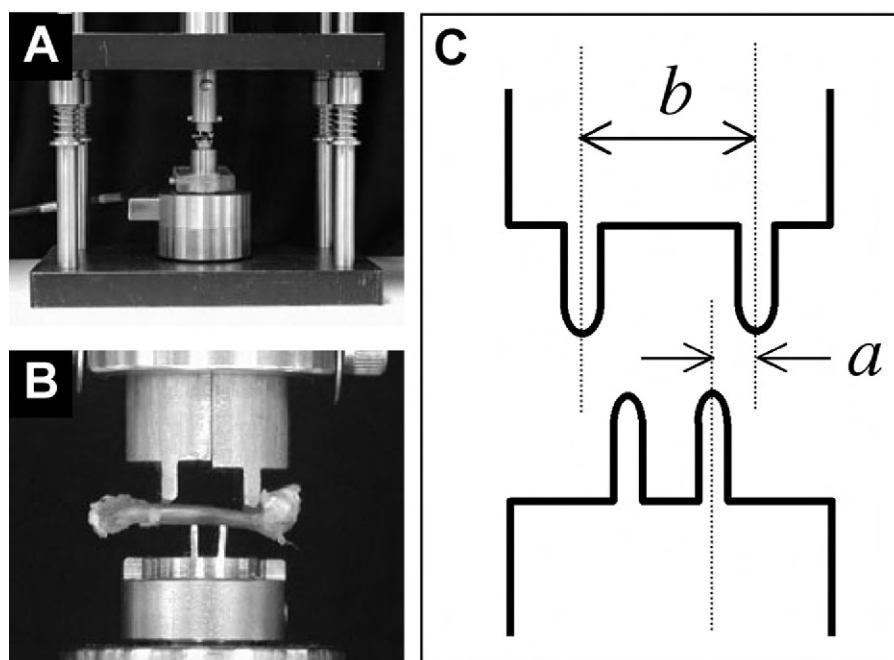


FIG. 1. (A) Custom-testing apparatus used for four-point bending tests of femurs. (B) Femurs were loaded in a posterior to anterior direction so that the posterior surface was under tension and the anterior surface was under compression. (C) Spatial parameters used to estimate elastic modulus in Eq. 1.

corresponding displacement. Postyield displacement was calculated as the displacement at failure minus the displacement at the yield point. Energy to failure was determined with numerical integration as the area under the load-displacement curve up to the fail point. A displacement ratio was calculated as the ratio of ultimate displacement to yield displacement to characterize the relative magnitudes of elastic and plastic deformation. Additionally, elastic modulus (E) and ultimate strength (σ) were estimated using these equations:

$$E = \frac{S(3ab^2 - 4b^3)}{12I} \quad (1)$$

$$\sigma = \frac{MC}{I} \quad (2)$$

where S is the whole bone stiffness determined with four-point bending, I is the moment of inertia with respect to the medial-lateral axis of the bone, a and b relate to the spacing of the contact points and are defined as shown in Fig. 1C, M is the moment at maximum load, and C is the distance from the centroid of the bone to the periosteal surface in the posterior direction. I and C were determined for each femur from μ CT data.

Testing was performed on 6 different days. Each day, a set of assays was preceded by tests of pieces of steel music wire (type 302/304 stainless steel spring wire, 0.020 in diameter, McMaster-Carr product 8908K21; Aurora, OH, USA) to evaluate the consistency of the assay system. This wire was chosen because it has a stiffness within the same range as the murine femurs. Six wire specimens were evaluated at the beginning of each day's work and every 2–3 h thereafter. ANOVA showed no significant differences

across the series of assays ($p = 0.22$). The means and SD for the 6 testing days were 169.7 ± 2.6 , 169.2 ± 3.0 , 168.6 ± 2.3 , 167.9 ± 3.1 , 167.4 ± 1.7 , and 169.7 ± 3.3 , respectively, with an average CV of 1.62% (1.56%, 1.75%, 1.38%, 1.83%, 1.00%, and 1.97%, respectively).

Statistical methods

A single-point, genome-wide search was performed for each trait to detect QTL that may be associated with the trait. To make the analysis consistent for all partially and fully informative markers, four-way informative markers were split into two sets of biallelic markers that were informative for either the maternally or paternally transmitted alleles. One-way ANOVA models, with a trait as the dependent variable and a biallelic marker as the factor with two levels, were used to perform genome-wide searches for all 185 biallelic markers. The strength of linkage associations between genetic markers and mechanical traits was evaluated using a permutation-based test of statistical significance. This test generates an "experiment-wise" acceptance criterion to take into account the multiple hypotheses that were tested in this search and to avoid type I error inflation.⁽²⁵⁾ A null distribution for permutation analysis was generated based on 1000 shuffles of original phenotype data. Throughout the experiment, $p \leq 0.05$ was considered statistically significant. The percent of variance in each mechanical trait that can be explained by genetic effects was estimated in a standard way from corresponding regression models.

The animals used in this study were of various sizes and weights. To account for overall animal size, covariance analyses were performed with a trait as the dependent variable, a biallelic marker as the factor with two levels, and body weight at 3 or 18 months of age as the covariate.

TABLE 1. SUMMARY OF MECHANICAL TRAITS

<i>Trait</i>	<i>Mean ± SD</i>
Stiffness (N/mm)	451.3 ± 94.0
Yield load (N)	33.3 ± 7.7
Ultimate load (N)	42.6 ± 10.4
Yield displacement (mm)	0.076 ± 0.015
Ultimate displacement (mm)	0.13 ± 0.04
Postyield displacement (mm)	0.056 ± 0.041
Displacement ratio (unitless)	1.79 ± 0.66
Energy to failure (N · mm)	3.56 ± 1.96
Predicted modulus (GPa)	12.5 ± 3.0
Predicted ultimate strength (MPa)	188.6 ± 47.3

Femurs were tested to failure in four-point bending, and 10 properties were determined for each femur. The mean value of each trait is shown with the SD. Displacement ratio is the ratio between ultimate displacement and yield displacement. Predicted modulus and predicted ultimate strength were calculated according to Eqs. 1 and 2, respectively.

Permutation-based statistical tests were used to evaluate statistical significance as described above. Because whole bone mechanical properties are dependent on the geometry of the bone, a second set of covariance analyses was performed to account for variations in geometric properties of the femur. Femoral cross-sectional area, cortical thickness, and moment of inertia with respect to the medial/lateral axis of the bone were used simultaneously as covariates. These measures of femoral geometry were determined with μCT as described previously.⁽¹⁸⁾

RESULTS

Of the 525 mice used in this study, 38 died before 18 months of age and were not included in this analysis. Mechanical data could not be obtained on 1 additional mouse; therefore, the final population consisted of 486 UM-HET3 mice. On average, there were 4.5 marker loci per autosome, and the average distance between marker loci varied from 15 to 20 cM.

Ten variables were determined for each specimen from the four-point bending tests. These variables are shown in Table 1 with their means and SD among the UM-HET3 mice used in this study. Table 2 shows Spearman rank-order correlations among these mechanical traits and between the traits and body weight measured either at 3 or 18 months of age. Not surprisingly, many of these indices show significant correlations with one another, although the many correlations below $r = 0.5$ suggest that most of these measurements provide information about bone properties not fully captured by any other single variable. Body weight measures show weak correlations with the bone measurements other than predicted modulus and predicted ultimate strength, which are calculated using information about bone geometry likely to be modulated by overall body size and weight.

Table 3 shows significant linkage associations between mechanical traits and genetic markers that were determined from the permutation analysis. Because the maternal and paternal alleles were separated for the linkage analysis, the origin of each marker is indicated with an *M* or a *P* in Table

3. The chromosomal position of each marker is reported in centimorgans and millions of basepairs from the centromere. The estimated genetic effect for each significant association is given with the SE in parentheses. The estimated genetic effect is the difference between mean levels of the indicated trait in the two groups of mice differing at the indicated marker locus. Units of estimated effects are the same as the variable units shown in Table 1. The column labeled "Comparison" indicates the background allele at a particular marker that results in the larger value of the trait. The maternally inherited alleles were either *C* or *B6* alleles, and the paternally inherited alleles were either *C3* or *D2* alleles. The genome survey thus indicated the presence of QTL on eight chromosomes, including maternal chromosomes 11 and 13 and paternal chromosomes 2, 4, 7, 10, 11, and 17.

The percent variance estimated in each mechanical trait that can be attributed to genetic effects was determined, and the results are shown in Table 4. The variance explained by individual chromosomes was determined, considering only the significant marker/trait associations shown in Table 3. The last row in Table 4 shows the total variance that can be attributed to all QTL that were significantly associated with each trait. The total variance explained by genetic effects ranges from 2.9% to 15.4%.

We conducted analyses of covariance to determine if the QTL of interest listed in Table 3 might directly affect body weight, and therefore, indirectly affect mechanical properties. Body weights at 3 and 18 months of age were used as covariates, and the results are shown in Table 5. The estimated genetic effects on the mechanical traits are shown before and after adjustment for body weight. Estimated effects are reported for all significant linkage associations shown in Table 3 as well as for a few associations (chromosomes 2, 4, 5, 7, and 11; Table 5, bold) that obtained significance only after adjustment for one of the weight measures. Genome scan-seeking QTL that modulate weight, per se, found no loci on any of these chromosomes that had a significant effect on body weight at 3 or 18 months.

A similar analysis was conducted to determine if the effects presented in Table 3 were potentially mediated by the geometry of the femoral diaphysis. The results are shown in Table 6. Linkage associations involving predicted elastic modulus and predicted ultimate strength were not included in these analyses, because femoral geometry has already been accounted for in the calculation of these traits. The regression equation included cross-sectional area (CSA), cortical thickness (CT), and moment of inertia with respect to the medial-lateral axis of the bone (I_{ML}) as covariates.

DISCUSSION

We have shown evidence for QTL on maternal chromosomes 11 and 13 and paternal chromosomes 2, 4, 7, 10, 11, and 17 that affect whole bone mechanical and material properties of the femur. Together, these QTL account for 2.9–15.4% of the variance estimated in the mechanical traits. Paternal chromosomes 2, 4, 7, and 11 contained multiple markers associated with the mechanical properties.

TABLE 2. CORRELATIONS AMONG MECHANICAL FACTORS, INCLUDING BODY WEIGHT AT 3 AND 18 MONTHS

	<i>Yield load</i>	<i>Ultimate load</i>	<i>Yield displacement</i>	<i>Ultimate displacement</i>	<i>Postyield displacement</i>	<i>Displacement ratio</i>	<i>Energy to failure</i>	<i>Predicted modulus</i>	<i>Predicted ultimate strength</i>	<i>Weight at 3 months</i>	<i>Weight at 18 months</i>
Stiffness	0.72	0.69	-0.10	-0.01	0.04	0.06	0.29	0.52	0.43	0.03	0.07
Yield load		0.67	0.54	0.05	-0.13	-0.22	0.31	0.46	0.49	0.10	0.12
Ultimate load			0.12	0.61	0.54	0.48	0.83	0.46	0.78	-0.04	0.02
Yield displacement				0.07	-0.26	-0.42	0.08	0.05	0.17	0.12	0.10
Ultimate displacement					0.93	0.84	0.93	0.08	0.59	-0.11	-0.09
Postyield displacement						0.98	0.87	0.08	0.52	-0.16	-0.13
Displacement ratio							0.79	0.07	0.45	-0.15	-0.15
Energy to failure								0.26	0.73	-0.10	-0.06
Predicted modulus									0.78	-0.46	-0.34
Predicted ultimate strength										-0.39	-0.31
Weight at 3 months											0.69

Values tabulated are Spearman rank correlation coefficients, with pairwise exclusion for missing data.

Bold indicates $p < 0.001$.

$N \sim 550$ for correlations between mechanical traits. $N \sim 450$ for correlations between mechanical traits and weight at 3 months. $N \sim 205$ for correlations between mechanical traits and weight at 18 months.

TABLE 3. ASSOCIATIONS WITH EXPERIMENTWISE SIGNIFICANCE OF $p \leq 0.05$

<i>Trait</i>	<i>Marker</i>	<i>Chromosomal position (cM)</i>	<i>Chromosomal position (Mb)</i>	<i>Estimated genetic effect (SE)</i>	<i>Experiment-wise p value</i>	<i>Comparison</i>
Stiffness	D11Mit2 (P)	2.4	12.25	39.4 (8.5)	0.004	C3 > D2
	D11Mit83 (P)	16.0	28.85	43.1 (8.7)	0.002	C3 > D2
Yield load	D4Mit55 (P)	19.8	44.54	2.58 (0.71)	0.048	C3 > D2
	D4Mit84 (P)	37.7	74.51	2.64 (0.71)	0.034	C3 > D2
	D4Mit55 (P)	49.6	100.28	2.77 (0.72)	0.025	C3 > D2
	D11Mit2 (P)	2.4	12.25	3.35 (0.70)	<0.0001	C3 > D2
	D11Mit83 (P)	16.0	28.84	3.15 (0.72)	0.002	C3 > D2
	D11Mit156 (P)	34.0	63.96	2.92 (0.70)	0.004	C3 > D2
	D11Mit289 (P)	55.0	95.63	2.71 (0.71)	0.030	C3 > D2
Ultimate load	D4Mit155 (P)	49.6	100.28	3.59 (0.97)	0.043	C3 > D2
Ultimate displacement	D10Mit40 (P)	29.0	48.82	0.015 (0.004)	0.006	C3 > D2
Postyield displacement	D10Mit40 (P)	29.0	48.82	0.014 (0.004)	0.036	C3 > D2
Displacement ratio	D2Mit434 (P)	41.5	71.66	0.23 (0.06)	0.033	C3 > D2
	D2Mit285 (P)	86.0	153.66	0.22 (0.06)	0.049	C3 > D2
Predicted modulus	D11Mit83 (M)	16.0	28.85	1.3 (0.3)	<0.001	C > B6
	D11Mit83 (P)	16.0	28.85	1.3 (0.3)	0.002	C3 > D2
	D11Mit156 (P)	34.0	63.96	1.1 (0.3)	0.016	C3 > D2
	D11Mit289 (P)	55.0	95.63	1.2 (0.3)	<0.001	C3 > D2
	D13Mit26 (M)	38.0	69.31	1.1 (0.3)	0.019	C > B6
	D17Mit185 (P)	40.6	67.59	1.0 (0.3)	0.017	C3 > D2
Predicted ultimate strength	D7Mit25 (P)	16.0	27.39	17.3 (4.3)	0.012	D2 > C3
	D7Mit91 (P)	28.1	48.22	19.9 (4.3)	<0.001	D2 > C3
	D7Mit253 (P)	52.8	105.19	16.5 (4.3)	0.027	D2 > C3
	D11Mit289 (P)	55.0	95.63	21.1 (4.3)	<0.001	C3 > D2

A permutation-based test was used to detect significant associations between genetic markers and mechanical traits. This test generates experiment-wise p values, which account for the effect of testing multiple hypotheses. The origin of the marker (maternal or paternal) is indicated in parentheses in the Marker column. The position of the marker on the chromosome is given in centimorgans (cM) and millions of base pairs (Mb) from the centromere, as defined in the mouse draft sequence build MGSCv3. The estimated genetic effect is the difference between mean levels of the indicated trait in the two groups of mice differing at the indicated marker locus. SE is shown in parentheses, and units for each variable are as stated in Table 1. Comparison indicates which background allele results in the larger value of a particular trait. B6 and C are maternal alleles, whereas C3 and D2 are paternal alleles.

It should be noted that this does not necessarily prove the existence of multiple genes that affect mechanical traits on these chromosomes. Closely linked SSLP markers may

show associations with traits because of linkage to a single effector gene locus. This initial QTL analysis does not allow for high-resolution mapping of the various markers to their

TABLE 4. VARIANCE CAUSED BY INDIVIDUAL AND COMBINED GENETIC EFFECTS

<i>Chromosome</i>	<i>Stiffness</i>	<i>Yield load</i>	<i>Ultimate load</i>	<i>Ultimate displacement</i>	<i>Postyield displacement</i>	<i>Displacement ratio</i>	<i>Predicted modulus</i>	<i>Predicted ultimate strength</i>
2P [D2Mit285, 434]	—	—	—	—	—	4.37	—	—
4P [D4Mit55, 84, 155]	—	3.72	2.90	—	—	—	—	—
7P [D7Mit25, 91, 253]	—	—	—	—	—	—	—	5.14
10P [D10Mit40]	—	—	—	3.52	2.86	—	—	—
11M [D11Mit83]	—	—	—	—	—	—	4.72	—
11P [D11Mit2, 83, 156, 289]	5.80	7.27	—	—	—	—	6.85	4.96
13M [D13Mit26]	—	—	—	—	—	—	3.12	—
17P [D17Mit185]	—	—	—	—	—	—	3.07	—
Total variance explained	5.80	10.20	2.90	3.52	2.86	4.37	15.44	10.64

The amount of variance observed in each trait that can be explained by genetic effects is shown here, expressed as a percentage of total variance observed for each trait. The total variance explained by each chromosome was determined with regression analysis. The chromosome number is listed with an M or a P to indicate maternal or paternal origin. The relevant markers are listed in brackets beneath the chromosome number. Only those associations for which experiment-wise $p < 0.05$, as listed in Table 3, are included in this analysis. The last row shows the total variance that can be attributed to all significant markers associated with each trait.

TABLE 5. EFFECT SIZES BEFORE AND AFTER ADJUSTMENT FOR BODY WEIGHT

<i>Trait</i>	<i>Marker</i>	<i>Chromosomal position (cM)</i>	<i>Estimated genetic effect (SE, p[t])</i>			<i>Comparison</i>
			<i>Unadjusted</i>	<i>3-month weight</i>	<i>18-month weight</i>	
Stiffness	D11Mit2 (P)	2.4	39.4 (8.5, 0.000)	36.1 (9.4, 0.000)	31.9 (13.6, 0.000)	C3 > D2
	D11Mit83 (P)	16.0	43.1 (8.7, 0.000)	40.5 (9.8, 0.000)	37.5 (13.5, 0.006)	C3 > D2
Yield load	D4Mit55 (P)	19.8	2.58 (0.71, 0.000)	2.85 (0.78, 0.000)	2.79 (1.13, 0.014)	C3 > D2
	D4Mit84 (P)	37.7	2.64 (0.71, 0.000)	2.98 (0.79, 0.000)	3.28 (1.12, 0.004)	C3 > D2
	D4Mit155 (P)	49.6	2.77 (0.72, 0.000)	3.00 (0.80, 0.000)	3.04 (1.18, 0.011)	C3 > D2
	D7Mit25 (P)	16.0	1.56 (0.71, 0.029)	0.83 (0.80, 0.301)	4.16 (1.09, 0.000)	D2 > C3
	D11Mit2 (P)	2.4	3.35 (0.70, 0.000)	3.10 (0.78, 0.000)	3.65 (1.10, 0.001)	C3 > D2
	D11Mit83 (P)	16.0	3.15 (0.72, 0.000)	2.63 (0.82, 0.002)	3.90 (1.09, 0.000)	C3 > D2
	D11Mit156 (P)	34.0	2.92 (0.70, 0.000)	2.72 (0.78, 0.000)	3.61 (1.10, 0.001)	C3 > D2
Ultimate load	D11Mit289 (P)	55.0	2.71 (0.71, 0.000)	2.29 (0.80, 0.044)	3.78 (1.12, 0.000)	C3 > D2
	D4Mit84 (P)	37.7	3.45 (0.96, 0.000)	3.66 (1.09, 0.000)	4.82 (1.30, 0.000)	C3 > D2
	D4Mit155 (P)	49.6	3.59 (0.97, 0.000)	4.00 (1.09, 0.000)	3.98 (1.36, 0.004)	C3 > D2
Yield displacement	D7Mit25 (P)	16.0	0.004 (0.001, 0.006)	0.003 (0.002, 0.054)	0.008 (0.002, 0.000)	D2 > C3
Ultimate displacement	D10Mit40 (P)	29.0	0.015 (0.004, 0.000)	0.017 (0.004, 0.000)	0.002 (0.005, 0.771)	C3 > D2
Postfield displacement	D10Mit40 (P)	29.0	0.014 (0.004, 0.000)	0.016 (0.004, 0.000)	0.005 (0.005, 0.310)	C3 > D2
Displacement ratio	D2Mit434 (P)	41.5	0.23 (0.06, 0.000)	0.17 (0.07, 0.011)	0.20 (0.08, 0.012)	C3 > D2
	D2Mit285 (P)	86.0	0.22 (0.06, 0.000)	0.24 (0.07, 0.000)	0.09 (0.08, 0.269)	C3 > D2
Energy to failure	D2Mit58 (M)	51.4	0.56 (0.18, 0.002)	0.58 (0.21, 0.005)	0.85 (0.22, 0.000)	B6 > C
Predicted modulus	D11Mit83 (M)	16.0	1.3 (0.3, 0.000)	1.3 (0.3, 0.000)	1.6 (0.4, 0.000)	C > B6
	D11Mit83 (P)	16.0	1.3 (0.3, 0.000)	1.3 (0.3, 0.000)	1.4 (0.4, 0.000)	C3 > D2
	D11Mit156 (P)	34.0	1.1 (0.3, 0.000)	1.2 (0.3, 0.000)	1.6 (0.4, 0.000)	C3 > D2
	D11Mit289 (P)	55.0	1.2 (0.3, 0.000)	1.3 (0.3, 0.000)	1.8 (0.4, 0.000)	C3 > D2
	D13Mit26 (M)	38.0	1.1 (0.3, 0.000)	0.9 (0.3, 0.001)	1.2 (0.4, 0.007)	C > B6
	D17Mit185 (P)	40.6	1.0 (0.3, 0.000)	0.7 (0.3, 0.011)	0.9 (0.4, 0.039)	C3 > D2
Predicted ultimate strength	D5Mit292 (P)	80.0	11.4 (4.6, 0.011)	17.4 (4.6, 0.000)	4.4 (6.5, 0.497)	D2 > C3
	D7Mit25 (P)	16.0	17.3 (4.3, 0.000)	11.1 (4.5, 0.014)	21.8 (6.0, 0.000)	D2 > C3
	D7Mit91 (P)	28.1	19.9 (4.3, 0.000)	12.2 (4.5, 0.008)	20.1 (6.1, 0.001)	D2 > C3
	D7Mit253 (P)	52.8	16.5 (4.3, 0.000)	13.1 (4.5, 0.004)	12.7 (6.1, 0.039)	D2 > C3
	D11Mit156 (P)	34.0	14.6 (4.3, 0.001)	16.4 (4.4, 0.000)	23.0 (6.0, 0.000)	C3 > D2
	D11Mit289 (P)	55.0	21.1 (4.3, 0.000)	21.6 (4.4, 0.000)	27.7 (6.0, 0.000)	C3 > D2

Two body weight measures, obtained at 3 and 18 months of age, were used as predictive covariates to determine if differences seen in mechanical traits were actually caused by differences in body weight. The estimated genetic effects on the mechanical traits are shown before and after adjustment for body weight. The estimated genetic effect is the difference between mean levels of the indicated trait in the two groups of mice differing at the indicated marker locus. SE is shown in parentheses, along with probability evaluated by the t -statistic, and units for each variable are as stated in Table 1. Estimated effects are reported for all significant associations shown in Table 2, as well as a few associations (shown in bold) that obtained significance only after adjustment for one of the weight measures. Comparison indicates which background allele results in the larger value of a particular trait. B6 and C are maternal alleles, whereas C3 and D2 are paternal alleles.

TABLE 6. EFFECT SIZES BEFORE AND AFTER ADJUSTMENT FOR GEOMETRY

Trait	Marker	Position (cM)	Estimated genetic effect (SE)		Comparison
			Unadjusted	Adjusted	
Stiffness	D1Nds2 (M)	59.0	19.6 (8.7)	27.2 (7.1)	B6 > C
	D11Mit2 (P)	2.4	39.4 (8.5)	23.9 (7.0)	C3 > D2
	D11Mit83 (P)	16.0	43.1 (8.7)	25.3 (7.3)	C3 > D2
Yield load	D4Mit55 (P)	19.8	2.58 (0.71)	1.34 (0.55)	C3 > D2
	D4Mit84 (P)	37.7	2.64 (0.71)	1.19 (0.54)	C3 > D2
	D4Mit155 (P)	49.6	2.77 (0.72)	1.20 (0.58)	C3 > D2
	D11Mit2 (P)	2.4	3.35 (0.70)	1.83 (0.55)	C3 > D2
	D11Mit83 (P)	16.0	3.15 (0.72)	1.26 (0.57)	C3 > D2
	D11Mit156 (P)	34.0	2.92 (0.70)	0.58 (0.56)	C3 > D2
	D11Mit289 (P)	55.0	2.71 (0.71)	0.77 (0.57)	C3 > D2
	D4Mit155 (P)	49.6	3.59 (0.97)	1.48 (0.75)	C3 > D2
Ultimate load	D10Mit40 (P)	29.0	0.015 (0.004)	0.015 (0.004)	C3 > D2
Ultimate displacement	D10Mit40 (P)	29.0	0.014 (0.004)	0.014 (0.004)	C3 > D2
Postyield displacement	D2Mit434 (P)	41.5	0.23 (0.06)	0.23 (0.06)	C3 > D2
Displacement ratio	D2Mit285 (P)	86.0	0.22 (0.06)	0.23 (0.06)	C3 > D2

Three measures of geometry, cross-sectional area (CSA), cortical thickness (CT), and moment of inertia with respect to the medial lateral axis of the bone (I_{ML}), were used simultaneously as predictive covariates to determine if differences seen in mechanical traits were actually caused by differences in geometry. Predicted modulus and predicted ultimate strength were not included in this analysis because these variables have already been adjusted for by geometry. Genetic effects on the mechanical traits are shown before and after adjustment for femoral geometry. The estimated genetic effect is the difference between mean levels of the indicated trait in the two groups of mice differing at the indicated marker locus. SE is shown in parentheses, and units for each variable are as stated in Table 1. Genetic effects are reported for all significant associations shown in Table 3, as well as one association (shown in bold) that obtained significance only after adjustment for geometry.

chromosomal positions. Therefore, multiple markers on a chromosome may be linked to a single gene of interest. Additional genotyping using more closely spaced markers is now underway and will help to determine the chromosomes that contain more than one locus with effects on the mechanical properties of the femur. Although we have used a permutation-based significance test to control type I error rate and produce an “experiment-wise” p value for each genome scan, we have not adjusted the significance criterion with respect to the number of traits evaluated; thus, Table 3 may well contain a small proportion of false positive conclusions. In addition, we note that a study of 500–600 mice has only limited statistical power. Power analysis using a synthetic data set suggests that a population of this size will detect only 27% of the QTL with heritability of 0.10 and only 45% of QTL with heritability 0.15. Thus, there is a good likelihood that our compilation (Table 3) has missed many QTL with substantial effects on the bone traits we have measured.

The mechanical properties studied here (stiffness, yield load and displacement, ultimate load and displacement, postyield displacement, displacement ratio, and energy to failure) depend on material properties of the bone tissue (such as modulus and ultimate strength that we have estimated in this study) and the size and cross-sectional shape of the bone. Our previous geometric analysis revealed QTL that strongly associate with various measures of femoral size and shape on maternal chromosomes 1, 5, 6, 7, 11, 12, 15, and 17 and paternal chromosomes 1, 3, 4, 8, 9, 11, 14, and 15.⁽¹⁸⁾ A direct comparison of these results with the current mechanical trait results (not including material properties like modulus and ultimate strength) reveals two areas of overlap: paternal chromosomes 4 and 11 have QTL that

associate with both femoral geometry and mechanical properties. It is possible that one or more genes on these chromosomes actually affect the geometry of the femur, which in turn affects mechanical properties. Because the remaining QTL that associate with mechanical properties are not strongly associated with geometric properties, they may instead directly affect bone tissue quality or they may affect bones indirectly (e.g., through the alteration of a hormone that in turn influences bone quality).

Material properties of femoral diaphyseal cortical bone in the UM-HET3 mice were estimated by calculating elastic modulus and ultimate strength according to Eqs. 1 and 2, respectively. These estimated material properties were significantly associated with markers on maternal chromosomes 11 and 13 and paternal chromosomes 7, 11, and 17, indicating that genes on these chromosomes affect the material properties of cortical bone, independent of the femoral geometry. However, it is noteworthy that one of these markers, *D11Mit83* on the maternal chromosome 11, is also strongly associated with various femoral geometry traits. True material properties should be independent of geometry. It is possible that the elastic modulus and ultimate strength values used here may not completely account for femoral geometry, because they are estimates based on beam theory. Another possibility is that a gene near the *D11Mit83* marker affects some other factor, such as calcium metabolism or osteoblast regulation, that could indirectly affect both geometry and material properties. Future plans include producing uniform microbeams from femoral cortical tissue of the same animals and testing the beams in micro-four-point bending to determine the material properties of femoral cortical tissue more directly.

There are a relatively small number of previous studies that have identified QTL and associate it with femoral mechanical properties and BMD in mice. In 1999, Beamer et al.⁽¹³⁾ identified four QTL on chromosomes 1, 5, 13, and 15 that were strongly linked with femoral BMD in an F₂ cross between C57BL/6J and CAST/EiJ strains. Using a different mouse model (F₂ cross between C57BL/6J and C3H/HeJ), Beamer et al.⁽¹⁵⁾ performed a similar study in 2001 and found QTL on chromosomes 1, 4, 6, 11, 13, 14, and 18 that strongly associate with femoral BMD. Klein et al.⁽¹⁶⁾ measured whole body BMD in mice derived from C57BL/6 and DBA/2 strains in 2001. The results showed links with QTL on chromosomes 1, 2, 4, and 11.⁽¹⁶⁾ Comparing our current results with these previous BMD studies, we find commonalities on chromosomes 2, 4, 11, and 13. Inconsistencies among other significant QTL may reflect differences in outcome measures or in the specific genetic crosses used; these inconsistencies could also reflect type II errors in one or more of these studies.

Li et al.^(21,22) used an F₂ cross between MRL/MpJ and SJL/J strains to identify QTL-affecting femoral failure load and energy to failure. The results identified markers on chromosomes 1, 2, 8, 9, 10, and 17 that associated with failure load and markers on chromosomes 2, 7, 8, 9, and X that associated with energy to failure. We found no QTL that strongly associated with energy to failure and only one on chromosome 4 that associated with ultimate load; this is similar to failure load in the UM-HET3 mice. The lack of consistency between our results and the findings of Li et al.^(21,22) are most likely attributable the different mouse models used in the studies.

We considered the possibility that some of the genetic effects listed in Table 3 might act primarily on body weight, with only secondary effects on mechanical properties. To test this idea, we conducted analyses of covariance using body weight at either 3 or 18 months of age as the covariates. The results shown in Table 5 show that, in most cases, the genetic effects have similar magnitudes before and after adjustment for body weight. However, there are a few exceptions. First, the associations between the paternal alleles of *D10Mit40* and ultimate displacement and postyield displacement were reduced after adjustment for 18-month body weight. It is possible that the linkage association of this QTL with displacement measures is mediated indirectly through an effect on body weight throughout midlife. It is also possible that some third factor, perhaps hormones, modulates both bone properties and body weight and is under control of a locus on paternal chromosome 10. Similarly, the association between displacement ratio and the paternal allele at *D2Mit285* is diminished in calculations involving 18-month body weight. It is interesting to note that the relationship between *D2Mit434* and displacement ratio is not similarly affected by 18-month weight. This difference may suggest that chromosome 2 harbors two different loci with effects on displacement ratio—one that is associated with body weight dependence, and one that is not. Further studies involving a higher density of markers on chromosome 2 are required to confirm this.

Table 5 displays six linkage associations (bold) in which QTL had significant increases in effect size only after ad-

justment for body weight. Three of these associations involve *D4Mit84*, *D7Mit25*, and *D11Mit156*, which were already noted in Table 3 because of their associations with other mechanical traits. Two other loci, however, are new. The estimated genetic effect of the gene associated with *D2Mit58* on energy to failure increased only after adjustment for body weight at 18 months. It is possible that this maternal QTL modulates the process by which bone properties adjust to differences in body weight or to physiological factors, perhaps hormonal, that modulate both body weight and bone fragility. The other new QTL modulates predicted ultimate strength of the bone and is associated with the paternal alleles at *D5Mit292*. Here, the effect size increases after adjustment for weight at 3 months. However, the effect size increase is much less dramatic after adjustment for weight at 18 months.

A second set of covariance analyses were conducted to determine if effects noted in Table 3 were potentially mediated by genetic influences on the geometry of the femoral diaphysis. These results are presented in Table 6. For associations involving markers on paternal chromosomes 4 and 11, the estimated genetic effect is reduced after adjustment for femoral geometry. These results are consistent with the fact that paternal chromosomes 4 and 11 contained markers that were significantly associated with both femoral geometry and mechanical properties. These genetic markers may represent QTL whose effects on mechanical properties are mediated, at least in part, by modulation of femoral geometry. However, the associations shown in Table 6, involving markers on paternal chromosomes 2 and 10, do not seem to be affected by femoral geometry and presumably reflect modulation of bone quality. Only one new locus, *D1Nds2*, was found to have a stronger association after adjustment for geometry. In this case, mice inheriting the *B6* allele were found to show greater stiffness in calculations adjusted for bone geometrical traits, suggesting that this QTL might modulate compensation of bone mechanical properties to bone size or shape.

In conclusion, we have shown the complex nature of the genetic control of cortical bone in mice that is caused by the multiple QTL that were found to associate with various measures of femoral mechanical and material properties. We found evidence for QTL on paternal chromosomes 4 and 11 whose effects on mechanical properties may be mediated, at least in part, by modulation of femoral geometry. Other genetic markers identified in this survey may be linked to QTL that directly affect bone tissue quality and material properties, but further studies are needed to clarify the role of these QTL in the modulation of femoral mechanical integrity. Although the results of this study do not allow us to positively identify candidate genes that affect femoral mechanical properties in mice, we now have an appropriate starting point from which we can begin the search to find specific genes. In addition, further analysis of this four-way cross-population should help to delineate interactions among bone traits, underlying hormonal and biochemical differences among mice, and the genes that modulate bones both during and after developmental maturation. Finally, the results of this study may have important implications with respect to fragility or fracture risk in humans. The data in

this study relate to 10–15 QTL, each of which corresponds to one or two human syntenic regions with 200–500 known genes. Testing or review of these genes is beyond the scope of this study, but focused searches for human alleles at the same (syntenic) positions of the mouse genes may provide additional insight (beyond BMD) into fracture risk prediction. In addition, identification of the true effector genes and their function in regulating bone extracellular matrix properties in the mouse may support the development of new therapeutic strategies for treating or preventing fragility in humans.

ACKNOWLEDGMENTS

The authors thank Gretchen Buehner, Maggie Vergara, Steve Pinkosky, Shu Chen, and Zhihong Shao for contributions to this study. This work was supported by National Institutes of Health Grants P01-AG16699, AG08808, and P30-AR46024.

REFERENCES

1. National Osteoporosis Foundation 2003 National Osteoporosis Foundation disease statistics. Available online at <http://www.nof.org/osteoporosis/stats.htm>. Accessed September 8, 2003.
2. Pocock NA, Eisman JA, Hopper JL, Yeates MG, Sambrook PN, Eberl S 1987 Genetic determinants of bone mass in adults. *J Clin Invest* **80**:706–710.
3. Seeman E, Hopper JL, Bach LA, Cooper ME, Parkinson E, McKay J, Jerums G 1989 Reduced bone mass in daughters of women with osteoporosis. *N Engl J Med* **320**:554–558.
4. Krall EA, Dawson-Hughes B 1993 Heritable and life-style determinants of bone mineral density. *J Bone Miner Res* **8**:1–9.
5. Arden NK, Baker J, Hogg C, Baan K, Spector TD 1996 The heritability of bone mineral density, ultrasound of the calcaneus and hip axis length: A study of postmenopausal twins. *J Bone Miner Res* **11**:530–534.
6. Danielson ME, Cauley JA, Baker CE, Newman AB, Dorman JS, Towers JD, Kuller LH 1999 Familial resemblance of bone mineral density (BMD) and calcaneal ultrasound attenuation: The BMD in mothers and daughters study. *J Bone Miner Res* **14**:102–110.
7. Beamer WG, Donahue LR, Rosen CJ, Baylink DJ 1996 Genetic variability in adult bone density among inbred strains of mice. *Bone* **18**:397–403.
8. Akhter MP, Iwaniec UT, Covey MA, Cullen DM, Kimmel DB, Recker RR 2000 Genetic variations in bone density, histomorphometry, and strength in mice. *Calcif Tissue Int* **67**:337–344.
9. Li X, Mohan S, Gu W, Wergedal J, Baylink DJ 2001 Quantitative assessment of forearm muscle size, forelimb grip strength, forearm bone mineral density, and forearm bone size in determining humerus breaking strength in 10 inbred strains of mice. *Calcif Tissue Int* **68**:365–369.
10. Klein RF, Shea M, Gunness ME, Pelz GB, Belknap JK, Orwoll ES 2001 Phenotypic characterization of mice bred for high and low peak bone mass. *J Bone Miner Res* **16**:63–71.
11. Turner CH, Hsieh YF, Muller R, Bouxsein ML, Rosen CJ, McCrann ME, Donahue LR, Beamer WG 2001 Variation in bone biomechanical properties, microstructure, and density in BXH recombinant inbred mice. *J Bone Miner Res* **16**:206–213.
12. Klein RF, Mitchell SR, Phillips TJ, Belknap JK, Orwoll ES 1998 Quantitative trait loci affecting peak bone mineral density in mice. *J Bone Miner Res* **13**:1648–1656.
13. Beamer WG, Shultz KL, Churchill GA, Frankel WN, Baylink DJ, Rosen CJ, Donahue LR 1999 Quantitative trait loci for bone density in C57BL/6J and CAST/EiJ inbred mice. *Mamm Genome* **10**:1043–1049.
14. Benes H, Weinstein RS, Zheng W, Thaden JJ, Jilka RL, Manolagas SC, Shmookler Reis RJ 2000 Chromosomal mapping of osteopenia-associated quantitative trait loci using closely related mouse strains. *J Bone Miner Res* **15**:626–633.
15. Beamer WG, Shultz KL, Donahue LR, Churchill GA, Sen S, Wergedal JR, Baylink DJ, Rosen CJ 2001 Quantitative trait loci for femoral and lumbar vertebral bone mineral density in C57BL/6J and C3H/HeJ inbred strains of mice. *J Bone Miner Res* **16**:1195–1206.
16. Klein RF, Carlos AS, Vartanian KA, Chambers VK, Turner RJ, Phillips TJ, Belknap JK, Orwoll ES 2001 Confirmation and fine mapping of chromosomal regions influencing peak bone mass in mice. *J Bone Miner Res* **16**:1953–1961.
17. Shultz KL, Donahue LR, Bouxsein ML, Baylink DJ, Rosen CJ, Beamer WG 2003 Congenic strains of mice for verification and genetic decomposition of quantitative trait loci for femoral bone mineral density. *J Bone Miner Res* **18**:175–185.
18. Volkman SK, Galecki AT, Burke DT, Paczas MR, Moalli MR, Miller RA, Goldstein SA 2003 Quantitative trait loci for femoral size and shape in a genetically heterogeneous mouse population. *J Bone Miner Res* **18**:1497–1505.
19. Turner CH, Hsieh YF, Muller R, Bouxsein ML, Baylink DJ, Rosen CJ, Grynpas MD, Donahue LR, Beamer WG 2000 Genetic regulation of cortical and trabecular bone strength and microstructure in inbred strains of mice. *J Bone Miner Res* **15**:1126–1131.
20. Jepsen KJ, Pennington DE, Lee YL, Warman M, Nadeau J 2001 Bone brittleness varies with genetic background in A/J and C57BL/6J inbred mice. *J Bone Miner Res* **16**:1854–1862.
21. Li X, Masinde G, Gu W, Wergedal J, Mohan S, Baylink DJ 2002 Genetic dissection of femur breaking strength in a large population (MRL/MpJ x SJL/J) of F2 mice: Singel QTL effects, epistasis, and pleiotropy. *Genomics* **79**:734–740.
22. Li X, Masinde G, Gu W, Wergedal J, Hamilton-Ulland M, Xu S, Mohan S, Baylink DJ 2002 Chromosomal regions harboring genes for the work to femur failure in mice. *Funct Integr Genomics* **1**:367–374.
23. Sambrook J, Fritsch EF, Maniatis T 1989 Analysis and cloning of eukaryotic genomic DNA. In: Ford N, Nolan C (eds.) *Molecular Cloning: A Laboratory Manual*. Cold Spring Harbor Laboratory Press, Cold Spring Harbor, NY, USA, pp. 9.16–9.23.
24. Jackson AU, Fornes A, Galecki A, Miller RA, Burke DT 1999 Multiple-trait quantitative trait loci analysis using a large mouse sibship. *Genetics* **151**:785–795.
25. Churchill GA, Doerge RW 1994 Empirical threshold values for quantitative trait mapping. *Genetics* **138**:963–971.

Address reprint requests to:

Steven A Goldstein, PhD
Orthopaedic Research Laboratories
University of Michigan
400 North Ingalls, Room G-161
Ann Arbor, MI 48109, USA
E-mail: stevegl@umich.edu

Received in original form September 12, 2003; in revised form January 8, 2004; accepted May 7, 2004.

Brittle IV Mouse Model for Osteogenesis Imperfecta IV Demonstrates Postpubertal Adaptations to Improve Whole Bone Strength

Kenneth M Kozloff,¹ Angela Carden,² Clemens Bergwitz,³ Antonella Forlino,³ Thomas E Uveges,³ Michael D Morris,² Joan C Marini,³ and Steven A Goldstein¹

ABSTRACT: The Brl mouse model for type IV osteogenesis imperfecta improves its whole bone strength and stiffness between 2 and 6 months of age. This adaptation is accomplished without a corresponding improvement in geometric resistance to bending, suggesting an improvement in matrix material properties.

Introduction: The Brittle IV (Brl) mouse was developed as a knock-in model for osteogenesis imperfecta (OI) type IV. A Gly349Cys substitution was introduced into one *coll1a1* allele, resulting in a phenotype representative of the disease. In this study, we investigate the effect of the Brl mutation on whole bone architecture, strength, and composition across a range of age groups.

Materials and Methods: One-, 2-, 6-, and 12-month-old Brl and wildtype (WT) mice were analyzed. Femurs were assessed at the central diaphysis for cortical geometric parameters using μ CT and were subsequently mechanically tested to failure by four-point bending. Matrix material properties were predicted using μ CT data to normalize data from mechanical tests. Raman spectroscopy and DXA were used to assess matrix composition.

Results: Our findings show a postpubertal adaptation in which Brl femoral strength and stiffness increase through a mechanism independent of changes in whole bone geometry. These findings suggest an improvement in the material properties of the bone matrix itself, rather than improvements in whole bone geometry, as seen in previous mouse models of OI. Raman spectroscopic results suggest these findings may be caused by changes in mineral/matrix balance rather than improvements in mineral crystallinity.

Conclusions: Our findings parallel the currently unexplained clinical observation of decreased fractures in human OI patients after puberty. The Brl mouse remains an important tool for investigating therapeutic interventions for OI. *J Bone Miner Res* 2004;19:614–622. Published online on January 12, 2004; doi: 10.1359/JBMR.040111

Key words: biomechanics, osteogenesis imperfecta, collagen, knock-in, mouse model

INTRODUCTION

OSTEOGENESIS IMPERFECTA (OI) is an autosomal dominant genetic disorder of the extracellular matrix.^(1,2) The hallmark feature of OI is bone fragility and susceptibility to fracture from minimal trauma. Patients with OI are customarily grouped in types I to IV, according to the Sillence classification, based on clinical and radiographic features.⁽¹⁾ About 90% of OI cases are caused by mutations in type I collagen, the major structural component of the extracellular matrix of bone and skin. The severity of the disorder is related to the location and type of mutation in each collagen alpha chain. Recently, a small percentage of OI patients (about 10%) have been reclassified as types V–VII based on skeletal histology and radiographic features; these cases do not result from collagen mutations.^(3–6) Type IV OI is the moderately severe form of the disorder, with phenotypes

ranging between the milder phenotype of OI type I and the more severe complications of OI type III.⁽¹⁾ Infants are often born with fractures, but fracture rate can be quite variable throughout childhood.⁽¹⁾ Interestingly, patients with type IV OI show a marked decrease in fracture rate near the age of puberty,^(1,7) suggesting the existence of an unidentified adaptation mechanism which increases whole bone structural integrity.

Although rearrangements and exon skipping mutations have been described, OI type IV typically (85%) results from a glycine substitution in one of the collagen I chains.⁽¹⁾ Understanding how a single point mutation in the collagen gene can alter the susceptibility of an entire bone to fracture requires observations over multiple hierarchical levels of the tissue. Furthermore, the development of effective therapeutic agents for OI may require manipulation at one or more of these hierarchical levels. Thus, a critical examination of an appropriate and reproducible model for OI is required.

The authors have no conflict of interest.

¹Orthopaedic Research Laboratories, Department of Orthopaedic Surgery, University of Michigan, Ann Arbor, Michigan, USA; ²Department of Chemistry, University of Michigan, Ann Arbor, Michigan, USA; ³Bone and Extracellular Matrix Branch, National Institute of Child Health and Human Development, Bethesda, Maryland, USA.

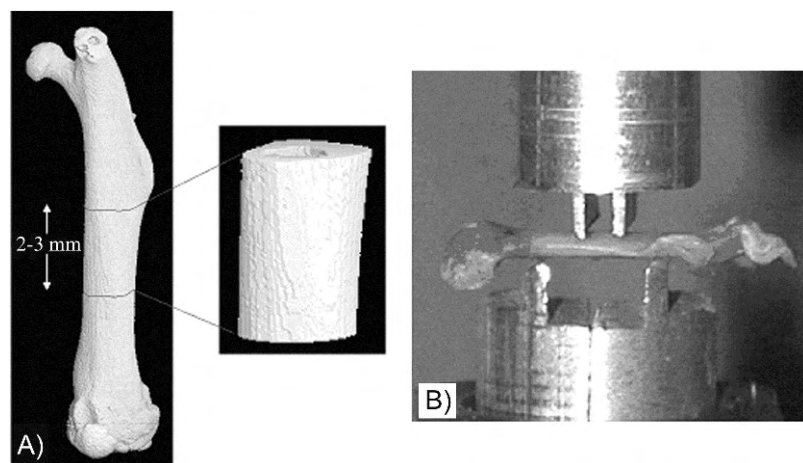


FIG. 1. (A) μ CT image of central diaphyseal region of analysis. (B) Femurs were subjected to four-point bending with the posterior surface under tension.

Several murine models of OI have been reported,^(8–11) however, none of these mice result from dominant negative transmission of a typical glycine substitution mutation. Only naturally occurring and knock-in mutations will have both the physiological tissue distribution of the mutant collagen transcripts and the physiological levels of mutant alpha chain, because their expression is under the control of endogenous promoters. For these reasons, the Brittle IV, or Brtl mouse, was developed as the first knock-in murine model for OI.⁽¹²⁾ Brtl is heterozygous for a Gly349→Cys (G349C) substitution in one *coll1a1* allele, reproducing the genetic mutation found in a type IV child.⁽¹³⁾ Brtl mice show a moderately severe skeletal phenotype, with long bone deformities and bone fragility. Furthermore, the Brtl mouse reproduces the molecular, biochemical, and radiographic features of OI type IV,⁽¹²⁾ making it an excellent model for studying this disease.

The purpose of this investigation was to evaluate the effects of a single glycine substitution in the alpha 1(I) collagen chain on the whole bone properties of the Brtl mouse model for OI. This involves examination of the inherent material properties of the bone matrix, the relative levels of mineral and extracellular matrix constituents, and the structural organization of the femur. In addition, these studies were performed in mice over a range of ages, from skeletally immature to mature adult, to observe any changes in parameters over time.

MATERIALS AND METHODS

Specimens

Seventy nine male Brtl and WT mice were killed at 1 (Brtl, $n = 10$; WT, $n = 14$), 2 (Brtl, $n = 10$; WT, $n = 12$), 6 (Brtl, $n = 11$; WT, $n = 12$), and 12 (Brtl, $n = 5$; WT, $n = 5$) months of age, corresponding to developmental status of childhood, puberty, mature young adult, and adult. Brtl mice have a mixed background of Sv129/CD-1/C57BL/6S and are bred by crossing heterozygous Brtl with WT, each generated through separate Brtl \times WT matings.⁽¹²⁾ After death, femurs were harvested, stripped of soft tissue, and stored frozen in saline until ready for testing. In one-half of

the specimens, left femurs were analyzed for geometric properties, and right femurs were mechanically tested. In the remainder of the population, bone geometry and mechanical properties were both measured in left femurs. In a subpopulation of 11 mice, both femurs were evaluated to assess left-right differences in structural properties. A separate group of 43 Brtl and WT mice were used to determine BMD of the left femur. All experiments were performed in accordance with approval from the NICHD ACUC committee.

Evaluation of femoral geometry by μ CT

A custom μ CT scanner developed and validated in our laboratory^(14–16) was used to scan femurs at 25- μ m voxel resolution to assess geometric properties of the central diaphysis (Fig. 1A). The 3D data set generated by μ CT is organized as a series of slices 25 μ m thick, oriented along the long axis of the bone. A threshold was applied to each slice,⁽¹⁵⁾ and transverse cross-sections were analyzed over 2 (1 month) or 3 mm (2, 6, and 12 months) segments starting at the distal insertion of the third trochanter and extending toward the distal end of the bone. Each slice was analyzed for its cross-sectional area, cortical thickness, and bending moment of inertia in the anterior-posterior direction about the medial-lateral axis. Data within each femur was averaged over the 2- or 3-mm segment to provide representative values over the entire 3D mid-diaphysis.

Whole bone mechanical properties

Femurs were loaded to failure in four-point bending at 0.5 mm/s in the anterior-posterior direction using a servohydraulic testing machine (810 Material Test System; MTS Systems Corporation, Eden Prairie, MN, USA; Fig. 1B). Regions loaded in four-point bending corresponded to those measured by μ CT. Load head displacement was monitored using an external linear variable differential transducer (LVDT; Lucas Schavitts, Hampton, VA, USA), and load data were collected with a 50-lb load cell (Sensotec, Columbus, OH, USA). Data were sampled at 200 Hz on a Macintosh IICI computer through an A/D system (Labview; National Instruments, Austin, TX, USA). Load-

displacement curves were analyzed for whole bone yield load, stiffness, yield energy, maximum load, failure energy, and post-yield displacement.

Predicted matrix properties

Results obtained from whole bone mechanical tests are influenced by the material properties of the bone matrix, as well as by the structural organization of the whole bone. Therefore, to separate the relative contribution of matrix material properties from whole bone structural organization, material properties of the extracellular matrix were predicted using beam theory⁽¹⁷⁾ based on the geometric properties of the femur measured by μ CT. Predicted ultimate stress is assumed to be greatest at the posterior surface, which is the area under greatest tension during bending experiments, and is calculated as

$$\sigma = \frac{Fac}{2I} \quad (1)$$

whereas the equation for predicted elastic modulus is

$$E = S \frac{a^2}{12I} (3L - 4a) \quad (2)$$

where F equals the measured maximum load, c is the distance from the centroid of the bone to the posterior periosteal surface, I is the moment of inertia of bending in the anterior-posterior direction, S is the initial stiffness of the bone, and L and a are geometric constants based on the four-point bending setup (3.57 and 0.99 mm).

These equations predict inherent material properties of the extracellular matrix, assuming a bending mode of failure.

Raman spectroscopy

Vibrational spectroscopy is ideal for probing the material properties of biological specimens nondestructively.⁽¹⁸⁾ Both Raman and infrared spectroscopy yield simultaneous information about both the inorganic and organic components of bone, yet leave the specimen intact for further testing. Because it is a light scattering measurement, Raman spectroscopy is especially advantageous for the thick specimens used in this study. An epi-illumination excitation/collection optical configuration is used, and specimens do not have to be transparent. As a preliminary investigation into the collagen-mineral ultrastructure of the Brl bone matrix, 12 specimens from 2- and 6-month-old animals ($n = 3$ per group) were prepared for Raman spectroscopic imaging from contralateral femurs by using a custom micromilling device to create barbell-shaped specimens.^(19–21) Gauge sections were $\sim 200 \times 300 \mu\text{m}$ in cross-section and 1000 μm long.

The Raman imaging system has been previously described.^(22–25) Raman scatter was excited using a high-aspect ratio rectangular laser beam at 785 nm (Kaiser Optical Systems). The total laser power at the specimen surface was ~ 150 mW. The beam was focused onto the center of the specimen's gauge length through a $10\times/0.5$ NA objec-

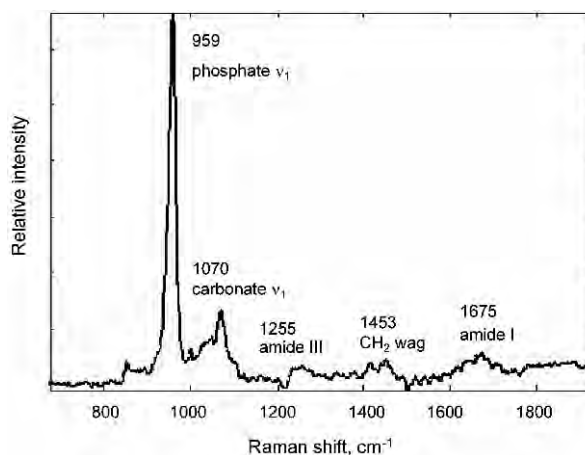


FIG. 2. Raman spectrum of a 6-month-old WT mouse femur. Important bands discussed in this paper are indicated together with their vibrational assignments. The amide II, CH_2 wag, and amide I bands result from vibrations of the collagenous matrix, whereas the phosphate ν_1 and carbonate ν_1 bands arise from the bone mineral.

tive (Zeiss), and the resulting Raman scatter was collected in an epi-illumination mode through the same objective. In this manner, Raman spectra were excited at every point along the $\sim 200\text{-}\mu\text{m}$ -long laser rectangle. The Raman scatter was focused into an axial-transmissive spectrograph (Kaiser Optical Systems) and detected using a thermoelectrically cooled CCD detector (Andor Technologies). To increase the number of spectra available for analysis, the specimen was translated in $1\text{-}\mu\text{m}$ steps using a computer-controlled X-Y translation stage (New England Affiliated Technologies), and a new line of spectra was acquired at each new specimen position. This was repeated 10 times for each specimen, creating a small Raman image $\sim 184 \times 11 \mu\text{m}$ in size and containing a total of 1260 Raman spectra. The total acquisition time for each image was ~ 50 minutes. Specimens were kept frozen before and after these experiments.

Two different approaches were used for the analysis of the Raman spectroscopic data. A multivariate approach known as factor analysis^(26,27) was used to determine whether different types of mineral and/or collagenous matrix were present within the areas imaged. This methodology is used to extract Raman spectra from large data sets, such as the hyperspectral images presented here. The details of application to bone tissue spectra have been previously reported.^(28,29) Differences in mineral or organic matrix composition affect the Raman spectrum in subtle but observable ways. If the composition of the mineral and/or matrix varies across the area imaged, factor analysis is able to separate the spectra of the different mineral and/or matrix species. Thus, multiple mineral or matrix species, each represented by its own Raman spectrum, may be observed within a single image area. Alternatively, if there is no variation in mineral and/or matrix composition within the area imaged, only a single mineral and/or matrix species will be observed. Univariate analysis, in the form of band height ratios, was also performed on the Raman spectra, a

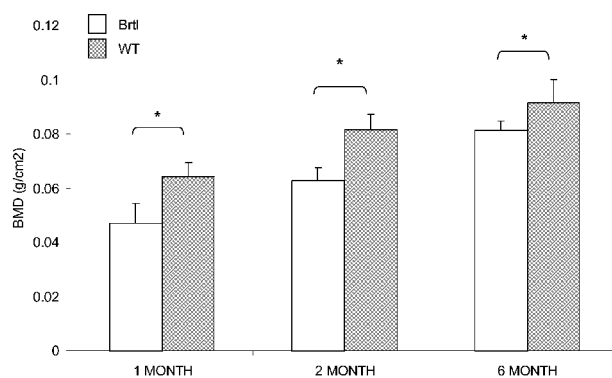


FIG. 3. Brtl femoral areal BMD is significantly less than WT at each age ($*p < 0.05$). Additionally, the gain in Brtl aBMD between 2 and 6 months of age is significantly greater than that of WT ($*p < 0.05$).

sample of which is shown in Fig. 2. Carbonate-to-phosphate ratios were computed from the ν_1 band heights of the relative carbonate ($\sim 1070 \text{ cm}^{-1}$) and phosphate ($\sim 959 \text{ cm}^{-1}$) peaks. Full-width half-maximum (FWHM) values of the ν_1 phosphate band were calculated to provide a qualitative indication of the quality, or crystallinity, of the mineral phase.^(30,31) Representative mineral-to-matrix ratios were calculated by ratioing the height of the phosphate peak to the height of the amide I peak ($\sim 1675 \text{ cm}^{-1}$).

Evaluation of aBMD by Piximus

Male mice aged 1 (Brtl, $n = 5$; WT, $n = 5$), 2 (Brtl, $n = 7$; WT, $n = 8$), and 6 (Brtl, $n = 9$; WT, $n = 8$) months were killed by lethal injection. Areal BMD (aBMD) scans of Brtl mouse femurs were compared with those of age-matched, littermate controls using a GE Lunar PIXImus2 (Madison, WI, USA) on the whole mouse specimen and the internal calibration standards provided by GE.

Statistical analysis

μ CT and four-point bending data were statistically analyzed using multivariate general linear models for each age group, with significance attributed to $p < 0.05$. A nonparametric repeated measures model (Wilcoxon signed-rank test) was used to test for within-mice differences in the subset of μ CT data. Raman spectra were analyzed using factor analysis to identify numbers of mineral and organic species in the matrix. Univariate analysis was performed for phosphate to carbonate ratios and measures of full width half-maximum of the ν_1 phosphate band. aBMD values of Brtl and WT age-matched littermates were analyzed using a Mann-Whitney U with exact significances test for genotypic differences, and differences in BMD gain between 2 and 6 months were assessed using a general linear model and testing for interactions between age and genotype. Data are presented as mean \pm SD.

RESULTS

aBMD of Brtl femurs

Figure 3 shows a comparison of left femoral bone densities of male Brtl femurs and WT counterparts. At 1, 2, and

TABLE 1. GEOMETRIC PARAMETERS DERIVED FROM μ CT

Age	Genotype	Cross-sectional area (mm ²)	Cortical thickness (mm)	n
1 Month	Brtl	0.58 \pm 0.11*	0.16 \pm 0.02*	8
	WT	0.73 \pm 0.09	0.19 \pm 0.02	13
2 Month	Brtl	0.75 \pm 0.07*	0.20 \pm 0.02*	10
	WT	1.05 \pm 0.11	0.24 \pm 0.03	12
6 Month	Brtl	1.03 \pm 0.17*	0.28 \pm 0.04	11
	WT	1.26 \pm 0.23	0.28 \pm 0.04	12
12 Month	Brtl	1.18 \pm 0.20	0.26 \pm 0.05	5
	WT	1.22 \pm 0.13	0.26 \pm 0.04	5

Values are means \pm SD.

* $p < 0.05$; Brtl vs. WT.

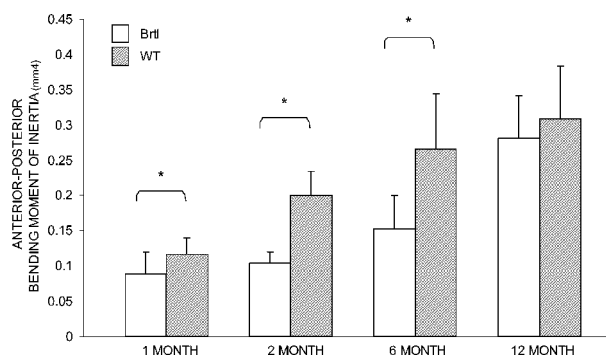


FIG. 4. Bending moments in the anterior-posterior direction show that the structure of the Brtl femur at 1, 2, and 6 months is less resistant to fracture than WT ($*p < 0.05$).

6 months of age, Brtl femurs have significantly lower aBMD than WT. Both genotypes show significant increases in aBMD at each age point; however, Brtl significantly improves its rate of mineralization from 72.8% and 76.2% of WT values at 1 and 2 months of age, respectively, to 88.9% of WT aBMD at 6 months of age ($p < 0.05$).

Intraspecimen variation in biomechanical studies

No significant differences were found between left and right femurs in the subset of mice analyzed by μ CT. Therefore, where necessary, geometric data from left femurs were used to predict matrix material properties from right femoral four-point bending data in the same mouse. Two 1-month-old Brtl specimens were excluded from μ CT analysis because of artifact during scanning. One 1-month-old Brtl specimen was fractured during the preload segment of loading and was excluded from the results.

Structural analysis

Results from μ CT show that Brtl mouse femurs have significantly smaller cross-sectional areas at 1, 2, and 6 months than do their WT counterparts (Table 1). Cortical thickness values at 1 and 2 months were also significantly reduced (Table 1), but at the postpubertal age of 6 months, the Brtl mouse femur achieved parity with controls. Results from bending moments of inertia in the anterior-posterior direction (Fig. 4) show significant differences in Brtl com-

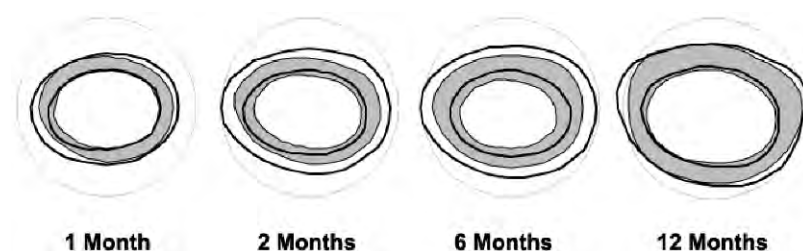


FIG. 5. Average cross-sectional views of WT femur diaphysis (heavy outline) superimposed on top of Brtl femur diaphysis (gray) (2-mm-diameter circle shown in light gray for reference). From left to right, 1, 2, 6, and 12 months.

TABLE 2. MECHANICAL PROPERTIES DERIVED FROM FOUR-POINT BENDING TESTS

Age	Genotype	Post-yield displacement (mm)	Yield energy (N-mm)	Failure energy (N-mm)	Yield load (N)
1 Month	Brtl	0.1946 ± 0.077*	0.27 ± 0.19	1.90 ± 0.71*	6.11 ± 2.37*
	WT	0.3829 ± 0.138	0.51 ± 0.37	5.96 ± 2.06	9.26 ± 2.62
2 Month	Brtl	0.1759 ± 0.071*	0.32 ± 0.19	3.03 ± 1.49*	8.84 ± 1.85
	WT	0.3016 ± 0.128	0.34 ± 0.20	7.37 ± 3.14	11.24 ± 3.93
6 Month	Brtl	0.1244 ± 0.056	0.55 ± 0.23*	3.96 ± 2.05	17.12 ± 3.85
	WT	0.1214 ± 0.88	1.15 ± 0.92	4.97 ± 3.33	22.67 ± 10.52
12 Month	Brtl	0.250 ± 0.014	0.63 ± 0.46	1.09 ± 0.71	17.81 ± 8.93
	WT	0.0572 ± 0.037	0.61 ± 0.18	2.16 ± 1.12	19.07 ± 5.46

Values are means ± SD.

* $p < 0.05$; Brtl vs. WT.

pared with controls at 1, 2, and 6 months. These results suggest that, based on structural geometry alone, independent of matrix-level material properties, the Brtl femur should be less resistant to an applied load than WT through 6 months of age. Average cross-sectional views shown in Fig. 5 summarize these results.

Mechanical testing

Femurs from young Brtl mice show a more brittle phenotype compared with WT, as shown by reduced post-yield displacement and reduced failure energy at 1 and 2 months (Table 2). Brtl mice show reduced yield (Table 2) and maximum loads (Fig. 6) at 1 and 2 months of age but equal WT values at 6 and 12 months. Brtl femurs are significantly less stiff at 2 months but comparable with WT at 6 and 12 months (Fig. 7). These findings show a postpubertal alteration whereby mechanical integrity of the femur is substantially improved to the level of the WT. These findings are contrary to geometric results from μ CT, which suggested that based on structural geometry alone, Brtl mice at 6 months should be less stiff and less strong than WT. Therefore, we hypothesize that alterations occur in the Brtl matrix after puberty that dramatically improve the matrix material properties measured at 6 months of age.

Predicted matrix properties

When four-point bending results are normalized by bending moments of inertia to predict matrix material properties, predicted elastic modulus of the 6-month-old Brtl femur was significantly increased compared with WT (Table 3).

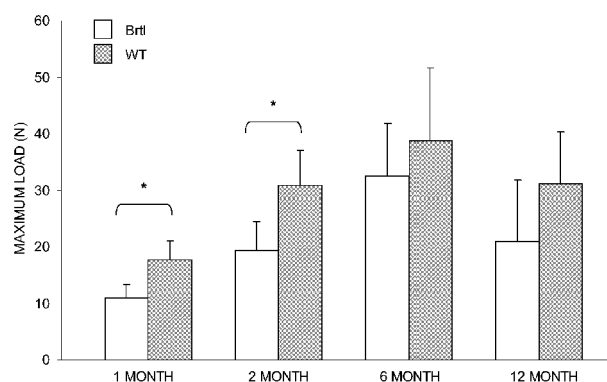


FIG. 6. Maximum load is reduced in Brtl femurs compared with WT at 1 and 2 months, while at 6 and 12 months, no significant differences were found. (* $p < 0.05$)

Additionally, 6-month-old Brtl femurs showed a strong trend toward increased predicted ultimate strength over WT ($p = 0.068$).

Raman spectroscopy

Predicted matrix properties suggest a dynamic period of alteration leading to increased material properties at the matrix level. To evaluate the potential mechanisms causing this change, specimens from 2- and 6-month-old animals were evaluated by Raman spectroscopy (Table 4). One 2-month-old Brtl specimen was dropped from the analysis

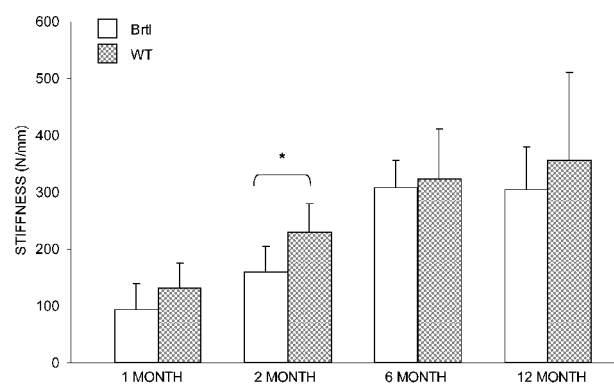


FIG. 7. Stiffness of the Brtl femur achieves equivalence to WT at 6 months of age. (* $p < 0.05$)

TABLE 3. PREDICTED ULTIMATE STRENGTH AND PREDICTED ELASTIC MODULUS

Age	Genotype	Ultimate strength (MPa)	Elastic modulus (MPa)
1 Month	Brtl	43.03 \pm 10.28	612.65 \pm 192.42
	WT	48.58 \pm 7.21	624.98 \pm 189.92
2 Month	Brtl	58.43 \pm 12.12	862.44 \pm 267.28
	WT	57.85 \pm 12.66	645.24 \pm 159.65
6 Month	Brtl	74.20 \pm 22.27 ($p = 0.068$)	1180.99 \pm 322.81*
	WT	58.33 \pm 17.20	686.01 \pm 133.9
12 Month	Brtl	29.83 \pm 12.89	611.35 \pm 147.15
	WT	44.04 \pm 16.15	660.35 \pm 268.39

Values are means \pm SD.

* $p < 0.05$; Brtl vs. WT.

because of a poor signal-to-noise ratio, making baselining of the spectra difficult. One 6-month-old Brtl specimen was dropped from the analysis because of a failed Q-test. Analysis of both the mineral subregion and organic subregion of the Raman spectra revealed no trends in the number of mineral or matrix factors with respect to disease status. Six-month-old Brtl specimens seemed to have higher carbonate-to-phosphate ratios than WT specimens, and this trend was not evident at 2 months. Measures of phosphate ν_1 band width show no difference in mineral crystallinity with respect to age or disease state. However, results suggest that the Brtl mouse has a significantly reduced mineral-to-matrix ratio compared with WT at 6 months of age.

DISCUSSION

The Brtl mouse was generated as a model for OI type IV by introducing a classic glycine substitution in one *colla1* allele.⁽¹²⁾ Individuals with type IV OI have moderately severe skeletal fragility, with decreased fracture susceptibility after puberty. The Brtl mouse results presented here model the clinical course of the disorder in children. The femurs of prepubertal 1-month-old and pubertal 2-month-old Brtl mice were structurally less able to withstand a load than age-matched WT controls. This finding was verified

through whole bone mechanical tests. At the postpubertal age of 6 months, however, the Brtl mouse femurs had whole bone strength and stiffness comparable with WT, despite having a bone geometrical organization less resistant to applied loads. Predicted material properties of elastic modulus and ultimate strength are increased, accounting for increases in whole bone strength through an increase in matrix-level material properties without corresponding structural adaptations. These findings are bolstered by results from the aBMD measurements. Brtl aBMD was significantly lower than WT at all ages; however, Brtl aBMD increased between 2 and 6 months at a rate greater than associated with the pubertal changes in WT mice. Raman results suggest a change in the balance of ultrastructural components, as mineral:matrix ratios adjust in Brtl from being nonsignificantly larger than WT at 2 months to being significantly lower at 6 months. The 2-month-old Raman data do not contradict the findings of reduced Brtl aBMD at all ages, because Raman measures the ratio, not total amount, of mineral and collagen constituencies at the ultrastructural level. If Brtl produces less collagen than WT at the ultrastructural level, it could still show a higher mineral:matrix ratio by Raman, but a lower aBMD because of the difference in the two measurement techniques.

Together, these findings suggest a period of adaptation between 2 and 6 months of age in which bone stiffness and strength attain WT values through a strengthening mechanism at the level of the extracellular matrix rather than through alterations in whole bone structural layout.

Significant further gains in bone strength are not demonstrated beyond 6 months of age. This finding is consistent with other studies showing minimal gains in bone strength and stiffness beyond 18 weeks of age in the C57BL/6J mouse⁽³²⁾ and constant peak torque between 6 and 12 months in C57BL/6J X C3H/He mice.⁽³³⁾ Furthermore, WT ductility is decreased at 6 and 12 months compared with earlier ages, rendering differences in failure energy and post-yield displacement no longer significant. This suggests a natural aging process in the WT mouse leading to age-related decreases in ductility. Similar decrements in femoral ductility have been shown in SAMR1 control mice and the SAMP6 mouse model for senile osteoporosis between 4 and 12 months of age.⁽³⁴⁾

Other models of OI have demonstrated adaptations in response to a matrix-altering mutation. The Mov13 mouse carries a provirus preventing transcription of the $\alpha 1(I)$ collagen gene.⁽³⁵⁾ Mice heterozygous for the Mov13 mutation show a 50% decrease in normal type I collagen and serve as a model for OI type I,⁽⁸⁾ in which patients produce a reduced quantity of structurally normal type I collagen. At 8 weeks of age, Mov13 femurs are more brittle than WT because of microstructural differences between the two animals.⁽³⁶⁾ Furthermore, microbeams machined from the Mov13 femur show decreased matrix material properties and a reduced fatigue life compared with controls.⁽²¹⁾ To compensate for these mechanical impairments, between the ages of 8 and 15 weeks, Mov13 mice deposit new bone matrix on the periosteal surfaces of the femur, significantly increasing their cortical area and bending moment of inertia.⁽³⁷⁾ This structural adaptation significantly improves the whole bone

TABLE 4. RESULTS FROM RAMAN SPECTROSCOPY SUGGEST AN ALTERATION IN MINERAL-TO-MATRIX RATIOS AT 6 MONTHS OF AGE

Age	Genotype	Mineral factors	CO ₃ :PO ₄ ratio	FWHM ν I PO ₄ band	Mineral/matrix ratio
2 Month	Brtl	1, 1, 1	0.144 \pm 0.011	16.25 \pm 1.17	12.50 \pm 4.79
	WT	1, 1, 1	0.162 \pm 0.068	16.94 \pm 0.46	8.45 \pm 1.65
6 Month	Brtl	1, 2, 1	0.209 \pm 0.027	17.15 \pm 2.16	5.75 \pm 0.11*
	WT	2, 1, 1	0.193 \pm 0.056	17.13 \pm 0.65	11.17 \pm 2.99

* $p < 0.05$; Brt vs. WT.

bending strength of the Mov13 mouse to a level greater than control specimens.

The *oim/oim* mouse has a naturally occurring mutation that prevents pro- α 2(I) chains from incorporating into type I collagen. The *oim/oim* extracellular matrix does not contain any normal type I collagen but is instead composed of α 1(I) homotrimers.⁽⁹⁾ This model for OI type III show reduced indices of whole bone strength compared with WT at all ages.^(33,38) Whereas geometric-based indices of bone strength suggest an improved bone geometry in older *oim/oim* mice, this alteration fails to improve bone strength to the level of the WT femur.⁽³³⁾

Our current findings show improvements in whole bone strength through improved matrix level material properties rather than geometrical adaptation. Raman spectroscopy was used as a means to investigate specific mineral-matrix interactions to help determine what alterations lead to the improvement in whole bone strength. Our results yielded no difference in number of mineral factors or mineral crystallinity with respect to disease state. Rather, a higher CO₃:PO₄ ratio and reduced mineral-to-matrix ratios were observed in 6-month-old Brtl specimens compared with WT. At this hierarchical level, it is unclear how these fundamental changes might affect the mechanical properties of the tissue. Bohic et al.⁽³⁹⁾ have shown similar increases in carbonation of tooth enamel from a patient with dentinogenesis imperfecta compared with an age-matched control. These findings differ from investigations in the *oim/oim* mouse. Camacho et al.⁽⁴⁰⁾ used Fourier-transform infrared spectroscopy, an imaging modality that provides similar information to Raman spectroscopy, to show differences in phosphate species⁽⁴⁰⁾ and crystallinity⁽³⁸⁾ compared with controls. *oim/oim* mice show trends opposite Brtl in CO₃:PO₄ and mineral:matrix ratios compared with the milder phenotype of *oim/+* at 6 months and compared with WT at 1 year.⁽⁴⁰⁾ Differences in these findings may be because of differences in the collagen defect. Matrix containing only α 1(I) homotrimeric molecules in the *oim/oim* mice may induce a different mineralization template than formed by Brtl matrix, which contains a mixture of normal collagen and mutant collagen with a glycine to cysteine substitution. Neither Mov13 nor *oim/oim* mice show a compensatory mechanism at the level of the extracellular matrix capable of significantly improving whole bone mechanical strength to the level of controls, independent of changes in whole bone geometry. The femur of the Brtl mouse demonstrates this type of alteration.

Vetter et al.⁽⁴¹⁾ have demonstrated small but significant decreases in apatite crystal size in children and adolescents

with type IV OI compared with controls. In the current study, no changes in mineral crystallinity were found between Brtl and WT mice; however, we cannot definitively rule out this possibility because no studies have yet calibrated Raman band width to mineral crystallinity as measured by X-ray diffraction.

Another limitation to this study is the small sample size used in the Raman analysis. Additionally, milling of the microspecimens may have introduced artifact because of mechanical deformation of the bone.^(22,25) Further analysis of the Brtl extracellular matrix is warranted. Changes in tissue microarchitecture, such as percent porosity and relative balance of woven versus lamellar bone, have been demonstrated to be important mediators of mechanical behavior in the Mov13 mouse.⁽³⁶⁾ Alterations in porosity or remodeling spaces, as seen in human cases of OI, may lead to the inclusion or deduction of stress risers within the bone matrix, which would be unaccounted for in our current calculations for predicted strength and modulus. Furthermore, woven and lamellar bone distribution may change as Brtl ages, altering the mechanical profile of the bone. In addition to microarchitecture, further investigation of the mineral and organic phase of the Brtl bone through methods such as small-angle X-ray scattering⁽⁴²⁾ and transmission electron microscopy⁽⁴³⁾ may lend insight into mineral crystal size, shape, orientation, and arrangement within the matrix. These methods may be needed to lend further understanding into the results generated through Raman spectroscopy.

Results from this study and others⁽³⁷⁾ suggest two general avenues of therapeutics for the disease: (1) improving geometric resistance to fracture, as in the Mov13 mouse, and (2) improving the material properties of the extracellular matrix itself, as shown here in the Brtl mouse. Hormones such as parathyroid hormone (PTH) or other anabolic drugs may be useful as a means of improving geometric resistance to fracture by adding bone to the cortex as seen in both animal^(44,45) and human⁽⁴⁶⁾ histomorphometric studies. Bisphosphonates have been hypothesized to change the material properties of bone, possibly through increases in secondary matrix mineralization.^(47–49) Indeed, alendronate, a third-generation bisphosphonate, has been demonstrated to reduce the number of fractures and increase femoral metaphyseal density in the growing *oim/oim* mouse model for OI.⁽⁵⁰⁾ The Brtl mouse is an appropriate model in which to address these two avenues of therapeutics and their potential implications on OI bone mechanics and geometry.

The findings presented here parallel clinically observed decreases in OI patient fracture rate after puberty without

administration of drug therapies.⁽⁷⁾ The mechanism of this improvement in patient bone integrity is not well understood. The postpubertal decrease in fracture rate occurs with both glycine substitutions and exon skipping defects of collagen. Our results are the first to suggest a possible matrix-level adaptation leading to improved whole bone strength without corresponding increases in structural geometry in a model of OI. It is apparent that nature has developed mechanisms to adapt whole bone integrity to the fragility induced by type I collagen mutations. Further investigations are underway to determine the molecular mechanisms triggering this adaptation in Brtl matrix properties and the nature of the changes in postpubertal matrix composition. Exploiting these naturally occurring adaptation strategies may provide novel therapeutic interventions for OI.

ACKNOWLEDGMENTS

This study was supported by National Institutes of Health AR46024 (SAG), National Institutes of Health AR47969 (MDM) and NICHD, National Institutes of Health Intramural Funding (JCM). KMK is supported by a Whitaker Foundation Graduate Student Fellowship. We thank EP Frankenburg, M Spurchise, R Rae Jr, J Hall, S Volkmann, D Kayner and C Roehm for their valuable contributions to this study.

REFERENCES

- Byers PH 2002 Osteogenesis imperfecta. In: Royce PM, Steinmann B (eds.) *Connective Tissue and Its Heritable Disorders*, 2nd ed. Wiley-Liss, Inc., New York, NY, USA, pp. 385–430.
- Kuivaniemi H, Tromp G, Prockop DJ 1991 Mutations in collagen genes: Causes of rare and some common diseases in humans. *FASEB J* **5**:2052–2060.
- Glorieux FH, Rauch F, Plotkin H, Ward L, Travers R, Roughley P, Lalic L, Glorieux DF, Fassier F, Bishop NJ 2000 Type V osteogenesis imperfecta: A new form of brittle bone disease. *J Bone Miner Res* **15**:1650–1658.
- Labuda M, Morissette J, Ward LM, Rauch F, Lalic L, Roughley PJ, Glorieux FH 2002 Osteogenesis imperfecta type VII maps to the short arm of chromosome 3. *Bone* **31**:19–25.
- Ward LM, Rauch F, Travers R, Chabot G, Azouz EM, Lalic L, Roughley PJ, Glorieux FH 2002 Osteogenesis imperfecta type VII: An autosomal recessive form of brittle bone disease. *Bone* **31**:12–18.
- Glorieux FH, Ward LM, Rauch F, Lalic L, Roughley PJ, Travers R 2002 Osteogenesis imperfecta type VI: A form of brittle bone disease with a mineralization defect. *J Bone Miner Res* **17**:30–38.
- Marini JC 1988 Osteogenesis imperfecta: Comprehensive management. *Adv Pediatr* **35**:391–426.
- Bonadio J, Saunders TL, Tsai E, Goldstein SA, Morris-Wiman J, Brinkley L, Dolan DF, Altschuler RA, Hawkins JE Jr, Bateman JF 1990 Transgenic mouse model of the mild dominant form of osteogenesis imperfecta. *Proc Natl Acad Sci USA* **87**:7145–7149.
- Chipman SD, Sweet HO, McBride DJ Jr, Davisson MT, Marks SC Jr, Shuldiner AR, Wenstrup RJ, Rowe DW, Shapiro JR 1993 Defective pro alpha 2(I) collagen synthesis in a recessive mutation in mice: A model of human osteogenesis imperfecta. *Proc Natl Acad Sci USA* **90**:1701–1705.
- Saban J, Zussman MA, Havey R, Patwardhan AG, Schneider GB, King D 1996 Heterozygous oim mice exhibit a mild form of osteogenesis imperfecta. *Bone* **19**:575–579.
- Khillan JS, Olsen AS, Kontusaari S, Sokolov B, Prockop DJ 1991 Transgenic mice that express a mini-gene version of the human gene for type I procollagen (COL1A1) develop a phenotype resembling a lethal form of osteogenesis imperfecta. *J Biol Chem* **266**:23373–23379.
- Forlino A, Porter FD, Lee EJ, Westphal H, Marini JC 1999 Use of the Cre/lox recombination system to develop a non-lethal knock-in murine model for osteogenesis imperfecta with an $\alpha 1(I)$ G349C substitution. Variability in phenotype in BrtlIV mice. *J Biol Chem* **274**:37923–37931.
- Sarafova AP, Choi H, Forlino A, Gajko A, Cabral WA, Tosi L, Reing CM, Marini JC 1998 Three novel type I collagen mutations in osteogenesis imperfecta type IV probands are associated with discrepancies between electrophoretic migration of osteoblast and fibroblast collagen. *Hum Mutat* **11**:395–403.
- Feldkamp LA, Goldstein SA, Parfitt AM, Jesion G, Kleerekoper M 1989 The direct examination of three-dimensional bone architecture in vitro by computed tomography. *J Bone Miner Res* **4**:3–11.
- Kuhn JL, Goldstein SA, Feldkamp LA, Goulet RW, Jesion G 1990 Evaluation of a microcomputed tomography system to study trabecular bone structure. *J Orthop Res* **8**:833–842.
- Goulet RW 1993 The quantification of the structure and mechanical properties of trabecular bone. Ph.D. thesis, University of Michigan, Ann Arbor, MI.
- Turner CH, Burr DB 1993 Basic biomechanical measurements of bone: A tutorial. *Bone* **14**:595–608.
- Carden A, Morris MD 2000 Application of vibrational spectroscopy to the study of mineralized tissues. *J Biomed Opt* **5**:259–268.
- Choi K, Goldstein SA 1992 A comparison of the fatigue behavior of human trabecular and cortical bone tissue. *J Biomech* **25**:1371–1381.
- Kuhn JL, Goldstein SA, Choi K, London M, Feldkamp LA, Matthews LS 1989 Comparison of the trabecular and cortical tissue moduli from human iliac crests. *J Orthop Res* **7**:876–884.
- Jepsen KJ, Schaffler MB, Kuhn JL, Goulet RW, Bonadio J, Goldstein SA 1997 Type I collagen mutation alters the strength and fatigue behavior of Mov13 cortical tissue. *J Biomech* **30**:1141–1147.
- Carden A, Rajachar RM, Morris MD, Kohn DH 2003 Ultrastructural changes accompanying the mechanical deformation of bone tissue: A Raman imaging study. *Calcif Tissue Int* **72**:166–175.
- Pezzuti JA, Morris MD, Bonadio JF, Goldstein SA 1998 Hyper-spectral Raman imaging of bone growth and regrowth chemistry. *Proc SPIE* **3261**:270–276.
- Timlin JA, Carden A, Morris MD, Bonadio JF, Hoffler CE, Kozloff KM, Goldstein SA 1999 Spatial distribution of phosphate species in mature and newly generated mammalian bone by hyperspectral Raman imaging. *J Biomed Opt* **4**:28–34.
- Timlin JA, Carden A, Morris MD, Rajachar RM, Kohn DH 2000 Raman spectroscopic imaging markers for fatigue-related micro-damage in bovine bone. *Anal Chem* **72**:2229–2236.
- Malinowski ER 1991 *Factor Analysis in Chemistry*, 2nd ed. John Wiley & Sons, Inc., New York, NY, USA.
- Reyment R, Joreskog KG 1996 *Applied Factor Analysis in the Natural Sciences*. Cambridge University Press, New York, NY, USA.
- Morris MD, Crane NJ, Gomez LE, Ignelzi MA Jr 2004 Compatibility of staining protocols for bone tissue with Raman imaging. *Calcif Tissue Int* (in press).
- Tarnowski CP, Ignelzi MA Jr, Morris MD 2002 Mineralization of developing mouse calvaria as revealed by Raman microspectroscopy. *J Bone Miner Res* **17**:1118–1126.
- Freeman JJ, Wopenka B, Silva MJ, Pasteris JD 2001 Raman spectroscopic detection of changes in bioapatite in mouse femora as a function of age and in vitro fluoride treatment. *Calcif Tissue Int* **68**:156–162.
- de Mul FF, Hottenhuis MH, Bouter P, Greve J, Arends J, ten Bosch JJ 1986 Micro-Raman line broadening in synthetic carbonated hydroxyapatite. *J Dent Res* **65**:437–440.
- Ferguson VL, Ayers RA, Bateman TA, Simske SJ 2000 Development of endogenous osteoporosis in male C57BL/6J mice. *J Bone Miner Res* **15**:S461.
- McBride DJ Jr, Shapiro JR, Dunn MG 1998 Bone geometry and strength measurements in aging mice with the oim mutation. *Calcif Tissue Int* **62**:172–176.
- Silva MJ, Brodt MD, Ettner SL 2002 Long bones from the senescence accelerated mouse SAMP6 have increased size but reduced whole-bone strength and resistance to fracture. *J Bone Miner Res* **17**:1597–1603.
- Schnieke A, Dziadek M, Bateman J, Mascara T, Harbers K, Gelinas R, Jaenisch R 1987 Introduction of the human pro alpha 1(I) collagen gene into pro alpha 1(I)-deficient Mov-13 mouse cells leads to formation of functional mouse-human hybrid type I collagen. *Proc Natl Acad Sci USA* **84**:764–768.

36. Jepsen KJ, Goldstein SA, Kuhn JL, Schaffler MB, Bonadio J 1996 Type-I collagen mutation compromises the post-yield behavior of Mov13 long bone. *J Orthop Res* **14**:493–499.
37. Bonadio J, Jepsen KJ, Mansoura MK, Jaenisch R, Kuhn JL, Goldstein SA 1993 A murine skeletal adaptation that significantly increases cortical bone mechanical properties. Implications for human skeletal fragility. *J Clin Invest* **92**:1697–1705.
38. Camacho NP, Hou L, Toledano TR, Ilg WA, Brayton CF, Raggio CL, Root L, Boskey AL 1999 The material basis for reduced mechanical properties in oim mice bones. *J Bone Miner Res* **14**:264–272.
39. Bohic S, Heymann D, Pouezat JA, Gauthier O, Daculsi G 1998 Transmission FT-IR microspectroscopy of mineral phases in calcified tissues. *Comptes Rendus de l'Academie des Sciences Serie III, Sciences de la Vie* **321**:865–876.
40. Camacho NP, Landis WJ, Boskey AL 1996 Mineral changes in a mouse model of osteogenesis imperfecta detected by Fourier transform infrared microscopy. *Connect Tissue Res* **35**:259–265.
41. Vetter U, Eanes ED, Kopp JB, Termine JD, Robey PG 1991 Changes in apatite crystal size in bones of patients with osteogenesis imperfecta. *Calcif Tissue Int* **49**:248–250.
42. Fratzl P, Paris O, Klaushofer K, Landis WJ 1996 Bone mineralization in an osteogenesis imperfecta mouse model studied by small-angle x-ray scattering. *J Clin Invest* **97**:396–402.
43. McKee MD, Nanci A 1995 Postembedding colloidal-gold immunocytochemistry of noncollagenous extracellular matrix proteins in mineralized tissues. *Microsc Res Tech* **31**:44–62.
44. Hirano T, Burr DB, Turner CH, Sato M, Cain RL, Hock JM 1999 Anabolic effects of human biosynthetic parathyroid hormone fragment (1–34), LY333334, on remodeling and mechanical properties of cortical bone in rabbits. *J Bone Miner Res* **14**:536–545.
45. Wronski TJ, Yen CF 1994 Anabolic effects of parathyroid hormone on cortical bone in ovariectomized rats. *Bone* **15**:51–58.
46. Dempster DW, Cosman F, Kurland ES, Zhou H, Nieves J, Woelfert L, Shane E, Plavetic K, Muller R, Bilezikian J, Lindsay R 2001 Effects of daily treatment with parathyroid hormone on bone microarchitecture and turnover in patients with osteoporosis: A paired biopsy study. *J Bone Miner Res* **16**:1846–1853.
47. Chavassieux PM, Arlot ME, Reda C, Wei L, Yates AJ, Meunier PJ 1997 Histomorphometric assessment of the long-term effects of alendronate on bone quality and remodeling in patients with osteoporosis. *J Clin Invest* **100**:1475–1480.
48. Meunier PJ, Boivin G 1997 Bone mineral density reflects bone mass but also the degree of mineralization of bone: Therapeutic implications. *Bone* **21**:373–377.
49. Bourrin S, Ammann P, Bonjour JP, Rizzoli R 2002 Recovery of proximal tibia bone mineral density and strength, but not cancellous bone architecture, after long-term bisphosphonate or selective estrogen receptor modulator therapy in aged rats. *Bone* **30**:195–200.
50. Camacho NP, Raggio CL, Doty SB, Root L, Zraick V, Ilg WA, Toledano TR, Boskey AL 2001 A controlled study of the effects of alendronate in a growing mouse model of osteogenesis imperfecta. *Calcif Tissue Int* **69**:94–101.

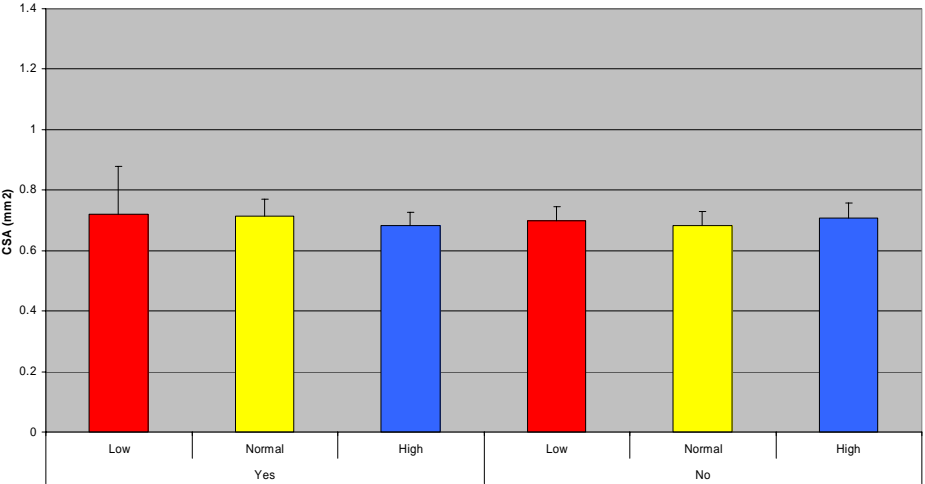
Address reprint requests to:

Steven A Goldstein, PhD
 Orthopaedic Research Laboratories
 Department of Orthopaedic Surgery
 University of Michigan
 Room G-161
 400 North Ingalls
 Ann Arbor, MI 48109-0486, USA
 E-mail: steveglld@umich.edu

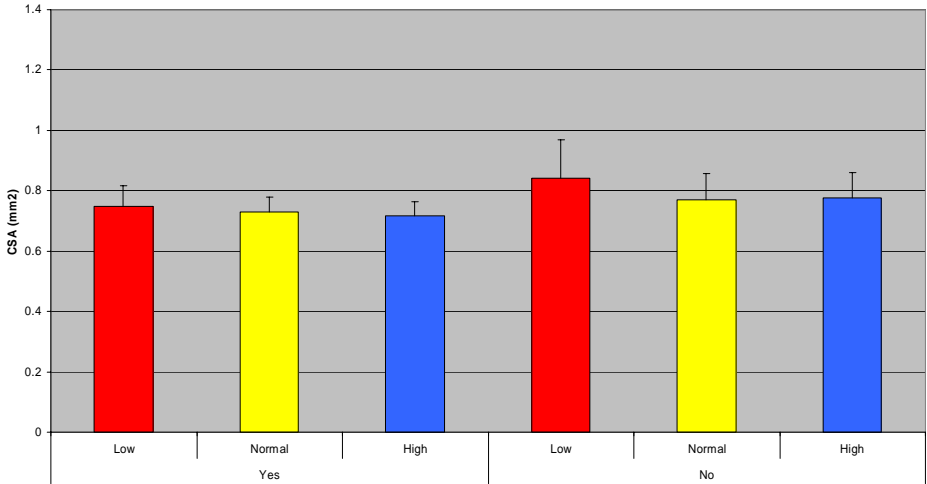
Received in original form May 21, 2003; in revised form October 28, 2003; accepted November 14, 2003.

Femur Mid-diaphyseal Cross-sectional Area by Diet and Exercise

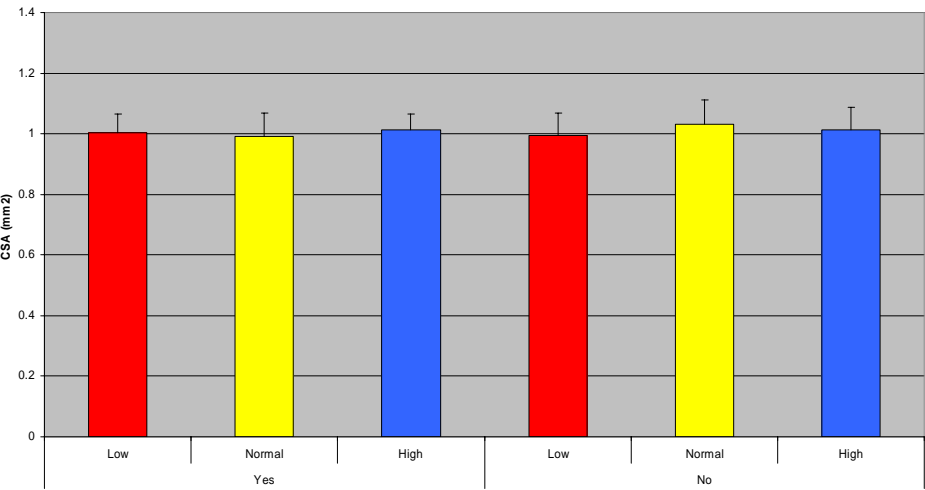
Cross Sectional Area by Diet and Exercise (Female C57 Only)



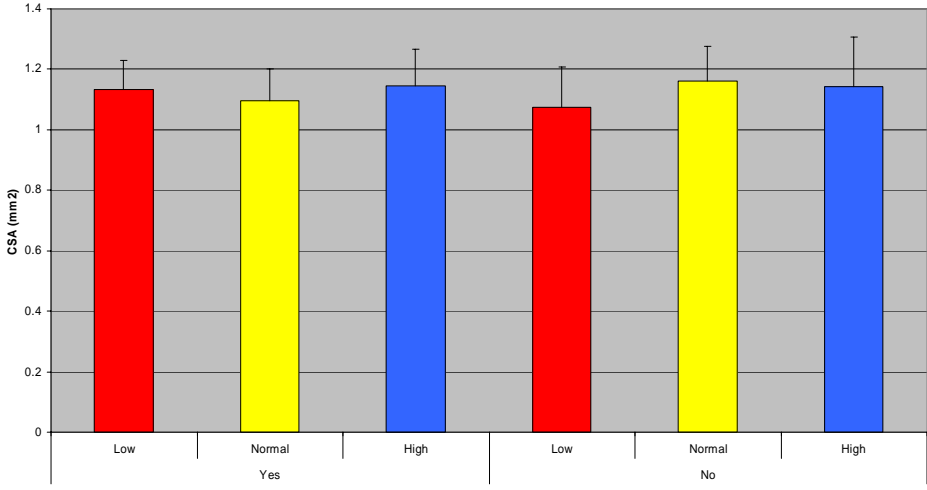
Cross Sectional Area by Diet and Exercise (Male C57 Only)



Cross Sectional Area by Diet and Exercise (Female C3 Only)

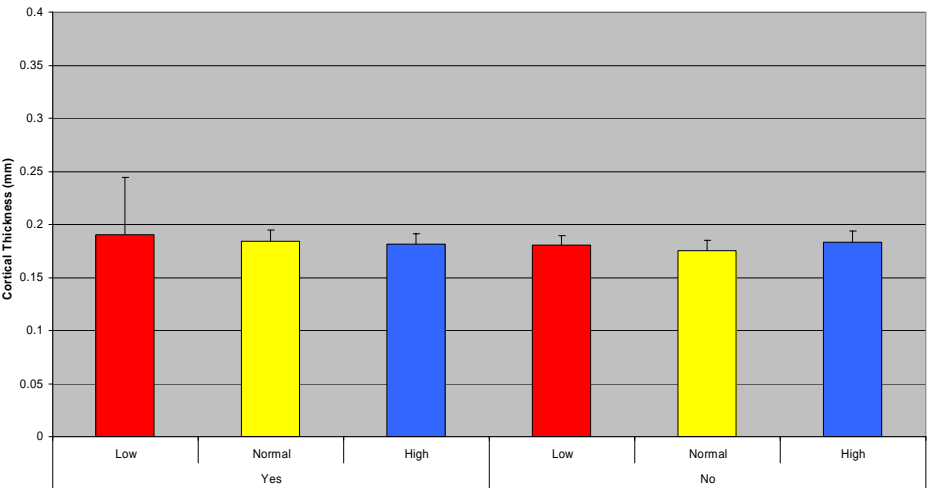


Cross Sectional Area by Diet and Exercise (Male C3 Only)

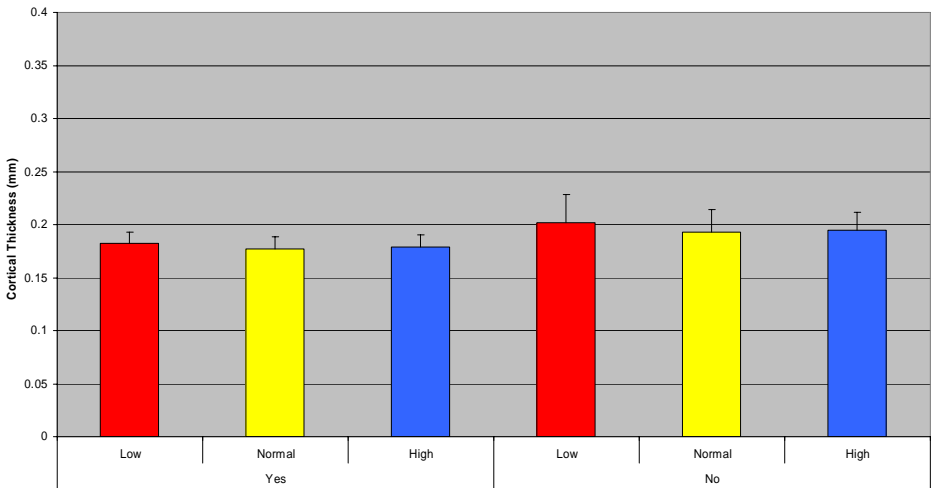


Femur Mid-diaphyseal Cortical Thickness by Diet and Exercise

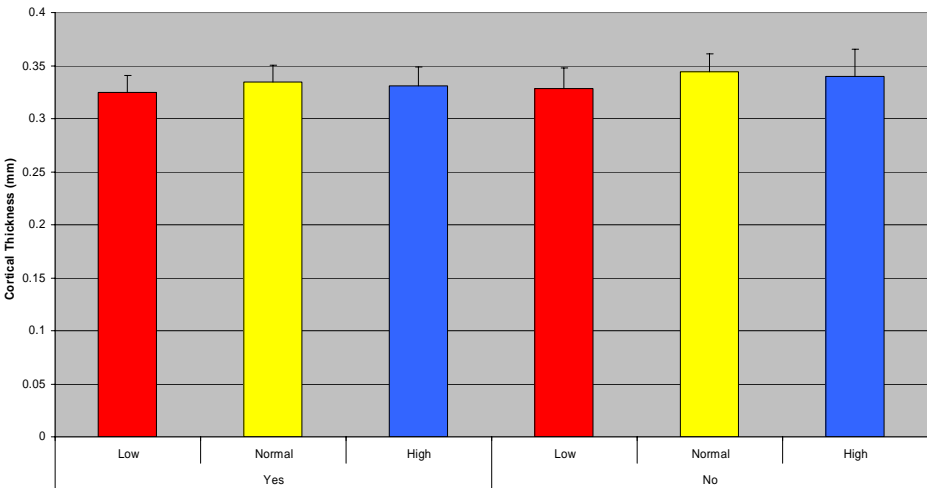
Cortical Thickness by Diet and Exercise (Female C57 Only)



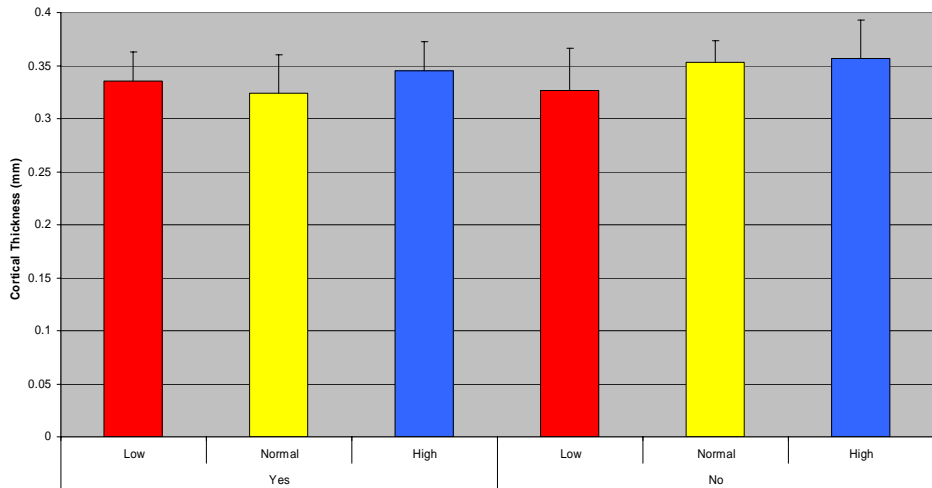
Cortical Thickness by Diet and Exercise (Male C57 Only)



Cortical Thickness by Diet and Exercise (Female C3 Only)

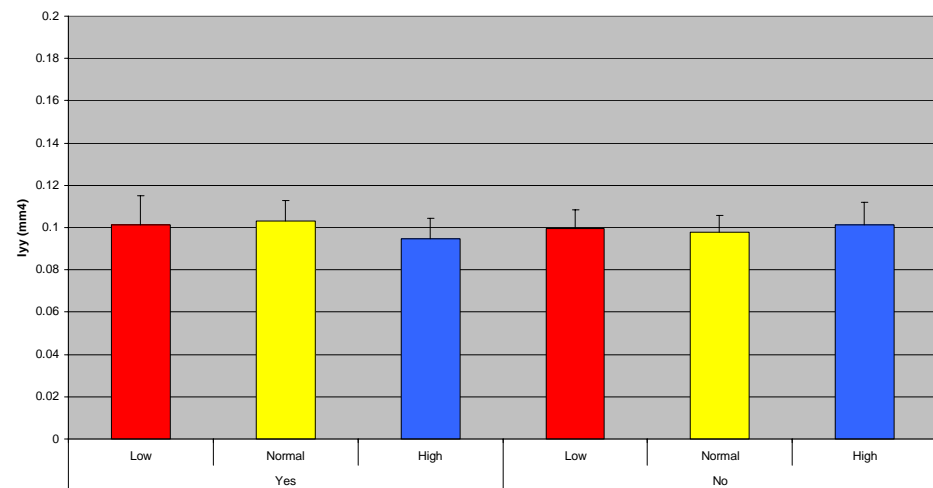


Cortical Thickness by Diet and Exercise (Male C3 Only)

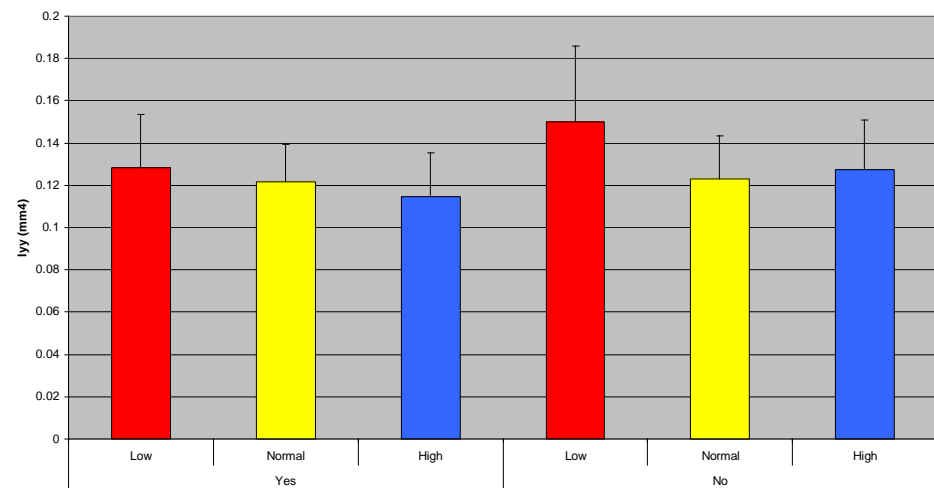


Femur Mid-diaphyseal Bending Moment of Inertia by Diet and Exercise

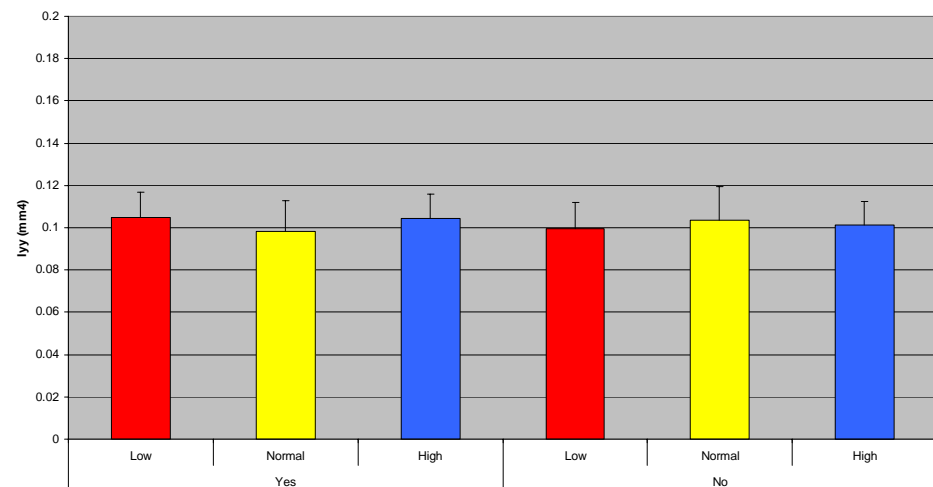
Bending Moment of Inertia by Diet and Exercise (Female C57 Only)



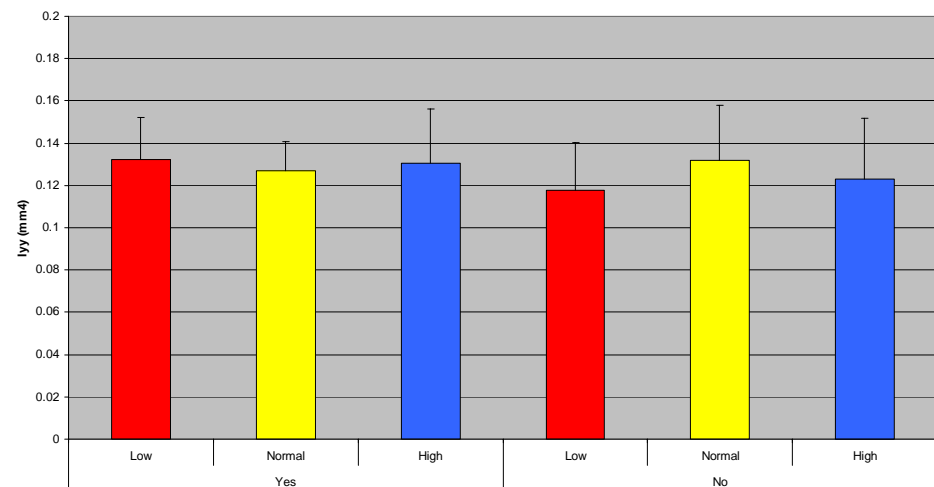
Bending Moment of Inertia by Diet and Exercise (Male C57 Only)



Bending Moment of Inertia by Diet and Exercise (Female C3 Only)

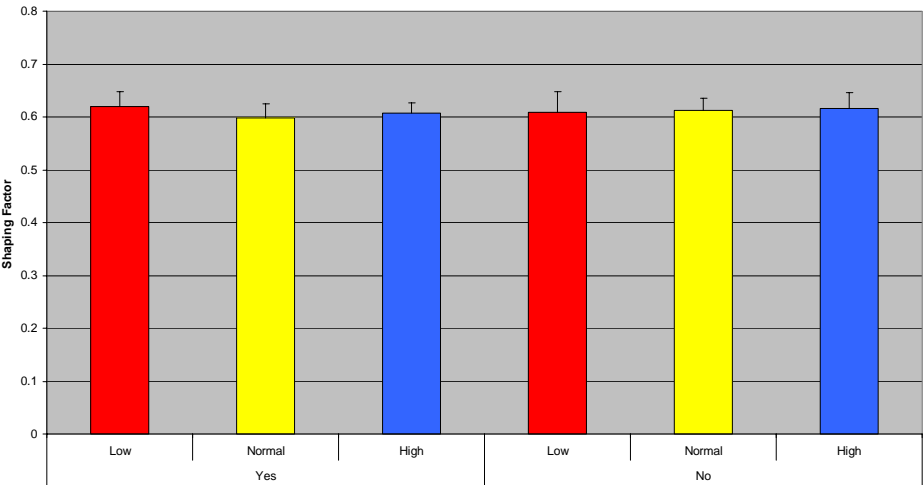


Bending Moment of Inertia by Diet and Exercise (Male C3 Only)

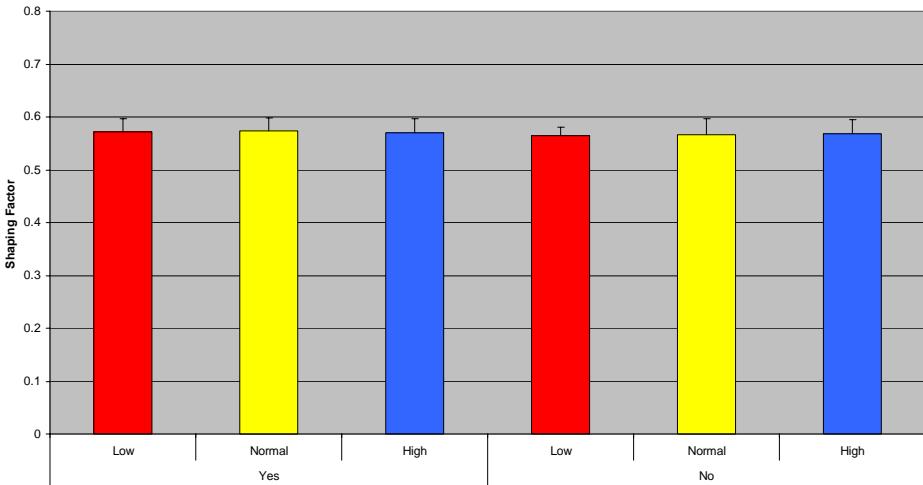


Femur Mid-diaphyseal Shaping Factor by Diet and Exercise

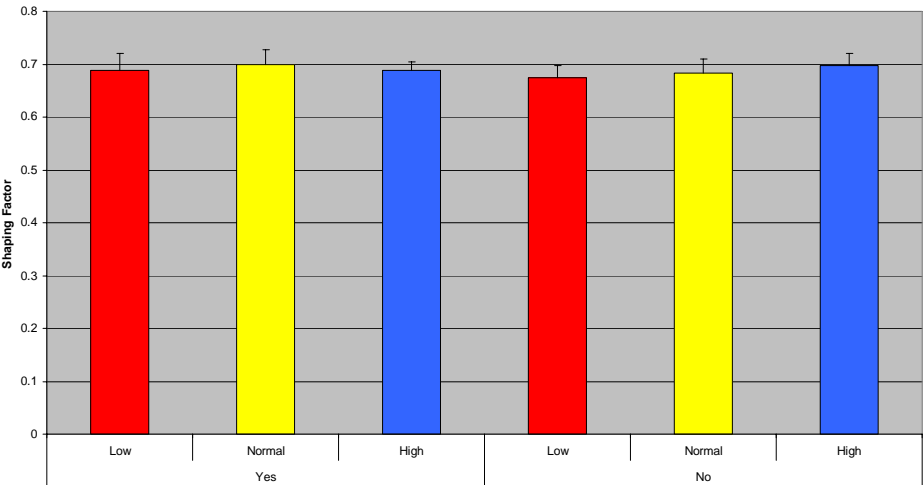
Shaping Factor by Diet and Exercise (Female C57 Only)



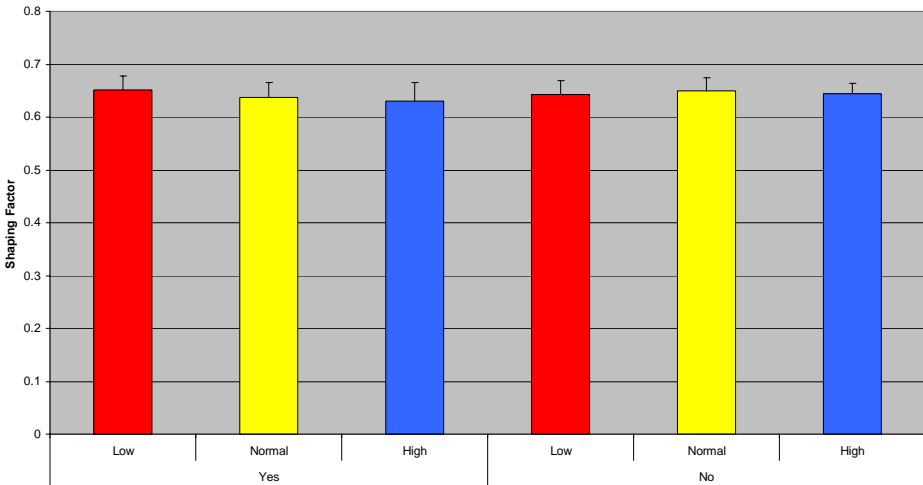
Shaping Factor by Diet and Exercise (Male C57 Only)



Shaping Factor by Diet and Exercise (Female C3 Only)

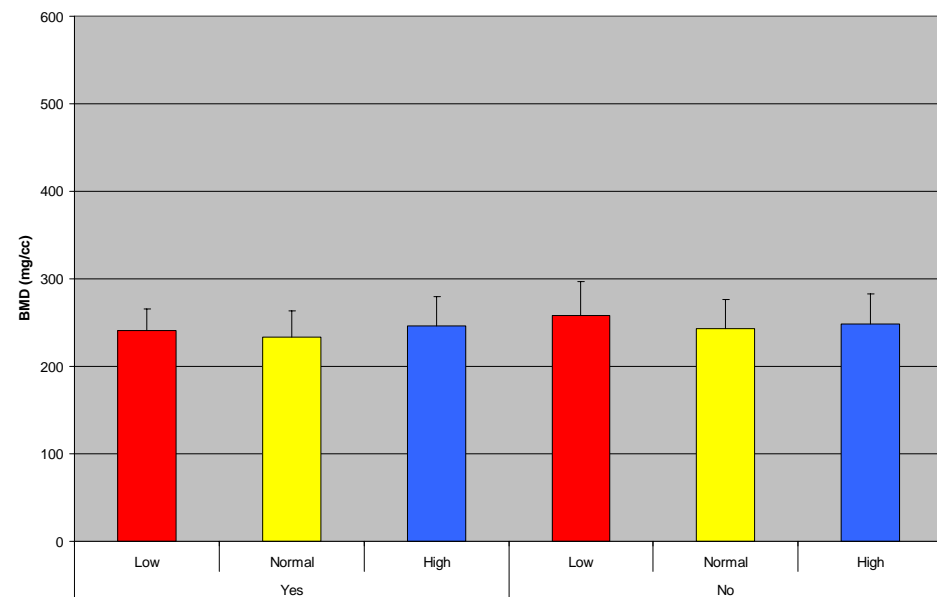


Shaping Factor by Diet and Exercise (Male C3 Only)

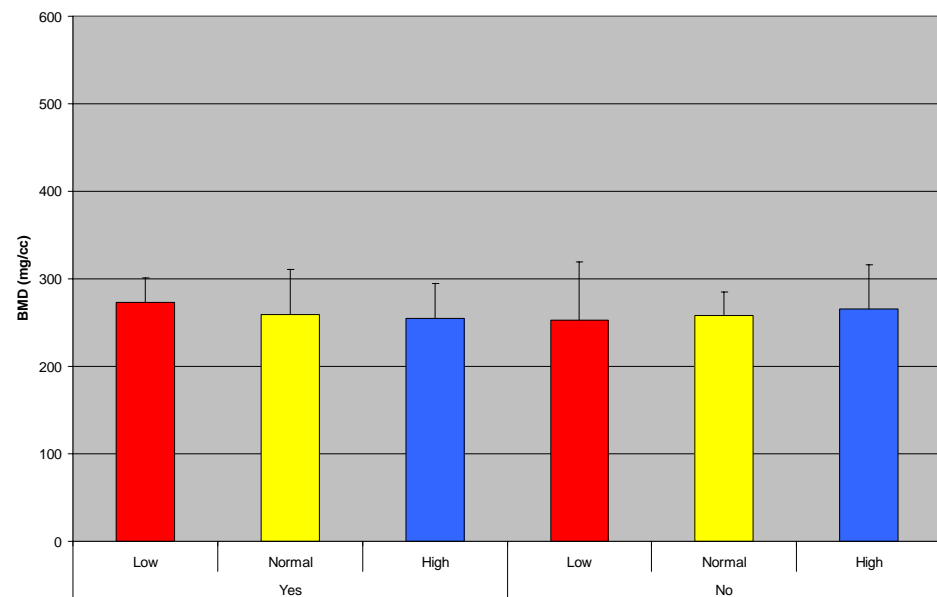


Femur Mid-diaphyseal Bone Mineral Density by Diet and Exercise

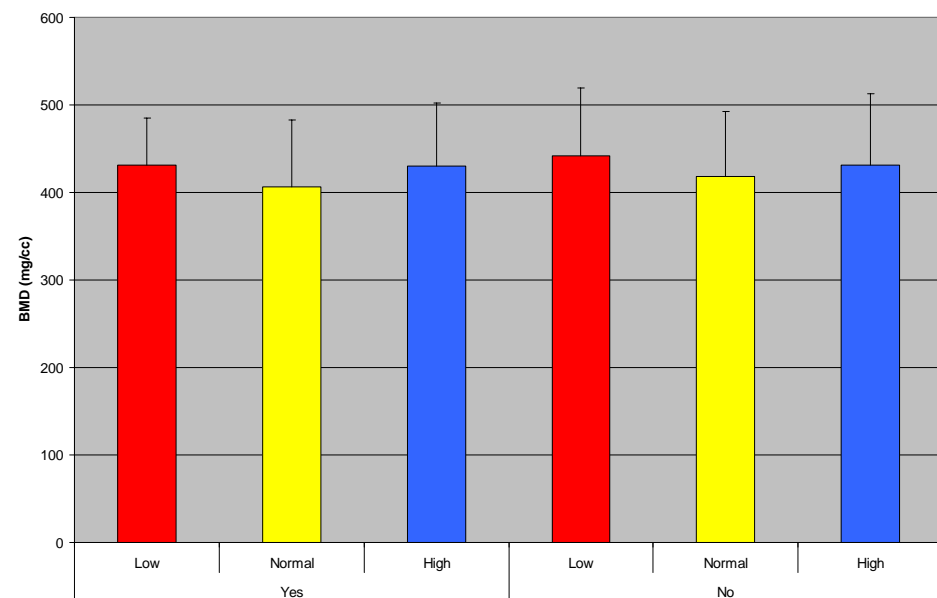
BMD by Diet and Exercise (Female C57 only)



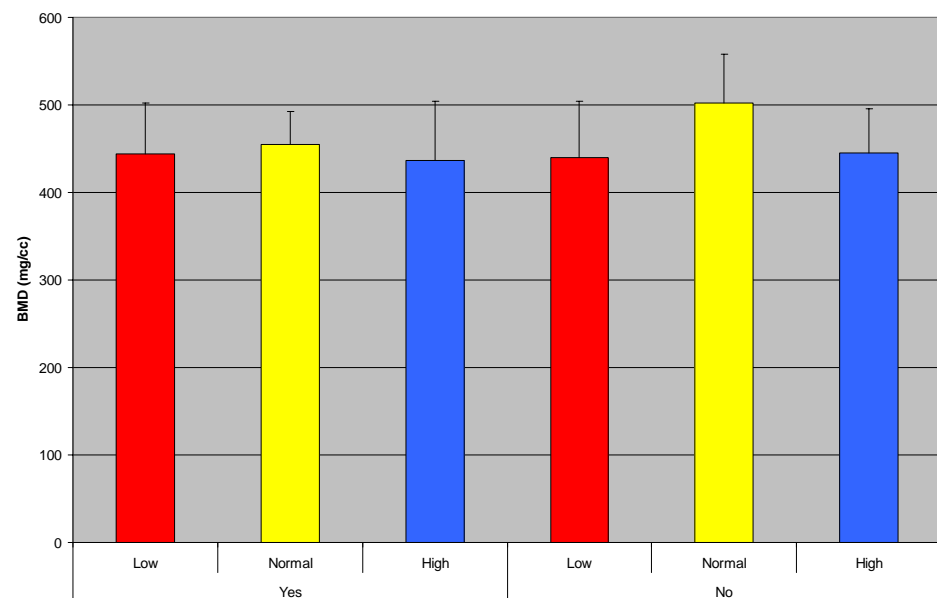
BMD by Diet and Exercise (Male C57 only)



BMD by Diet and Exercise (Female C3 Only)

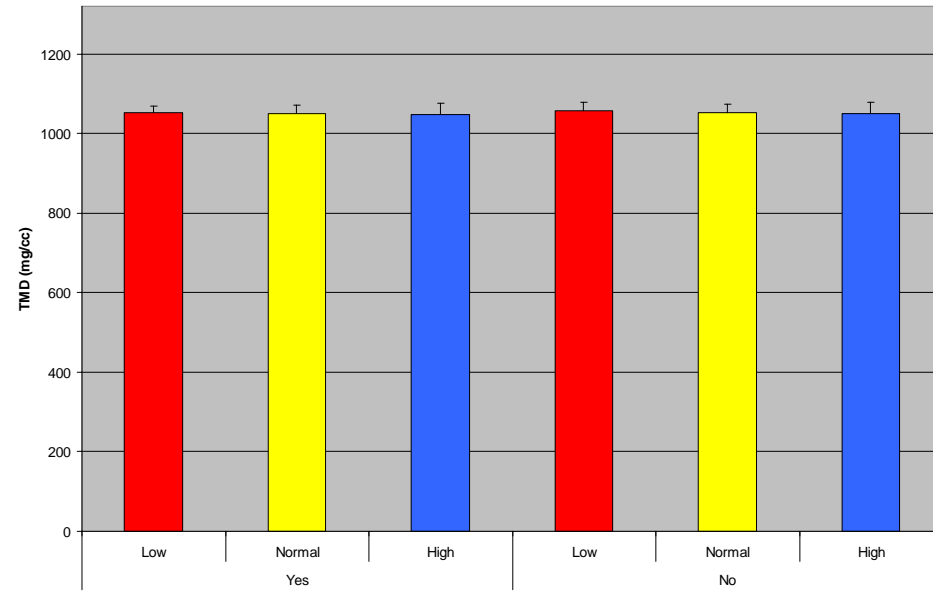


BMD by Diet and Exercise (Male C3 Only)

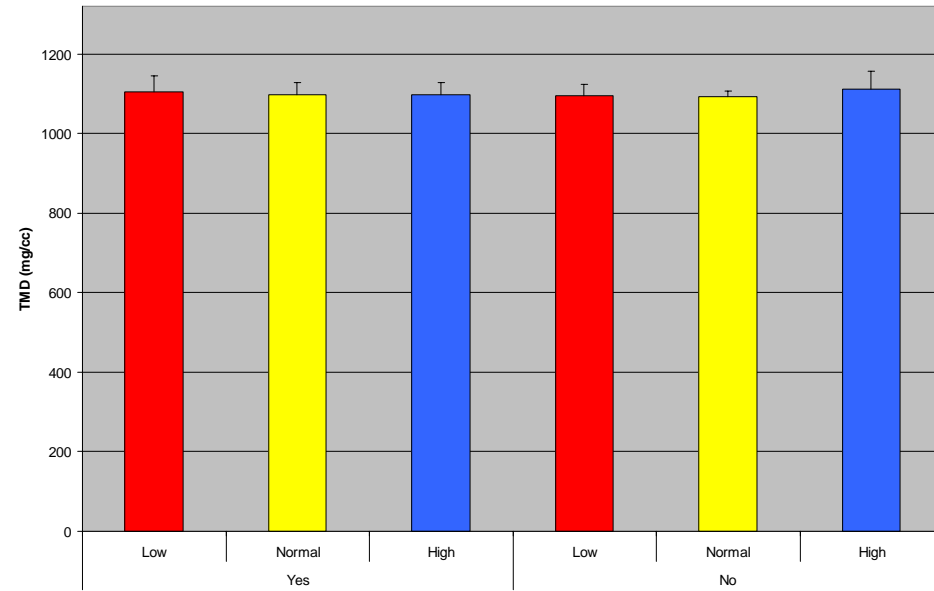


Femur Mid-diaphyseal Tissue Mineral Density by Diet and Exercise

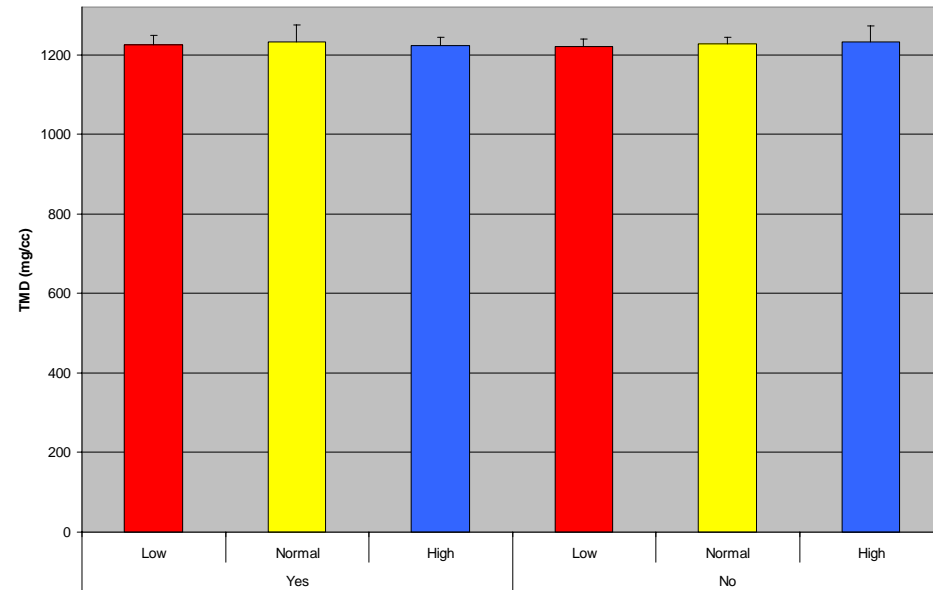
Tissue Mineral Density by Diet and Exercise (Female C57 Only)



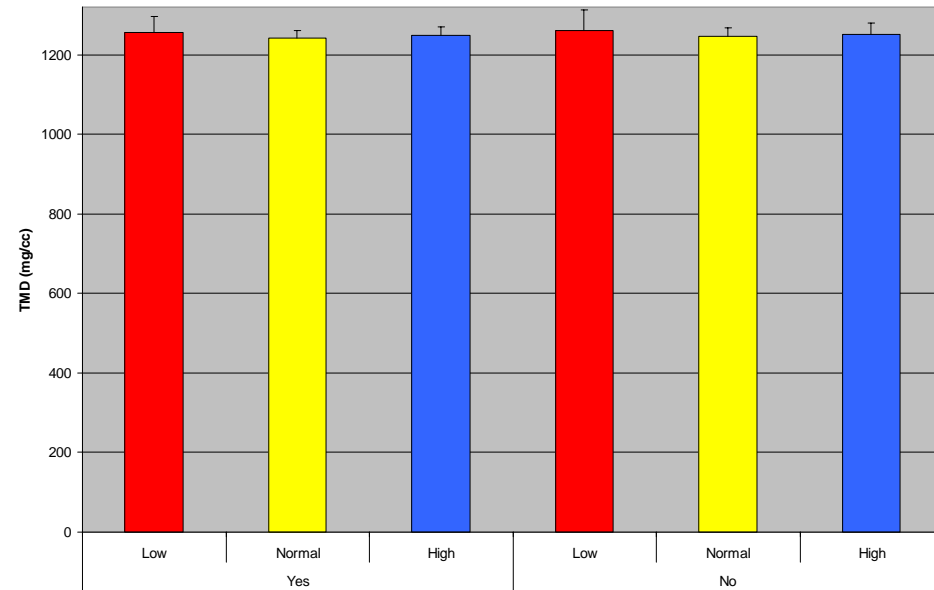
Tissue Mineral Density by Diet and Exercise (Male C57 Only)



Tissue Mineral Density by Diet and Exercise (Female C3 Only)

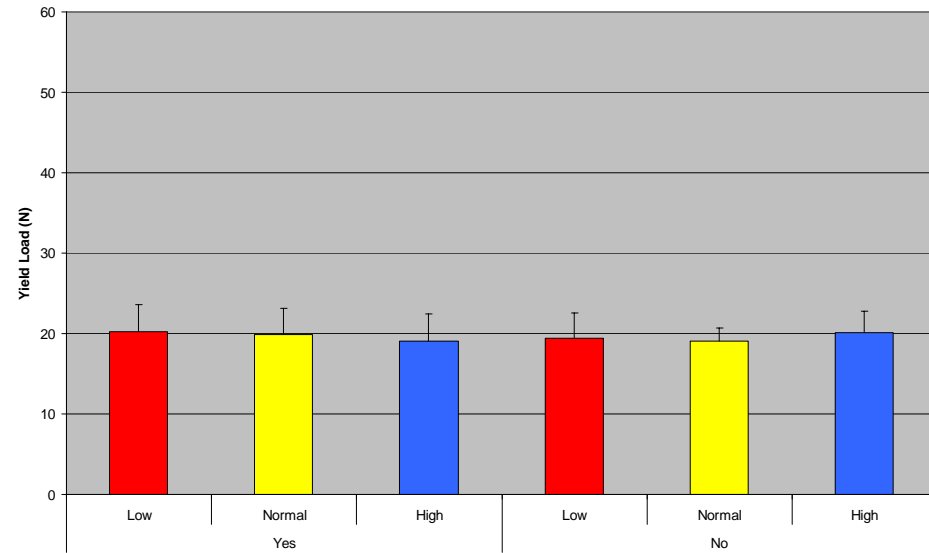


Tissue Mineral Density by Diet and Exercise (Male C3 Only)

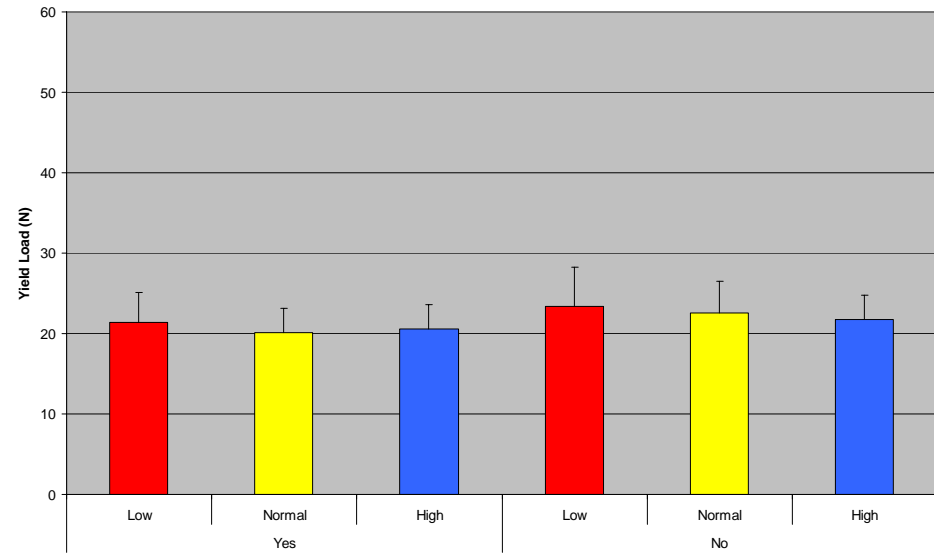


Femur Yield Load by Diet and Exercise

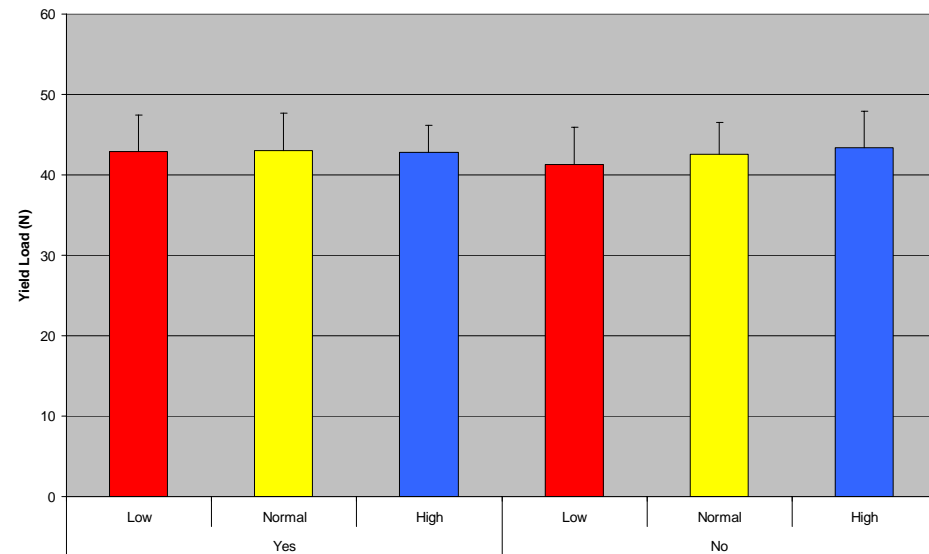
Yield Load by Exercise and Diet (Female C57 Only)



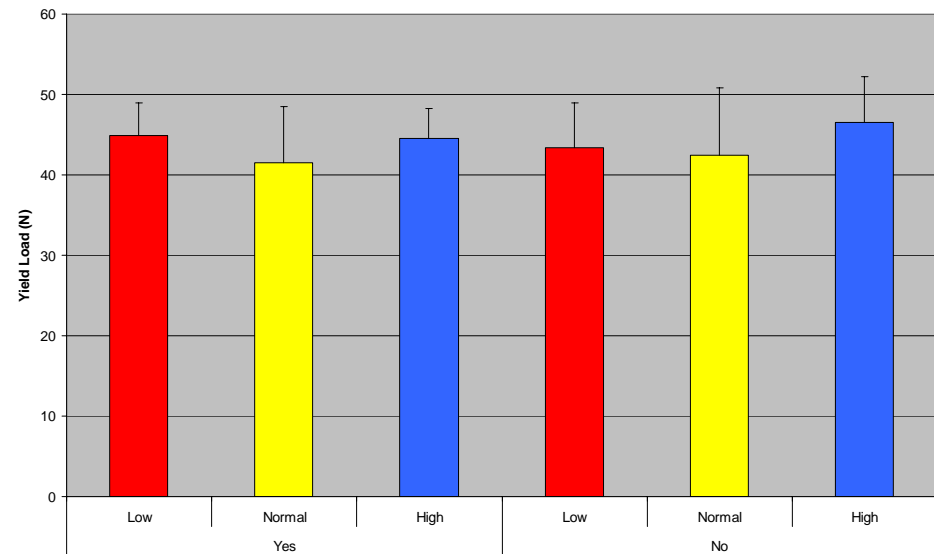
Yield Load by Exercise and Diet (Male C57 Only)



Yield Load by Exercise and Diet (Female C3 Only)

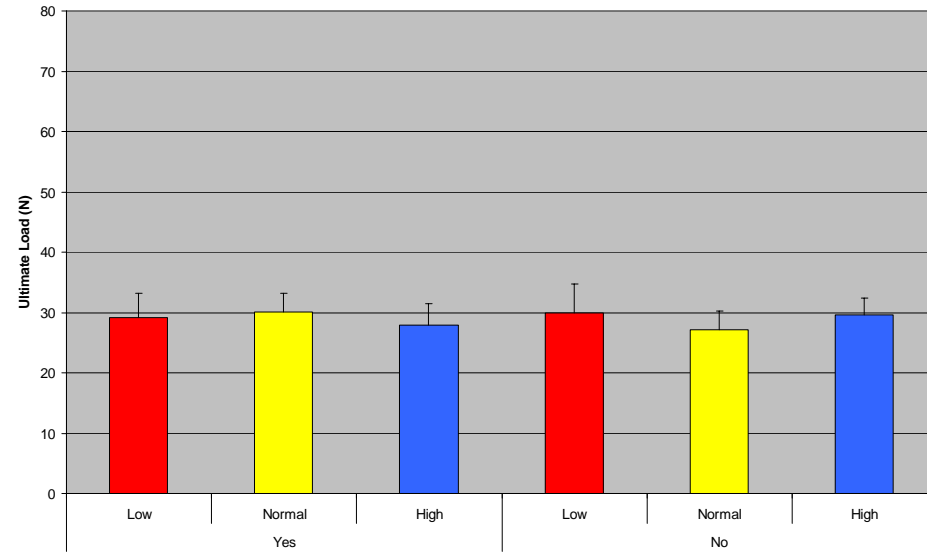


Yield Load by Exercise and Diet (Male C3 Only)

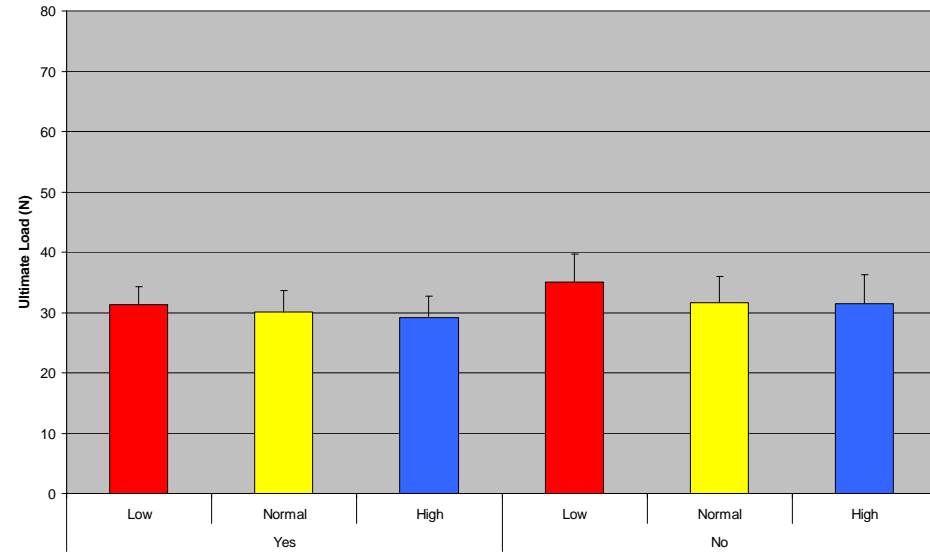


Femur Ultimate Load by Diet and Exercise

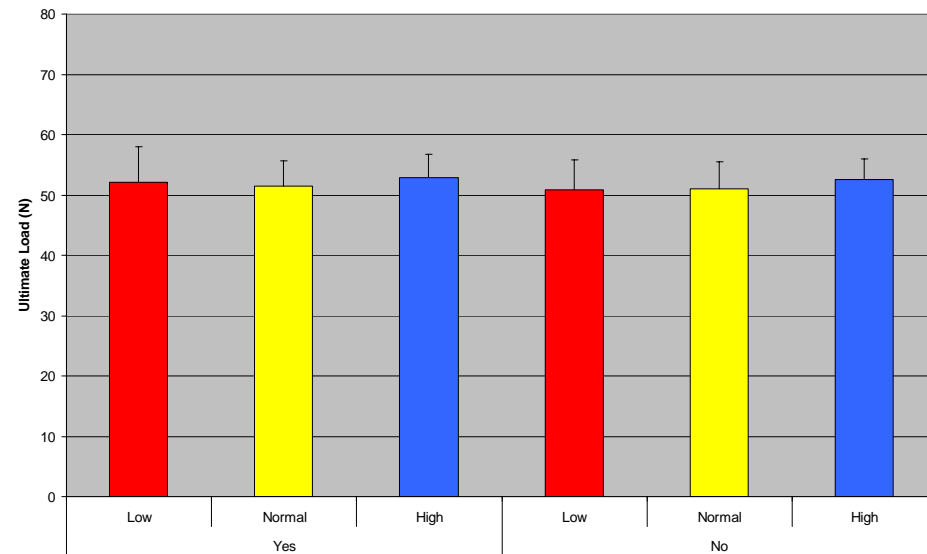
Ultimate Load by Exercise and Diet (Female C57 Only)



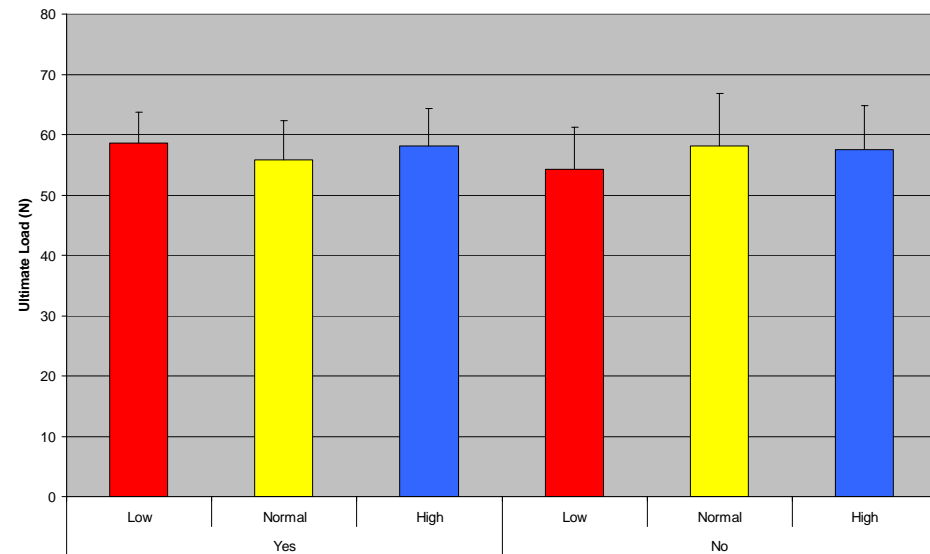
Ultimate Load by Exercise and Diet (Male C57 Only)



Ultimate Load by Exercise and Diet (Female C3 Only)

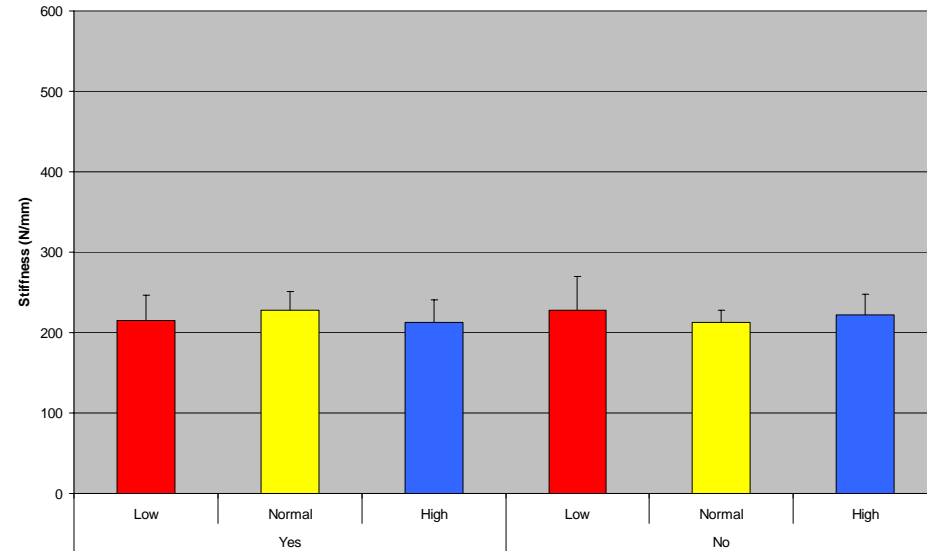


Ultimate Load by Exercise and Diet (Male C3 Only)

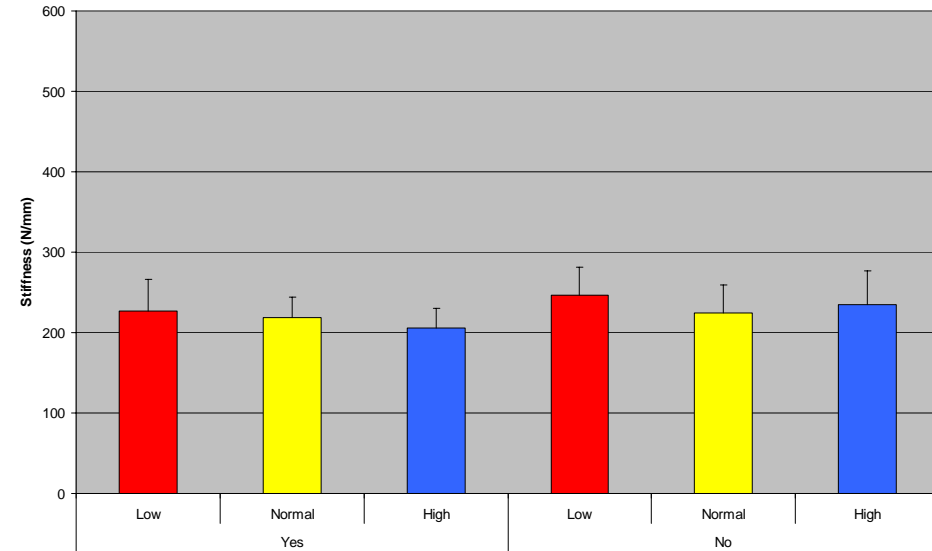


Femur Stiffness by Diet and Exercise

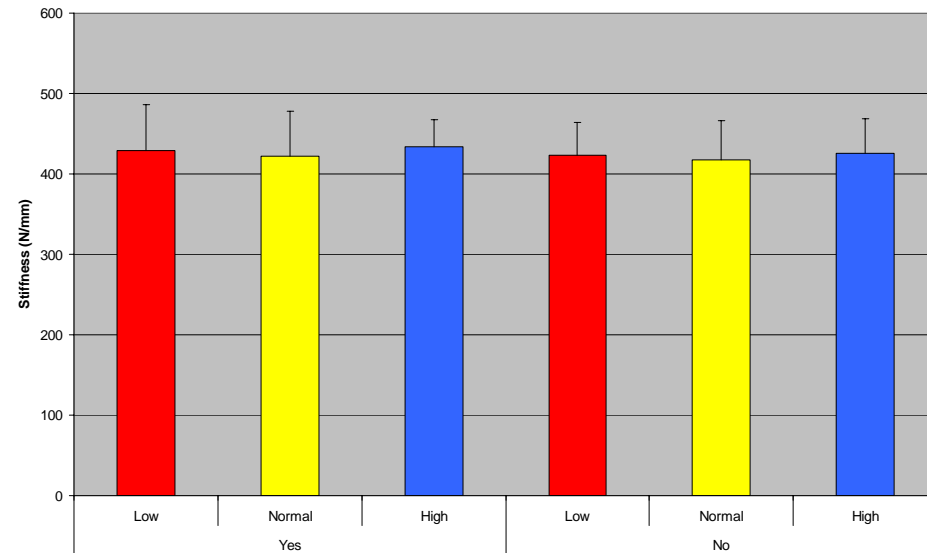
Stiffness by Exercise and Diet (Female C57 Only)



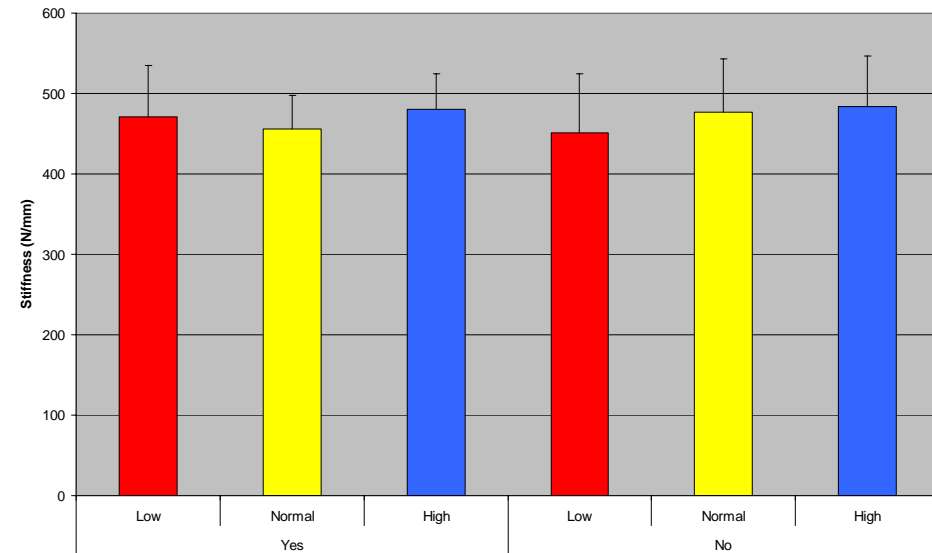
Stiffness by Exercise and Diet (Male C57 Only)



Stiffness by Exercise and Diet (Female C3 Only)

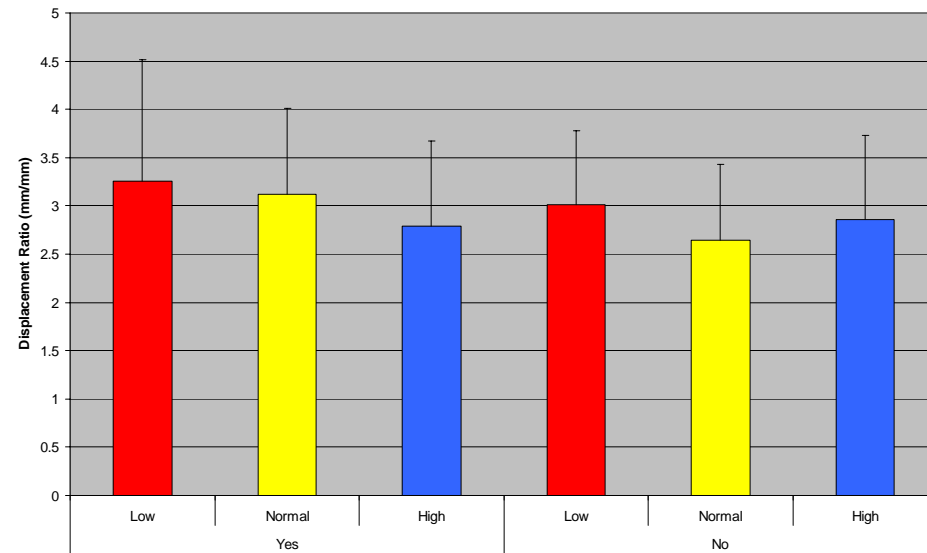


Stiffness by Exercise and Diet (Male C3 Only)

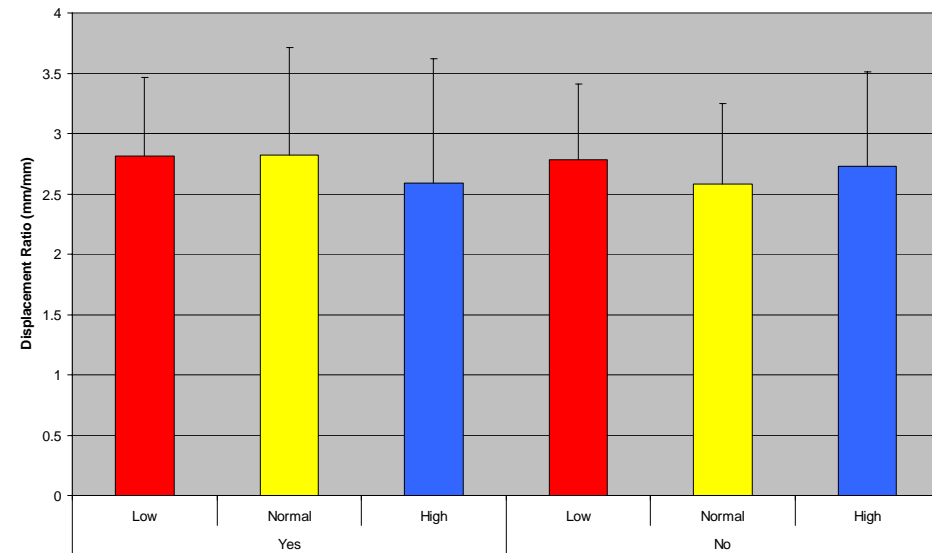


Femur Displacement Ratio by Diet and Exercise

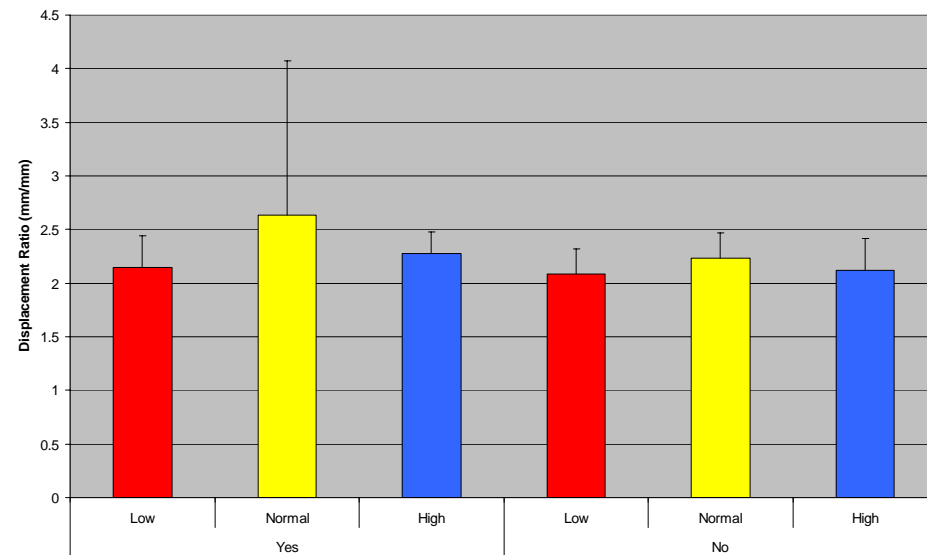
Displacement Ratio by Exercise and Diet (Female C57 Only)



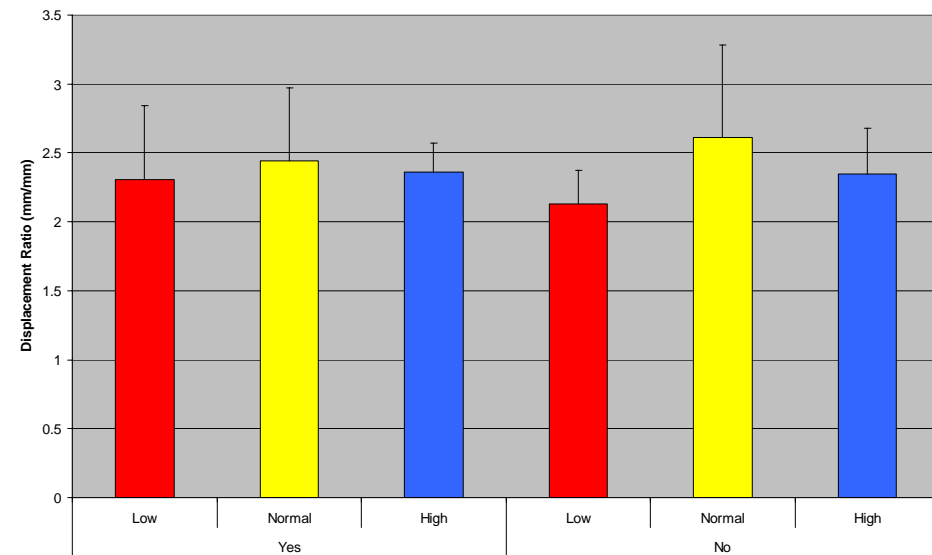
Displacement Ratio by Exercise and Diet (Male C57 Only)



Displacement Ratio by Exercise and Diet (Female C3 Only)

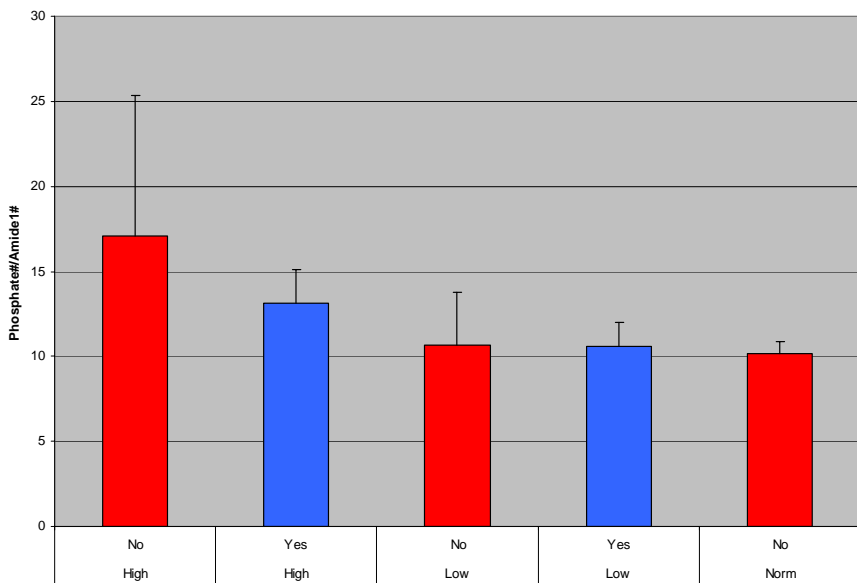


Displacement Ratio by Exercise and Diet (Male C3 Only)

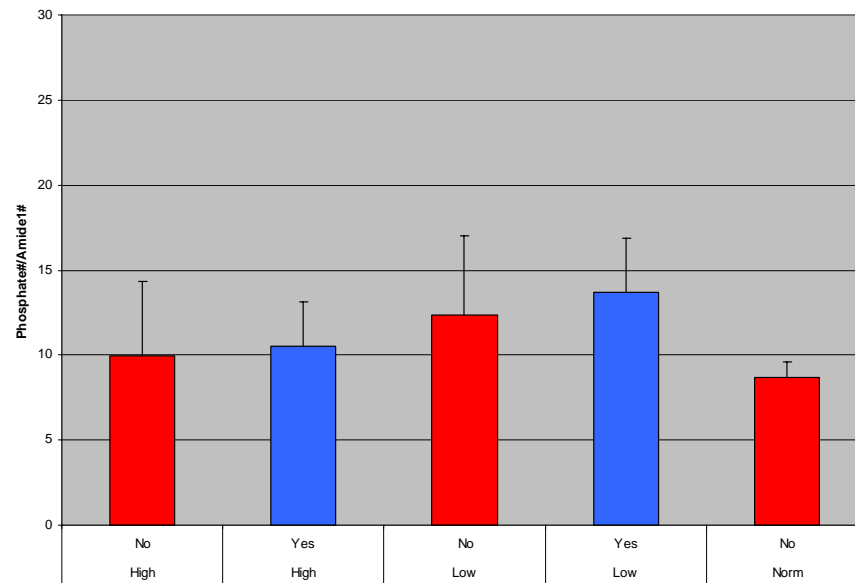


Femur Phosphate/Amide 1 Peak by Diet and Exercise

Mineral to Matrix Ratio by Exercise and Diet (Female C57 Only)

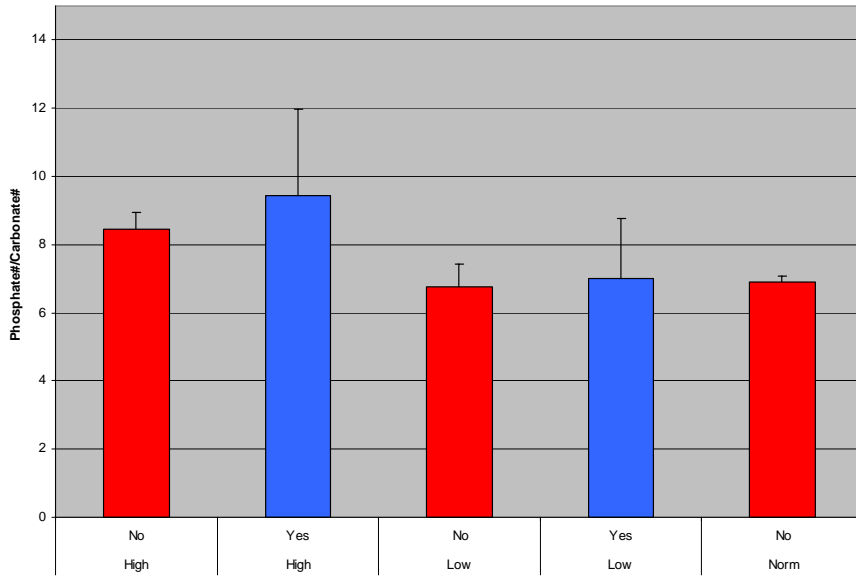


Mineral to Matrix Ratio by Exercise and Diet (Female C3 Only)

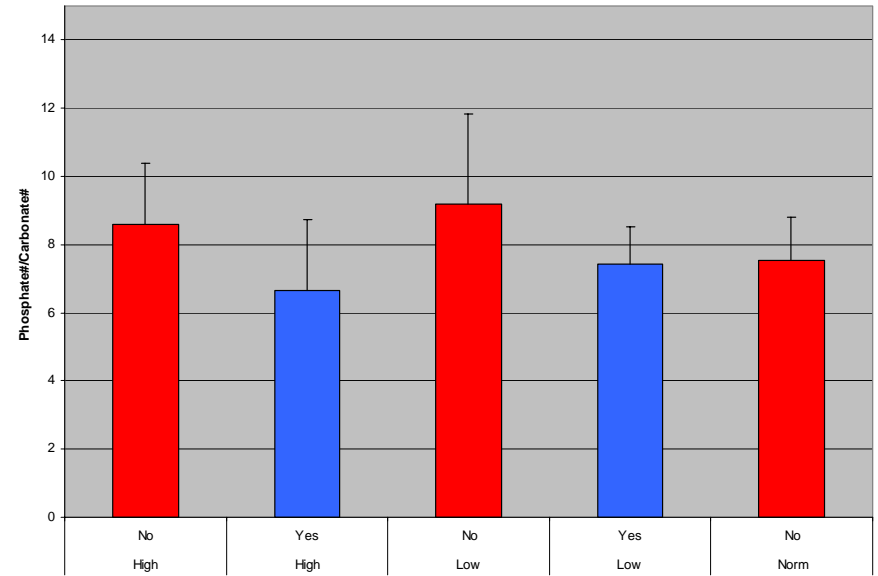


Femur Phosphate/Carbonate Peak by Diet and Exercise

Phosphate to Carbonate Peak by Exercise and Diet (Female C57 Only)

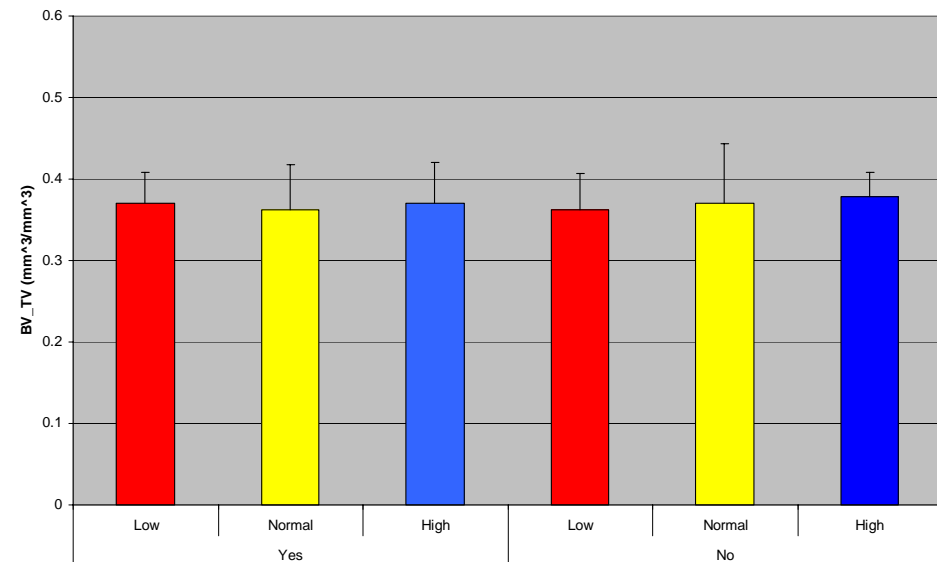


Phosphate to Carbonate Peak by Exercise and Diet (Female C3 Only)

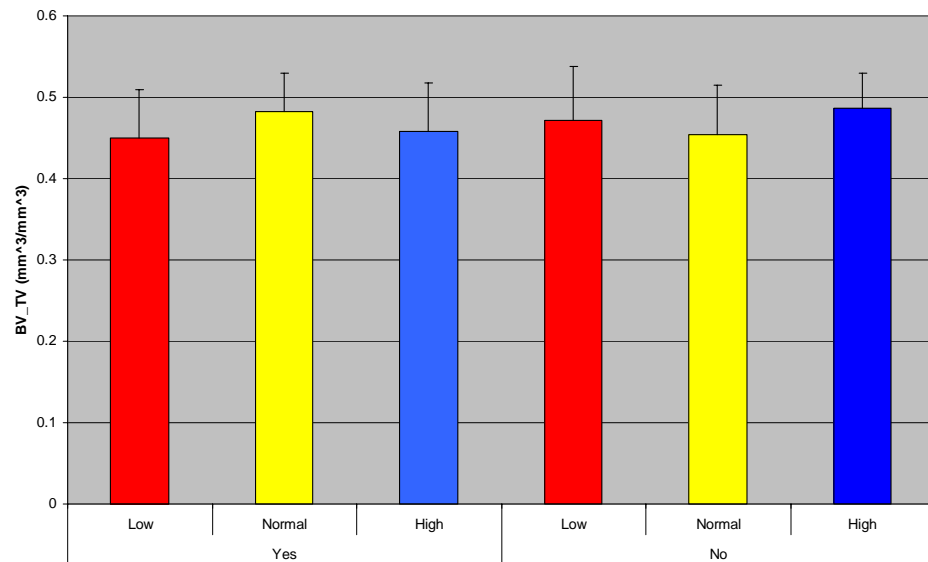


Proximal Vertebral Bone Volume Fraction by Diet and Exercise

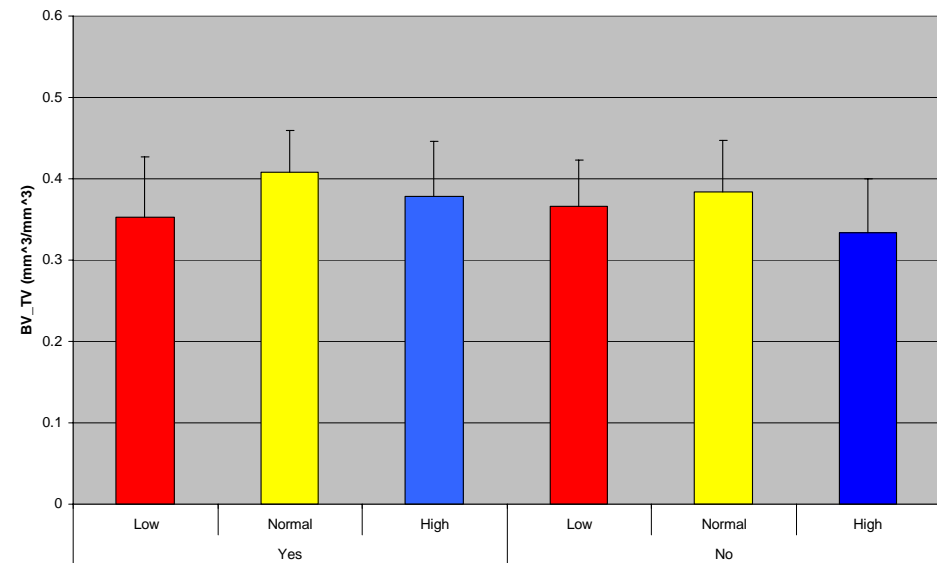
Bone Volume Fraction by Diet and Exercise (Female C57 Only)



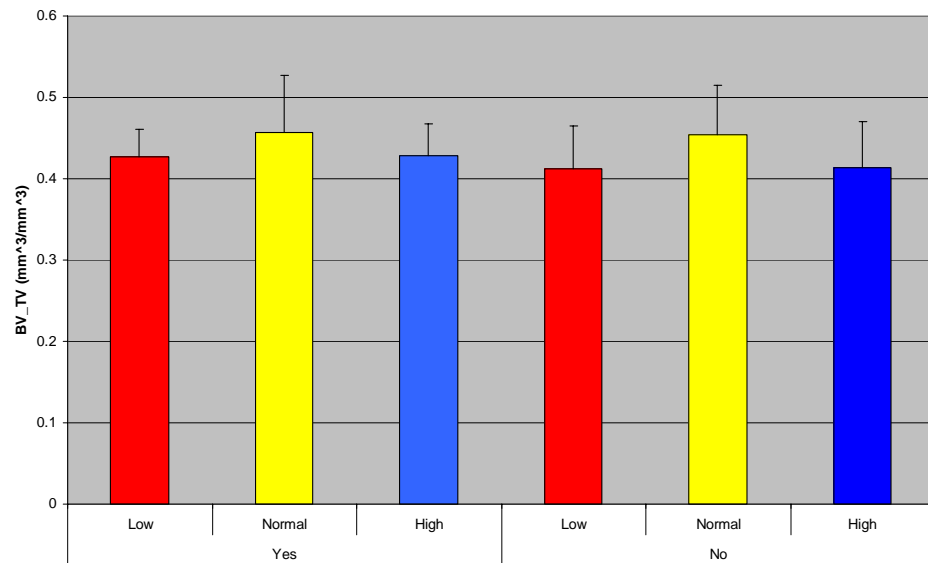
Bone Volume Fraction by Diet and Exercise (Male C57 Only)



Bone Volume Fraction by Diet and Exercise (Female C3 Only)

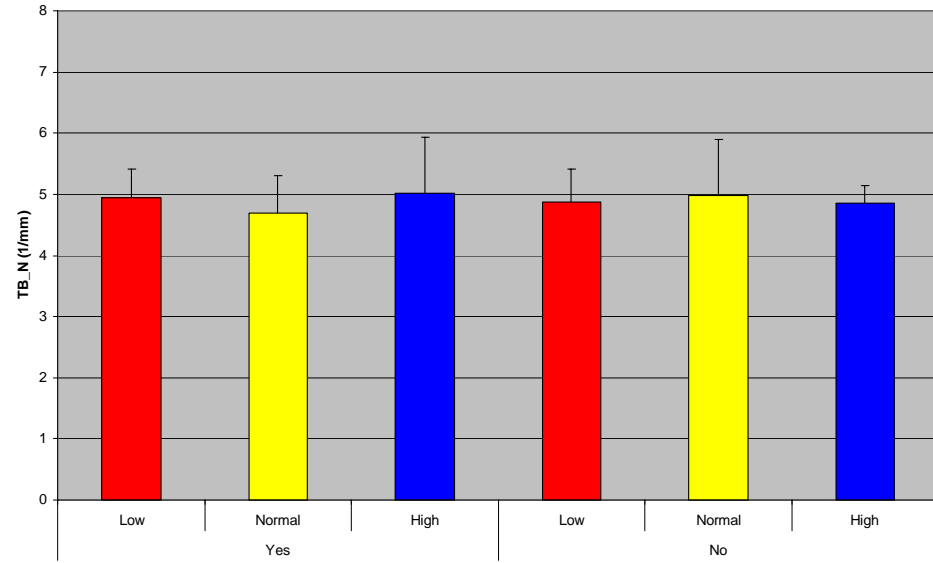


Bone Volume Fraction by Diet and Exercise (Male C3 Only)

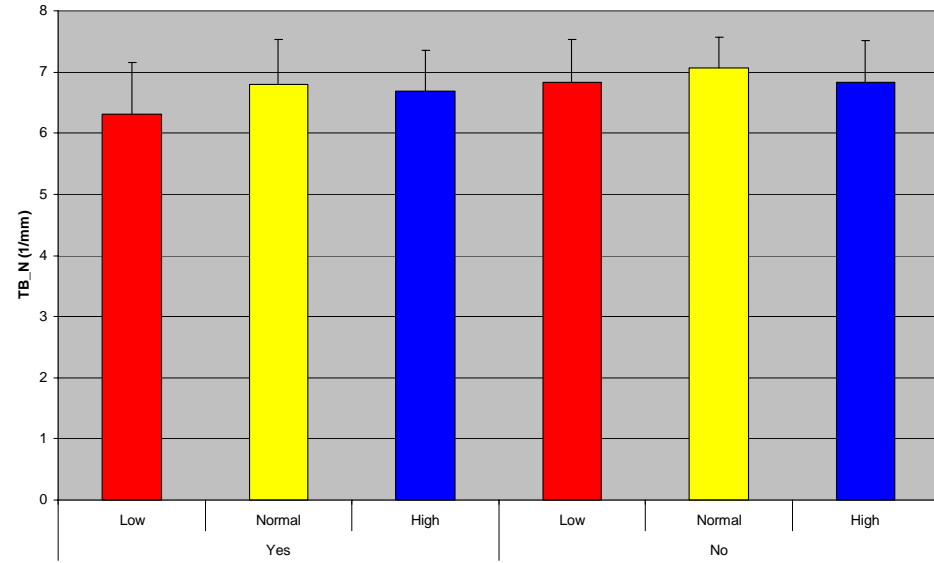


Proximal Vertebral Trabecular Number by Diet and Exercise

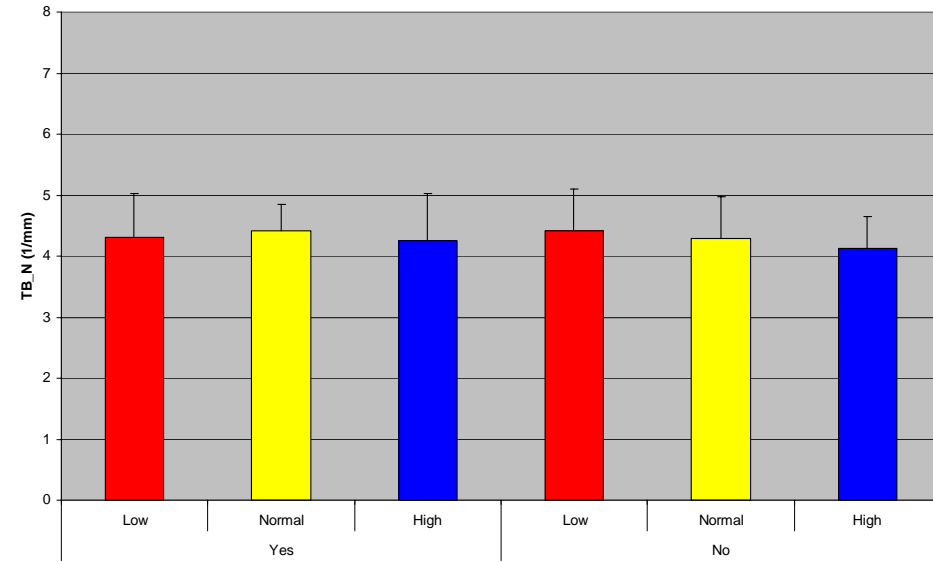
Trabecular Number by Diet and Exercise (Female C57 Only)



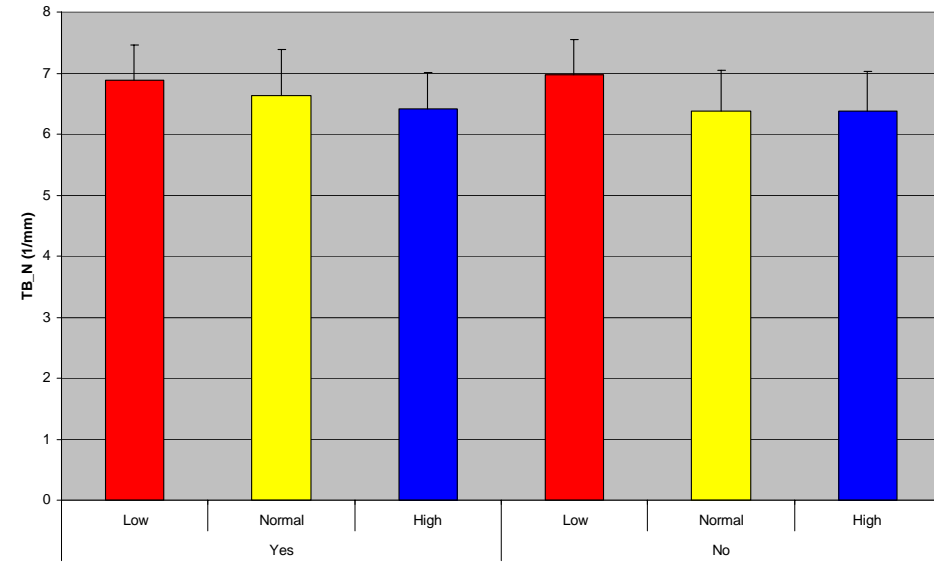
Trabecular Number by Diet and Exercise (Male C57 Only)



Trabecular Number by Diet and Exercise (Female C3 Only)

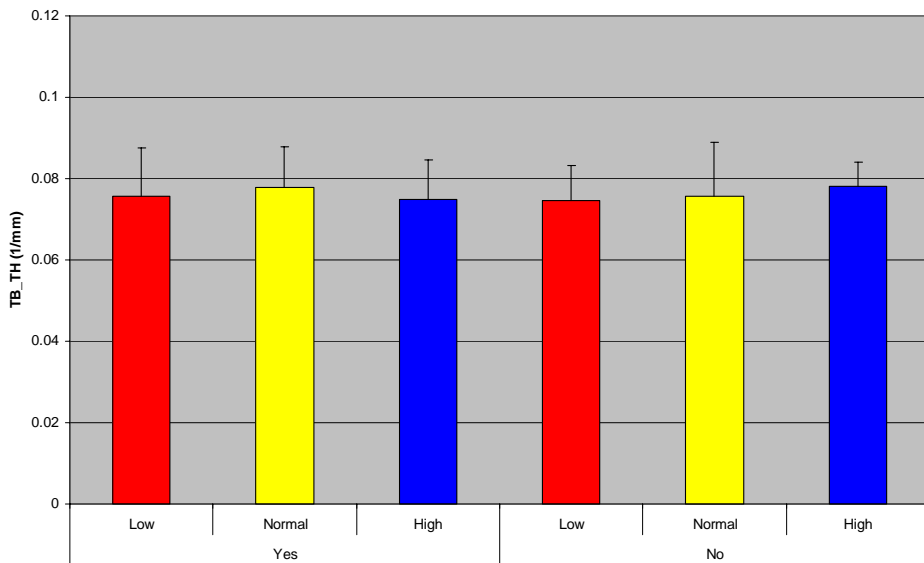


Trabecular Number by Diet and Exercise (Male C3 Only)

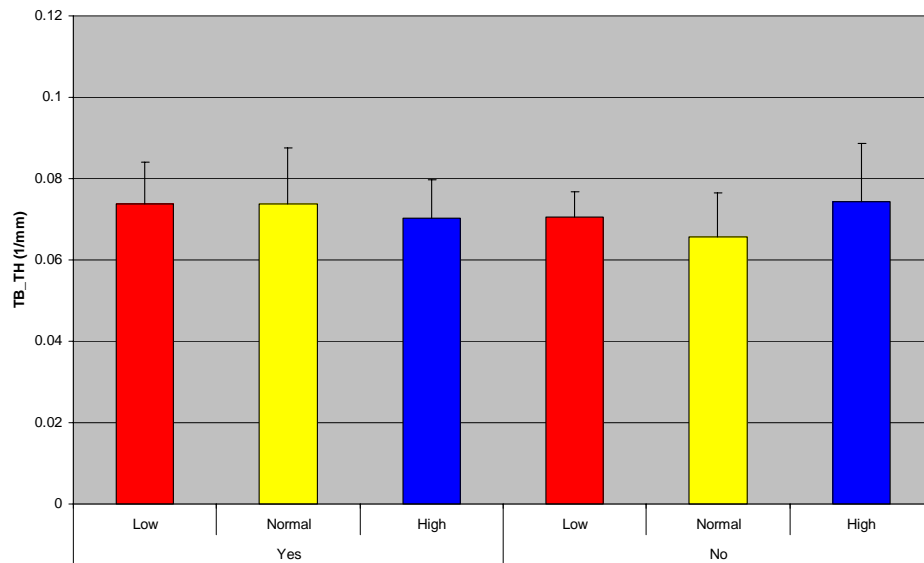


Proximal Vertebral Trabecular Thickness by Diet and Exercise

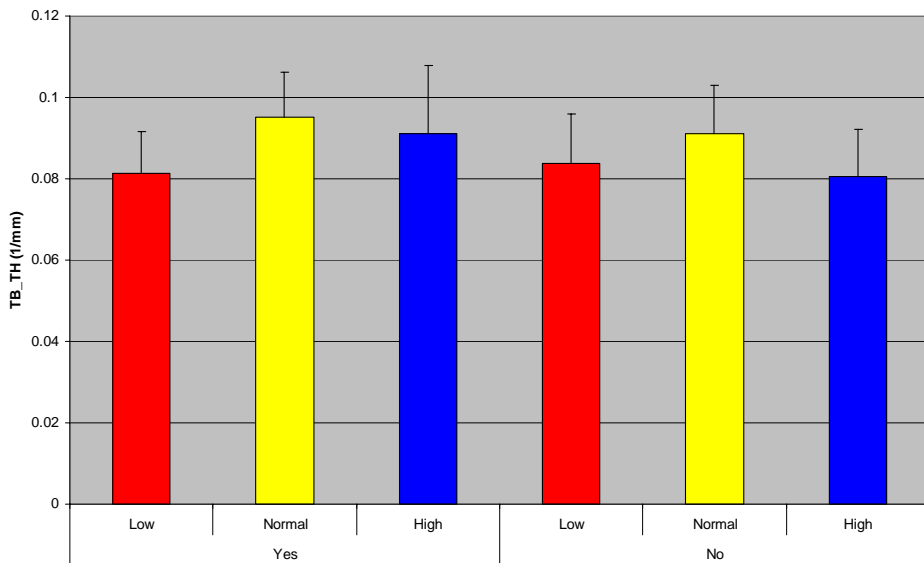
Trabecular Thickness by Diet and Exercise (Female C57 Only)



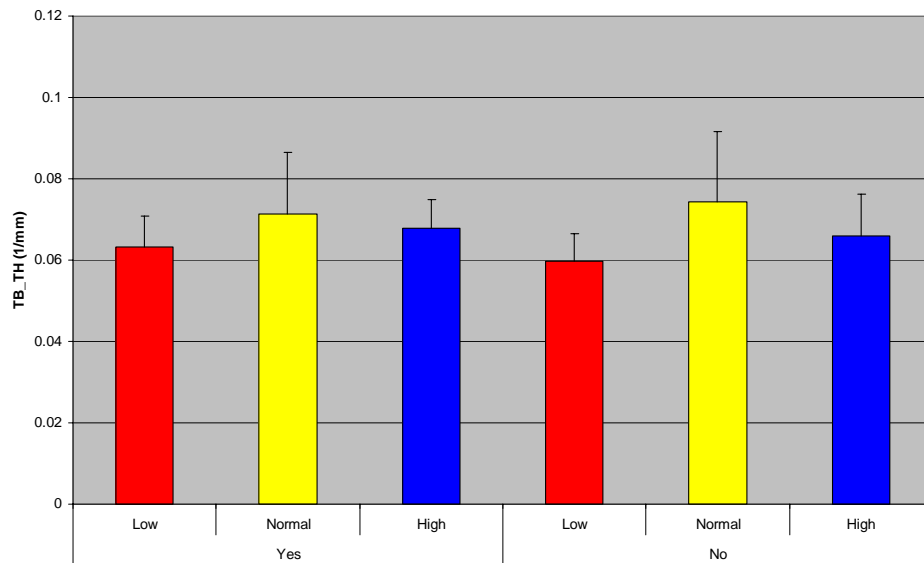
Trabecular Thickness by Diet and Exercise (Male C57 Only)



Trabecular Thickness by Diet and Exercise (Female C3 Only)

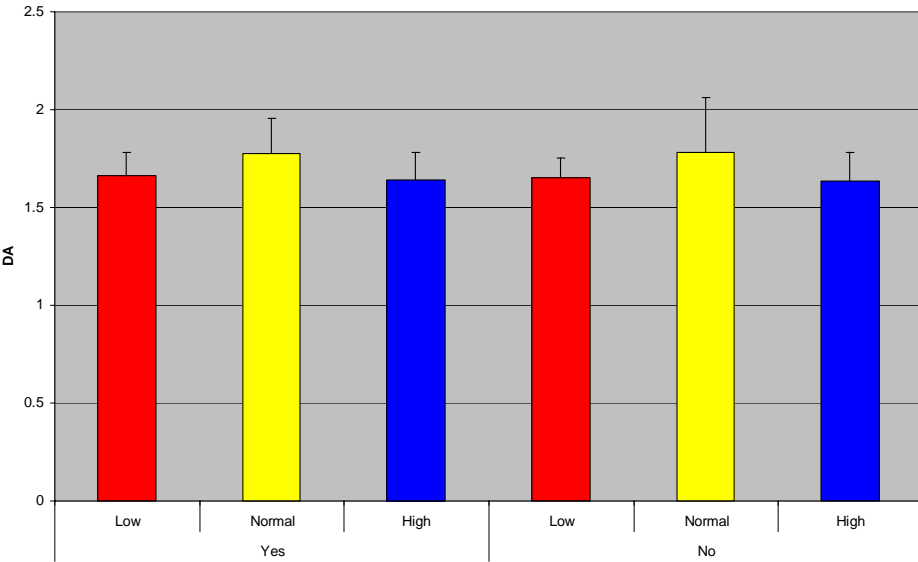


Trabecular Thickness by Diet and Exercise (Male C3 Only)

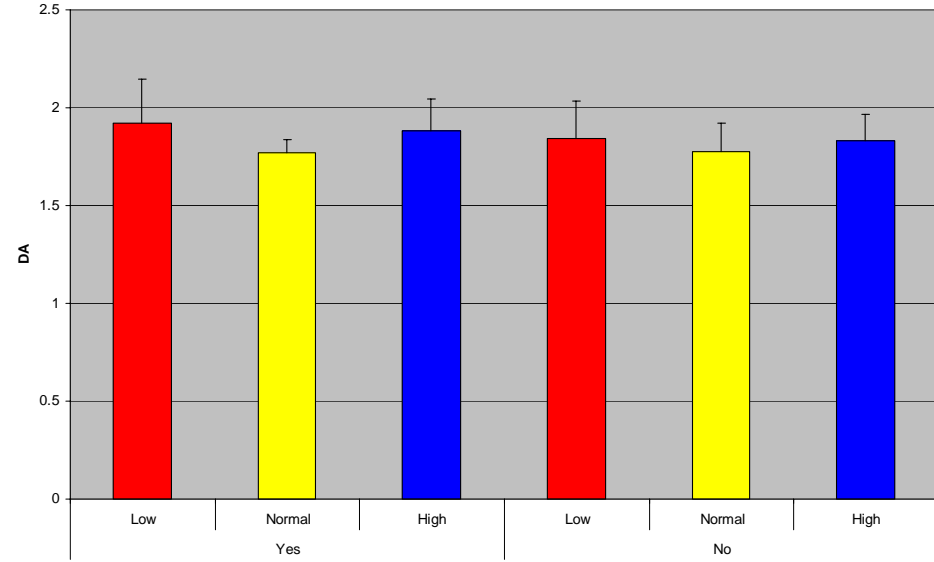


Proximal Vertebral Degree of Anisotropy by Diet and Exercise

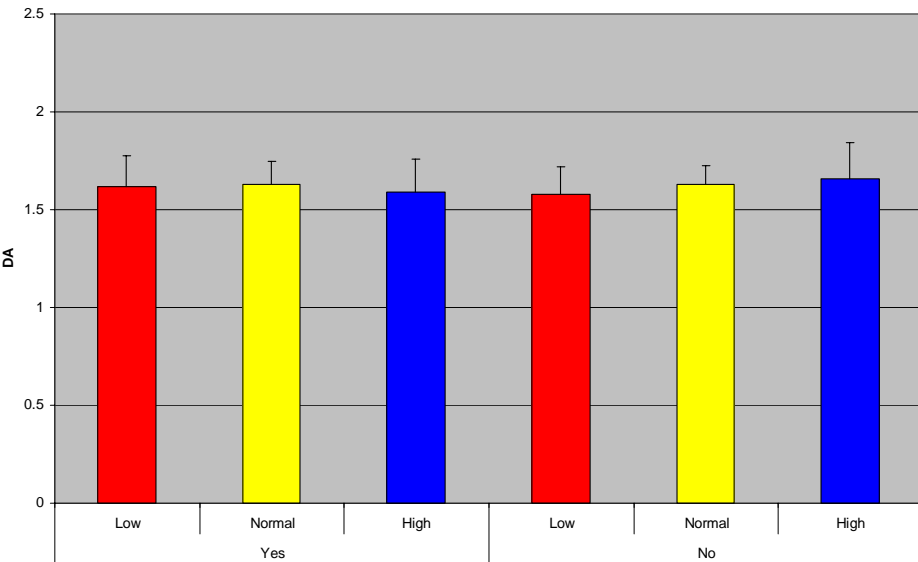
Degree of Anisotropy by Diet and Exercise (Female C57 Only)



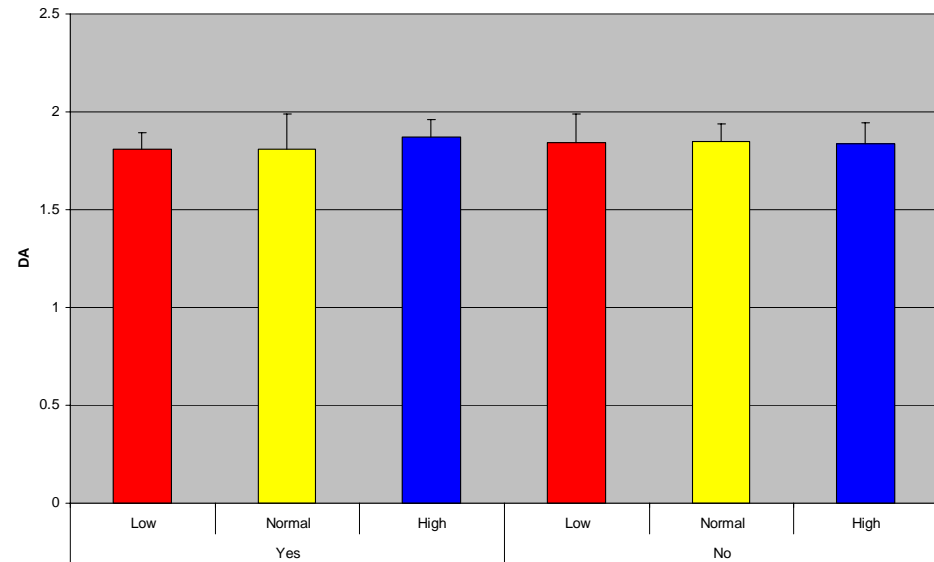
Degree of Anisotropy by Diet and Exercise (Male C57 Only)



Degree of Anisotropy by Diet and Exercise (Female C3 Only)

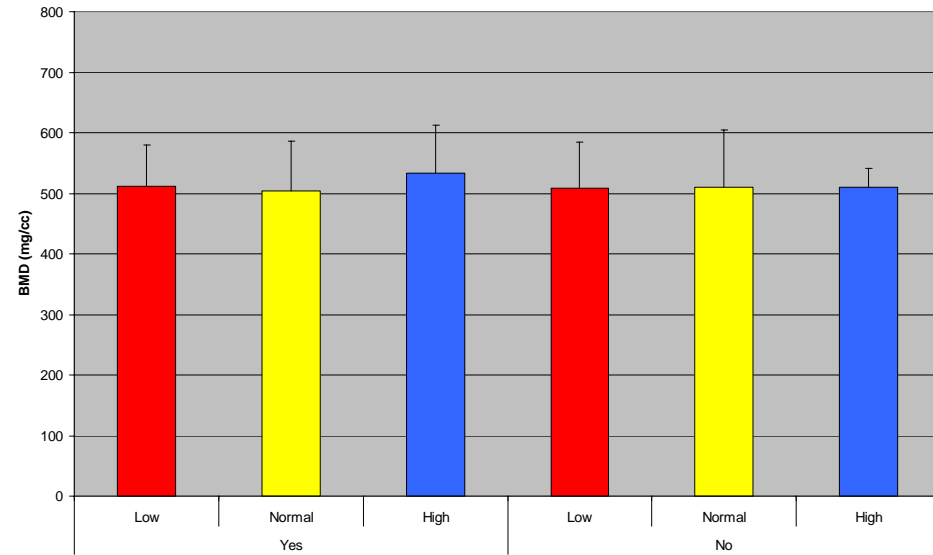


Degree of Anisotropy by Diet and Exercise (Male C3 Only)

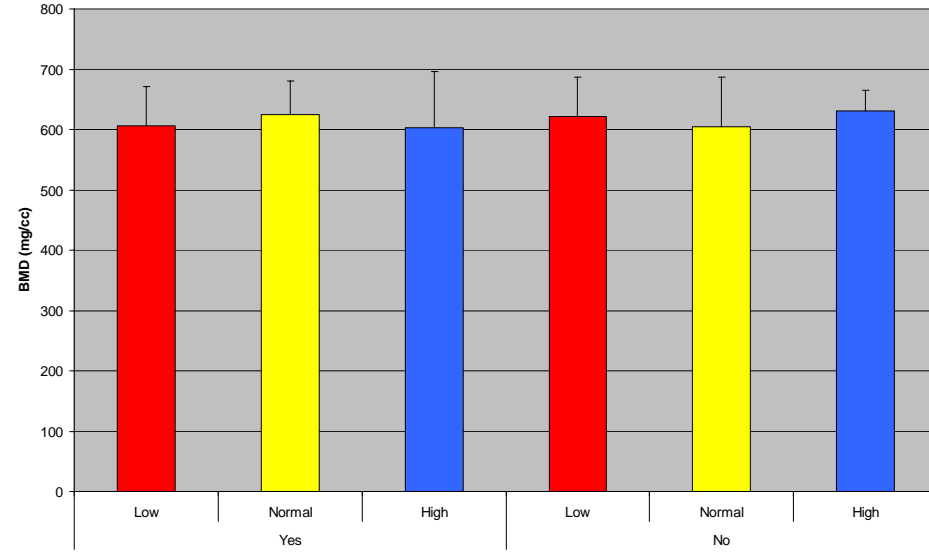


Proximal Vertebral Bone Mineral Density by Diet and Exercise

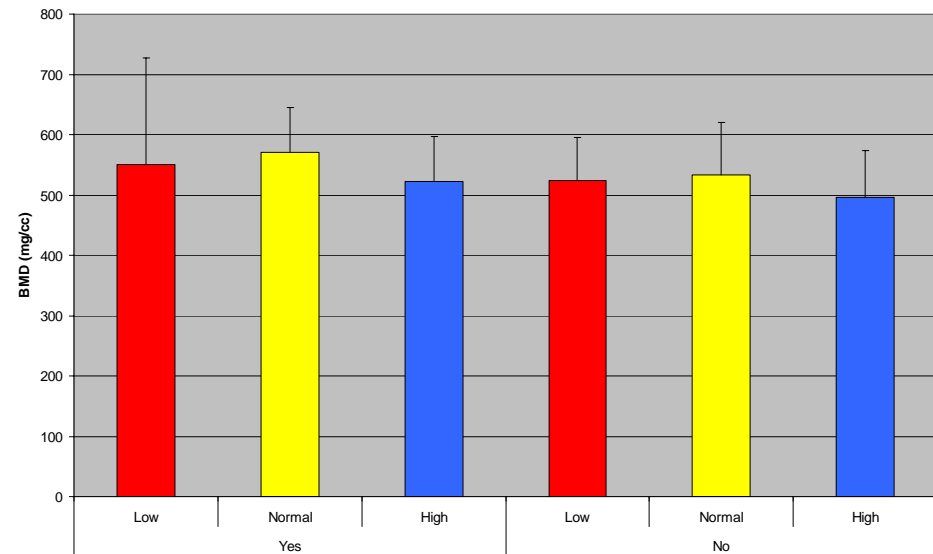
Bone Mineral Density by Diet and Exercise (Female C57 Only)



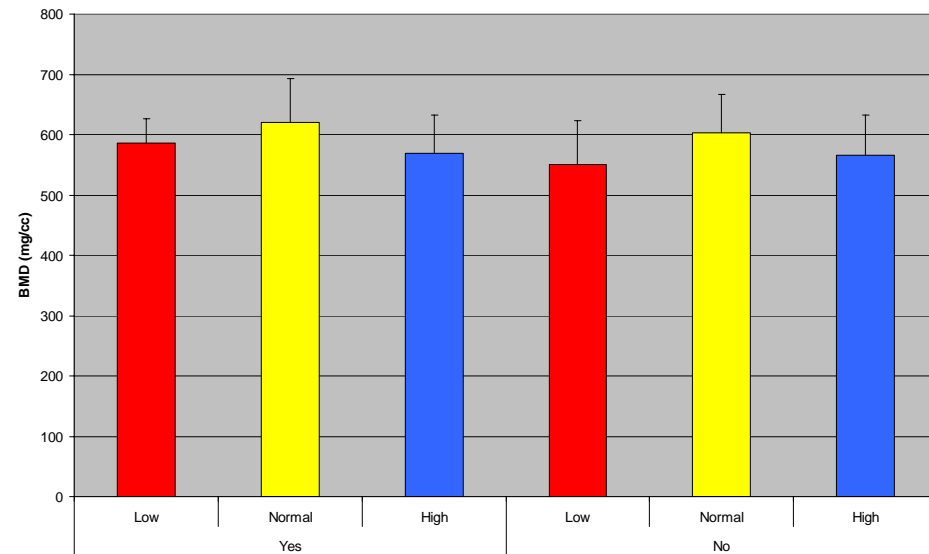
Bone Mineral Density by Diet and Exercise (Male C57 Only)



Bone Mineral Density by Diet and Exercise (Female C3 Only)

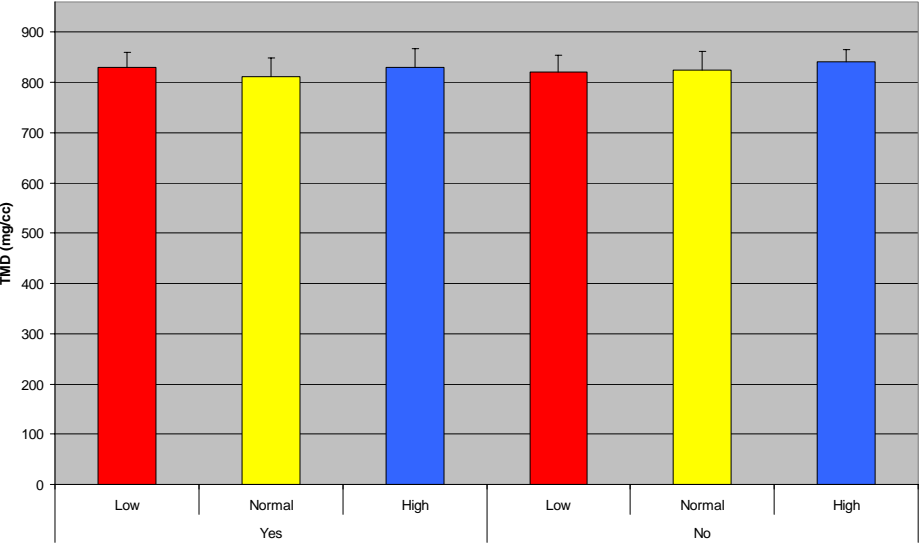


Bone Mineral Density by Diet and Exercise (Male C3 Only)

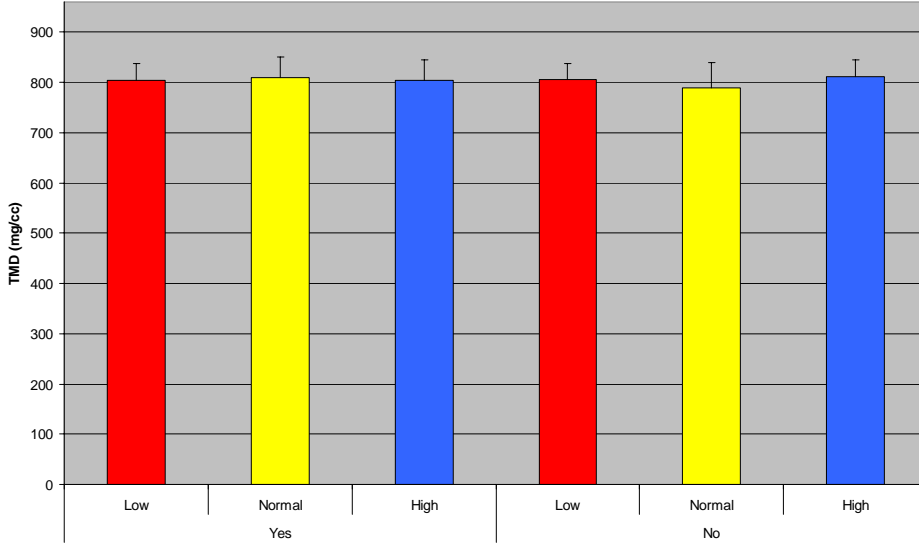


Proximal Vertebral Tissue Mineral Density by Diet and Exercise

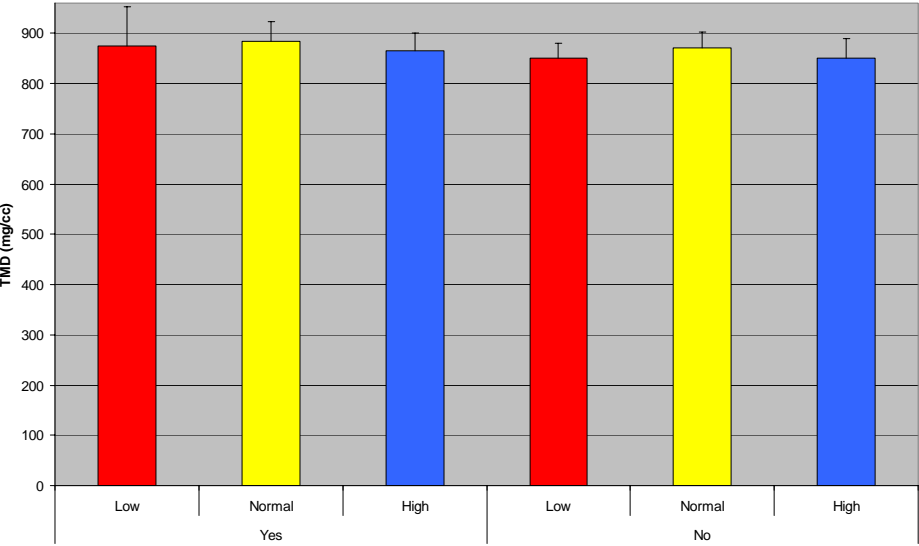
Tissue Mineral Density by Diet and Exercise (Female C57 Only)



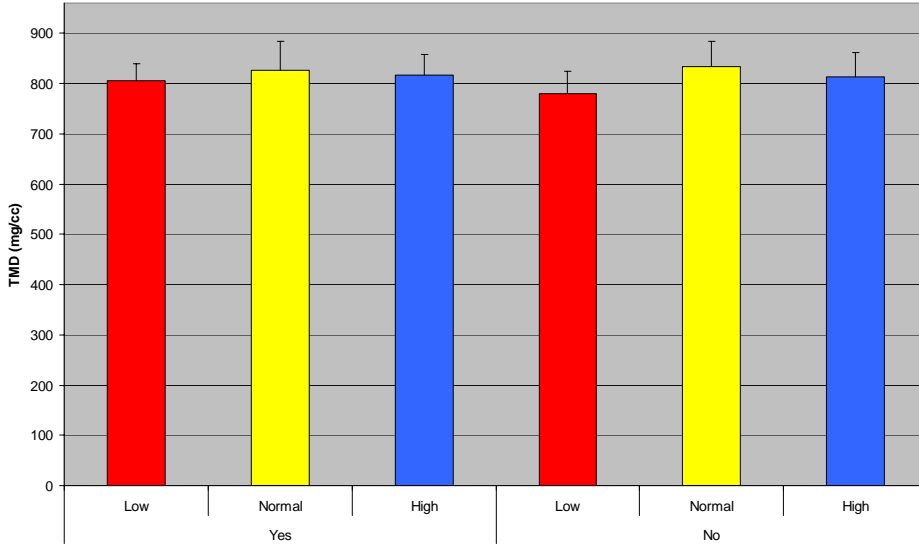
Tissue Mineral Density by Diet and Exercise (Male C57 Only)



Tissue Mineral Density by Diet and Exercise (Female C3 Only)

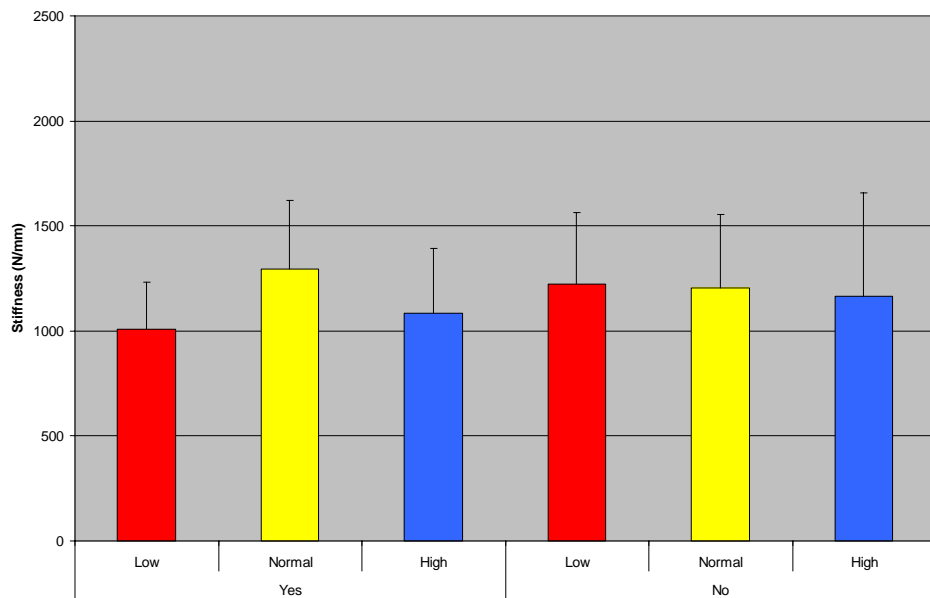


Tissue Mineral Density by Diet and Exercise (Male C3 Only)

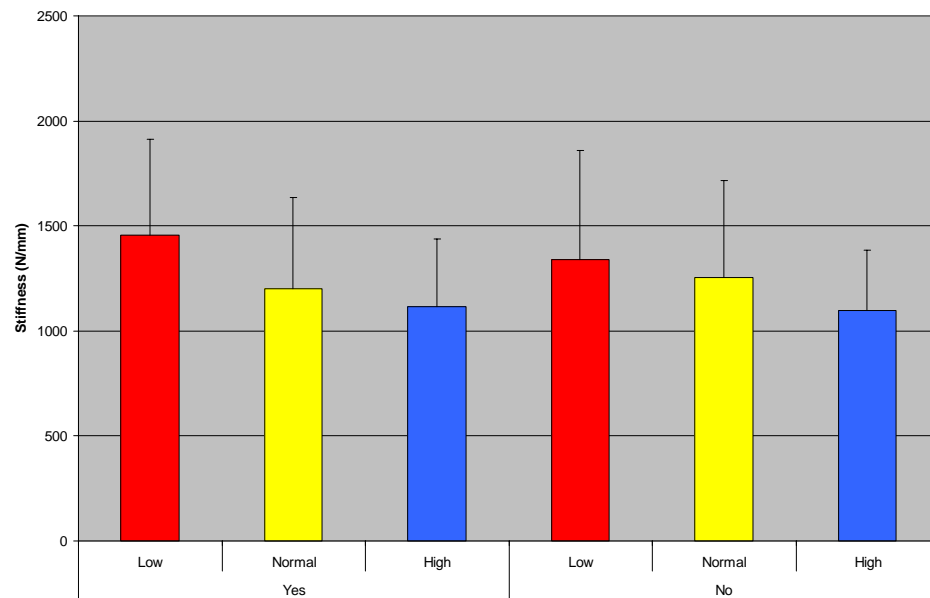


Vertebral Stiffness by Diet and Exercise

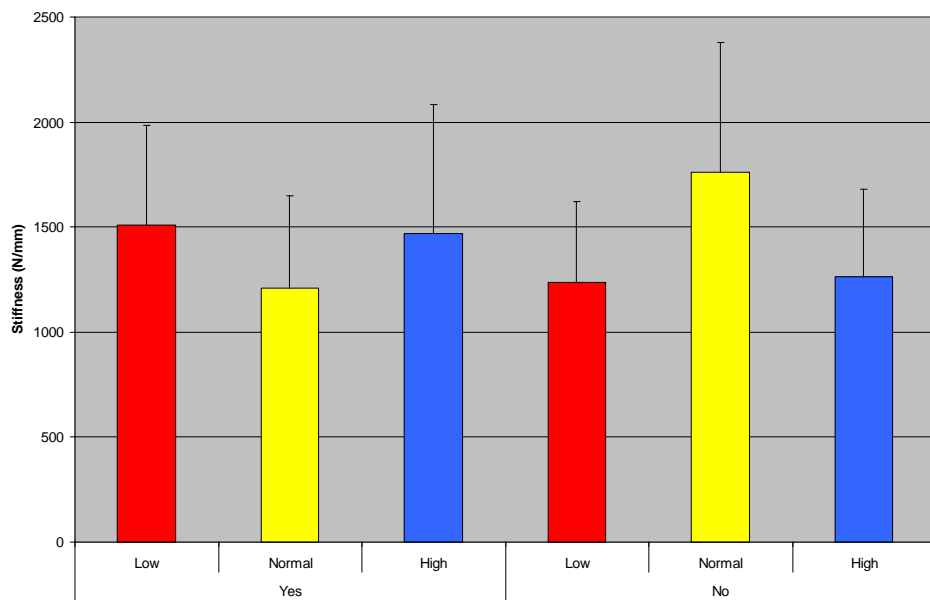
Stiffness by Exercise and Diet (Female C57 Only)



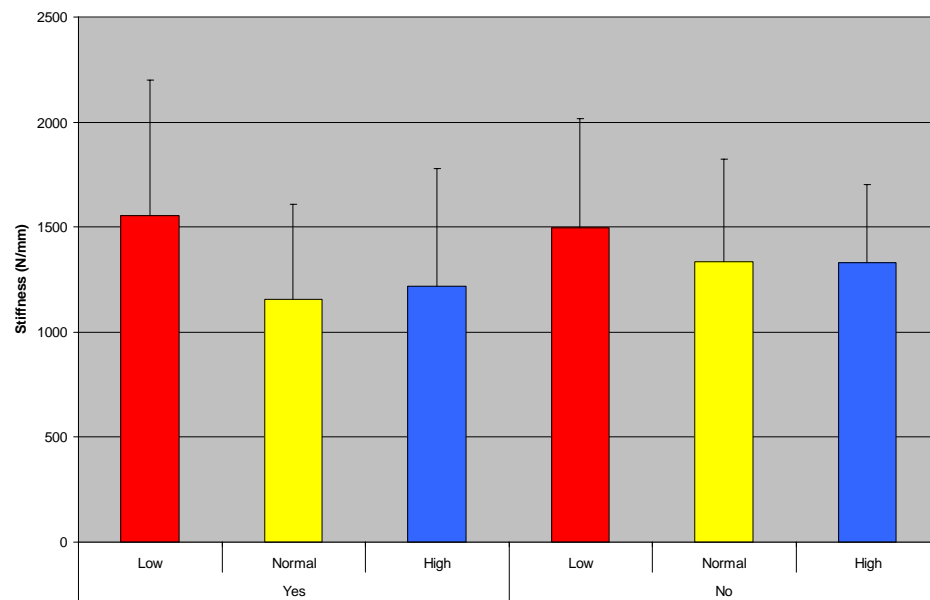
Stiffness by Exercise and Diet (Male C57 Only)



Stiffness by Exercise and Diet (Female C3 Only)

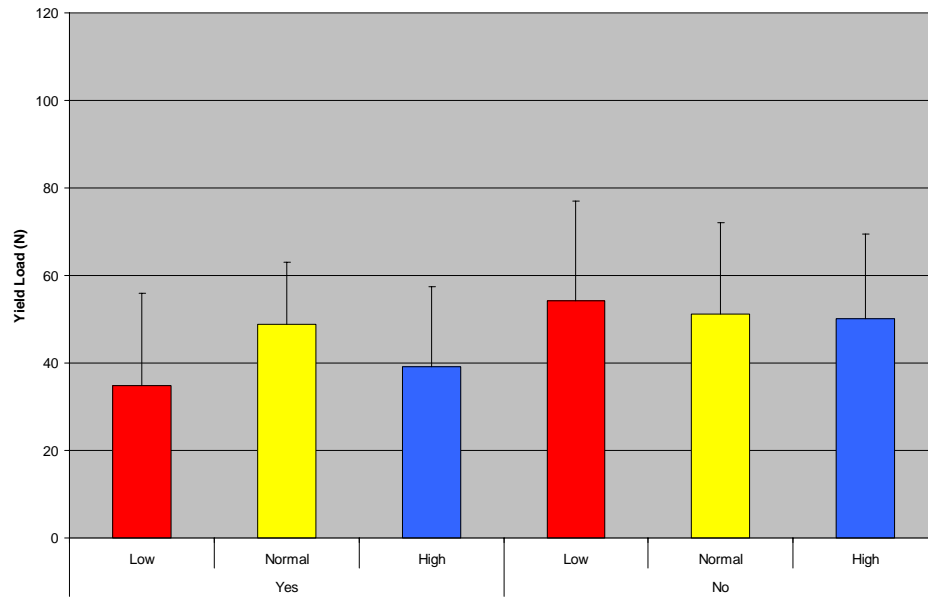


Stiffness by Exercise and Diet (Male C3 Only)

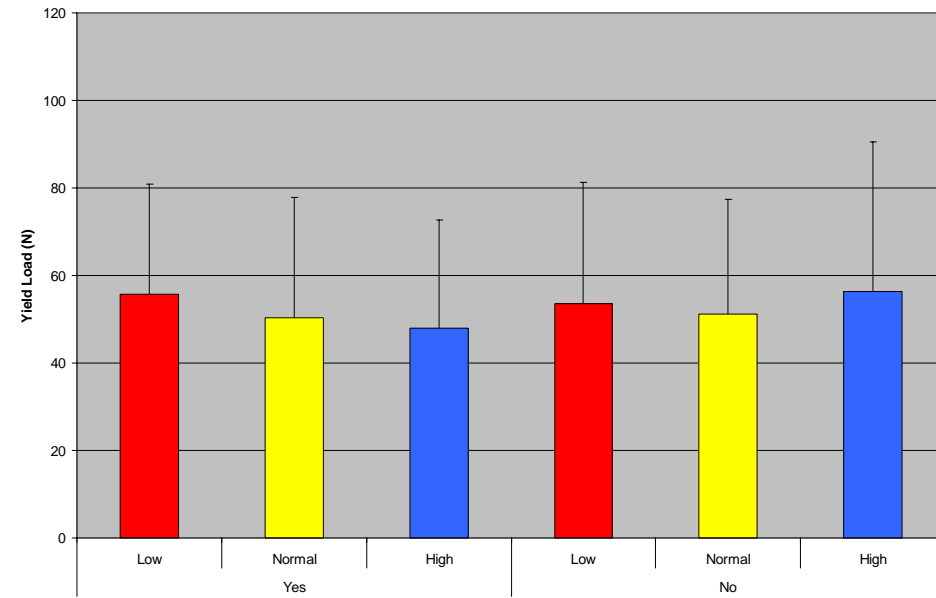


Vertebral Yield Load by Diet and Exercise

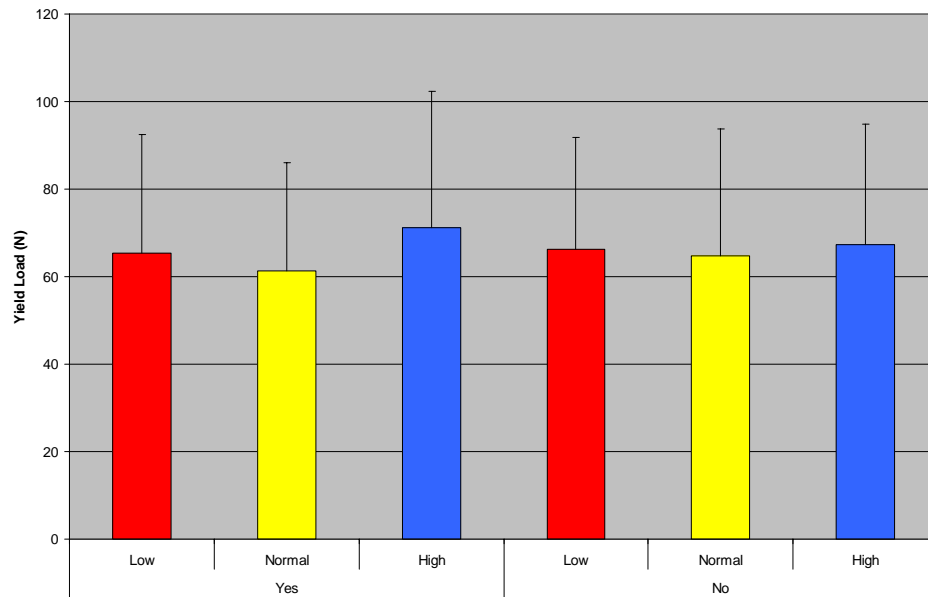
Yield Load by Exercise and Diet (Female C57 Only)



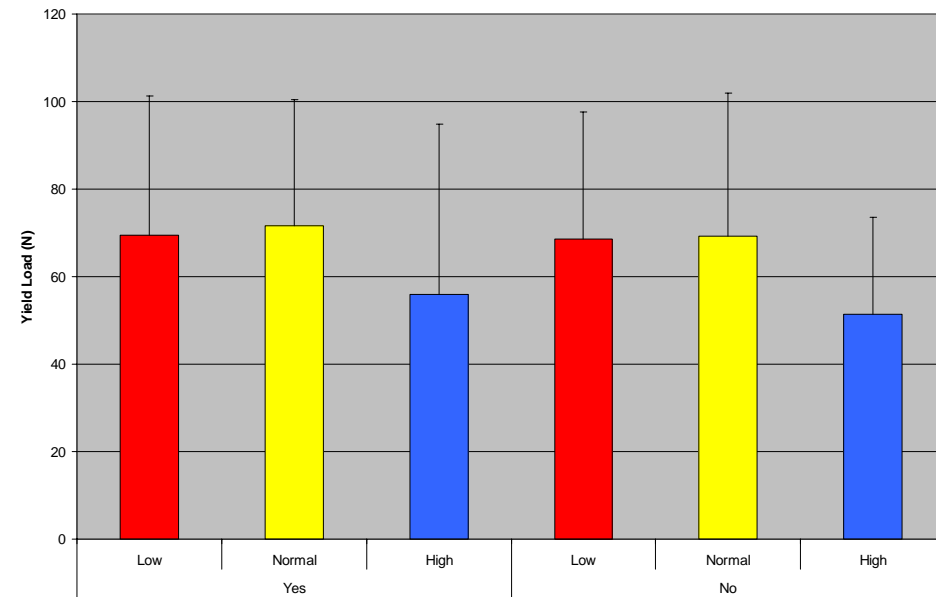
Yield Load by Exercise and Diet (Male C57 Only)



Yield Load by Exercise and Diet (Female C3 Only)

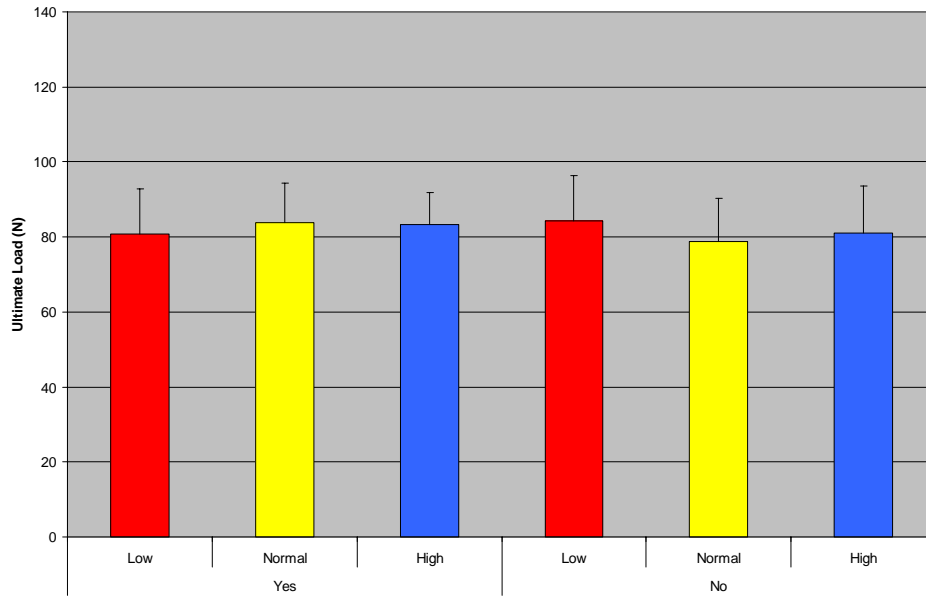


Yield Load by Exercise and Diet (Male C3 Only)

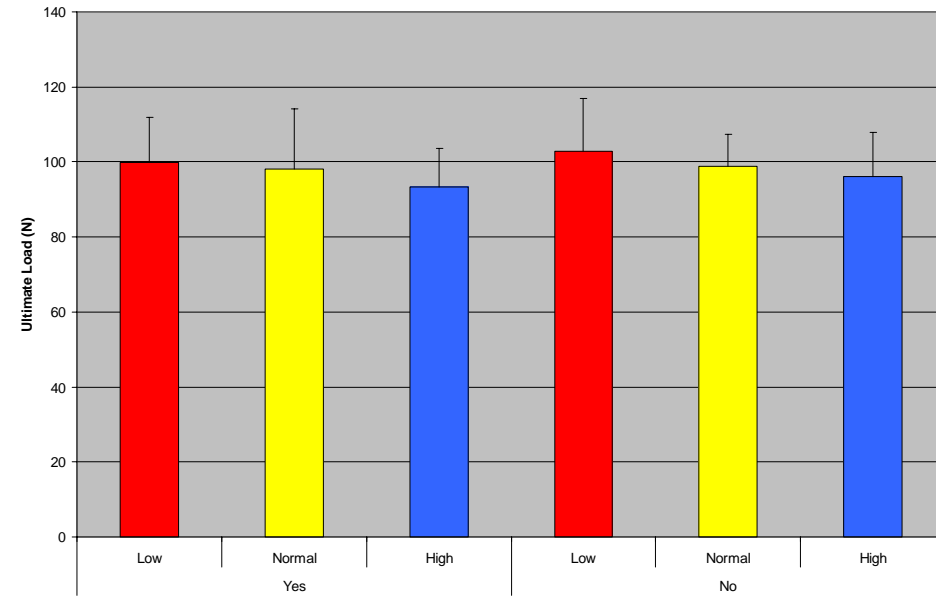


Vertebral Ultimate Load by Diet and Exercise

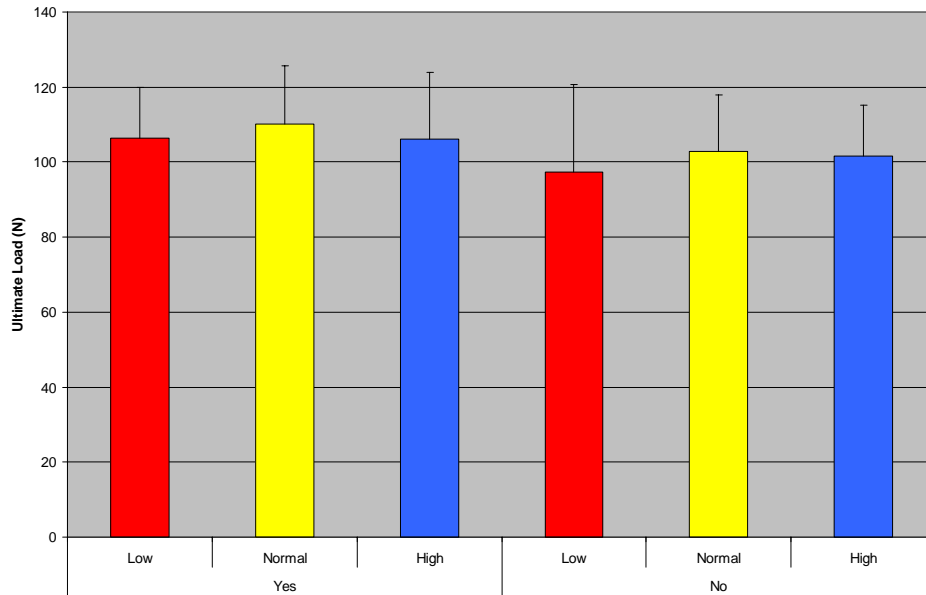
Ultimate Load by Exercise and Diet (Female C5/7 Only)



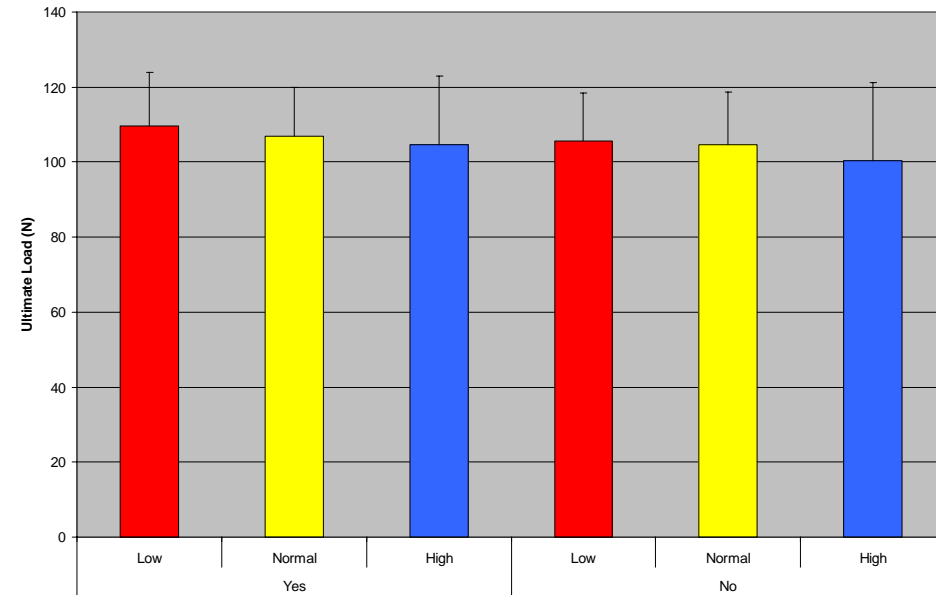
Ultimate Load by Exercise and Diet (Male C5/7 Only)



Ultimate Load by Exercise and Diet (Female C3 Only)

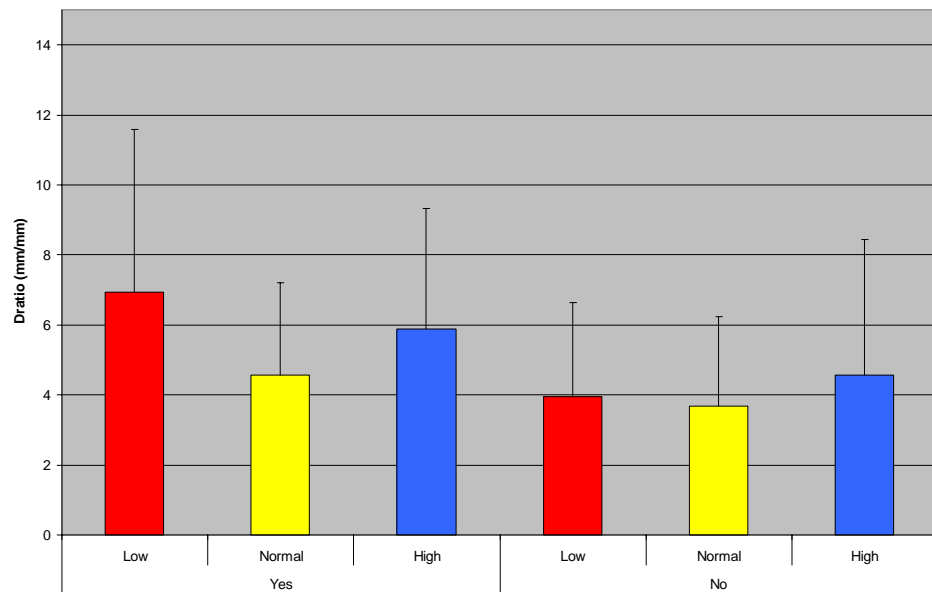


Ultimate Load by Exercise and Diet (Male C3 Only)

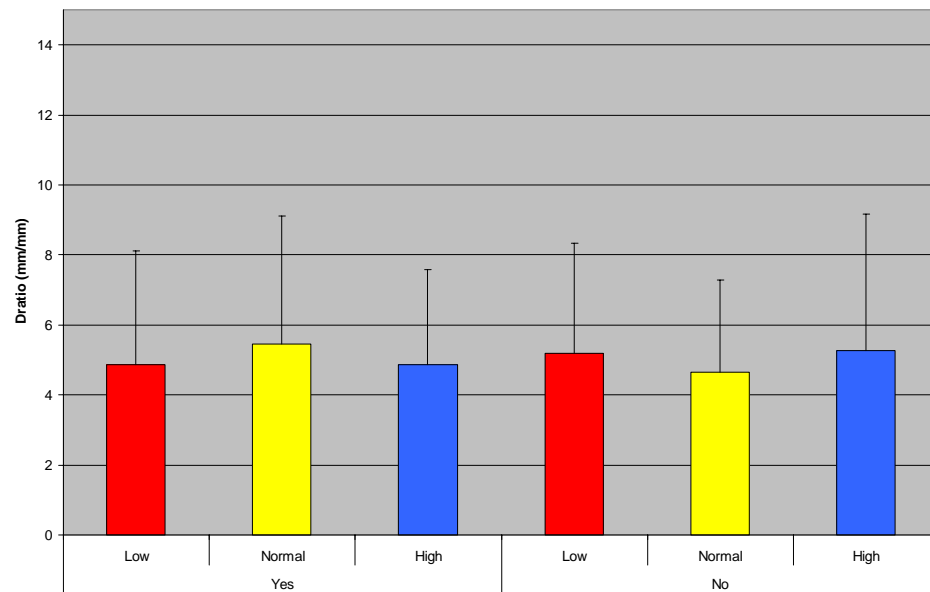


Vertebral Displacement Ratio by Diet and Exercise

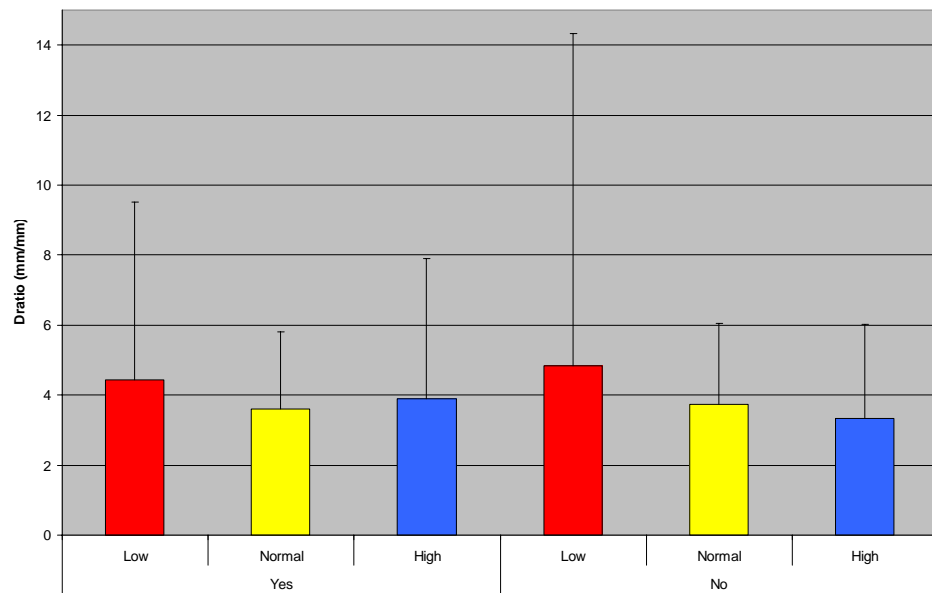
Displacement Ratio by Exercise and Diet (Female C5/7 Only)



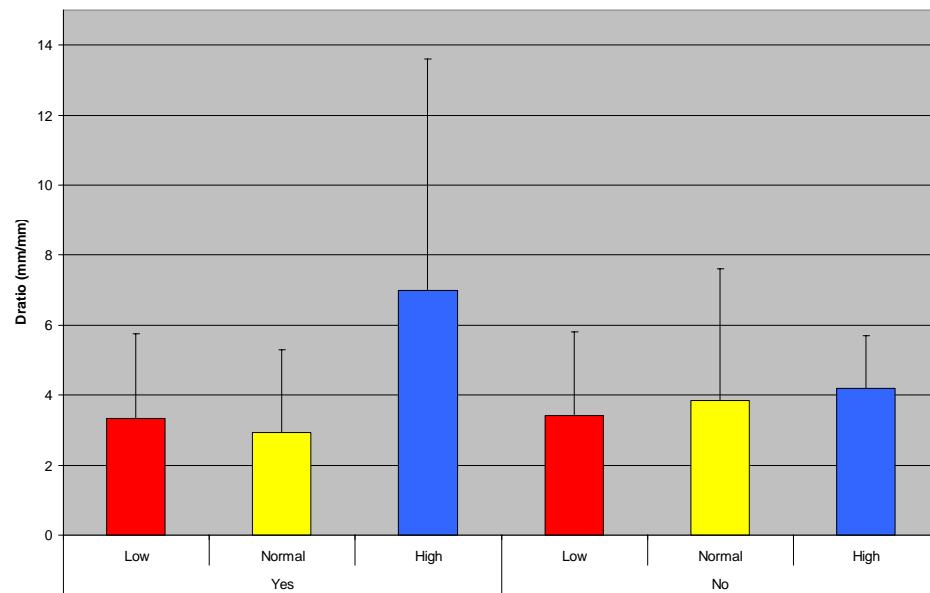
Displacement Ratio by Exercise and Diet (Male C5/7 Only)



Displacement Ratio by Exercise and Diet (Female C3 Only)

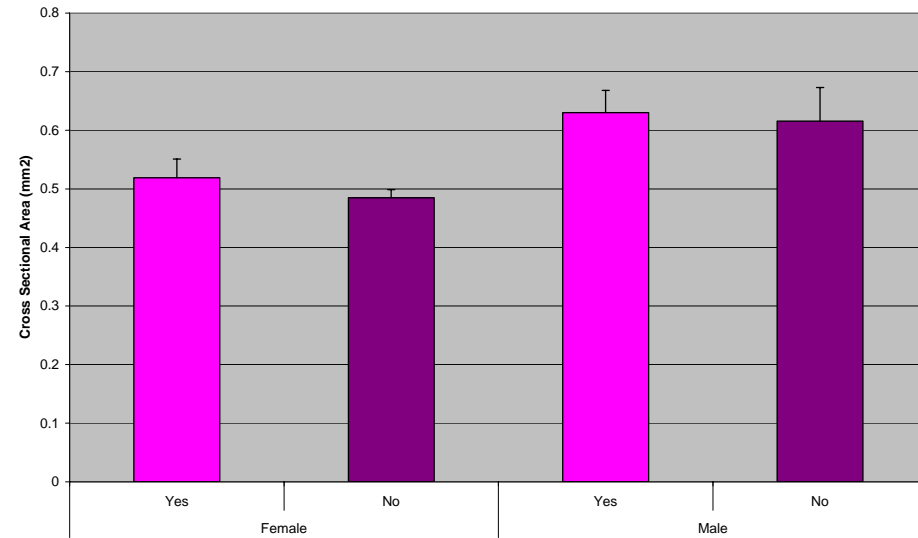


Displacement Ratio by Exercise and Diet (Male C3 Only)

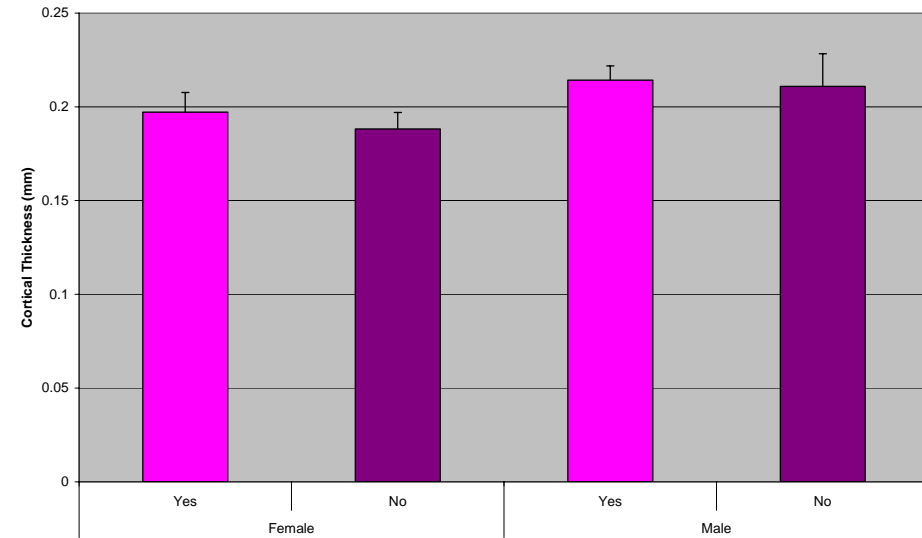


Tibial Mid-diaphyseal Cortical Parameters by Sex and Exercise

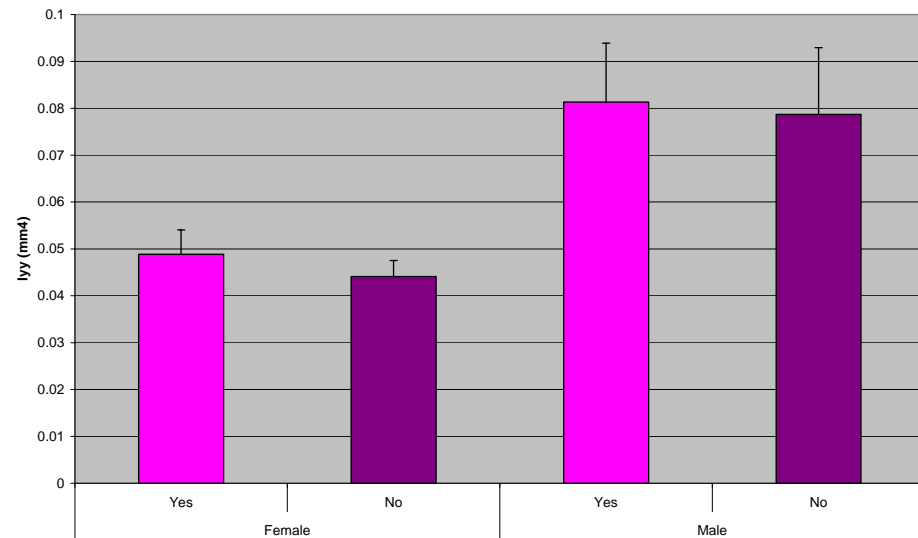
Cross Sectional Area by Sex and Exercise
(Normal Diet, C57 Strain)



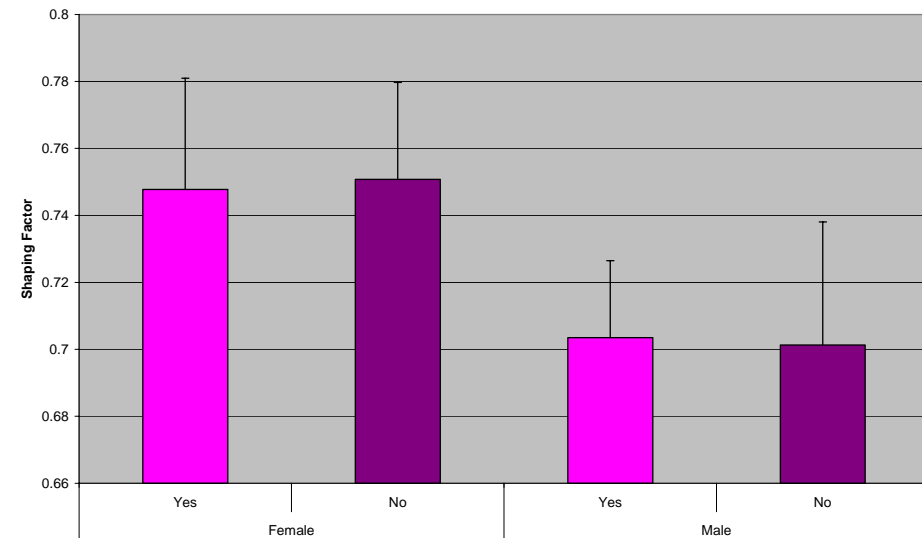
Cortical Thickness by Sex and Exercise
(Normal Diet, C57 Strain)



Bending Moment of Inertia by Sex and Exercise
(Normal Diet, C57 Strain)

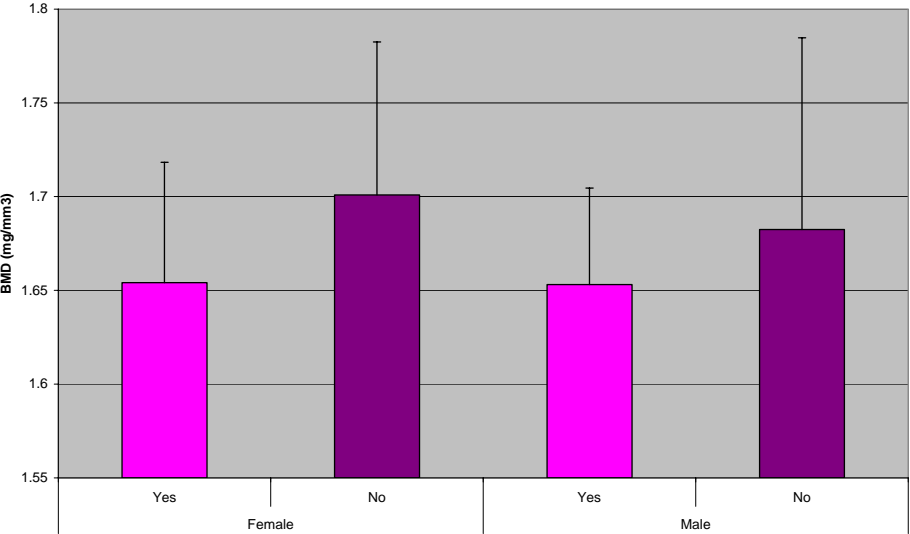


Shaping Factor by Sex and Exercise
(Normal Diet, C57 Strain)

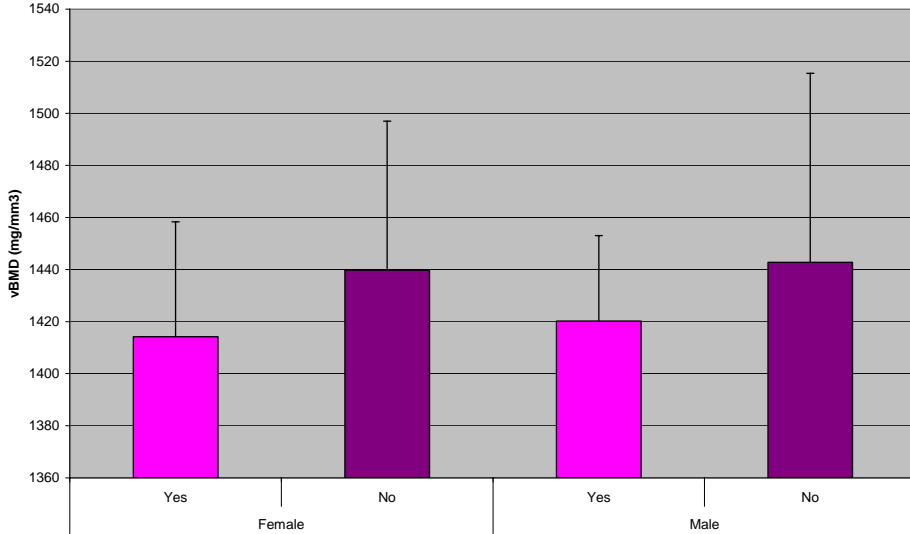


Tibial Mid-diaphyseal Cortical Parameters by Sex and Exercise

Bone Mineral Density by Sex and Exercise
(Normal Diet, C57 Strain)

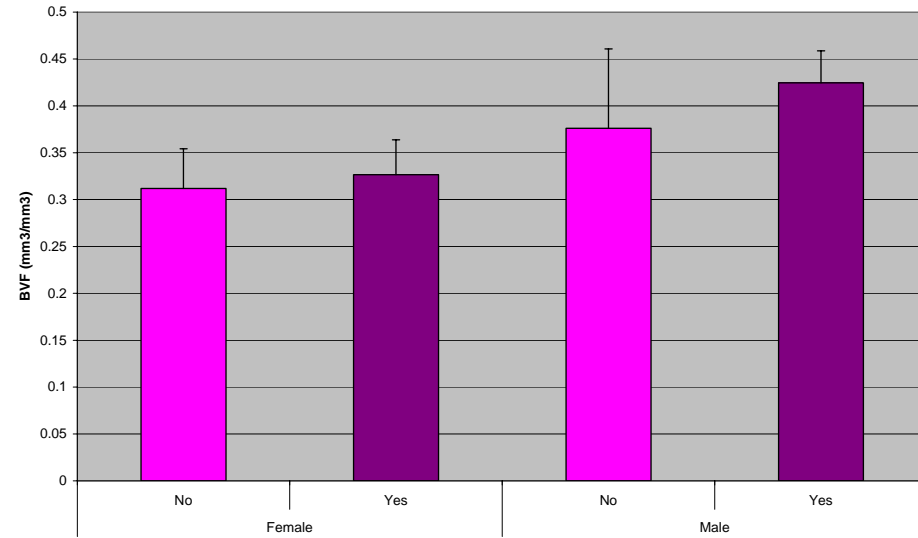


Volumetric Bone Mineral Density by Sex and Exercise
(Normal Diet, C57 Strain)

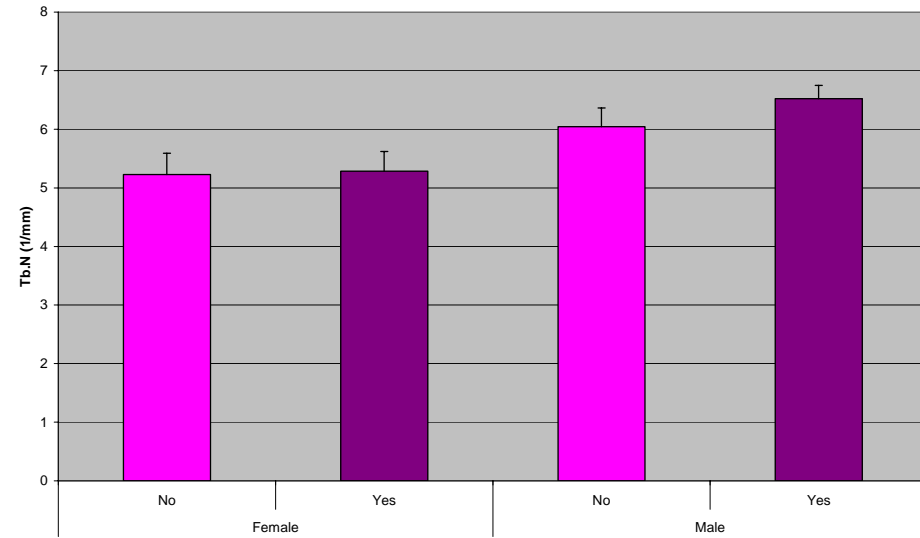


Tibial Proximal Metaphyseal Trabecular Parameters by Sex and Exercise

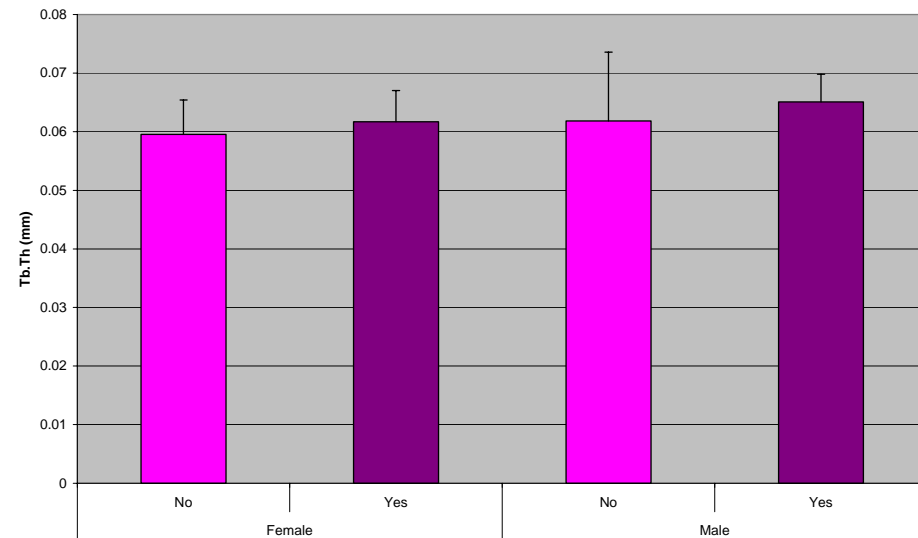
**Tibia Metaphyseal Bone Volume Fraction by Sex and Exercise
(Normal Diet, C57 Strain)**



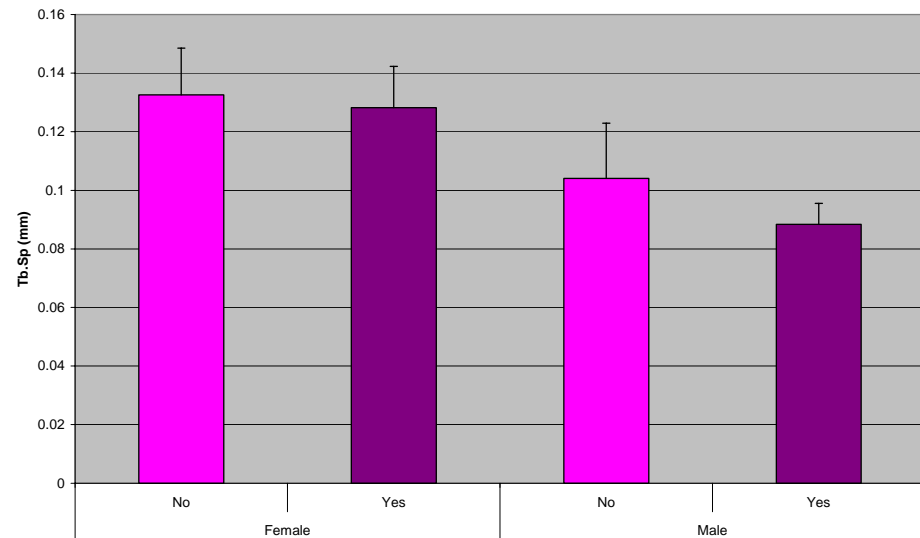
**Tibia Metaphyseal Trabecular Number by Sex and Exercise
(Normal Diet, C57 Strain)**



**Tibia Metaphyseal Trabecular Thickness by Sex and Exercise
(Normal Diet, C57 Strain)**

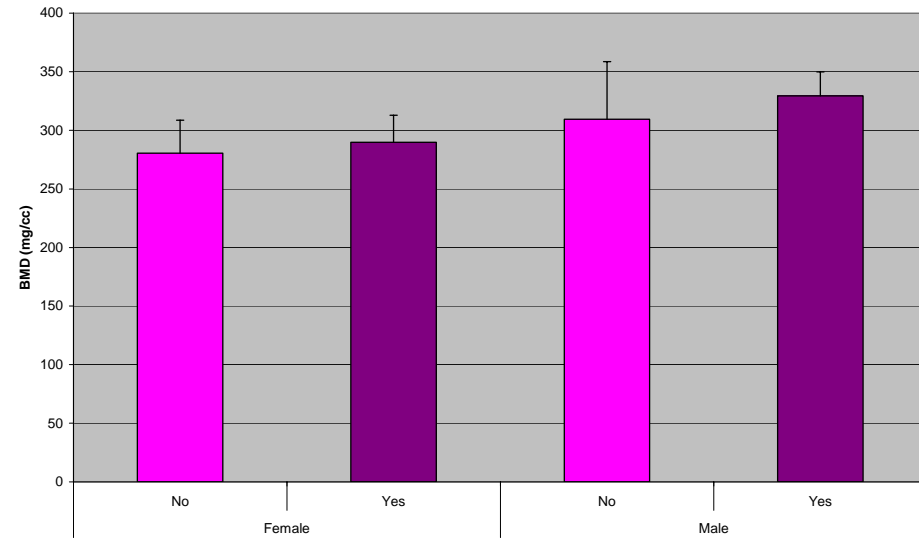


**Tibia Metaphyseal Trabecular Spacing by Sex and Exercise
(Normal Diet, C57 Strain)**

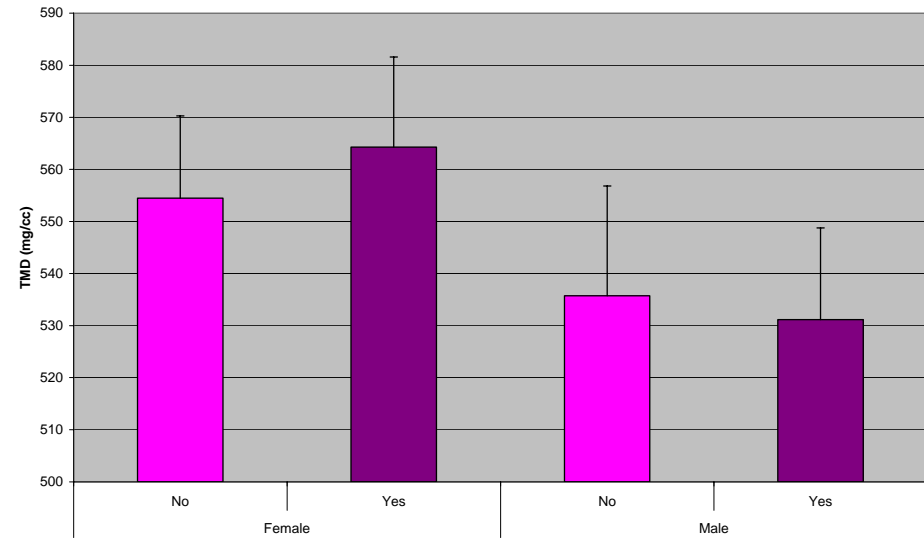


Tibial Proximal Metaphyseal Trabecular Parameters by Sex and Exercise

Tibia Metaphyseal Bone Mineral Density by Sex and Exercise
(Normal Diet, C57 Strain)

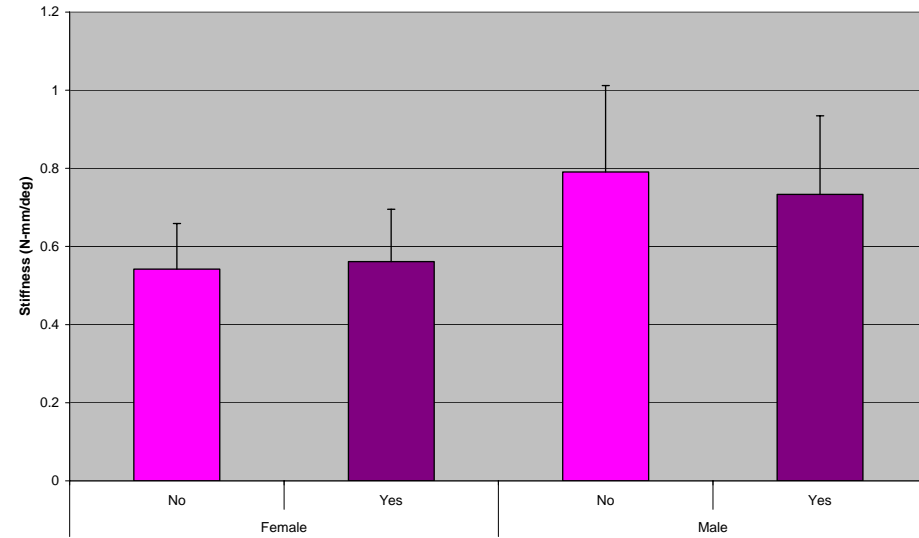


Tibia Metaphyseal Tissue Mineral Density by Sex and Exercise
(Normal Diet, C57 Strain)

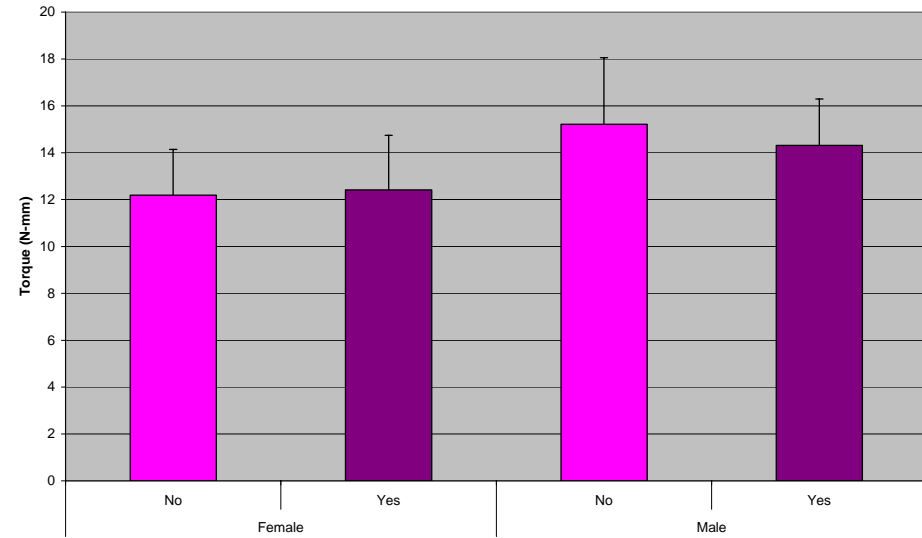


Tibial Torsion Parameters by Sex and Exercise

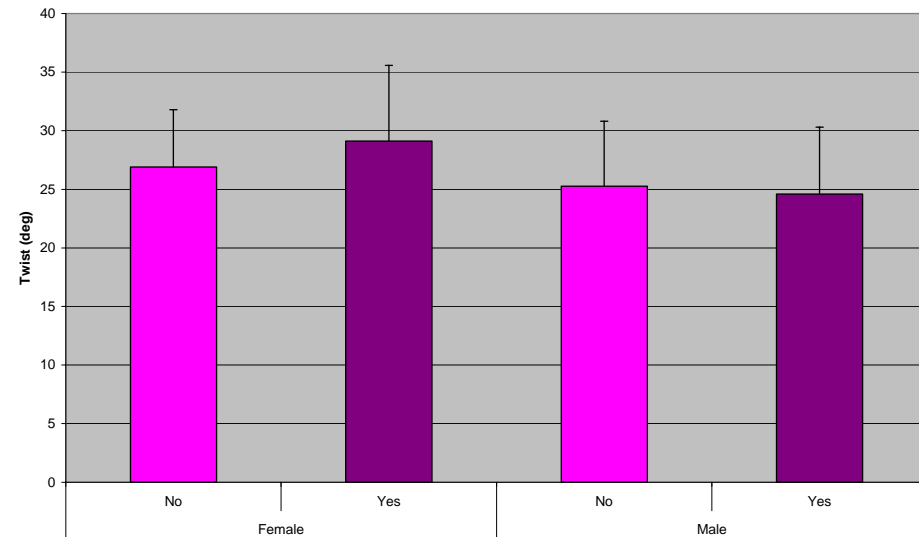
Stiffness by Sex and Exercise
(Normal Diet, C57 Strain)



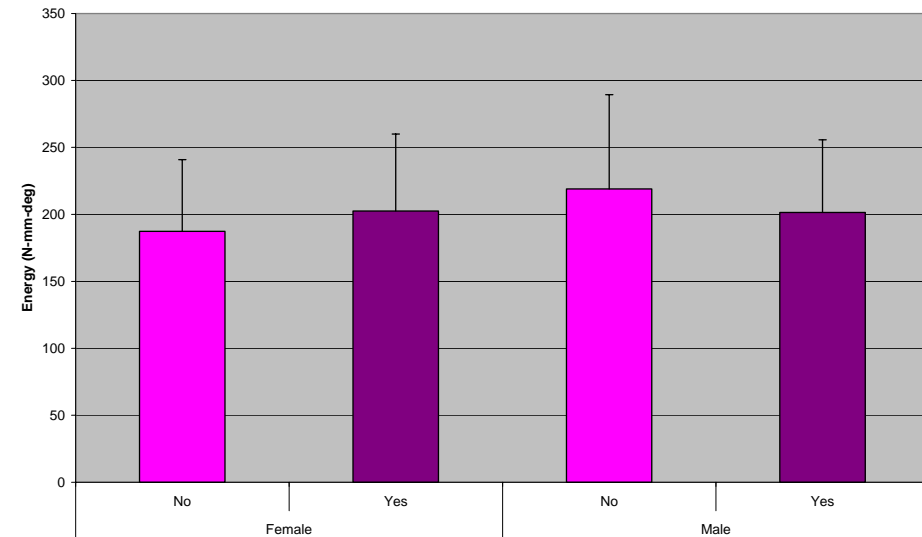
Failure Torque by Sex and Exercise
(Normal Diet, C57 Strain)



Failure Twist by Sex and Exercise
(Normal Diet, C57 Strain)

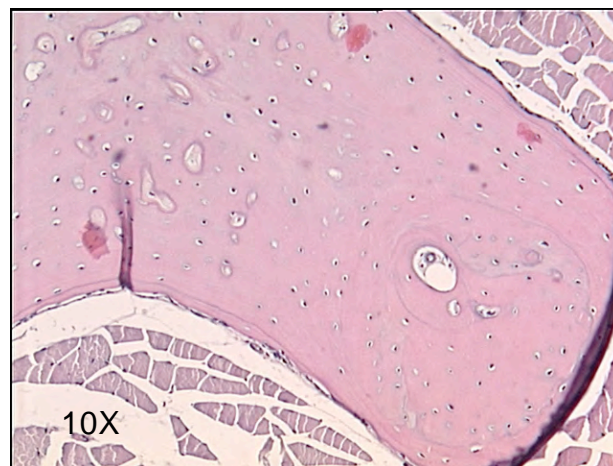
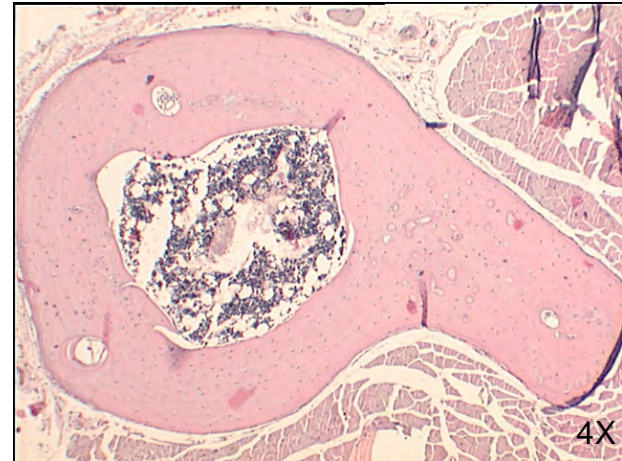
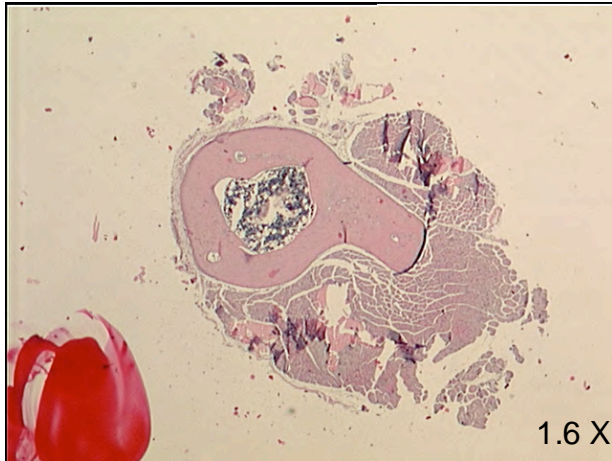


Energy by Sex and Exercise
(Normal Diet, C57 Strain)



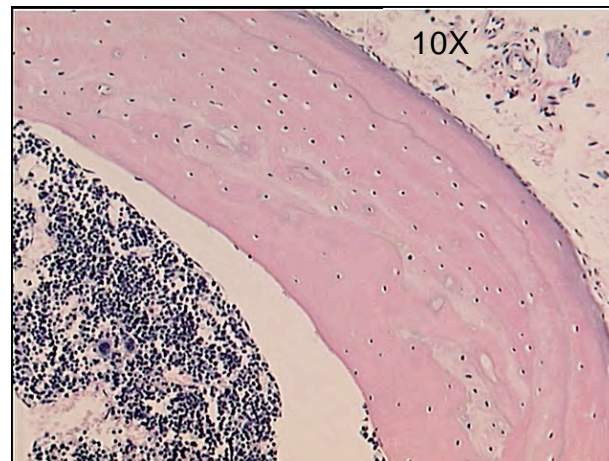
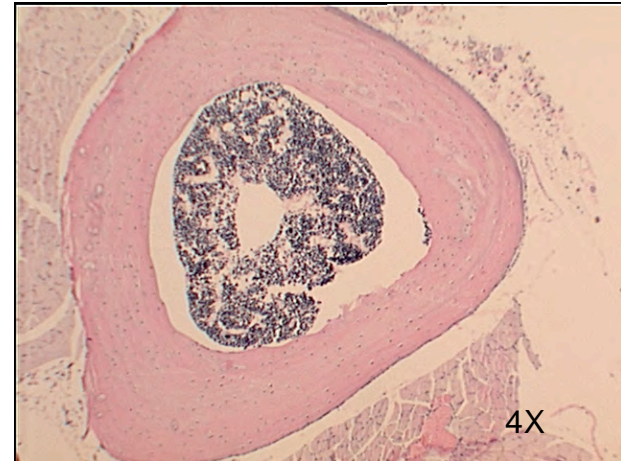
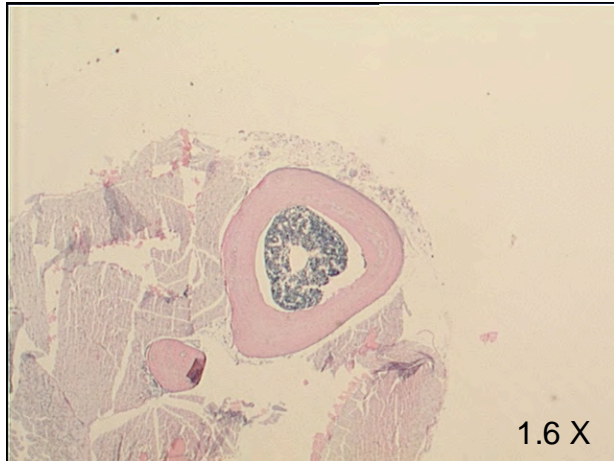
2T d3

M C57 Low Yes

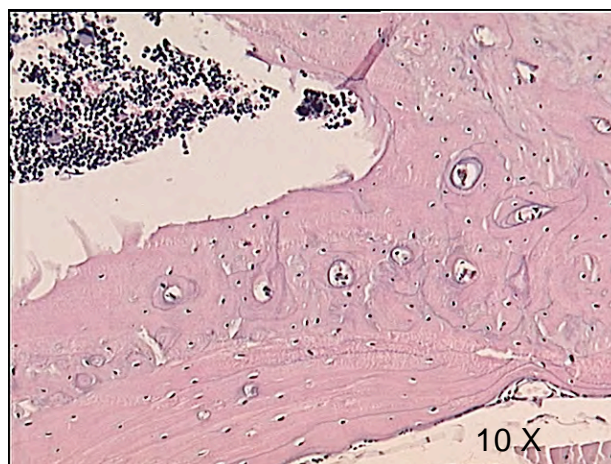
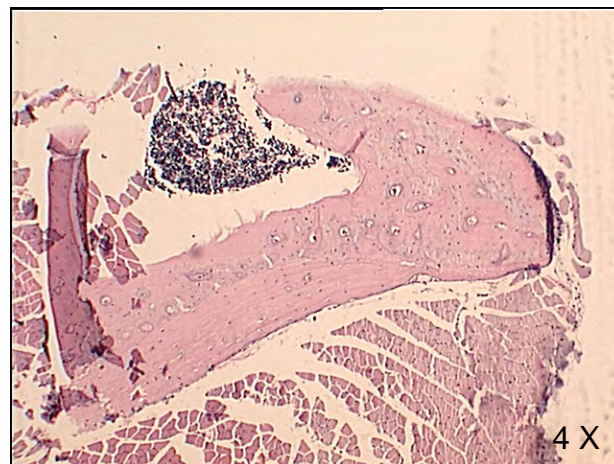
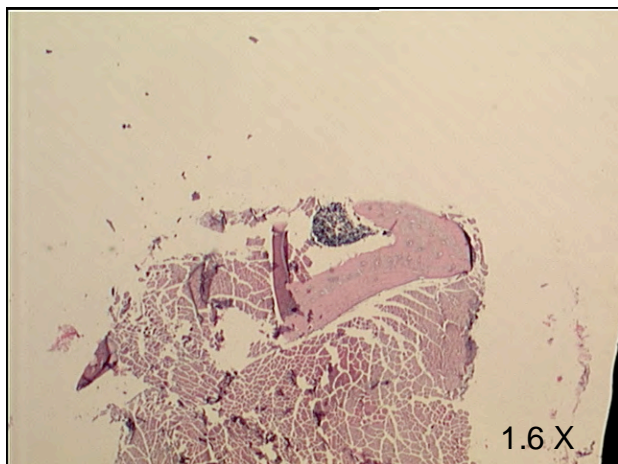


128T d3

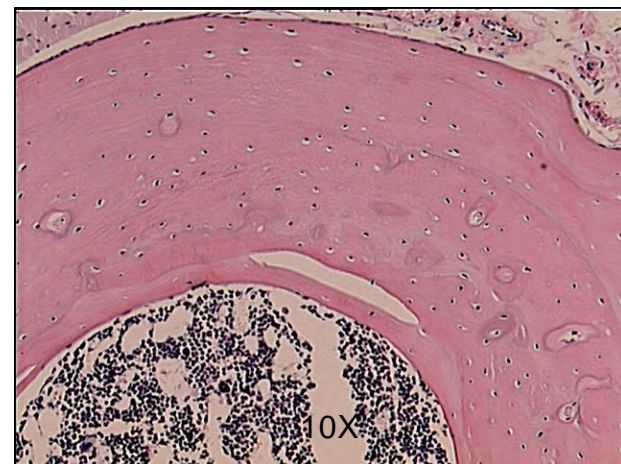
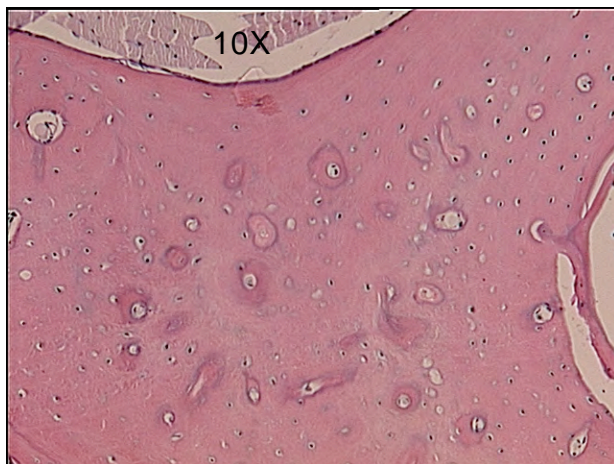
M C57 High Yes



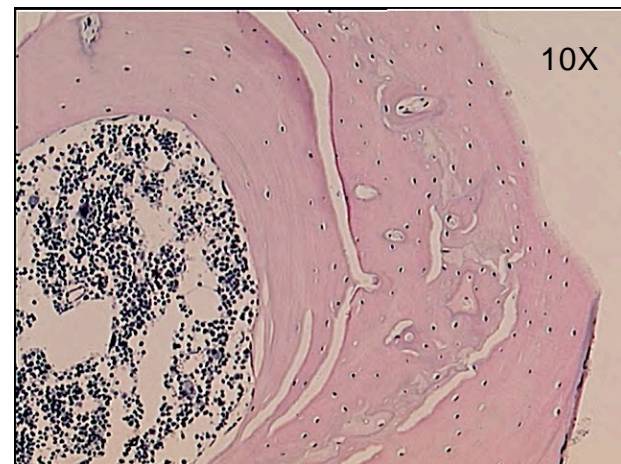
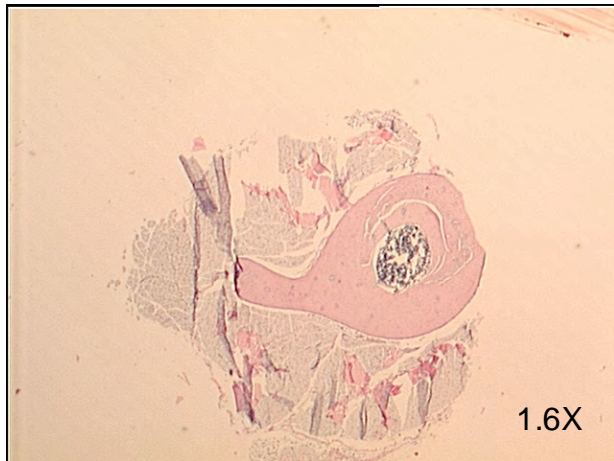
184T
m³
M³C3 Low Yes



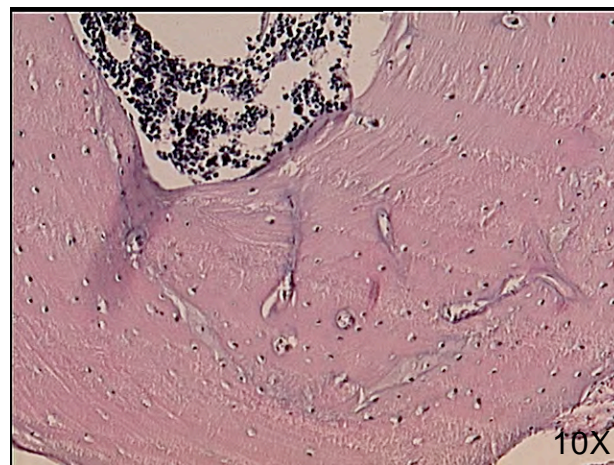
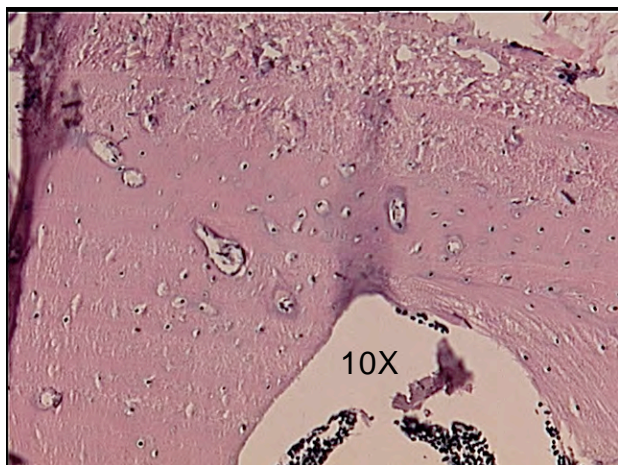
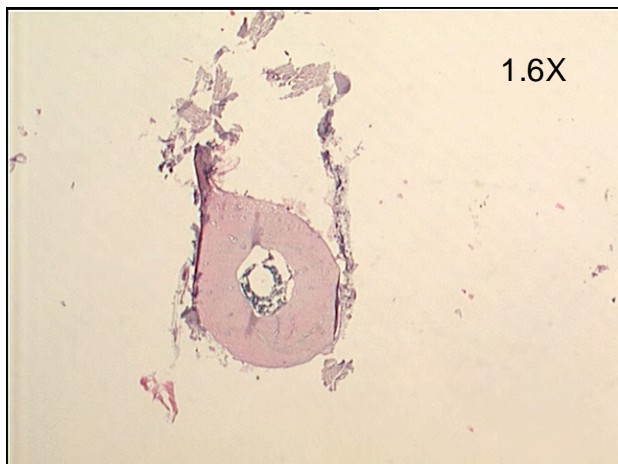
198T d1
M C3 Low No



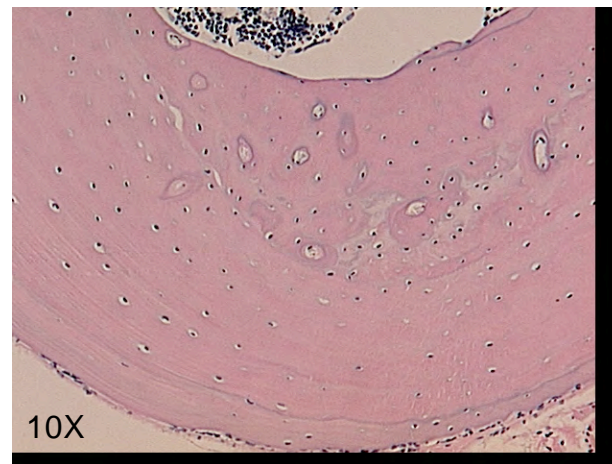
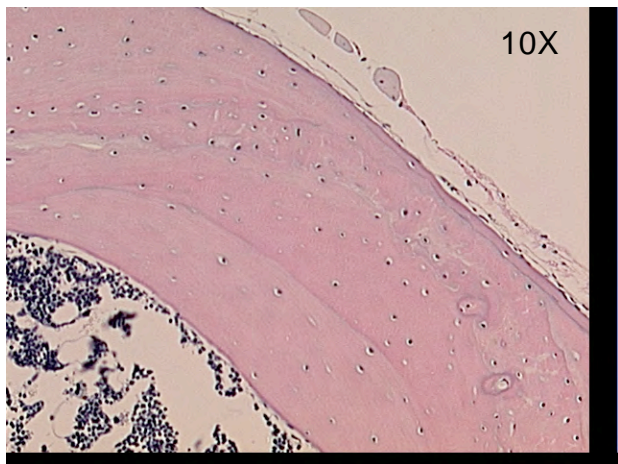
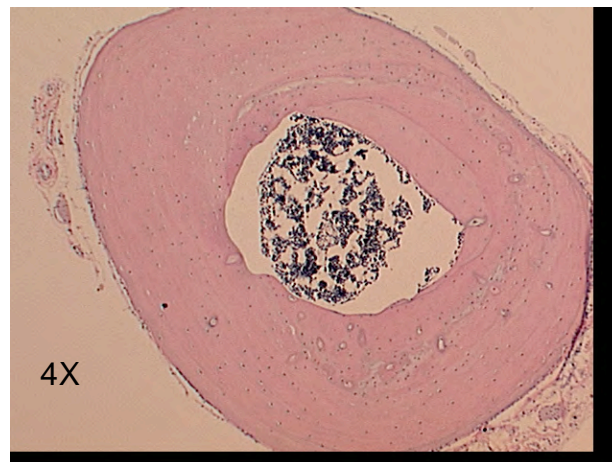
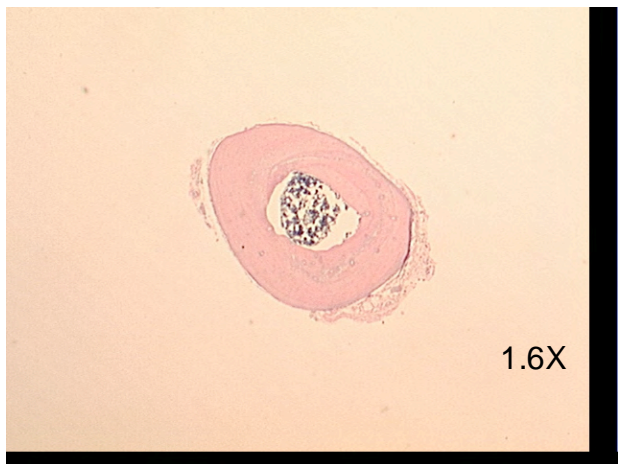
226T m1
F C3 Normal Yes



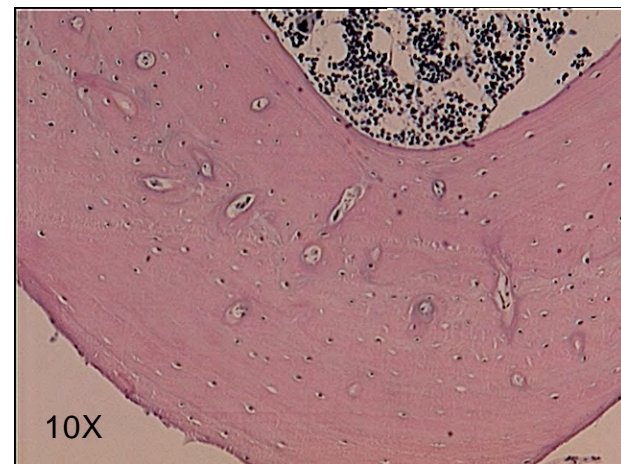
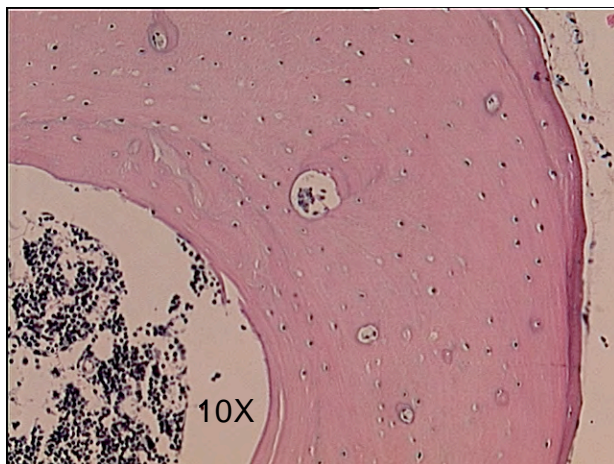
261T d1
F C3 Normal No



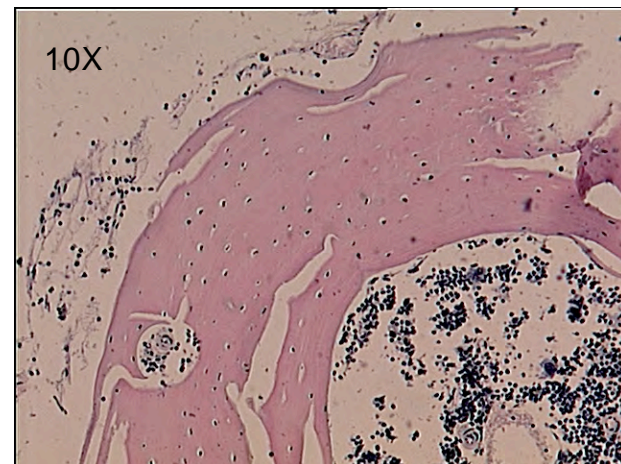
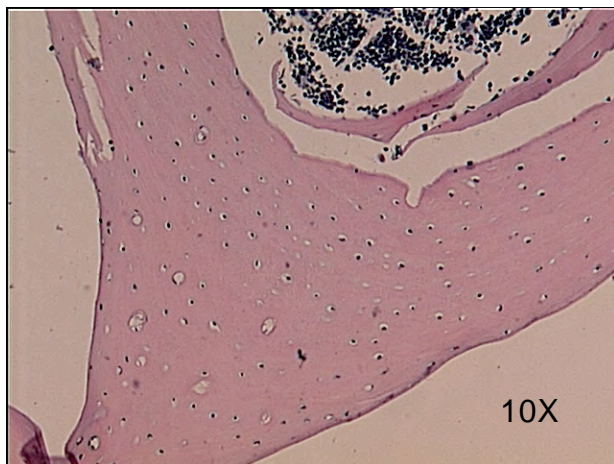
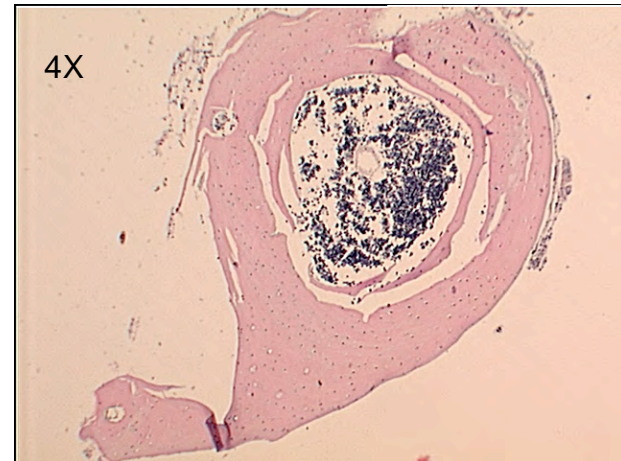
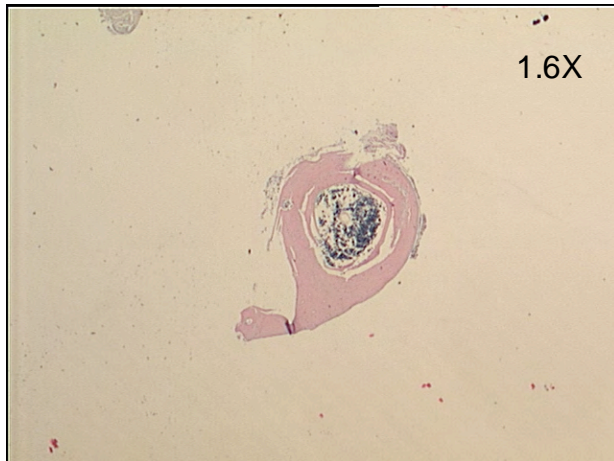
296T d3
M C3 High Yes



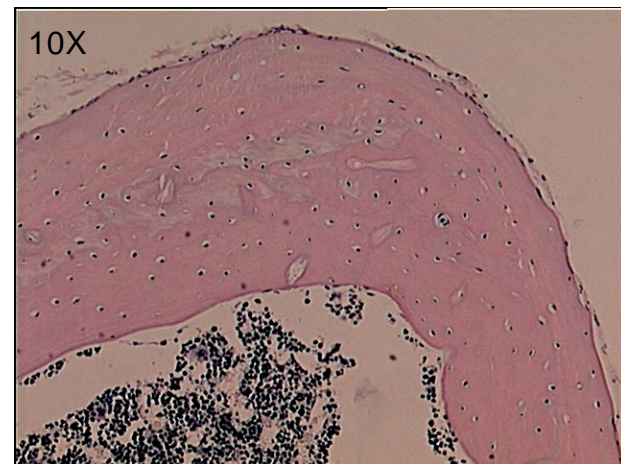
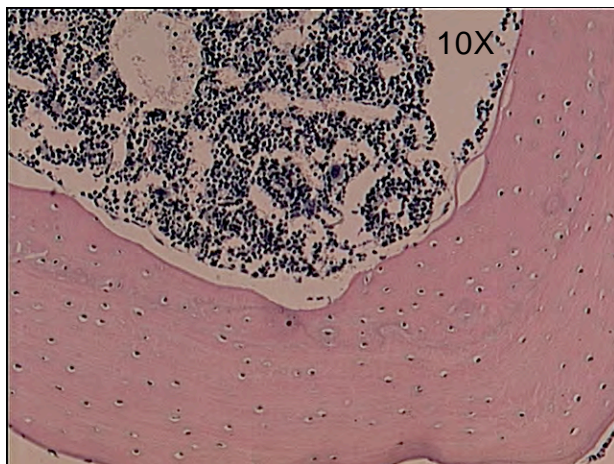
317T d3
M C57 High No



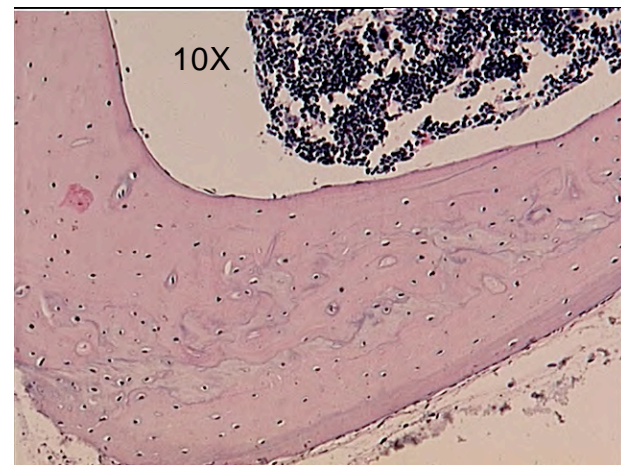
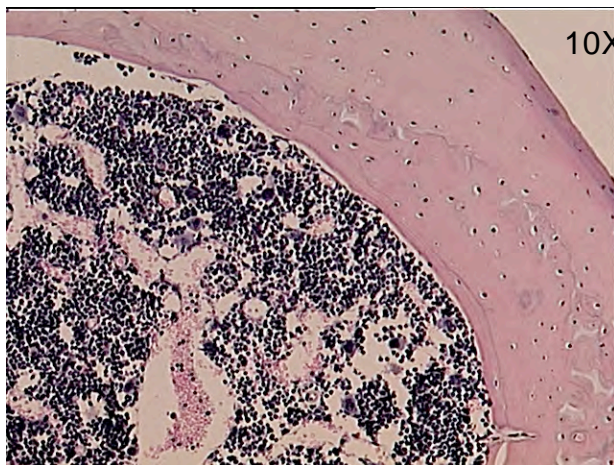
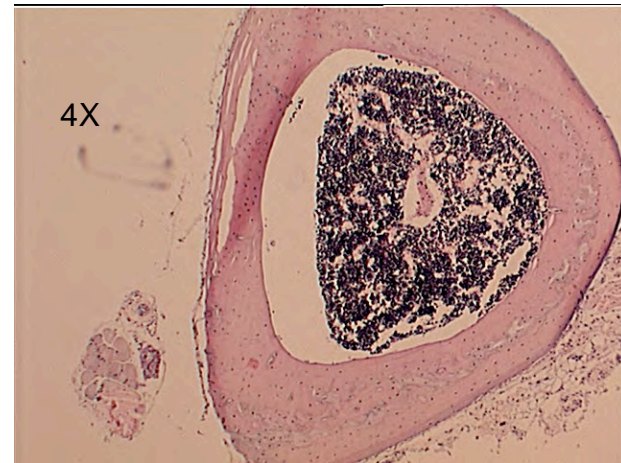
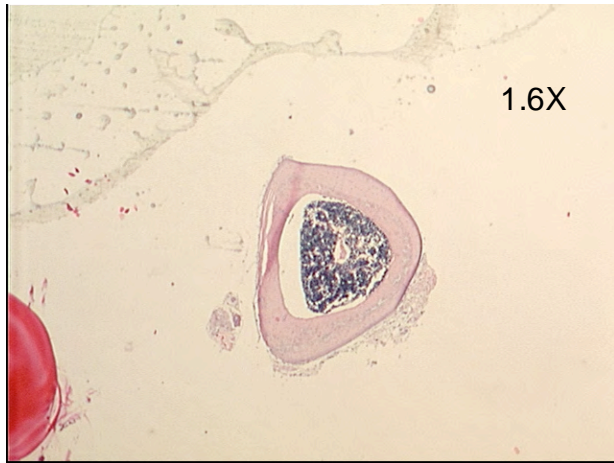
366T d3
F C57 Low No



415T d3
M C57 Normal Yes



443T d1
M C57 Normal No



478T d3
F C57 High No

